Experimental and numerical investigation of flash floods and their interaction with urban settlements

Stamataki, Ioanna

Award date:
2020

Awarding institution:
University of Bath

Experimental and numerical investigation of flash floods and their interaction with urban settlements

Ioanna Stamataki

A thesis submitted for the degree of Doctor of Philosophy

University of Bath

Department of Architecture and Civil Engineering

August 2019

DECLARATION OF ANY PREVIOUS SUBMISSION OF THE WORK

The material presented here for examination for the award of a higher degree by research has not been incorporated into a submission for another degree.

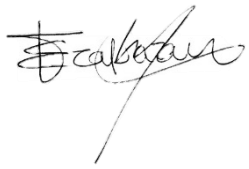

DECLARATION OF AUTHORSHIP

I am the author of this thesis, and the work described therein was carried out by myself personally.

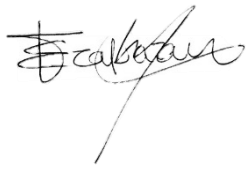

ABSTRACT

Flash floods remain a challenging global problem and due to their dynamic nature combined with their limited spatial and temporal scales. Flash flood modelling is a complex process and numerical simulation of the phenomena requires a deep understanding of the event and complex, three-dimensional modelling if the processes involved are to be replicated to a high level of detail. This thesis explores flash floods and aims to provide further insight into their numerical simulation.

A new dataset for flash floods has been created through a comprehensive set of dam break experiments on ramps of different resistance undertaken in the Department of Mechanical Engineering in University College London (UCL). This dataset illustrates high Froude number flows on slopes and their interaction with buildings and provides further insight into the effect that land use and intensity have on flash flood propagation.

The obtained experimental results were then used to validate a flash flood hydrodynamic model. The numerical investigation was undertaken using the open source software OpenFOAM and its solver interFOAM which showed that the complexity of these events requires different parametrisation for different stages of the process and cannot be described with one set of parameters for the whole progression, thus demonstrating the need for either full 3D simulations or 2D-3D coupled models.

Useful insights regarding the modelling of flash floods were also acquired assessing the Defra and Environment Agency (2010) benchmarking test case for extreme events and comparing the 3D OpenFOAM model's performance with other industrial software. Finally, through the analysis of applied forces acquired from the experimental and numerical work of flood wave interaction with structures, mitigation strategies were suggested for flood risk in flash flood prone areas.

ACKNOWLEDGMENTS

My PhD research has been truly the most difficult and most rewarding experience of my life. Through these years I have learned more about myself than I knew, I have been inspired, I have grown as a person, I have felt loved and supported and at the same time alone and struggling and through it all I have met incredible people and grew closer with many in my life. This PhD would not have been the same without the support and encouragement of all these people so *thank you to all of you*.

My most sincere acknowledgements are dedicated to Dr Jun Zang for always supporting me, for knowing I would do a PhD before I even knew it myself, for always being there and for always being in my life as a mentor and guide.

I would like to thank Dr Thomas Kjeldsen for his support and supervision, for always reminding me to look at the big picture and helping me develop into an independent researcher.

I would also like to show my gratitude to Dr Eugeny Buldakov and Dr Dimitris Stagonas for giving me the opportunity to conduct my experiments at UCL, for caring so much about my work, for being incredible teachers and always being helpful with their comments and suggestions.

I want to especially thank Will Bazeley for his invaluable help and support during many critical stages of the research and the technicians in UCL, especially Les Ansdell for being supportive, always positive and helping me immensely during the experiments.

Special thanks go to WISE and EPSRC for offering me this incredible opportunity, funding me through this research (EP/L016214/1) and for creating a wonderful network that I am so happy and proud to be part of. To the whole of WEIR for creating a wonderful team and research group. I would also like to thank the University of Bath and the HPC facility at Bath for facilitating my numerical work.

I would also like to take this opportunity to thank my examiners Dr Chris Blenkinsopp and Dr Catherine Wilson for offering their time, reading my thesis with such interest and creating a wonderful environment for discussion.

To all friends and loved ones. Especially thanks to Irini for believing in me and being more like a sister full of infinite positive energy and to everyone I met along the way and made this journey better in so many ways Olivia, Ludo, Mariano, Naomi and Ernesto- this adventure

would not have been the same without you and your support! Eleni, thank you for introducing me to Iyengar yoga. Kirsten and Richard Agar Ward your help has been irreplaceable, thank you for everything.

Above all, I want to thank my parents for making all of this possible, for their unconditional support, love and belief in me. I could never thank you enough!

To you Mour, for your support, encouragement and love – I could not have done this without you. I love you!

CONTENTS

TABLE OF FIGURES

TABLE OF TABLES

SYMBOLS AND ABBREVIATIONS

Symbols

∇^2	Laplace operator
h_L	Local water depth on left cell (m)
h_R	Local water depth on right cell (m)
h_o	Initial water depth (m)
C_o	Courant number
C_μ	Empirical constant $(C_\mu = 0.09)$
L_0	Reservoir length (m)
S_{fx}	Friction slope in the x-direction (m/m)
S_{fy}	Friction slope in the y-direction (m/m)
S_o	Slope (m/m)
T_c	Time of flood concentration (s)
T_o	Operational response time (s)
U_r	Compressive velocity (m/s)
c_s	Roughness constant
d_{max}	Eddy maximum diameter (m)
d_{min}	Eddy minimum diameter (m)
d_o	Initial water depth (m)
k_s	Roughness height (m)
$\vec{n}$	Unit normal direction vector
t_{op}	Gate opening time (s)
u^o_{max}	Eddy maximum orbital velocity (m/s)
u^o_{min}	Eddy minimum orbital velocity (m/s)
x_f, x_s	The dam break's wave tip position (m)
y_c	Critical depth (m)
z_{bL}	Bed elevation in the left cell (m)
z_{bR}	Bed elevation in the right cell (m)
η_L	Local water depth within left cell (m)
η_R	Local water depth within right cell (m)
μ_t	Eddy viscosity $(Pa\ s)$
h	Water depth (m)

i	Unit vector in the x-direction
j	Unit vector in the y-direction
M	Mass (kg)
A	Area of flow (m^2)
E	Specific energy (m)
F	Flux $(m^3/s \cdot m^2)$
Fr	Froude number
L	Length (m)
P	Wetted perimeter (m)
Q	Volume flux, flow rate (m^3/s)
U	Velocity (m/s)
V	Velocity (m/s)
d, D	Hydraulic mean depth (m)
dS	The differential-sized control surface area
dV	The differential-sized control volume
ds	Control surface area (m^2)
fx	Applied force in x-direction (N)
fy	Applied force in y-direction (N)
fz	Applied force in z-direction (N)
g	Gravity acceleration (m/s^2)
k	Kinetic energy (m^2/s^2)
n	Manning's roughness coefficient
p	Pressure (Pa)
q	Discharge per unit width (m^2/s)
t	Time (s)
u	Velocity component in the x-direction (m/s)
v	Velocity component in the y-direction (m/s)
w	Velocity component in the z-direction (m/s)
x	Distance in the x-direction (m)
Δt	Change in time (s)
Δx	Grid spacing in the x-direction (m)
Δx	Change in position (m)
Δy	Grid spacing in the y-direction (m)
α	Extension of the breach (m)

α	Water volume fraction
ε	Turbulent dissipation (m/s^3)
κ	Surface curvature $(1/m)$
λ	Geometric scaling factor
μ	Dynamic viscosity $(Pa \cdot s)$
ρ	Density (kg/m^3)
σ	Surface tension coefficient (N/m)

Abbreviations

1D	One dimensional
2D	Two dimensional
3D	Three dimensional
B0	No building
B1	Single building
B2	Two buildings
B4	Four buildings
CFD	Computational Fluid Dynamics
CRED	Centre for Research on the Epidemiology of Disasters
DEFRA	The Department for Environment, Food and Rural Affairs in the United Kingdom
EA	Environment Agency in the United Kingdom
EEA	European Environmental Agency
ESSL	European Severe Storms Laboratory
FDM	Finite Difference Method
FEM	Finite Element Method
FVM	Finite Volume Method
G	Grass
G_n	Gauge number n
H100	Initial water depth in reservoir $0.1\ m$
H200	Initial water depth in reservoir $0.2\ m$
IPCC	Intergovernmental Panel on Climate Change
MARIN	Maritime Research Institute Netherlands
OEI	Operation Efficiency Index
PC	Personal Computer
R	Mesh size

RANS	Reynolds-averaged Navier–Stokes equations
SWEs	Shallow Water Equations
UCL	University College London
U_n	Ultrasonic probe number n
UNISDR	UN Office for Disaster Risk Reduction
WG_n	Wave Gauge number n
WMO	World Meteorological Organisation
δ-SPH	Smoothed Particle Hydrodynamics model with numerical diffusive terms
δ	Dirac delta function

1 INTRODUCTION AND BACKGROUND

1.1 BACKGROUND

One expected consequence of climate change is an increase in the frequency and magnitude of flooding. The UN Office for Disaster Risk Reduction (UNISDR et al.) in collaboration with the Belgian-based Centre for Research on the Epidemiology of Disasters (CRED) produced a report in 2015 entitled "The Human Cost of Weather Related Disasters" and found that since 1995 there were 157,000 deaths associated with flooding. Furthermore, floods accounted for 47% of all other weather disasters, with 3,062 events in the last 20 years resulting in 2.3 billion people being affected by floods (UNISDR et al., 2015).

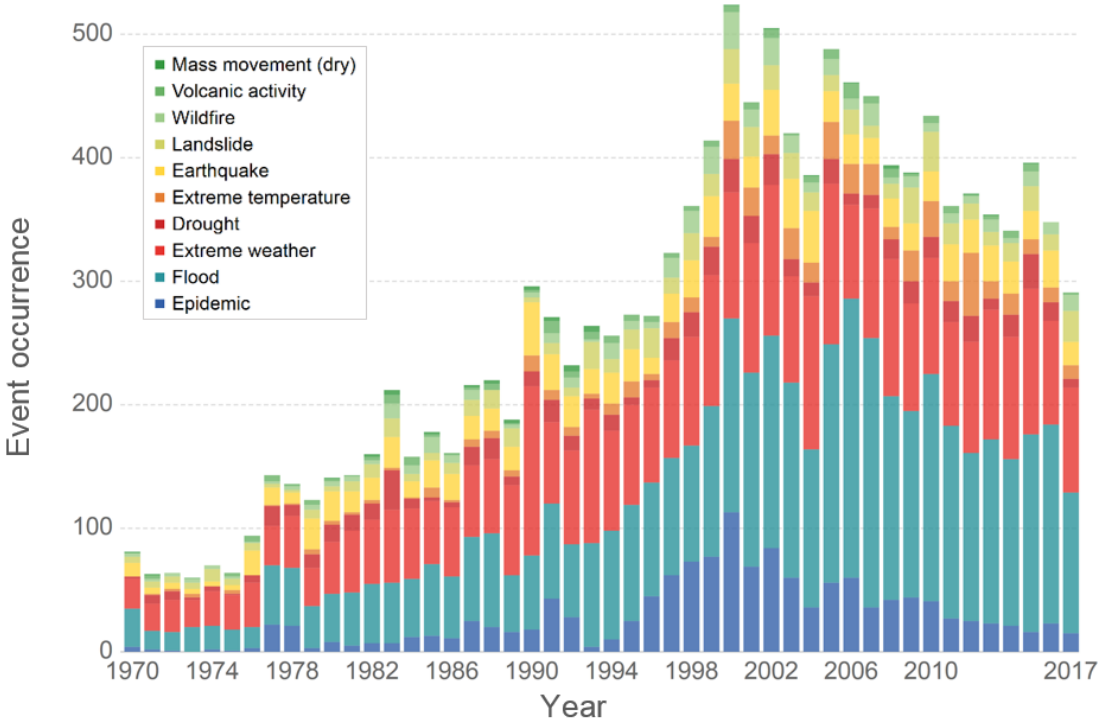

Figure 1-1- Data accumulated by the International Disaster Database showing the number of disasters from 1970 to 2017 looking at geophysical, meteorological, hydrological and climatological events. (EMDAT, 2017)

Figure 1-1 shows data accumulated by the International Disaster Database in CRED and presents the event occurrence of different geophysical, meteorological, hydrological and climatological events from 1970 to 2017 showing a significant increase in the number of floods (EMDAT, 2017). In this research, flash floods are of particular interest as they are a destructive natural hazard with one of the highest mortalities (Sene, 2013). Flash floods are short duration floods associated with excessive amounts of water and are considered a

destructive natural hazard with one of the highest mortalities. There are different causes for such events: a short period intense rainfall, snow melt events, hydraulic structure failures or glacier lake outbursts (World Meteorological Organisation, 2012; Archer and Fowler, 2015).

In line with the above-mentioned predictions, the Intergovernmental Panel on Climate Change (IPCC) expects an increase in the intensity and frequency of extreme precipitation events in the future. Regular assessments of climate change and its impact are conducted, and Synthesis Reports produced and published every few years. In all of those reports there is a mention of an increase in frequency and intensity of extreme events such as flash floods. The 4th Synthesis Report (AR4) talks about the possibility of an accelerated water cycle, leading to an increased storage capacity of water in the atmosphere which will result in higher frequency and intensity storms (IPCC, 2007). In the 5th Synthesis Report (AR5) there is again discussion of an increase in intensity and frequency of extreme precipitation events (IPCC, 2014) and based on a scoping session in 2017 it is an issue that will also be included in the 6th Synthesis Report (AR6) which will be published in 2022 (IPCC, 2017). This increase in the intensity and frequency of extreme precipitation events will lead to an increase of flash flood events and this is why it is important that the scientific community works to develop new and improved tools to enhance the resilience of urban areas to the threat of extreme flooding through prediction and accurate modelling.

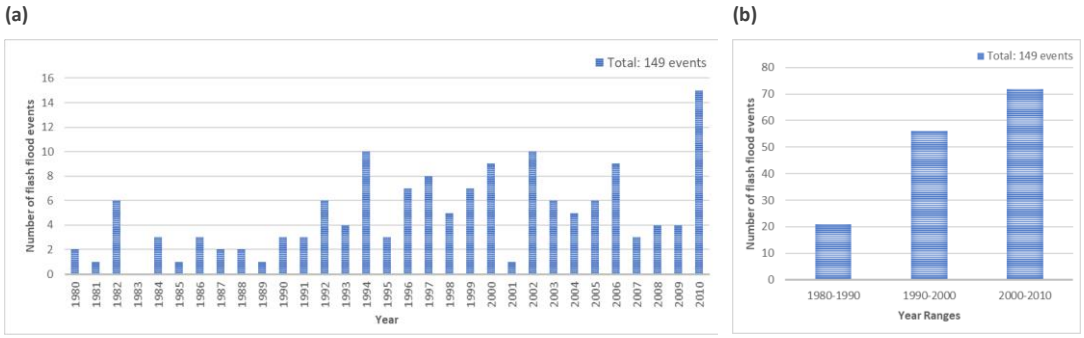

Figure 1-2- Number of flash flood events in Europe from 1980 to 2010 based on the European Environment Agency's dataset (a) by year and (b) by 10 year range (EEA, 2015)

The European Environment Agency has published a dataset containing information on past floods in Europe since 1980. All floods are characterised by type and from 1980 to 2010 a total of 149 events were generated by intense local precipitation events and were characterised as flash floods (Figure 1-2). Some interesting facts that were found through

this database is that there is a clear increase in flash floods when looking at the data in terms of decades. Between 1980 and 1990 there were 21 events recorded, 56 between 1990 and 2000 and 72 between 2000 and 2010. 50% of these events were recorded in the summer, 36% in autumn, 8% in winter and 6% in spring (EEA, 2015). Nevertheless, it is unclear whether the low number of flash floods between 1980-1990 was indeed due to a lack of occurrence or was influenced by the erroneous characterisation of flash floods as large flood events.

The European Severe Storms Laboratory (ESSL) also incorporating parts of northern Africa and the Middle East recorded 152 fatalities due to flash floods in 2018. They produced the map shown in Figure 1-3 and plotted all heavy rain events and flash floods events associated with fatalities. The major highlighted events in Europe were on October 15th in Trebes, France with 13 casualties, on October 9th in Mallorca, Spain with 12 casualties and on November 3rd in Sicily, Italy with 12 casualties (ESSL, 2018). Furthermore, there were more flash floods recorded with no casualties in Montenegro, Netherlands, Sweden, Belgium, Poland, Luxembourg, Slovakia, Slovenia, Bulgaria, Macedonia (FYROM), Greece, Ireland, Switzerland, Ukraine and Norway.

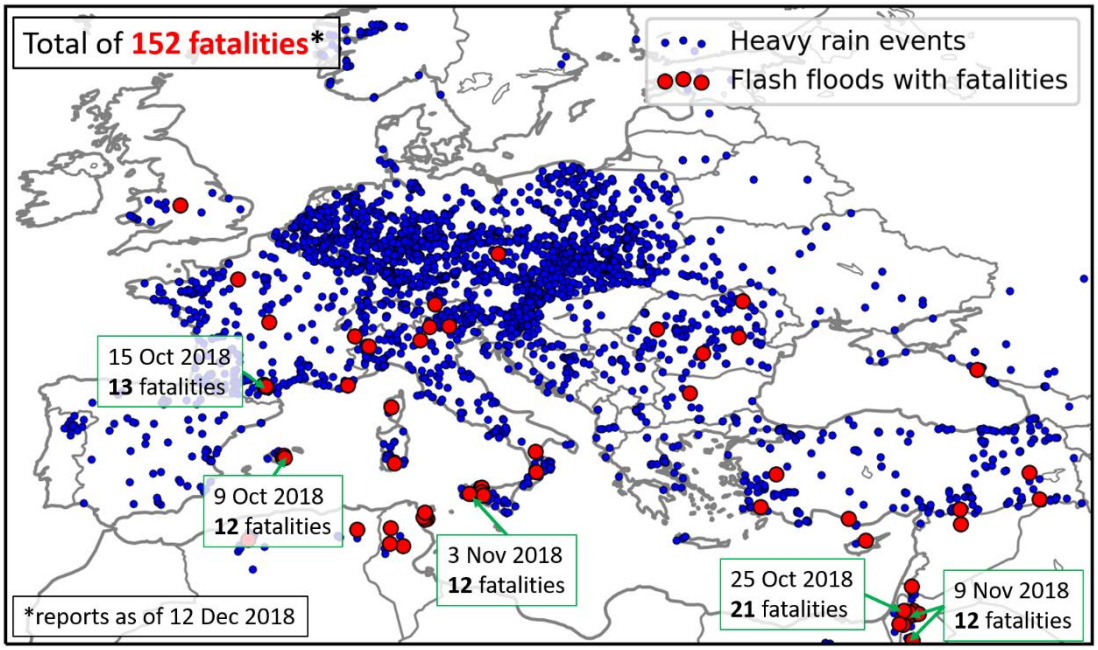

Figure 1-3- Map of deadly flash floods in 2018 produced by the European Severe Storms Laboratory. Heavy rain events are indicated in blue dots and flash floods with fatalities in red (ESSL, 2018)

Topography has proven to be an important characteristic in an area's predisposition to flash floods (World Meteorological Organisation, 2012). Small steep upland catchments often have a naturally flashy response to intense rainfall resulting in important damage from small localised events (Werner and Cranston, 2009). In the last 20 years, there have been several major flash flood events in the UK worth noting, including the 2004 flash flood in Boscastle, Cornwall where $200\ mm$ of rain fell in 5h, equivalent to 20% of the annual average rainfall. During this event, 100 people were evacuated, 60 buildings were flooded/damaged and 116 vehicles were carried by the flow (HR Wallingford, 2005b; Xia et al., 2011b). Secondly, the 2007 large flood in Hull, Yorkshire where $135\ mm$ of rain were measured in 24h equivalent to 20% of the annual average rainfall. 8657 houses and 600 streets were flooded/damaged (Coulthard et al., 2007; Marsh and Hannaford, 2007). Then, in 2011 the Bournemouth, Dorset event where $40.6\ mm$ of rain was recorded in 1h equivalent to 78% of the monthly average rainfall and 270 houses were flooded and/or damaged (Ambrose, 2011). In 2012, a flash flood in Honister Pass, Cumbria flooded 100 houses and $71\ mm$ of rain fell in 24h equivalent to 40% of the monthly average rainfall (Met Office, 2011b, 2013). $125\ mm$ of rain in 24h equivalent to twice the monthly average rainfall was then recorded in 2012 in Aberystwyth, Wales where 150 people had to be evacuated (Webb, 2013; Climate Data, 2018). Finally, in 2018 in Birmingham, West Midlands $81\ mm$ of rain in 1h, equivalent to 1.3 times the monthly average rainfall, resulted in 1 casualty (Met Office, 2011a; Muchan, 2018).

Flash floods remain a global problem and due to their dynamic nature combined with their limited spatial and temporal scales and short lead times, observation, modelling and forecasting of these events continues to be a challenge (World Meteorological Organisation, 2012). Even though the accuracy of flood estimation for extreme events and flash floods was found to be a common problem, shared databases or common guidelines do not exist, and each individual country is focusing their efforts primarily in national projects. This localised and site-specific approach has led to often simplistic and rarely generalised approaches and strategies resulting in further uncertainty in the reliability of flash flood prediction, estimation and mitigation (Kjeldsen et al., 2014). But improving the understanding of the origination and the physical processes of flash floods is a crucial step towards achieving an effective flood risk management strategy (Huang et al., 2015).

As very limited field data exist from flash floods, a practical approach to generate flash floods, both numerically and experimentally, is through a dam break. This guarantees the main characteristic features of flash flood events including rapid onset and the rate of rise in water level (Archer and Fowler, 2015).

1.2 HYDRAULIC MODELLING

Hydrodynamic modelling of flood events is usually considered through the use of mathematical models of varying complexity (Xia et al., 2011b). Regardless of a model's complexity, all numerical models make approximations and thus present limitations that can easily lead to inaccurate predictions (Toombes and Chanson, 2011; Rowiński and Radecki-Pawlik, 2015). The main problems presented in regards to hydraulic modelling of floods are: (a) the numerical instabilities present in high-resolution grids, (b) the computation time, (c) the modelling of the moving wet-dry interface, specifically the arrival time of the wave front in fluvial floods, (d) the peak water depth and, finally (e) the representation of complex boundaries (Liang and Borthwick, 2009; Defra and Environment Agency, 2010; Zech et al., 2015). All of the previously mentioned issues remain challenging limitations and emphasise the need for further advancement in numerical hydrodynamic modelling techniques.

There are several verified 2D hydraulic models commonly used to predict flood inundation extents, but their performance in extreme events, such as flash floods, where the flows are fast-transient remains an active area of research (Huang et al., 2015). Flash flood characteristics, especially their limited spatial and temporal scales, make modelling of these events challenging and complicated. They are rarely captured in the field and the data associated with such events is very limited. Specific flow characteristics (e.g. hydraulic jumps, wake zones etc) are difficult to model accurately and thus several researchers when modelling flash floods have tried to find a balance between model complexity and computation time, taking into account specific physical mechanisms such as infiltration for example (Huang et al., 2015).

It has been documented that, because flash floods cannot be accurately forecasted, traditional flood defence management approaches, such as building high flood walls, do not address flash floods sufficiently as they disrupt the natural processes (World Meteorological Organisation, 2012). Specifically, when modelling flash floods there are several aspects that need to be established. For example, determining which processes are most influential and which parameters most affect the shape of the sharp wave front are important steps for selecting the appropriate techniques. Furthermore, deciding which governing equations to use, which numerical method and which numerical scheme is most suitable for their modelling is also a factor that needs to be taken into account. Flash floods are localised impact events and therefore local knowledge is important for their modelling (World Meteorological Organisation, 2012).

When predicting the hydrodynamic behaviour of flash floods, a common problem is that the performance of most hydraulic models is not consistent across event magnitudes (Horritt and Bates, 2002). The majority of numerical models are calibrated using a limited number of historical events and thus, assessing a model's ability to predict the flash flood dynamics of the most extreme events (i.e. model validation), is an essential task to ensure the model's credibility (Horritt and Bates, 2002). Considering this in addition to all the previously mentioned challenges (i.e. numerical instabilities in high-resolution grids on complex topographies, computation time, modelling the wet-dry interface dynamics, and the sharp flood wave front), further research through both experimental and numerical modelling is needed.

The dam break problem has been widely researched and modelled both experimentally and numerically. Research started as early as 1960 with the US Army Engineers Waterways Experiment Station publishing a report on experimental cases on floods resulting from suddenly breached dams (Corps of Engineers, 1960). The research continued from simple experimental studies investigating the initial stages of a dam break (Stansby et al., 1998) to more complicated problems such as dam break induced mudflows (Peng and Chen, 2006). Numerically, the dam break problem has been modelled in 1D, 2D and 3D (Zhainakov and Kurbanaliev, 2013; Marsooli and Wu, 2014) and experimental and numerical results have been compared by several researchers (Peng and Chen, 2006; Aureli et al., 2015).

The phases of a more complicated dam break problem can be separated in three stages. First the emptying of the reservoir, secondly the water flowing down either a sloped or a horizontal bed, and finally the interaction of supercritical flow with structures. All three stages have been researched, analysed and modelled extensively but there has not yet been a study considering all stages combined. Furthermore, a report published by Defra and the Environment Agency (Defra and Environment Agency, 2010) showed that while most hydraulic models routinely used by industry provide an appropriate support tool for decision making in flood risk management, they do not provide enough precision when dam breaks are modelled, specifically regarding the detail of the transition from supercritical to subcritical flow which is an important stage especially when impact is involved (Soares-Frazão et al., 2003b).

The processes will be modelled experimentally in a sloping channel and then numerically using a 2D-3D coupled model. Using a coupled model provides a unique possibility to efficiently and robustly model flood simulations whilst taking into account the three-

dimensionality of the event, thus using it for extreme events can be valuable. Consequently, this encourages further investigations of the physical processes of flash floods and the interaction between structures and flash flood waves. Hence, to the author's knowledge, flash floods have never been modelled incorporating all aforementioned stages.

1.3 RESEARCH QUESTIONS

The following research questions will be answered in this research:

R1. Is a dam break a good representation of a flash flood? Does it guarantee the main characteristic features of flash floods?
R2. Which parameters most affect the flash flood propagation?
R3. How does the roughness affect velocities and impact forces associated with flash floods in the built environment?
R4. Can the initial stages of a flash flood be modelled using a 2D model?
R5. Is a 3D model required for the prediction of flow, velocities and applied load in an urban settlement?
R6. Can mitigation strategies be developed from the analysis of flow interaction with urban settlements?
R7. Is OpenFOAM an appropriate open source CFD model for simulating the critical transition from subcritical flow to supercritical flow needed when modelling flash floods?
R8. Is Defra's benchmarking scheme appropriate? Does it need to be reviewed for extreme events?

1.4 RESEARCH OBJECTIVES

Thus, the research objectives of this project are:

O1. Experimental and analytical description of the different phases of a dam break to analyse flash flood characteristics.
O2. Develop a new high-quality flash flood dataset in a large-scale test facility for the development and calibration of numerical models for extreme events.
O3. Experimental and numerical examination of velocities and impact forces associated with flash floods on the build environment.
O4. Evaluate the performance of 2D and 3D hydrodynamic models considering the movement of the flood wave during flash flood propagation.

O5. Develop mitigation strategies to re-assess building guidelines in flash flood prone areas.

O6. Validate OpenFOAM model with experimental data.

O7. Compare OpenFOAM with existing industry models for the modelling of dam breaks.

Table 1-1 shows which research questions correspond to each of the objectives and presents the expected research outcomes.

Table 1-1- Research outputs mapped against research questions and objectives

Chapter	**Research Questions**		**Objectives**		**Research Outputs**
Chapter 3	R1	Is a dam break a good representation of a flash flood? Does it guarantee the main characteristic features of flash floods?	O1	Experimental and analytical description of the different phases of a dam break to analyse flash flood characteristics.	Experimental setup Experimental data Qualitative description of different stages of dam break
Chapter 3 Chapter 4	R2	Which parameters most affect the flash flood propagation?	O2	Develop a new high-quality flash flood dataset in a large-scale test facility for the development and calibration of numerical models for extreme events.	Experimental setup Experimental data Analysis of the different parameters and their effect on flash flood propagation
Chapter 4 Chapter 5 Chapter 6	R3	How does the roughness affect velocities and impact forces associated with flash floods in the built environment?	O3	Experimental and numerical examination of velocities and impact forces associated with flash floods on the build environment.	Experimental data Numerical data
Chapter 5	R4	Can the initial stages of a flash flood be modelled using a 2D model?	O4	Evaluate the performance of 2D and 3D hydrodynamic models considering the movement of the flood wave during flash flood propagation.	Numerical results
	R5	Is a 3D model required for the prediction of flow, velocities and applied load in an urban settlement?			Assessment if OpenFOAM's accuracy
Chapter 8	R6	Can mitigation strategies be developed from the analysis of flow interaction with urban settlements?	O5	Develop mitigation strategies to re-assess building guidelines in flash flood prone areas.	Proposal of possible mitigation strategies
Chapter 5 Chapter 6	R7	Is OpenFOAM an appropriate open source CFD model for	O6	Validate OpenFOAM model with experimental data.	Numerical data

		simulating the critical transition from subcritical flow to supercritical flow needed when modelling flash floods?			Assessment if OpenFOAM's suitability
Chapter 7	R8	Is Defra's benchmarking scheme appropriate? Does it need to be reviewed for extreme events?	O7	Compare OpenFOAM with existing industry models for the modelling of dam breaks.	Discussion on suitability of Defra's benchmarking scheme

1.5 RESEARCH FINDINGS AND IMPORTANCE OF RESEARCH

Given the challenging nature of flash floods and their aggravation through climate change, being able to accurately predict flood propagation and likely inundation extents can contribute to the development of better adaptation and preparedness strategies (World Meteorological Organisation, 2017; Ahmadian et al., 2018). The development of an accurate and reliable model requires a deep understanding of flash flood dynamics including the effect of the different drivers (e.g. fluid characteristics, slope angles, roughness, building positions etc.) that influence the flood wave propagation. Additionally, the examination of velocities and impact forces associated with flash floods can provide a reference for structural innovations for resilient design and construction.

In this research, the following findings have been attained. First, a new dataset has been created through a comprehensive set of experiments. Secondly, from the experimental and numerical analysis a full physical characterisation of the processes of a dam break has been developed. Moreover, from the numerical analysis it can be shown that the approach to model dam breaks and thus flash floods needs different parametrisation for different stages of the process and cannot be described with one set of parameters for the whole progression, thus demonstrating the need for either full 3D simulations or 2D-3D coupled models. Lastly from the load data acquired from the experimental work of flood wave interaction with structures, mitigation strategies can be developed for the design of reinforced houses in flash flood prone areas. Possible impacts of this project are firstly a new approach of modelling flash floods by parametrising individually the different stages of the event, and secondly, an impact in policy in order to re-assess building guidelines in flash flood prone areas.

1.6 REPORT OUTLINE

This report has been divided into seven chapters. The introduction provides context for the research and presents the problem statement followed by research questions and objectives. Chapter 2 is a literature survey of research on the topic of hydrodynamic modelling, numerical schemes, dam break modelling and wave structure interaction. Chapter 3 provides a conceptual overview of flash floods including definitions, examples and presentation of their different types and presents the case study and inspiration of this work. The experimental results are reported in Chapter 4 together with and an analysis on the effect of land use and intensity on flash flood propagation. Chapter 5 describes the numerical model used and presents a new 2D/3D modelling approach to flash flood modelling. A benchmarking case study is outlined in Chapter 6 and finally the conclusion of the report and the future work are presented in the synthesis in Chapter 7.

Chapter 1	Introduction
Chapter 2	Literature survey
Chapter 3	A conceptual overview of flash floods and case study
Chapter 4	Effect of land use and intensity on flash flood propagation
Chapter 5	Numerical modelling of flash flood propagation
Chapter 6	Benchmarking of flash flood models
Chapter 7	Synthesis

2 LITERATURE REVIEW

Floods are likely to increase in intensity and occurrence due to population growth, climate change, land-use changes, increased irrigation, deforestation and urban development on the floodplains (Liang et al., 2004). It is important to understand the physical processes behind them and the best way to represent them numerically. To achieve this, a literature survey was undertaken to understand the already existing research first in hydraulic modelling in general and then in more detail on the dam break modelling problem.

2.1 2D HYDRODYNAMIC MODELLING

Hydrodynamic modelling forms the base for studying fluids in motion and can be achieved in 1-Dimension (1D), 2-Dimensions (2D) or 3-Dimensions (3D). In most hydrodynamic problems, the governing equations cannot be solved analytically, and this therefore raises the need for numerical schemes. In the next section these schemes will be explained in 2D and further information will be provided on modelling problems such as flash floods (Riemann problems), different mesh approaches will be described and the problem of accurately tracking the wet/dry boundary and providing a good fit on the boundaries of the simulation will be discussed.

2.1.1 Introduction

Even though 1D models are widely used, it was shown early on that the complexity of the flow can only be expressed by higher dimensional representations (Bates et al., 1998). The rapid progress achieved in computing power over the last 20 years has led to a shift from 1D to 2D models; not only in academia but also in industry more widely (Costabile and Macchione, 2015). In the recent past, 2D models have been the preferred choice in flood modelling and floodplain inundation modelling as 1D models are considered too simplistic and 3D models too complex (Horritt and Bates, 2001). In practice, when modelling urban flooding, the flood dynamics are very important due to the very irregular topography and thus 2D models are necessary (Meesuk et al., 2015). The advantages of 2D models are: improved representation of physical processes, results at every grid point, better definition of the sharp flood wave, prediction of scouring and sedimentation processes (Timbe, 2007; Huang et al., 2015).

2.1.2 Numerical schemes

The governing equations in fluid dynamics are the Shallow Water Equations SWEs that will be analytically presented in Chapter 5. As they cannot be solved analytically for the two-dimensional case, different numerical schemes must be used to solve them numerically. The most common methods are the finite difference method (FDM), the finite element method (FEM) and the finite volume method (FVM) (Timbe, 2007; Chaudhry, 2008).

2.1.2.1 Finite Difference Method (FDM)

The finite difference method (FDM) is considered to be one of the simplest numerical methods for the solution of differential equations but it is not very frequently applied when solving the SWEs. FDM was first developed by Euler (1770) and is solved using a Taylor series expansion of the second derivative. The method can be used directly on the partial differential equations by substituting them with finite difference equations (Adrien, 2004; Blazek, 2005; Liu, 2014). The FDM divides the domain into a simple grid as shown in Figure 2-1 and at the beginning of every timestep computes a solution at each node (Moler, 2011). The advantages of this method are the fixed grid, the computational efficiency and the fact that it deals well with wetting and drying (Nielsen, 2011).

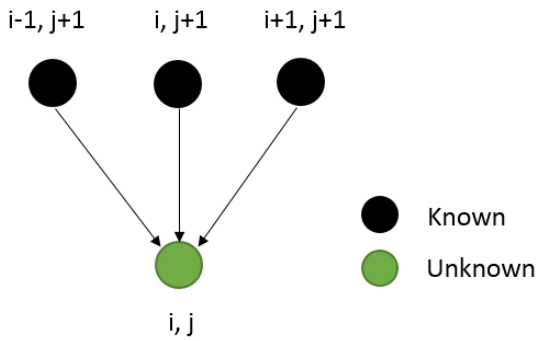

Figure 2-1- Schematic representation of the Finite Difference Method FDM. The black and green dots represent grid cells and are named using an (i, j) coordinate system. Known cell values are represented in black and the unknown value in green.

The nodes in Figure 2-1 are named using a (i, j) coordinate system and what the figure shows schematically is that each unknown solution (green) is computed using the known values of its neighbouring cells (black).

2.1.2.2 Finite Element Method (FEM)

The finite element method (FEM) is a scheme to approximate the solution by discretising the computational domain into several smaller pieces, finite elements. A solution is found for each of the elements, it is interpolated and then by a weighted residual construction a global solution is found for the complete system (Adrien, 2004). The advantages of this method are its computational efficiency and the more precise solutions within each element. But it is not so effective when dealing with wetting and drying and can produce numerical instabilities due to the mass balances (Nielsen, 2011).

2.1.2.3 Finite Volume Method (FVM)

The finite volume method (FVM) is similar to the FDM. The governing equation solutions are approximated by dividing the physical system into finite volumes, polyhedral control volumes (Adrien, 2004; Blazek, 2005). It was first proposed by Godunov (1959) who used this scheme to find an exact solution to the Riemann problem (see section 2.1.3) at all cell faces from which the flows, fluxes $F_{i\pm\frac{1}{2}}$ can be determined. The Godunov method in its conservative form is shown in Equation 2-1 where U is the cell average velocity for (x, t) in (m/s), F is the flux $(m^3 \cdot s^{-1} \cdot m^{-2})$.

$$U_i^{n+1} = U_i^n + \frac{\Delta t}{\Delta x}\left[F_{i-\frac{1}{2}} - F_{i+\frac{1}{2}}\right]$$

Equation 2-1

Where: $F_{i+\frac{1}{2}} = F\left(U_{i+\frac{1}{2}}(0)\right)$

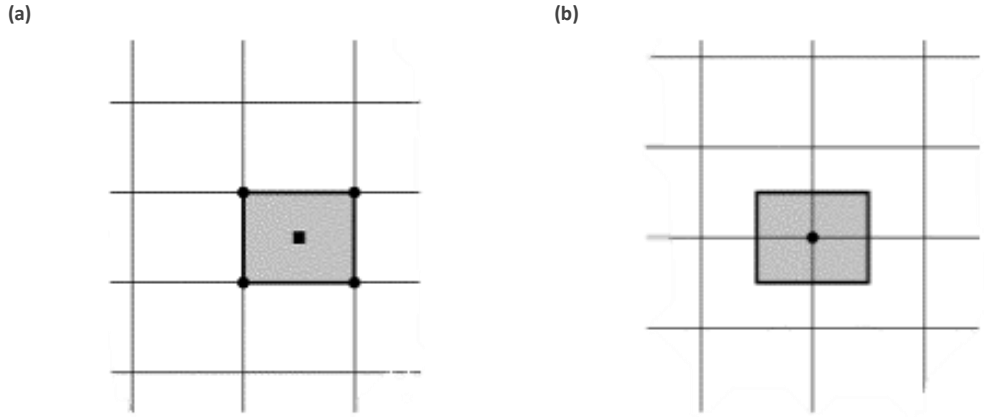

Figure 2-2- Schematic representation of finite-volume scheme. Control volume of (a) cell-centred and (b) cell-vertex scheme. The squares represent the grid of the physical domain where all corners are called grid points. The darker square represents the control volume (Blazek, 2005)

There are two main schemes used to define the position of the control volume on the grid: (a) cell-centred scheme and (b) cell-vertex scheme. The cell-centred scheme shown in Figure 2-2 (a) is a scheme where the control volumes and the grid cells are at the same location and the flow flux is calculated at the centre of the grid cell. In the cell-vertex scheme, shown in shown in Figure 2-2 (b), the control volume is centred around the grid point and the flow fluxes are therefore calculated at the grid points.

The main advantages of this approach include: simplicity, stability, easy implementation, sharp gradient handling and is appropriate for wetting and drying problems (Chaudhry, 2008; Nielsen, 2011). Within each cell, the mass and momentum are conserved, and the fluxes are calculated at the cell's interfaces by solving the Riemann problem. In this project the cell-type finite volume method will be applied where all values of dependent variables are stored in the centre of each cell (Marques, 2014).

2.1.3 Riemann problems

Flash floods and dam breaks share important hydraulic characteristics, especially, the sudden temporal and spatial changes of the flow as well as the interactions between the river and the floodplain. Problems with such discontinuities in the governing equations, are known as Riemann problems and the solution is complex due to the non-linear hyperbolic form of the SWEs (Balsara, 2013). To resolve the discontinuities, even though two-dimensional Riemann solvers exist, approximate Riemann solvers are being used in combination with the numerical schemes to represent the main features of the Riemann problem but also to provide a simpler solution (Kong, 2011). The main advantages of these coupled solvers are: their robustness, their high resolution in transcritical regimes and their accuracy in determining the location of the discontinuities (Zoppou and Roberts, 2000; Iglesias et al., 2006). Examples of approximate solvers include: Roe, Osher-Solomon, HHL, HHLC and others (Kong, 2011). More recently, Riemann solvers were coupled with flux limiters to minimise the numerical instabilities (Chaudhry, 2008). Such limiters are the minimod Limiter, van Leer Limiter, superbee Limiter and van Albada Limiter (Zhou et al., 2001).

Zoppou and Roberts (2000) developed a numerical model for the solution of the 2D unsteady dam break problem using Toro's second-order approximate Riemann solver (HHLC) with a Leer type limiter on a Cartesian grid. Toro's approximate method uses a solution averaged over space and time and the Leer type limiter is necessary to ensure continuity in steep slopes and avoid any oscillations while retaining the second-order accuracy. The choice of

limiters depends upon the local flow parameters and the Courant number. Zoppou and Roberts (2000) also examined the influence of different flux limiters, finding that for refraction waves, the superbee type limiter resulted in a more accurate solution but the minimod limiter provided a superior representation of the diffusion term. It was also found that the van Leer limiter was more diffusive than the superbee and reduced the computation time. The accuracy of Zoppou and Roberts (2000) model was tested with the example of a reservoir collapse, examining model stability, robustness and capability of modelling shock, difficult geometries and wetting and drying. Finally, they concluded that the weighted average flux scheme is very computationally efficient and thus should be further utilised (Zoppou and Roberts, 2000).

In this research, the OpenFOAM software solver used, interFoam (which will be analytically described), uses a finite volume method, and to account for the numerical instabilities, the multidimensional universal limiter for explicit solution (MULES) method (Greenshields, 2015). It is an application of the Flux Corrected Transport technique (FCT), a Eulerian finite-difference algorithm for the solution of the continuity equation which has the advantage of modelling accurately steep gradients and shocks (Boris and Book, 1971).

2.1.4 Mesh approaches

Dividing the simulation domain into a grid and choosing the most suitable approach in a CFD problem is an important task that can easily become a significant source of numerical errors and uncertainties. The method chosen should reflect upon the numerical scheme selected for the solution of the governing equations (Carrillo, 2013).

The grids can be structured (meaning that any mesh element can be identified by its (i, j, k) coordinates) or unstructured (where the order of the elements is unstructured). The simplest form of grid is a uniform rectangular grid that divides the numerical domain in rectangular elements perpendicular to the coordinate axes (Figure 2-3). The disadvantages of such a grid is that not all domains are rectangular resulting in the need for approximated solutions ignoring whole elements (Flow Science, 2016).

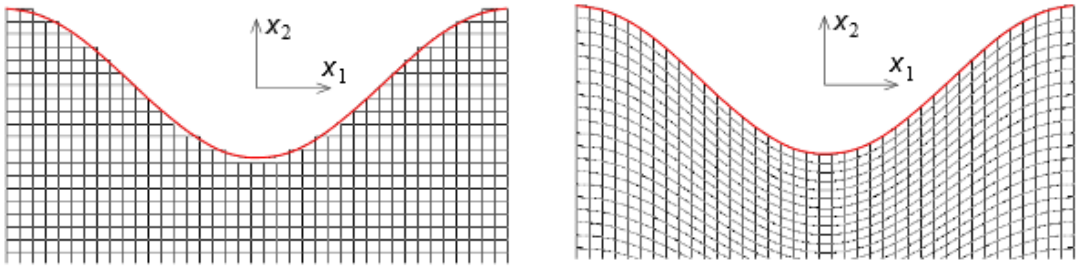

Figure 2-3- Uniform rectangular grid (left) where the numerical domain is divided in rectangular elements and body-fitted grid (right) that follows the shape of the body using curved gridlines (Craft, 2010)

A large number of CFD problems are solved using body fitted meshes, grids that follow the shape of the body using curved gridlines (Figure 2-3). The advantages of such meshes are the good resolution at the boundaries (Johnson, 2013), the optimal position of nodes to incorporate any geometrical shape, and the flexibility to have a finer mesh closer to the boundaries. But this method also has disadvantages, in particular it is not ideal when dealing with complicated geometries, often requires user intervention, and does not always lead to robust simulations (Carrillo, 2013). The solution of CFD problems has become more detailed and complex over the years, leading to alternative approaches of the body-fitted meshes, such as the Cartesian cut cell method (Johnson, 2013). The Cartesian cut cell methods first originated in the early 1980s for aerospace applications to deal with multi-component shapes. Since then, their development was extended to a wider range of applications (Causon et al., 2000). The cut cell method uses a simple Cartesian mesh and solid boundaries are cut out of the background mesh. This allows the boundaries to be discretized and cut cells to be created on the complicated boundaries. This allows the boundaries to be defined resulting in the most precise boundary representation (Liang et al., 2007).

2.1.5 Boundary fitting and wet/dry boundary tracking

Accurately solving the wet/dry interface in numerical models has always been challenging in numerical models, especially in Godunov-type solvers (Bi *et al.*, 2014). In all Finite Volume (FVM) schemes the calculations of water depths at the wet/dry interface often results in inaccurate predictions causing numerical instabilities in the models. This is due to the nature of FVM schemes where the depth-averaged velocities are calculated by dividing the discharge per unit width (q) by the local water depth (h) (Figure 2-4). At the wet/dry interface, where the local water depths $((h_1)$ and (h_2) in Figure 2-4 are very small, this

approach can lead to over predicting the velocities and thus resulting in negative water depths (Huang *et al.*, 2014). To avoid this, in most cases, the friction terms in the governing equations (which will be analytically derived in Chapter 5), are solved by a semi-implicit scheme (Bi *et al.*, 2014; Song *et al.*, 2011; Huang *et al.*, 2014). This does not invert the velocity's direction thus preventing numerical instabilities and ensuring stability.

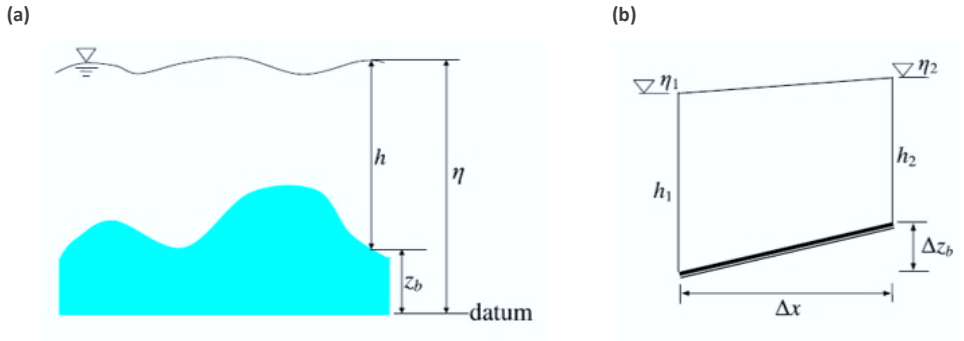

Figure 2-4- (a) Definition sketches for bed topography where η is defined as the surface water level above the datum, z_b is the bed elevation, h is the water depth calculated by $h = \eta - z_b$. (b) Momentum balance for the vertical column of fluid for a Δx size of the fluid element and h_1, h_2 the local water depths (Liang and Borthwick, 2009)

Several wetting and drying algorithms have been presented and implemented to solve the SWEs in order to work around this challenging issue. Hou et al. (2013) presented a technique to identify a potentially problematic cell based on two criteria: the first specifies that the water depth variation in the cell centroid needs to be lower than a specific limit, and the second one relates the small water depths with the bed elevation variation. If both criteria are fulfilled at the cell edges, the cell is considered problematic and the values of all parameters at the edges are set to the values of the cell centroid.

Audusse et al. (2004) argued that the only way to avoid negative simulated values due to wet/dry interface is to use the Minimod limiter. In simpler models there are algorithms that can be implemented to reduce the speed of the wetting and drying process making it more robust at the expense of accuracy (Jamieson et al., 2012). Another technique is to use pre-balanced SWE, using water level directly as a flow variable instead of the water depth and then treating the slope and friction terms separately (Wang and Liang, 2011).

Huang et al. (2014), improved the wetting and drying approach first established by Zhao et al. (1994) by using the Osher scheme to compute the mass and momentum fluxes across all

the element sides, truly accomplishing the modelling of the moving wet and dry interface (Zhao et al., 1994). The first step, is to categorise the cell edges based on a criterion, ε (Figure 2-5) into four categories (Huang et al., 2014) where η_L and η_R are the local water depths within the left and right cell (m) respectively.

a. dry edge: $h_L \leq \varepsilon$ and $h_R \leq \varepsilon$
b. wet edge: $h_L > \varepsilon$ and $h_R > \varepsilon$
c. partially wet edge (no flux): $h_L > \varepsilon$ and $h_R \leq \varepsilon$ and $\eta_L \leq \eta_R$
d. partially wet edge (with flux): $h_L > \varepsilon$ and $h_R \leq \varepsilon$ and $\eta_L > \eta_R$

Figure 2-5 represents a side view of these four categories schematically at the boundary of two cells. L and R stand for left and right cell respectively, η is the surface water level above the datum, z_b is the bed elevation and h is the water depth calculated by $h = \eta - z_b$.

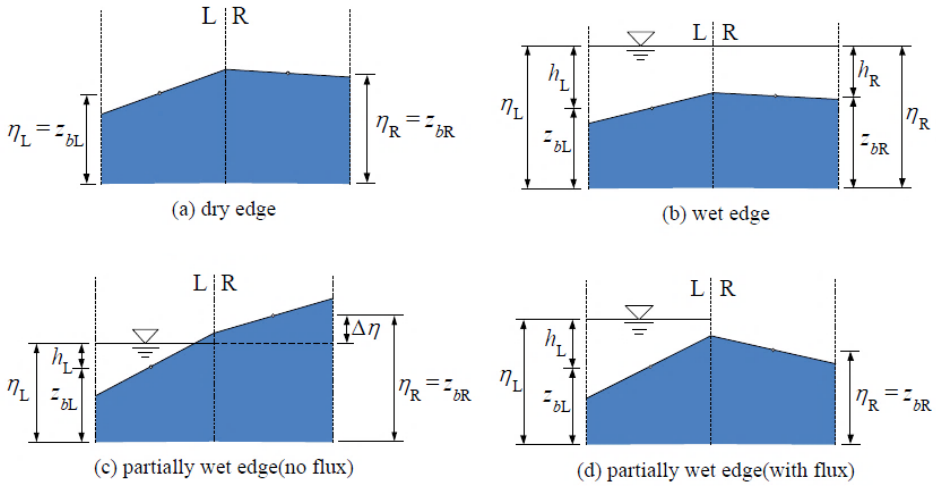

Figure 2-5- Four types of categorised edges: (a) dry edge, (b) wet edge, (c) partially wet edge (no flux) and (d) partially wet edge (with flux). Side view of these four categories schematically at the boundary of two cells. L and R stand for left and right cell respectively, η is the surface water level above the datum, z_b is the bed elevation and h is the water depth calculated by $h = \eta - z_b$ (Zhao et al., 1994)

From this categorisation, each cell can be classified as wet, dry or partially dry. A wet cell is defined as a cell that has all of its edges either wet or partially wet with flow (flux), and all of its points, nodes have a water depth. A dry cell is a cell that all of its edges are either dry or partially dry (with no flux) and finally, a partially wet cell is a cell that all of its edges are wet or partially wet except one (Huang et al., 2014; Maddock et al., 2013).

In partially wet cell, when a *dry cell* is next to a *wet cell* ($\eta_L \leq \eta_R$), there cannot be a flux across the interface. Therefore, the momentum flux is set to zero and only the mass flux (mass flow per unit area) within the cell is calculated. To avoid the calculation of a non-physical flux two modification values for the surface elevation and the bed level, η'_R and Z'_{bR}, are introduced (Figure 2-6) where $\Delta\eta$ is the difference in the surface water level (Huang *et al.*, 2014; Liang and Borthwick, 2009).

Thus: $\eta'_R = \eta_R - \Delta\eta$ and $Z'_{bR} = \eta'_R$

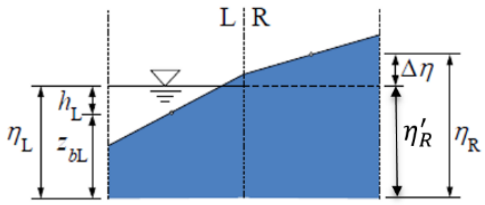

Figure 2-6- Partially wet edge (no flux) after modification. Side view of the boundary of two cells. L and R stand for left and right cell respectively, η is the surface water level above the datum, z_b is the bed elevation and h is the water depth. The two modification values for the surface elevation and the bed level, are η'_R and Z'_{bR}, where $\Delta\eta$ is the difference in the surface water level: $\eta'_R = \eta_R - \Delta\eta$ and $Z'_{bR} = \eta'_R$ (Huang et al., 2014; Liang and Borthwick, 2009).

Finally, to ensure complete balance of the scheme, when a cell is considered dry, its velocity components are set to zero and to conserve mass, the same amount of water is deducted from the neighbouring cells (Huang *et al.*, 2014; Liang and Borthwick, 2009).

The OpenFOAM code that will be used and analytically described in Chapter 5, uses the volume of fluid (VOF) method to track the water-air interface. Considering that out of the two fluids only air can be compressed makes it easier to track the position of the wet/dry boundary surface (Biscarini et al., 2009).

2.1.6 2D Models

A summary of many widely used 2D industrial models routinely used for flood hydrodynamic modelling is presented in Table 2-1, including the equations they solve, the numerical scheme used, and whether they can represent and capture shock such as a dam break.

Table 2-1- 2D industrial models used for flood hydrodynamic modelling, the equations and numerical schemes used and their shock capturing schemes (O'Brien et al., 1993; Timbe, 2007; Hunter et al., 2008; Vanderkimpen et al., 2009; Defra and Environment Agency, 2010; Zolghadr et al., 2010; DHI, 2011; Nielsen, 2011; Open TELEMAC, 2016)

Model	Equations	Numerical Scheme	Shock capturing
DIVAST	2D Shallow water equations	ADI implicit finite difference scheme	No
DIVAST-TVD	2D Shallow water equations	Explicit finite difference scheme	Yes
FLO-2D	2D Shallow water equations	Explicit central finite difference scheme	No
JFLOW	2D Diffusion wave equations	Explicit finite difference scheme	n/a
LISFLOOD-FP	2D Diffusion wave equations	Analytical approximation of equations	n/a
MIKE 21	2D Shallow water equations	Implicit finite difference scheme	No
Telemac 2D	Saint-Venant equations	Triangular finite element/ finite volume method	No/Yes
TRENT	2D Shallow water equations	Explicit Roe Riemann solver	Yes
TRIM2RD	2D Shallow water equations	Semi-implicit finite difference scheme	-
TUFLOW	2D Shallow water equations	ADI implicit finite difference scheme	No
TUFLOW FV	2D Shallow water equations	Finite volume scheme	Yes
Sobek	2D Shallow water equations	Finite difference number method	Yes

Most of the aforementioned models use the 2D SWEs which will be presented in detail in Chapter 5. Telemac 2D solves the Saint-Venant equations which are the SWEs in unidirectional form and thus are also derived from Navier Stokes. Finally, both LISFLOOD-FP and JFLOW use an approximation of the 2D Diffusion wave equations DSWs to calculate the flow between the cells. 2D DSWs are a further simplification to the SWEs assuming the horizontal momentum can be expressed in terms of water depth using an empirical equation and thus the final equation relates to nonlinear diffusion. LISFLOOD-FP, for example, solves the continuity equation (Equation 2-1) and the empirical Manning's equation (Equation 2-2) (Fewtrell et al., 2009), where: Q is the volume flux, h is the water depth, Δx is the grid spacing in the x-direction, Δy is the grid spacing in the y-direction and n is the Manning's coefficient (Fewtrell et al., 2009).

$$\frac{\partial \mathrm{h}}{\partial \mathrm{t}} = \frac{\partial \mathrm{Q_x}}{\partial \mathrm{x}} + \frac{\partial \mathrm{Q_y}}{\partial \mathrm{y}} \qquad \textit{Equation 2-2}$$

$$\mathrm{Q_x} = \frac{\mathrm{h_{flow}^{5/3}}}{\mathrm{n}} \left(\frac{\Delta \mathrm{h}}{\Delta \mathrm{x}}\right)^{1/2} \Delta \mathrm{y} \qquad \textit{Equation 2-3}$$

When modelling floodplain inundation, several approaches and different levels of model and data complexity have been considered (Horritt and Bates, 2001). Floodplain inundation remains a serious environmental hazard and in several of the models mentioned in Table 2-1, there is a way to incorporate it. The most common approaches are to either consider the floodplain as part of the river or to incorporate it as a storage reservoir (Timbe, 2007).

2.2 DAM BREAK MODELLING

The dam break problem has been researched by using theoretical, experimental and numerical methods. Even though it has been found that the shallow water equations are a suitable way to represent the sharp wave flow (Biscarini et al., 2010), the question still remains how much our assumptions influence other measured factors such as the impact forces on an obstacle (Aureli et al., 2015). Most physical characteristics of dam break flows are three-dimensional and a choice between accuracy, computation time and simplicity is often required.

2.2.1 Theoretical studies

Ritter (1892) contributed to the dam break problem with a landmark theory on the idealised dam break, solving the dam break wave shape (Chanson, 2004b). His theory describes a dam break in a dry channel where the dam has an initial water depth h_o and is separated from the rest of the channel by suddenly removed wall. As soon as the wall is removed, a dam break wave starts moving downstream (positive wave) and a negative wave (a wave moving opposite to the flow direction) starts propagating upstream within the reservoir (Ritter, 1892). Ritter's equation $x/t = 2\sqrt{gh_o} - 3\sqrt{gh}$ describes the surface profile between the dam break front and the negative wave, where h_o is the initial water depth and h is the depth at x for time (Ritter, 1892). Castro-Orgaz and Chanson (2017) represented Ritter's dam break theory schematically (Figure 2-7). The two equations $dx/dt = -(gh_o)^{1/2}$ and $dx/dt = 2(gh_o)^{1/2}$ represent the propagation of the negative and positive wave equations respectively. Ritter also developed equations for the critical water depth and critical velocity at the origin (gate) where $x = 0$. Equation 2-4 is the critical depth equation where h_o is the initial water depth in the reservoir and Equation 2-5 is the critical velocity equation (Ritter, 1892).

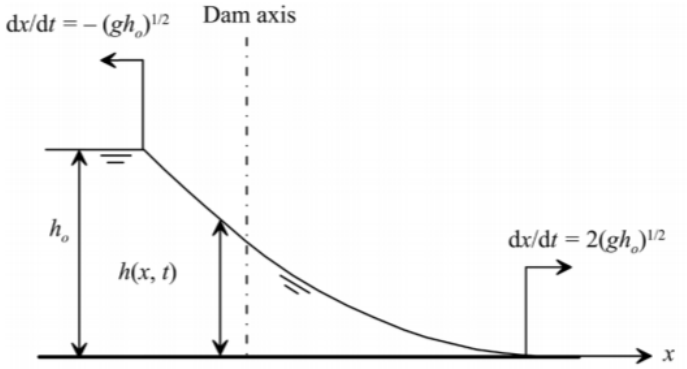

Figure 2-7- Schematic representation of Ritter's dam break theory where the dashed line represents the dam axis, x the distance in the x-direction, h the water depth at any point (x,t) and h_o the initial water depth in the reservoir. The arrows pointing left and right represent the propagation of the negative and positive wave equations respectively (Castro-Orgaz and Chanson, 2017)

$$h_{(x=0)} = 4/9\, h_o \qquad \textit{Equation 2-4}$$

$$V_{(x=0)} = 2/3\, \sqrt{g h_o} \qquad \textit{Equation 2-5}$$

Ritter's analytical solution, even though considered one of the most important theories, did not consider bed resistance and therefore in many cases cannot be used to provide a very realistic solution (Schoklitsch, 1917). In 1917, Schoklitsch continued research by performing experiments which proved that the measured velocities of the dam break wave were overestimated by 40% using Ritter's solutions, but the experimental results of the negative wave agreed with the theoretical calculations (Schoklitsch, 1917). Eguiazaroff (1935) conducted a series of experiments which supported these conclusions, highlighting the sensitivity of the dam break flow to the hydraulic resistance and raising the need for further research into resistance terms especially in the tip region of the dam break waves.

Craya (1946) developed a graphical method of characteristics solution using the Saint Venant Equations. This approach was later modified by Re (1946) and Levin (1952) where the flow from the dam break was calculated with a finite difference method of characteristics equation for a set slope and resistance coefficient.

Next, Dressler (1952) implemented a resistance term in the nonlinear SWEs based on the Chezy resistance formula. The explicit inclusion of resistance enabled the reconstruction of the dam break front and everywhere else resulted in a raised water surface and decreased velocities. In order to validate the analytical solution Dressler (1952) presented experimental

data on a dam break in a horizontal channel. The results showed several distinct flow regimes after the gate opening and thus showed that the Chezy resistance function was not acceptable to describe unsteady and not fully developed turbulent flow at the tip region. Whitham (1955) showed that at the tip (front leading part) of the dam break wave resistance effects cannot be neglected and described the existence of a boundary layer, which is the flow region adjacent to a boundary affected by the presence of the boundary (Chanson, 2004c). He applied a different model at the tip of the wave where the drag force is non-negligible and applied Ritter's solution to the rest of the domain.

All the aforementioned solutions considered dry bed conditions downstream and this critical limitation had already been identified as early as 1935 by Eguiazaroff (1935). Stoker (1957) presented a set of generalised equations based on Ritter's solution but for a wet bed. He developed equations for the free surface profile and the dam break's tip speed and depth in connection with the upstream and downstream water depths.

Su and Barnes (1970) revisited Dressler's method and modified it to be applicable to different channel cross-sectional shapes of uniform slope. They concluded that the hydrograph (rate of flow over time) is a function of different variables such as: time t, shape, the reservoir length L_0, initial reservoir water depth h_0 and the extension of the breach α (See Figure 2-8). Pilotti et al. (2010) contributed further on Su and Barnes' work and after investigating a more extensive set of parameters, they proposed a discharge hydrograph for the dam break derived from a fourth-degree polynomial expression.

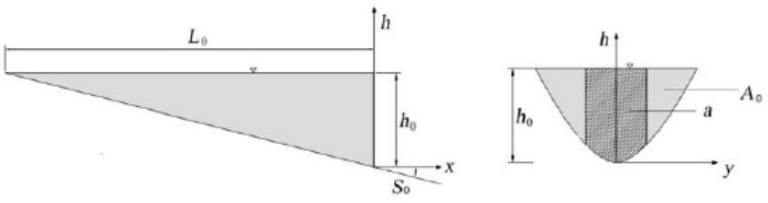

Figure 2-8-Reservoir schematic (x, y, h), side view (left) and cross section (right) where L_0 is the reservoir length, h_0 the initial reservoir water depth, A_o the flow cross sectional area, S_o the bed slope and α the extension of the dam break breach (Su and Barnes, 1970)

Most of the aforementioned solutions (with the exception of Dressler's work) assume a reservoir of infinite length and therefore an infinite volume of water. Hunt (1982) and (1984)

analysed more realistic problems such as dam breaks with a finite reservoir length (and thus volume), providing graphs of time evolution of the dam break wave front.

Hogg and Pritchard (2004) investigated the separation of the tip of the dam break wave which is affected by drag forces (Figure 2-9). They advanced the already existing research by considering shear stressed in the horizontal velocity and different types of resistance to accommodate for different types of fluids such as debris and mud. They found that by considering shear in the horizontal velocity has a considerable effect on the solutions, even in flows with little to no resistance. In general, the results showed very good agreement with the experimental data and thus provided new understanding of such flows. Figure 2-9 represents the dam break evolution where the x-axis represents the distance in the x-direction (m), the z-axis the water depth (m) in the z-direction, h the water depth (m) at any point (x, t), u the velocity (m/s) at any point (x, t) and $x_f(t)$ the position of the dam break (m) wave tip at time (t).

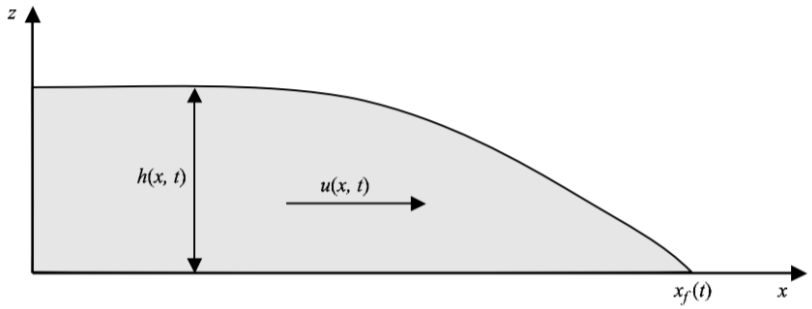

Figure 2-9- Schematic configuration of flow (x, z) where the flow is moving from left to right at a velocity $u(x,t)$, $h(x,t)$ is the water depth at point (x,t) and $x_f(t)$ is the position of the dam break wave tip at time (t) (Hogg and Pritchard, 2004)

A lot of the aforementioned works (Ritter, 1892; Dressler, 1952; Dressler, 1954; Hogg and Pritchard, 2004) were found to only be valid after the flow has travelled part of the distance after the reservoir release, and the velocity of the flow can be considered mainly horizontal (McMullin, 2015). Some researchers therefore analysed the initial stages of the flow using wet beds downstream, used Lagrangian equations to solve the initial stages of the flow and potential and linear wave equation theories to solve the flood wave evolution (Pohle, 1950; Stoker, 1957; Korobkin and Oguz, 2008).

Analytical solutions of laminar and turbulent dam break waves were presented for horizontal and sloping channels with non-constant friction constants and allowed future work on the method of characteristics for these cases (Chanson, 2003). The turbulent flow of these cases was also examined, providing new analytic solutions of turbulent dam break waves in dry downstream channels (Chanson, 2009). Some of the assumptions considered in these cases are the semi-infinity of the reservoir, the shape of the channel and the instantaneity of the dam break.

Recent analytical studies have concentrated primarily on solutions for finite reservoirs and horizontal channels without any friction (Wang and Pan, 2014), analytical solutions of the dam break flow on irregular-shaped cross-sectional channels (Wang et al., 2017) and the derivation of the relation between the dam break wave tip velocity and time (Deng et al., 2018).

2.2.2 Experimental studies

Experimentally, research started as early as 1960 in the US Army Engineers Waterways Experiment Station, where the Corps of Engineers (1960), published a report on experimental cases of floods resulting from suddenly breached dams. The research continued from simple experimental studies such as “the collapse of liquid columns” (Martin and Moyce, 1952) and the initial stages of a dam break (Stansby et al., 1998) to more complicated flows such as dam break induced mudflows (Peng and Chen, 2006) or the dam break flow of a non-Newtonian fluid (Smutek and Cordonnier, 2013). Unsteady dam break flows (Chanson, 2003), experimental (Bellos, 2004) versus numerical measurements of a dam break induced flood waves (Bellos and Hrissanthou, 2011). Flows through idealised cities (Testa et al., 2007; Soares-Frazão and Zech, 2008), prediction of impact forces (Yang et al., 2010) or dynamic pressure loads (Lobovský et al., 2014), flows over bed steps (Fraccarollo et al., 2010), humps (Ozmen-Cagatay et al., 2014), triangular sills (Soares-Frazão, 2007), dam breaks in channels with bends (Soares-Frazão and Zech, 2002b) and dam breaks in wet or dry channels (Ozmen-Cagatay et al., 2014).

More recently, experiments analysing the effect of the downstream water depth and reservoir length provided further insight into the hydrodynamic characteristics of the dam break problem (Liu and Liu, 2017). Some experiments were on full and partial dam breaks, some over mobile beds investigating different types of bed sediment compositions, some

looked at different initial reservoir depths (Qian et al., 2018; Fent et al., 2019) and some investigated the dam break hydrographs close to the gate (Liu et al., 2017).

2.2.3 Numerical studies

Examples of numerical investigations of the dam break problem include 1D (Peng, 2012), 2D (Bellos et al., 1991; Zhainakov and Kurbanaliev, 2013) and 3D (Marsooli and Wu, 2014). Detailed comparison between experimental and numerical results have been reported by several researchers (Peng and Chen, 2006; Aureli et al., 2015). In the last 15 years, many 2D and 3D models have been validated using Soares-Frazão's experimental results (Soares-Frazão, 2007; Soares-Frazão and Zech, 2007) and investigated several aspects of 2D and 3D flow from sudden dam break flows including: sediment transport in rivers, applications of swash on modelling dam breaks, 2D dynamic models, MUSCL methods and comparisons of different model applications to dam breaks (Soares-Frazão et al., 2003b; Vasquez and Roncal, 2009; Defra and Environment Agency, 2010; Hou et al., 2014; Yu and Duan, 2014; Costabile and Macchione, 2015; Trinh et al., 2018).

Many 2D depth-averaged models have been reported in literature for dam breaks, but have been found not to represent all of the open flow features well, especially in the initial stages (Fraccarollo and Toro, 1995; Canelas et al., 2013; He et al., 2017). Aureli et al. (2015) also pointed out the erroneous representation of some open channel flow features can also be found later in the simulations, not only in the initial stages, specifically when considering wave-structure interaction due to the curvature of the free surface and the vertical accelerations created by the interaction. To avoid the aforementioned limitations, 3D models have been used in dam break modelling. Numerical models have investigated the turbulence of the flow (Larocque et al., 2013), sediment transport (Marsooli and Wu, 2014, 2015) and again the initial stages of a dam break (Shigematsu et al.; Oertel and J.Bung, 2012; Hu et al., 2018). Even though differences exist between different models, the 3D models have found to predict the dam break flow reasonably well and provide improved representations of the hydrodynamics of dam breaks but, as expected, considerably increased the computation time and cost (Hu et al., 2018).

2.2.4 Flash flood models

There have been a limited number of publications on models specifically designed for flash flood modelling, usually as support tools for flash flood warning systems. In a laboratory

setting the most prominent flash flood experiment is the Testa et al. (2007) experiment (Figure 2-10) which was part of the IMPACT project; a project that assessed the risks from extreme flooding. Another large-scale experiment, part of the CADAM Project, was the Chatelet experiment which assessed the effect of a dam break on a triangular bottom sill in a 38 m long channel (Ferreira et al., 2006). The same experiment was later replicated as part of the IMPACT project in a smaller scale (Soares-Frazão, 2007). Other experiments include Chanson's flash flood surges (Chanson, 2004a)

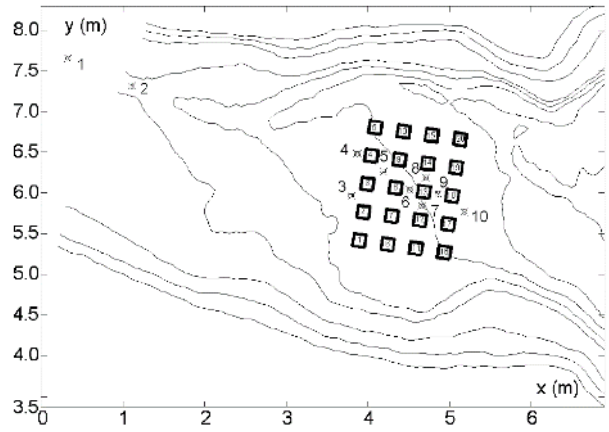

Figure 2-10- Plan view of Testa et al. (2007) flash flood experimental setup. It is plotted in an (x,y) coordinate system and all values are represented in metres. The light-coloured lines represent the topographical contour lines of the experiment, the black squares concrete buildings and the numbers 1 to 10 different gauge locations.

Numerically, flash floods have been modelled using either distributed hydrological models considering runoff at a catchment scale (Miao et al.; Ogden et al., 2000; Reed et al., 2007; Braud et al., 2010), or using hydrodynamic models examining the dynamic routing of the flood wave and the water levels within the river channel domain (Xia et al., 2011b; Huang et al., 2015). Traditional hydrological models solve the kinematic diffusion wave equations and thus do not explicitly consider all the physical processes. There have been hydrodynamic models that take into account rainfall and infiltration for but in the case of flash flood events do not provide an accurate representation as very limited infiltration is involved in these events, a topic that will be further discussed in the next chapter (Huang et al., 2015).

Furthermore, Defra and Environment Agency (2010) assessed seven hydrodynamic models (InfoWorks2D, ISIS2D, MIKE FLOOD, SOBEK, TUFLOW, ANUGA and TUFLOW FV) which were tested for two dam break problems. The first dam break experiment from the IMPACT

project evaluated the effect of a dam break on a structure. Water level and velocities were modelled and compared with the experimental results. The results showed that none of the models was distinctively superior when modelling discontinuous flows. Although it was shown that the performance of models including a shock capturing scheme was better. The second experiment was from the IMPACT project, but at a larger scale. Here the predictions by all models were more acceptable although TUFLOW, TUFLOW FV and InfoWorks overpredicted the water levels compared to the results obtained by SOBEK, ISIS, ANUGA and MIKE. The reason for this over prediction was not explained in the report but once again the outcome was that the models with the shock capturing schemes were considered to be more accurate. Therefore, the solver selected for this research was ensured to contain a shock capturing scheme.

2.2.5 Wave structure interaction

When fluids interact with structures, the complexity of the numerical simulation increases and requires considerations of the structural dynamics which are not simulated accurately by any numerical scheme (Novatech, 2015). Wave structure interaction is mainly investigated in the design of coastal and offshore structures as they are exposed to extreme situations with breaking waves that can result in very high impact forces at small temporal scales (Chella et al., 2012). Thus, many experimental and numerical studies have been used to examine wave loading, run-up and scattering around such structures (Chen et al., 2014b).

Experimental studies are very often used in these examinations as they provide the most accurate and realistic reproduction of the hydrodynamic forces, but the measurements often involve scaling problems (Chen et al., 2014b). Many experimental research projects have been undertaken to examine the impact forces resulting from wave run up and breaking waves (Wienke and Oumeraci, 2005; Zang et al., 2010; Arntsen et al., 2011; Ros, 2011). The aim of these projects was to measure impact forces from different waves on different shaped structures and compare the results with numerical simulations and earlier work such as Goda et al. (1966) and Sawaragi and Nochino (1984) which were found to provide good agreement.

From a theoretical approach, the most widely used method for calculating wave loading in wave structure interaction on offshore structures is the Morison equation based on potential flow theory (Chen et al., 2014b). Potential flow theory provides equations for the conservation of mass and momentum but assumes that the flow is incompressible, frictionless and irrotational (Mohanty, 2006). The Morison equation is used to calculate

inline forces on structures in flow and is the sum of two components: an inertia force component (potential flow theory) and a drag force component (body in steady flow) (Morison et al., 1950). From Morison's equation, all components of the applied force on a cylinder can be derived for all three directions fx, fy and fz (Boccotti, 2015). Both approaches (potential flow theory and Morison's equation) provide advantages compared to experimental approaches such as minimising scale effects and low cost. However, the Morison equation is not applicable in all flow regimes and cannot account for highly non-linear interactions and wave breaking. Similarly, potential flow theory is based upon the assumptions that the flow is incompressible, inviscid and irrotational thus doesn't account for high-non linearity (Chen et al., 2014b).

Many numerical models have been developed based on non-linear potential flow theory (Bai and Eatock Taylor, 2007; Ning et al., 2009) but due to the aforementioned assumptions do not provide a correct representation of many physical characteristics in wave breaking applications, therefore raising the need for more advanced CFD models for highly non-linear cases which solve the Navier Stokes equations (Chen et al., 2014b). Several studies applied CFD modelling to wave structure interaction and analysis (Lin and Huang, 2012; Chen et al., 2014b; Hamza et al., 2015), extreme wave forces, run-up on structures and wave structure interaction (Christensen et al., 2005; Corte and Grilli, 2006) and through correct calibration and parametrisation were found to be able to accurately represent the wave structure interaction.

All the aforementioned approaches are for offshore applications and in dam break flows there is only very limited research describing the dynamics of these events and which investigates flood wave structure interaction.

Zhou et al. (1999) contributed numerical data from a dam break case performed at the Maritime Research Institute Netherlands MARIN (Dillingham, 1981) for the impact on a vertical wall concluding that correctly predicting the height of the hydraulic jump height is an important step in computing the impact pressure. The experimental pressure results from the MARIN experiment were analysed by other researchers as well (Lee et al., 2001; Kleefsman et al., 2005; Wemmenhove et al., 2010). The applied forces on downstream structures following a dam break were also studied by Bukreev and Zykov (2008), Bukreev (2009) and later on by Lobovský et al. (2014) who examined the dynamics of the dam break and the applied pressure loads on the downstream walls. Lobovský et al. (2014) also found

that the peaks of the applied pressure on the wall showed some scattering which still remains an unresolved problem.

Trivellato (2004), Kleefsman et al. (2005) and Chen et al. (2014a) investigated forces in terms of bore impact on walls and applied pressure loads exerted on downstream dams by dam break flows. The most widely known experimental case in dam break impact forces is an experiment on the mechanics of tsunami bore runup completed at the University of Washington (Raad and Bidoae, 2005), and is one of the most widely used experimental sets (Figure 2-11) for numerical validations. This setup will be analytically described in Chapter 5 and will be used for the numerical validation of the 3D OpenFOAM model.

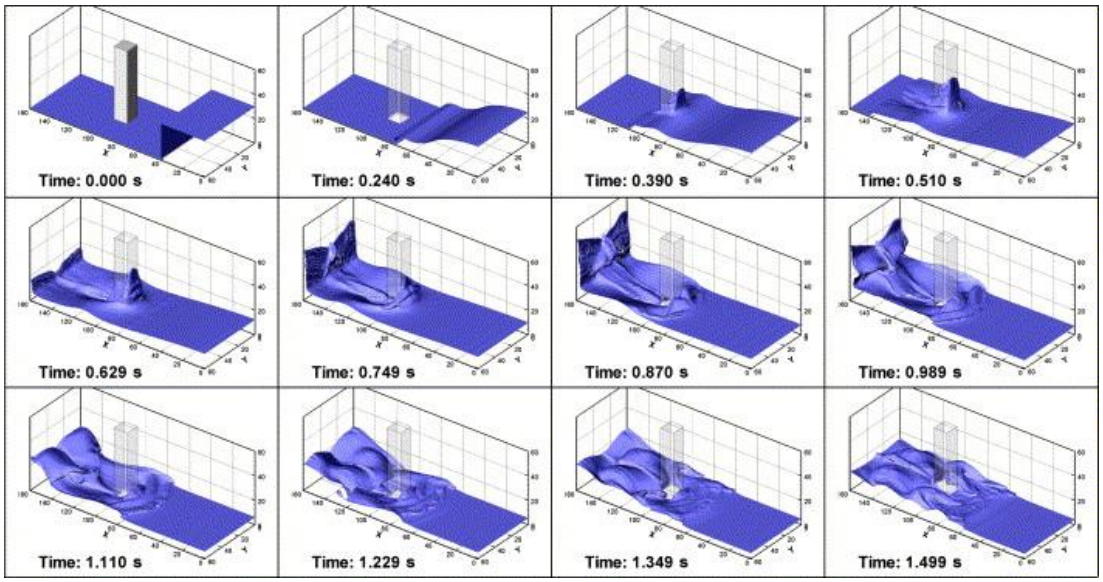

Figure 2-11- Numerical axonometric view of the University of Washington's experiment for tsunami bore runup. The sequence of images between times t=0.00 s and t=1.499 s shows a dam break and the wave propagation and impact with a vertical structure. At t=0.00 s, the water is at rest behind the reservoir's gate which is then released. The water propagates downstream (from right to left in the images), the water front impacts the structure, hits the downstream closed boundary and reflects upstream showing recirculation behaviour (Raad and Bidoae, 2005).

3 FLASH FLOODS, CASE STUDY AND INSPIRATION

Flash floods are short duration floods associated with excessive amounts of water and are a destructive natural hazard with one of the highest mortalities. The different causes of flash floods include a short duration intense rainfall event, snow melt events, hydraulic structure failures or glacier lake outbursts (World Meteorological Organisation, 2012; Archer and Fowler, 2015). This research will concentrate on intense rainfall events and dam breaks. This chapter will first define flash floods, it will then provide some detailed terminology related to the occurrence of such events and will discuss the difference between flash floods and riverine floods, in particular the characteristics that affect flash floods and the susceptibility of a catchment to flash floods. Finally, the 2004 Boscastle flash flood will be presented in detail and justification of why it has been selected as an inspiration to this research will be provided.

3.1 TERMINOLOGY

It has been recognised that traditional flood management approaches for flooding are not necessarily applicable to flash floods (Kobiyama and Goerl, 2007; World Meteorological Organisation, 2012) and in order to create a more appropriate framework, the differences between these types of events needs to be understood. In this research it is therefore essential to firstly define what a flash flood is, and then to clarify the difference between a large riverine flood and a flash flood.

The World Meteorological Organisation WMO, gives a descriptive definition of a flash flood as follows: *"A flash flood is a short and sudden local flood with great volume. It has a limited duration which follows within a few (usually less than six) hours of heavy or excessive rainfall, rapid snow melt caused by sudden increases in temperature or rain on snow, or after a sudden release of water from a dam or levee failure, or the break-up of an ice jam"* (World Meteorological Organisation, 2012).

From another perspective, Archer and Fowler (2015) defined flash floods in terms of their characteristic features. They defined it as a flood caused by a short period of intense rainfall and with the main characteristic features being the rapidity of onset and the rate of rise in water level. Additionally, other flash flood features that have been identified are the short lag times, the rapid recession and the peak flow (World Meteorological Organisation, 2012).

Kobiyama and Goerl (2007) assembled all definitions on flash floods (Table 3-1) which contain all important characteristics that will be discussed in the next section.

Table 3-1- Summary of recommended definitions for flash floods (Kobiyama and Goerl, 2007)

Term	Author	Definition
Flash flood	IAHS-UNESCO-WMO (1974)	Sudden floods with high peak discharges, produced by severe thunderstorms that are generally of limited areal extent.
Flash flood	Office of Technology Assessment (1980)	A flood that follows the causative event (this might be excessive rains, a dam failure, etc.) within a few hours.
Flash flood	NOAA (1981)	Operationally, flash floods are floods that are short fused and require the issuance of warnings by the local warning and forecast offices rather than by the regional River Forecast Centers.
Flash flood	FEMA (1981)	Flash flooding usually consists of a quick rise in water surface elevation with abnormally high water velocity often creating a 'wall' of water moving down the channel and floodplain.
Flash flood	Georgakakos (1986)	Any flood that occurs at a certain location within a few hours after the causative event (e.g., rainfall, dam break). The time interval of **12 hours** is adopted as the upper bound of the time interval between the time of occurrence of the causative event and the time of occurrence of the flash flood at a certain location.
Flash flood	WMO (1994)	In small catchment, with the time of concentration less than **6 hours**, intense precipitation can generate a flash flood.
Flash flood	Kömüşçü *et al.* (1998)	Are usually produced by intense convective storms which cause very rapid runoff, and the damaging flood usually occurs within hours of the causative rainfall and affects very limited areas.
Flash or Rapid flood	Castro (1996)	Are caused by intense and concentrated rainfall in steep slope regions, and characterized with rapid and violent rising of level of water which flows rapidly.
Flash flood	Doswell (1997)	Flood events where the rising water occurs during or a matter of a few hours after the associated rainfall. If the damaging water level increases occur more than a few hours after the rainfall, the event is considered to be a flood, not a flash flood.
Flash Flood	AMS (2000)	A flash flood is a flood that rises and falls quite rapidly with little or no advance warning, usually the result of intense rainfall over a relatively small area.
Flash flood	Kelsch *et al.* (2001)	Phenomena in which the important hydrologic processes area occurring on the same spatial and temporal scales as the intense precipitation.
Flash flood	Kron (2002)	They are produced by intense rainfall over a small area. Typically, flash floods have an extremely sudden onset.
Flash flood	National Disaster Education Coalition (2004)	Flash floods occur within **6 hours** of a rain event, or after a dam or levee failure, or following a sudden release of water held by an ice or debris jam.
Flash flood	Choudhury *et al.* (2004)	Flash floods are very short-lived floods lasting from several hours to a few days. Water in such flooding rises and falls rapidly.
Flash flood	Mendiondo (2005)	Is a flood event of short duration with a rapidly rising flood wave and a rapidly rising water level. Flash floods are caused by heavy, usually short precipitation, as a torrential rain, in an area that is often very small, typically in conjunction with a thunderstorm.
Flash flood	NWS/NOAA (2007)	A rapid and extreme flow of high water into a normally dry area, or a rapid water level rise in a stream or creek above a predetermined flood level, beginning within **6 hours** of the causative event (e.g., intense rainfall, dam failure, ice jam).

Due to the complexity and multiplicity of the above definitions, Kobiyama and Goerl (2007) created a quantitative method of distinguishing a flash flood from a large riverine flood by looking at a specific time between the flood occurrence and the available time of evacuation in order to be considered a flash flood. They derived an Operation Efficiency Index (OEI) where OEI is the ratio of time of the flood concentration to the operational response time. The flood concentration T_c is the time it takes for water to flow from the most remote point

in a catchment to the catchment outlet and is calculated based on some environmental indices and the operational response time T_o is defined based on four factors: the time of the weather forecasting, the time for the forecasting to be delivered to the Civil Defence, the time of the alert system and the evacuation process time.

$$OEI = \frac{Time\ of\ flood\ concentration}{Operational\ response\ time} = \frac{T_c}{T_o} \begin{cases} if\ OEI > 0 & "normal\ flood" \\ if\ OEI < 0 & "flash\ flood" \end{cases}$$

The interest of this method lies in that the time of flood concentration encompasses two key aspects: environmental factors (i.e. topography, land use and precipitation) and the operational response time considers human factors (i.e. previous accurate time of weather forecast, time for the information to be communicated from the forecasting centre to the Civil Defence, time for the Civil Defence to raise an alarm, time required for safe evacuation of the community).

Next, key terms related to floods, flash floods and dam breaks are defined. First, the selected definitions for *flood* and *flash flood* are given then terms related to the flood event itself such as *onset*, *water level rise*, *peak flow* and *peak* rainfall are provided. Terms relating to the event hydrographs are also defined such as *recession* or *falling limb*, *base flow* and *lag time*. Finally, vocabulary that is related to *dams*, *dam breaks* and *gravity currents* is presented such as *backwater* or *reservoir*, *dam break wave*, *negative wave* and *wave front*. All terms and their definitions are summarised and presented in Table *3-2*.

Table 3-2- *Summary of key terms related to flash floods and their respective definitions*

Term	Definition
Flood	"An overflow of a large amount of water beyond its normal limits, especially over what is normally dry land" (Oxford University Press, 2010).
Flash flood	"A flood that rises and falls quite rapidly with little or no advance warning, usually as the result of intense rainfall over a relatively small area" (Ahrens, 2006).
Flashy catchment	"A catchment area that, because of geographic, topographic, and geological factors, shows an almost immediate response to intense rainfall, resulting in a flash flood" (Oxford University Press, 2018).
Onset	The beginning of the flood event.
Water level rise	Difference in water level between the normal water level and the highest water depth during the flood event.

Peak flow	The maximum flow rate reached during the period of runoff caused by a rainfall event.
Peak rainfall	The maximum rainfall level during the flood event.
Recession or Falling limb	The decrease of flow rate after a flood event to what at one time has been regarded as the normal.
Rising limb	The rapid increase in flow rate resulting from rainfall causing surface runoff until peak flow is reached.
Base flow	Normal river flow rate.
Lag time	Difference in time between the peak rainfall and peak discharge.
Dam	"A barrier constructed to hold back water and raise its level, forming a reservoir used to generate electricity or as a water supply" (Oxford University Press, 2010).
Dam break	"The idealised release of a reservoir of water akin to that of a complete collapse of a dam" (McMullin, 2015).
Gravity current	"Gravity currents occur whenever fluid of one density flows primarily horizontally into a fluid of different density" (Huppert, 2006).
Backwater or Reservoir	"A part of a river not reached by the current, where the water is stagnant" (Oxford University Press, 2010).
Dam break wave	The volume of water propagating downstream after the dam break.
Negative wave	The wave moving upstream within the reservoir after the dam break.
Wave front	The leading part of the dam break wave.

3.2 DIFFERENCES BETWEEN RIVERINE FLOODS AND FLASH FLOODS

Using the definitions compiled in Table *3-2*, the main differences between riverine floods and flash floods can be further discussed. This was first attempted by Jianchu et al. (2006) who considered the management of flash floods and sustainable development in the Himalayas and created a table (see Appendix A.1) discussing the main differences between riverine floods and flash floods. Yet, his table remains incomplete for the aims of this research and hence, using additional sources (i.e. World Meteorological Organisation (2017), (2012), (2007), Shrestha et al. (2008), Archer and Fowler (2015), Merz and Bloschl (2003), Kobiyama and Goerl (2007)) this initial comparative table was further improved and is shown in Table *3-3*.

Table 3-3- Summary of differences between flash floods and riverine floods in terms of causes, characteristic features, associated problems, frequency, affected areas and forecasting based on initial table created by Jianchu et al. (2006)

	Flash floods	**Riverine floods**
Causes	– High intensity rainstorms or cloudbursts – Sudden snow/glacier melt – Dam breaks – Levee breaches – Wet/dry catchment	– Prolonged seasonal precipitation – Seasonal snow and glacial melt – Saturated catchment
Characteristic features	– Quick onset – Short storm/flood duration – Quick water level rise – Peak flow in minutes/few hours – Quick recession – Not related to base flow – Rapid response to rainfall, short lag time – Limited spatial extent (< 30km^2) – Steep slope catchments	– Slow onset – Long storm/flood duration – Slow water level rise – Peak flow in hours/days – Slow recession – High base flow – Slow response to rainfall, medium/ long lag time – Regional to large spatial extent – All catchments
Associated problems	– Large amount of debris – High hydraulic force associated with erosion and structural damage	– Inundation/ flooding
Frequency	– All year	– Rainy season
Affected areas	– River plains, valleys – Local extent – Small to medium areas	– River plains, valleys – Local to regional extent – Large areas
Forecasting	– Forecasting difficult – Local information essential – Hydro-meteorological problem – Coordination for flood response in real-time difficult	– Forecasting possible – Local information not essential – Hydrologic problem – Coordination for flood response in real-time possible

Here, the differences are presented in terms of causes, characteristic features, frequency, associated problems, affected areas and finally forecasting. Considering first the causes of flood events, important differences worth noticing between riverine and flash floods include in the case of flash floods, the intensity rainstorms compared to prolonged seasonal precipitation for riverine floods and also the state of the catchment, which can be dry for

flash floods, as opposed to typically saturated for riverine floods. In terms of their characteristic features, the main differences are related to the hydrograph specifications. In particular the rapidity of flash floods manifests itself through a fast onset, a quick rise in water level, a rapid response to rainfall and short lag time. Frequency and range are two other differentiating factors. While flash floods can happen throughout the year and tend to be local and associated with large amounts of debris and high hydraulic forces, riverine floods tend to be frequent mostly during the wet season and affect wider areas. Finally, forecasting of flash floods is typically more challenging and difficult because they are complex localised hydro-meteorological events compared to riverine floods which are considered hydrologic problems (Merz and Bloschl, 2003; Kobiyama and Goerl, 2007; World Meteorological Organisation, 2007; Shrestha et al., 2008; World Meteorological Organisation, 2012; Archer and Fowler, 2015; World Meteorological Organisation, 2017).

3.3 WHAT PARAMETERS AFFECT FLASH FLOODS?

As previously mentioned, flash floods due to extreme rainfall events are localised hydro-meteorological phenomena meaning that both the rainfall is important but also the topographical characteristics that affect all hydrological parameters (World Meteorological Organisation, 2007, 2012). Next, the effects of both meteorological phenomena and topographical characteristics will be detailed.

From a meteorological perspective most flash flood events are linked to intensive convective rainfall created by meteorological phenomena called cloudbursts (Shrestha et al., 2008; World Meteorological Organisation, 2012). The mechanism of a cloudburst is illustrated in Figure 3-1 for two different types of wind directions showing that the along-barrier low-level flow (parallel to a mountain ridge) can have a worse effect as the elevated convergence is not weakened after the cloudburst. These phenomena are very common in mountainous areas where orographic lifting occurs through the rising motion of warmer air over sloping topography (Alestalo and Savijärvi, 1985). Solantie (1975) found that the combination of orographic (topography of mountains) and coastal effect can result in an increase in precipitation of 40% close to the coast and a further 20% can be attributed solely to steep slopes. On-shore wind induces a rising motion of warm and humid air which usually follows the upward slope due to the roughness difference. In the cases where the wind currents at the top of the mountains are weak, the thunderclouds created cannot dissolve and all the water falls at the same time resulting in exceptionally localised rainfall. The reason for the

increased local precipitation in mountainous coastlines is attributed to the high vertical velocities in the air induced by the differences in roughness (Alestalo and Savijärvi, 1985). The most extreme storms due to cloudbursts known are 61.72 mm of rain within 5 $minutes$ in Panama in November 1911 and 38.10 mm of rain within 1 $minute$ in Barot, India in November 1970 (Rashid et al., 2012).

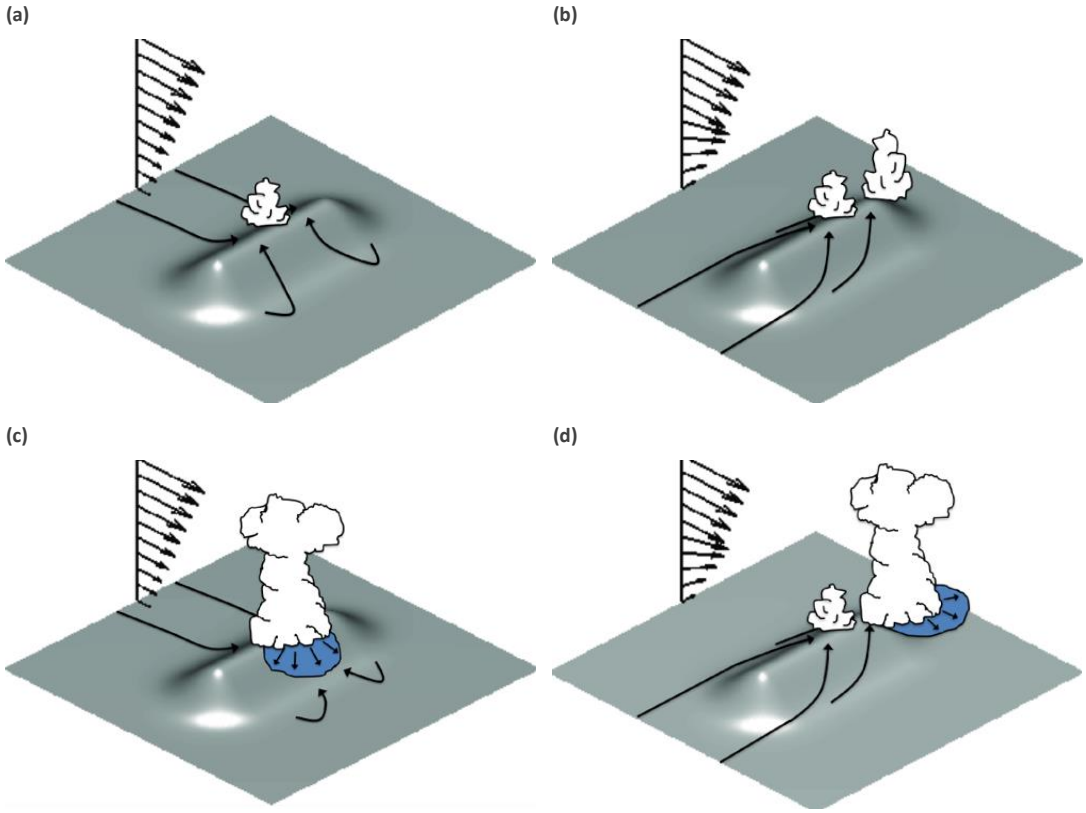

Figure 3-1- Cloudburst mechanism for different ground wind combinations. The grey colour represents the topogaphy with a ridge in the middle, the black arrows show the wind direction, the white shapes represent clouds and the blue the rain pools that flow downhill. Figures (a) and (c) represent cross-barrier low flow where the wind direction is perpendicular to the ridge and develops convergence when it merges with the sheltered side flow. The created clouds produce rain that flows downhill and thus cuts of the flow from sheltered side (back of the ridge) and weakens strength of the created convergence. Figures (b) and (d) show along-barrier low-level flow where the wind direction is parallel to the ridge and is drawn upsolope towards the ridge where convergence is created. The clouds created burst into cold pools where the water floods downhill without affecting the strength of the convergence (Kirshbaum et al., 2018)

The topographical characteristics that affect hydrological properties, and therefore flash floods include soil moisture, the soil depth, the soil permeability, land use, catchment size

and the catchment slope (World Meteorological Organisation, 2012). Soil moisture affects the infiltration and therefore the amount of water that contributes to runoff and the lag time. Flash floods tend to happen in extreme situations when the soil is completely saturated and no further infiltration is possible therefore contributing to higher runoff and therefore decreasing the lag time. It necessary to mention that flash floods can also occur in drought conditions (e.g. desert areas, Wadi) for the same as the precipitation is faster than the infiltration rate of the soil. Soil type (depth and permeability) play a role in infiltration rates and thus runoff as permeable rocks create rapid infiltration and therefore little runoff and thus a shallower rising limb (Colombo et al., 2002). Soil permeability can also accelerate infiltration and reduce runoff and thus cause a shallow rising limb. Land use and land cover also plays an important role as human activity increases the risk of flash floods. Urbanised areas can lead to short lag times with a very steep rising limb rather than lengthening of lag time and a shallow rising limb result of wooded areas (Colombo et al., 2002). According to the World Meteorological Organisation, land use can lead to a reduction of lag time and peak flow by a factor 2-6 in comparison to natural terrains (World Meteorological Organisation, 2007, 2012). The size of the catchment also has an effect as an increase in area will produce more runoff and result in longer lag times. Slope also influences the storm hydrograph as steeper slopes result in a steeper rising limb and shorter lag time.

3.4 CATCHMENT SUSCEPTIBILITY TO FLASH FLOODS

Lastly, beyond meteorological and topographical factors it is important to consider a catchment's susceptibility to flash floods because this could be used as an initial assessment before any numerical modelling is required. Research on this concept was first presented by Smith (2003) and then followed by Collier and Fox (2003), Collier (2007), COMET UCAR (2010), Zogg and Deitsch (2013), and Lincoln et al. (2016). The Collier (2007) method of assessing the susceptibility of a catchment to flash flooding was created by using a scoring system encompassing many of the hydro-meteorological parameters. His research looked at meteorological variables such as the probability of stationary heavy rain and topographical characteristics for instance the slope of the catchment, the soil conditions, the shape of the basin and the possibility for surge wave creation. Table *3-4* shows the criteria used and their assessment level. All criteria were equally weighted and a score from 0 to 4 (top row of Table *3-4*) was assigned to show whether a criterion facilitated flood development (Collier and Fox, 2003; Collier, 2007). They validated the assessment system by testing it with historical flood events in the United Kingdom and even though the method responded well for major floods,

it did not capture the susceptibility to extreme events such as flash floods well. The method was tested on the 2004 Boscastle flash flood which will be further discussed in the next section and returned a score of 28 out of 48, identifying a "major" rather than an "extreme" event. The reason for the weakness of the scoring system was accredited to the equal weighting of all parameters. In this event, the most important parameters were the rainfall depth and the steepness of a small catchment that resulted in the severity of this event. Defra and Environment Agency (2004) analysed the Collier and Fox (2003) method and concluded that more weighting should possibly be assigned to the aforementioned factors compared to other criteria. The Defra and Environment Agency (2004) built upon this and investigated the possibility to develop a tool to identify the relative catchment susceptibility to flooding under extreme conditions, but further investigation was deemed necessary for the development of such a tool and its incorporation to existing Flood Forecasting & Warning FFW systems (Defra and Environment Agency, 2004).

Table 3-4- *Collier and Fox's scoring system for flooding susceptibility of catchments (Collier and Fox, 2003)*

	Assessment level				
Score	0	1	2	3	4
Steep catchment?	<1 : 50	1 : 50–1 : 20	1 : 20–1 : 10	1 : 10–1 : 15	>1 : 5
DPSBAR km^2 km^{-1}	<0.02	0.02–0.05	0.05–0.10	0.10–0.20	>0.20
Land use/Veg.type (URBEXT)	Essentially rural <0.05	0.05–0.125	0.125–0.250	0.250–0.5	Extreme urban >0.5
AREA/DPLBAR (km^2 km^{-1})	8–14	14–30	5–8 or >30	1–5	<1
Channel constrictions	None	Some constrictions	Soft constrictions	Solid constrictions or soft ones that may act temporarily	Major, solid constrictions
Percentage runoff (SPRHOST)	<10	10–19.9	20–34.9	35–50	>50
Debris?	No dry spell – fast flow	No dry spell – slow flowing river	Dry spell before – slow flowing rural or fast urban	Short dry spell – urban medium to slow flow	Long dry spell before – urban medium to slow flow
SMD (mm)	>100	50–100	15–50	5–15	<5
Heavy rain? (Peak hourly catchment rainfall; mm h^{-1})	<4	4–10	10–20	20–40	>40
Long lasting (minutes)	Very short <15	Short 15–45	Medium 45–90	Long 90–180	Very long >180
Rain stationarity (m s^{-1})	Rapid >20	Fast 10–20	Medium 5–10	Slow 1–5	Stationary <1
Direction of motion (deg)	80–90	60–80	20–60	5–20	0–5–parallel
Snow depth (mm)	0	<10	10–50	50–100	>100

DPSBAR is the mean of all the inter-nodal slopes for the catchment which characterizes the overall steepness (m km^{-1}). URBEXT is the extent of urban and suburban land cover. AREA is the catchment drainage area (km). DPLBAR is the mean of distances between each node (on a regular 50 m grid) and the catchment outlet (km); it characterizes the catchment size and configuration. SPRHOST is the standard percentage runoff derived using the HOST (Hydrology Of Soil Types) classification. SMD is the soil moisture deficit.

The 2004 Boscastle flash flood will now be presented in detail considering the causes and characteristic features and justification of why it has been selected as an inspiration for this research will be provided.

3.5 THE BOSCASTLE CASE STUDY

The inspiration for the experimental and numerical modelling reported here was the August 2004 Boscastle flash flood. The Boscastle event is a common case in flood risk modelling and

has already been modelled by several researchers numerically and experimentally both from a hydrological but also a meteorological perspective.

A detailed study by HR Wallingford (2005) described the meteorological, hydrological and hydraulic aspects of the flash flood event. The event was reconstructed numerically and propagation mechanisms, peak flows and peak water levels were presented (HR Wallingford, 2005a, b). Next, Roca and Davison (2010) analysed main flash flood processes using a 2D numerical model and investigated specifically the flow regime changes, the blockage of structures, changes in flow paths and the effect of the geomorphology on flow characteristics conducted extensive research, both experimentally and numerically, looking at submerged vehicles during a flash flood and used the Boscastle flash flood as a case (Xia et al., 2011a; Xia et al., 2011b; Xia et al., 2014; Xia et al., 2016).

The Boscastle event hydrodynamics have also been modelled extensively. Important work was presented by Lhomme et al. (2010) who looked at flood extents and forces on buildings using a 2D model, Falconer (2012) looked at flow interactions of supercritical flow with buildings and Xia et al. (2011b) modelled flash flood risk in urban areas taking into account not only the flood extent but also the risk to people and properties.

Research has also been conducted on the Boscastle flash flood from a meteorological perspective. The forecasting department of the Met Office analysed the meteorological conditions before the flash flood both from observations but also using output from a high-resolution land surface model (Golding et al., 2005). Burt (2005) discussed specifically the rainfall observations recorded during the event and compared the Boscastle flash flood to other historical storms in Great Britain, concluding that even though it is considered as a very extreme event, the historical perspective is important as it showed that as there have been many other severe events in the area. Murray et al. (2012) modified a flash flood severity assessment, previously created by Collier and Fox (2003), and determined from a hydro meteorological point of view and using a scoring system, the flood susceptibility and severity of a catchment to extreme events. Warren et al. (2014) discussed the similarity of another quasi-convective stationary system in 2010 in the south west of England which had many similar characteristics to the Boscastle event.

As shown, Boscastle is a common case in flood risk modelling and the characteristics surrounding the event, have been analysed from many different perspectives. Therefore, this provides confirmation of the relevance of the 2004 Boscastle flash flood event and proves it

is considered a suitable case study for the inspiration of the undertaken experimental and numerical modelling of this research.

3.5.1 Catchment description

To understand the background of the flash flood and how extreme the 2004 flash flood was, the area will first be described in terms of geographical location, geology, catchment description and climate before describing the 2004 event.

Boscastle is a village located in North Cornwall on the South West Coast of the United Kingdom. It has an annual rainfall total of 918.2 mm (Met Office, 2010a). Figure 3-2 shows the average monthly rainfall in Bude, closest weather station to Boscastle, where November is typically the wettest month and April the driest. For comparison Figure 3-3 shows the average rainfall around the UK from 1821 to 2010 for (a) an annual average, (b) November (Boscastle's wettest month) and (c) April (Boscastle's driest month) (Met Office, 2010a; World Weather & Climate, 2016). When considering the rainfall profiles for Boscastle in Figure 3-2 and Figure 3-3 it is apparent that the highest monthly average is 100 mm of precipitation in November which is a typical value for the country.

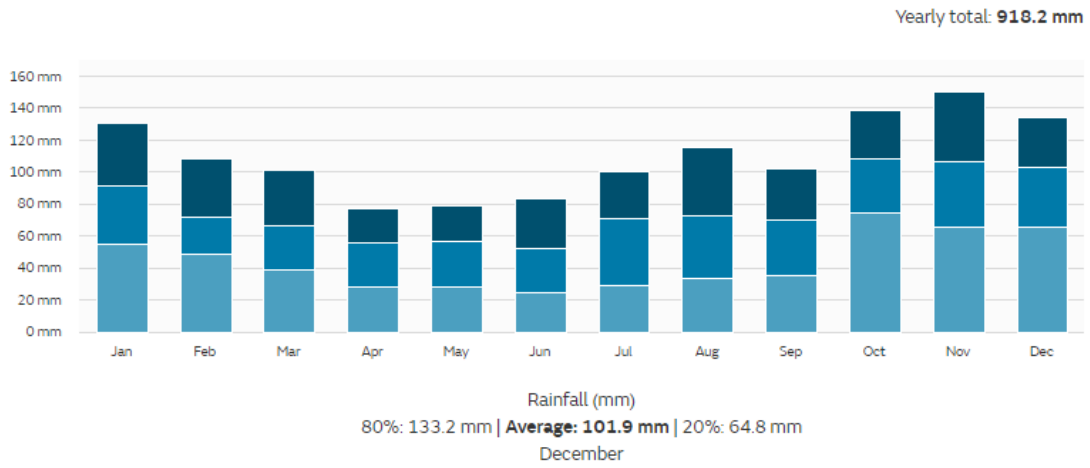

Figure 3-2- Average monthly rainfall in Bude, closest weather station to Boscatle, between 1981 and 2010 (Met Office, 2010b)

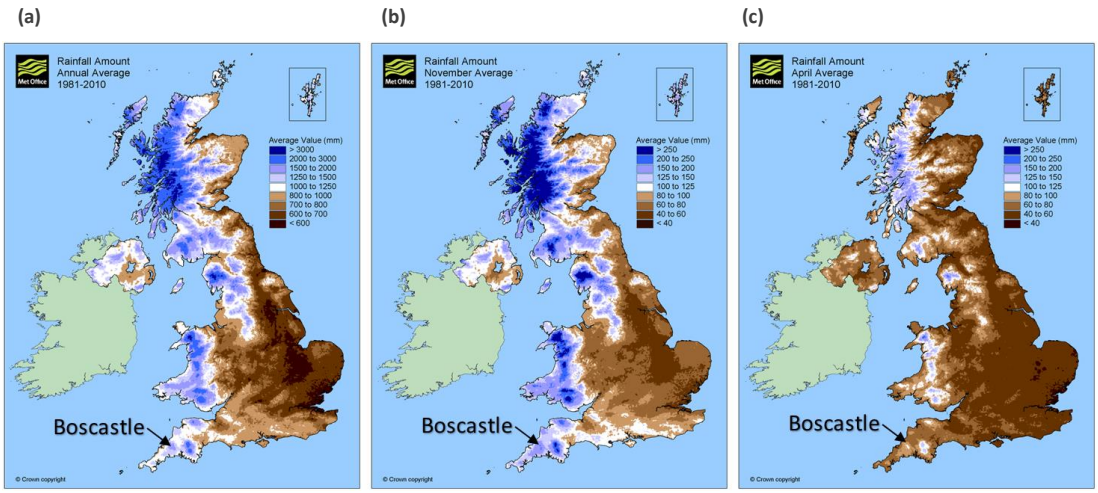

Figure 3-3- Average rainfall between 1821 and 2010 (a) annually (b) November and (c) April (Met Office, 2010a)

Boscastle, is positioned in the Valency catchment at the bottom of the valley where the two rivers, the Valency River and the Jordan River, meet (Into Cornwall, 2015). The catchment that drains into Boscastle is the Valency catchment which has a round shape (Figure 3-4a), is 8.04 km in length with an area of 20.4 km^2 (Environment Agency, 2016). It is mainly rural and areas of woodland surround the main river (Xia et al., 2011b).

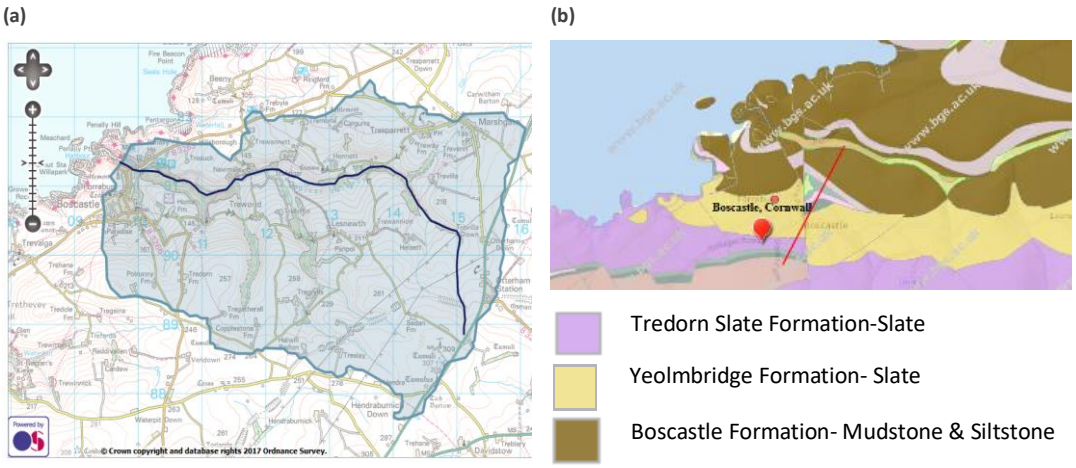

Figure 3-4- (a) Valency catchment (Environment Agency, 2016), (b) Boscastle and surrounding area's geology including slate, mudstone and siltstone (British Geological Survey, 2016)

The bedrock geology of the area is a Yeolmbridge formation which contains slate (Figure 3-4b) but there is also sedimentary bedrock and pelagite deposits, due to the preceding domination of sea water (British Geological Survey, 2016). Slate has a low hydraulic

conductivity of $5 \times 10-9$ to $5 \times 10-6\ m/s$ which results in relatively slow infiltration through the strata (British Geological Survey, 2006). This, in combination with the small steep rocky catchment results in increased runoff potential and a steep rising limb. Such catchments characterised by an almost instant response to intense rainfall are characterised as "flashy catchments".

3.5.2 The 2004 flash flood event

Heavy rainfall on the 16th August 2004 caused severe flooding in the Valency catchment and the River Jordan. This resulted in a flash flood in Boscastle which caused severe damage. Even though there were no casualties, at least 100 people had to be evacuated, 60 buildings were flooded, with some of them completely wrecked, and 116 vehicles were carried by the flow (Xia et al., 2011b). From a meteorological point of view, a cyclonic scale in the Atlantic Ocean resulted in a humid and unstable environment over Cornwall. Due to the lack of wind, clouds assimilated and moved north-east resulting in very concentrated rainfall on the Valency catchment with peak rates of precipitation up to 400 $mm \cdot h^{-1}$ (Golding et al., 2005). On that day, the soil was already saturated at the onset of the heavy rainfall. This combined with the overlay of impermeable rock (easily saturated), the steepness of the slopes (1/20) and the static cumulonimbus clouds, resulted in a rapid saturation of the soil and an increase in the surface run-off. $200\ mm$ of rainfall accumulated in 5 hours which corresponds to 2.5 times the monthly rainfall average in Boscastle and 21% of the year rainfall average. The annual probability of occurrence exceedance for the overall storm was calculated to be 0.05% (1 in 2000 years) (HR Wallingford, 2005b).

The peak flow rate was calculated and expected to have reached $140\ m^3/s$ upstream of the river Jordan and a maximum of 180 m^3/s downstream of the river (HR Wallingford, 2005b) with residents describing seeing a "wall of water" approaching the harbour (North Cornwall District Council, 2004) later translated to a $2\ m$ high flash flood wave (Xia et al., 2011b). As the catchments were not gauged, in order to derive the full hydrographs shown in Figure 3-5, two methods were used. The first was a statistical approach and the second one was a rainfall-runoff model (HR Wallingford, 2005b). Figure 3-5 shows the discharge hydrographs for different locations along the River Valency. Velocities were not measured during the flash flood but were computed based on the measured water levels on the Boscastle buildings (HR Wallingford, 2005b). Figure 3-6 shows the maximum modelled velocities which reached a maximum value of 10 m/s at the Valency River.

Some photos from the flood can be seen in Figure 3-7 showing the extent and damage of the flood. Despite the 2004 flash flood being a very famous and catastrophic event, it was not the first recorded case of a notably large flood nor flash flood in the village. The most important events since 1827 are listed below, supporting the concept that some catchments may be more predisposed to flash floods than others (North Cornwall District Council, 2004):

- 28th October 1827 – No rainfall recorded
- 16th July 1847 - No rainfall recorded
- 6th September 1950 - No rainfall recorded
- 8th June 1957 – $140\ mm$ in 2.5 hours
- 3rd June 1958 – River rose $4.5\ m$ in 20 minutes
- 6th February 1963 – No rainfall recorded

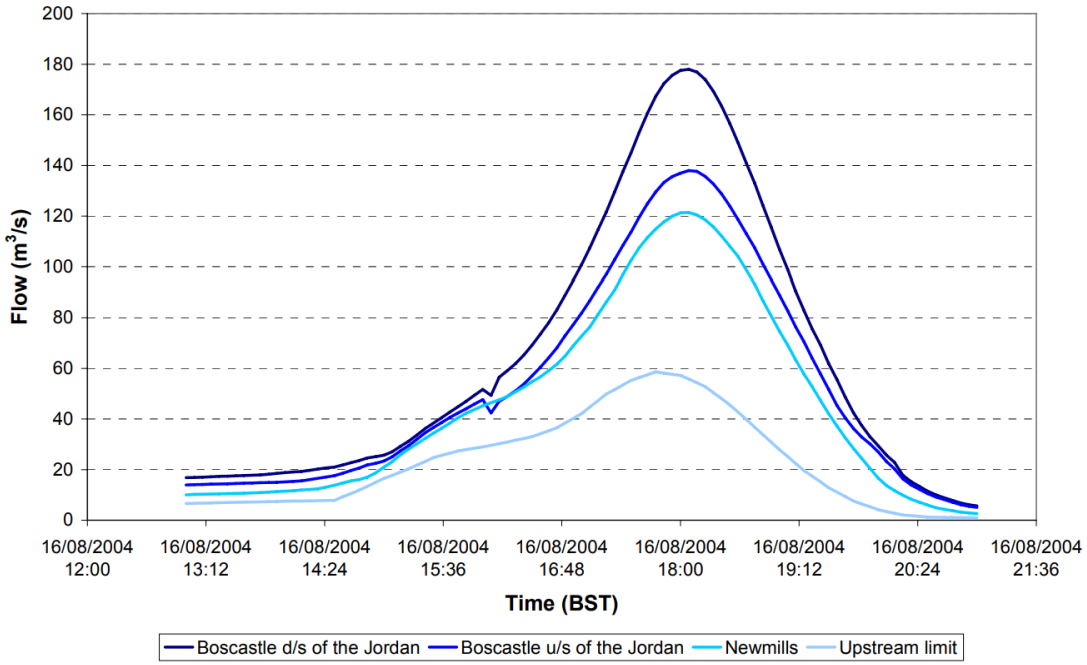

Figure 3-5- Discharge hydrographs for different locations at the Valency catchment. The dark blue line shows the discharge hydrograph in m^3/s at the downstream d/s boundary of the River Jordan in Boscastle. The next slightly lighter blue line shows the hydrograph at the upstream boundary of the river Jordan. The other two lines show the discharge hydrograph at Newmills in the middle of the two river's confluence and at the upstream boundary of the river Valency respectively (HR Wallingford, 2005b)

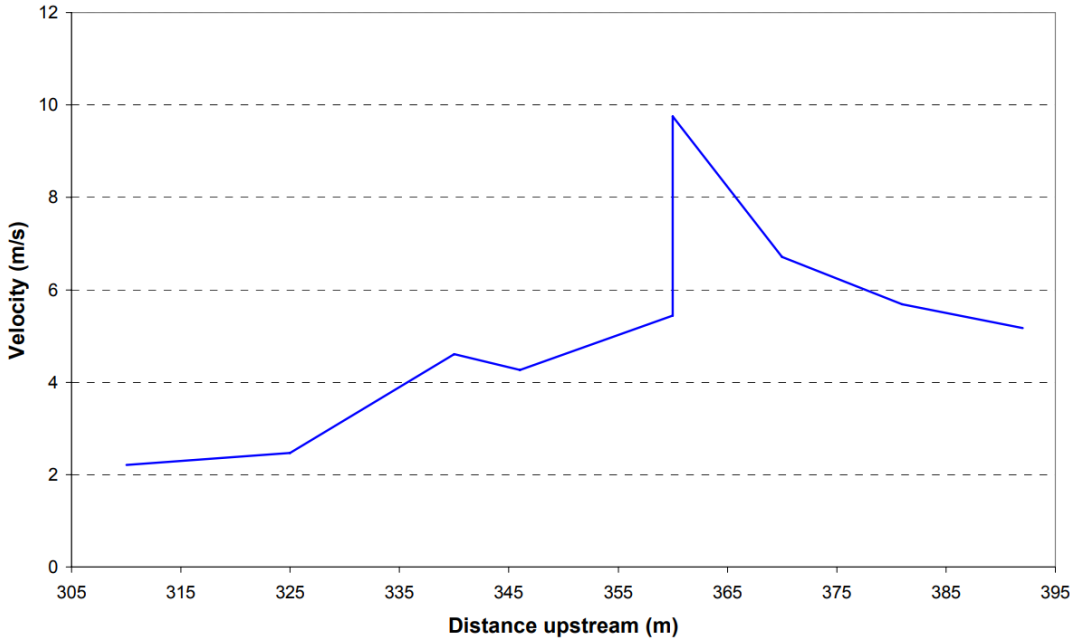

Figure 3-6- Maximum numerically calculated velocities in the Valency River plotted against the distance from the upstream limit of the model (HR Wallingford, 2005b)

Figure 3-7- Photographs from the Boscastle 2004 Flash Flood in the Boscastle harbour area: (a) Flooding of the Valency River, flooded Penally Hill and blockage of the bridge (b) Flooded Penally Hill (c) Flooding of the Valency River and bridge blockage (HR Wallingford, 2005b)

3.5.3 Site visit

A site visit to the Boscastle harbour area was undertaken in February 2017. The slope of Penally Hill (Points 0-7 Figure 3-8) was measured and the height of important flood water marks identified as being associated with the August 2004 event (Points A-E) were recorded (Figure 3-9). The vertical measurements of the water levels and the final elevation of the flood marks can be seen in Table 3-5 and the profile of the slope of Penally Hill is shown in Figure 3-10 with the observed data presented in Table 3-6.

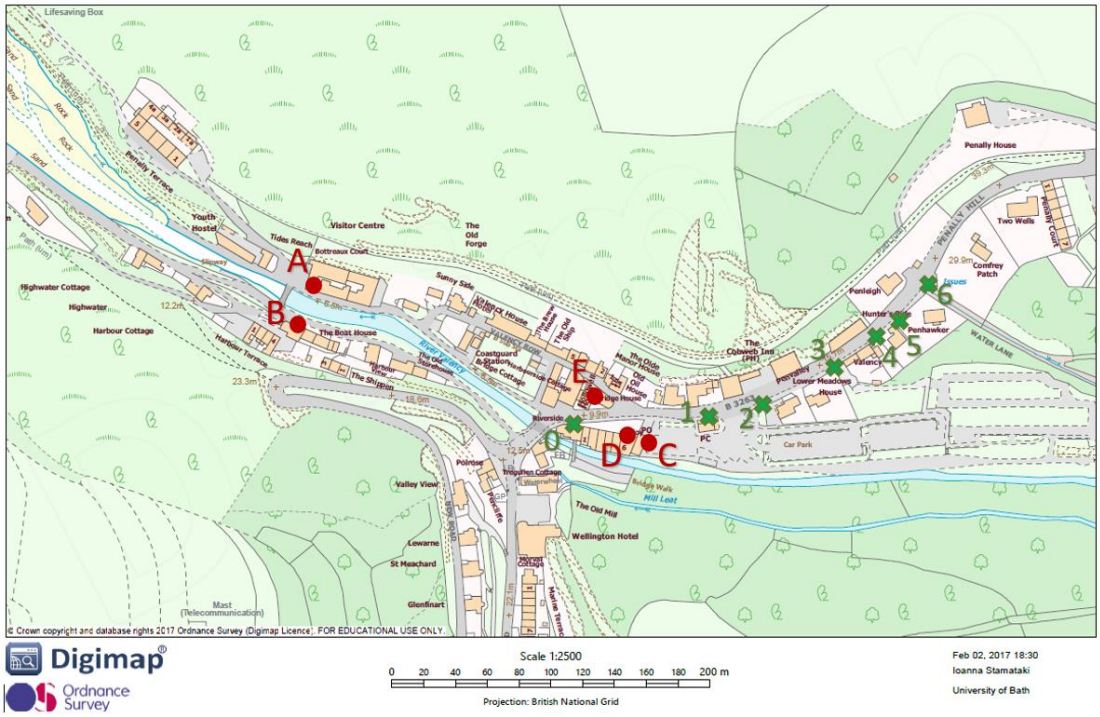

Figure 3-8- OS Map of the Boscastle harbour area with measurement locations. Points 0-7 in green represent the measurement locations for the calculation of Penally Hill's slope and points A-E in red represent where important flood water marks were recorded and measured (Ordnance Survey, 2017)

Figure 3-9- Water levels (red dots) from the Boscastle 2004 flash flood in the Boscastle Harbour area: (a) Flood water mark B (National Trust), 3.57 m (b) Flood water mark B (Seagulls), 2.98 m (c) Flood water mark E (Bridge House), 2.46 m

Table 3-5- Water level marks Boscastle

Location	OS Maps Elevation [m]	Vertical Height [m]	Final Elevation Levels [m]
A. National Trust	23.96	2.98	26.94
B. Seagulls	24.16	3.57	27.73
C. Cornish Stores	30.88	2.15	33.03
D. Toby Jug Café	30.73	3.81	34.54
E. Bridge House	29.58	2.46	32.04

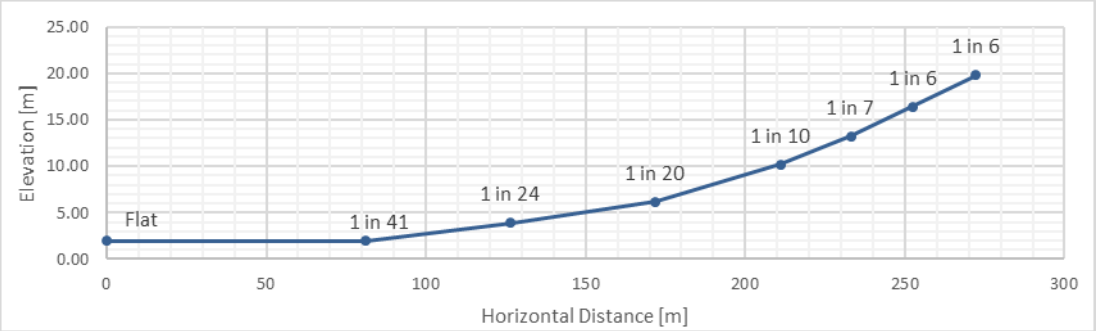

Figure 3-10- Topography of Penally Hill, Boscastle

Table 3-6- Slope measurements in Penally Hill, Boscastle describing the seven measured segments and the individually calculated slopes and angles

Location	Description	Slope		Angle [°]
Initial Part	Riverside hotel- Old visitor centre	1 in	41	1.4
Slope	Bus stop visitor centre- Corner of spar	1 in	24	2.4
Slope	Corner before spar-lamp post before steep slope	1 in	20	2.9
Steeper slope	Lamp post after spar before slope- end of destroyed building	1 in	10	5.8
Steeper slope	End of destroyed building- just after Penhawker house's entrance	1 in	7	8.0
Steeper slope	Opposite after Penhawker house's entrance- mid entrance	1 in	6	9.3
Steeper slope	Penleigh entrance to first pole on the bend	1 in	6	9.7

Following the 2004 event, mitigation solutions were implemented by the Environmental Agency in the village (Figure 3-11) including a £4.2m project in October 2006. The most important mitigation solutions were: (i) erosion control mats which could accommodate $5\ m/s$ flows, (ii) raising the car park level which previously flooded, (iii) installation of SUDS and permeable paving, river dredging, widening and realignment to avoid blockage from fallen trees and slow down its flow, (iv) installation of a flood overflow culvert for the River Jordan, (v) installation of concrete toe-rail at the foot of the embankment, and (vi) new flood defence walls and new wider span bridge downstream with a 1 in 100 year flood design life designed to fail in case of a similar event (Nicholas Pearson Associates, 2012; Halcrow Group Ltd, 2017). For a larger version of Figure 3-11, see Appendix A.2.

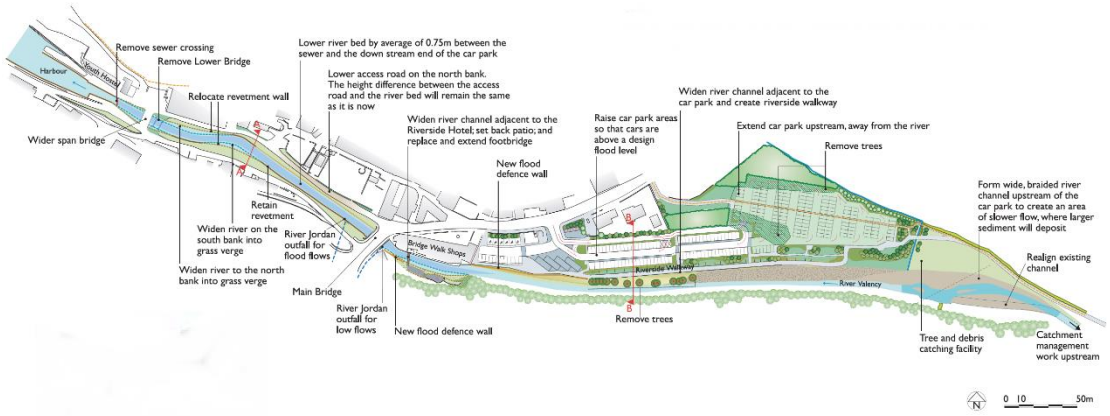

Figure 3-11- £4.2m flood defence mitigation project in Boscastle implemented by the Environmental Agency including erosion control mats, raised car park level, installation of SUDS and permeable paving, river dredging, widening and realignment, installation of a flood overflow culvert for the River Jordan, installation of concrete toe-rail at the foot of the embankment, new flood defence walls and new wider span bridge (Nicholas Pearson Associates, 2012)

3.6 DIMENSIONAL SIMILARITY AND SCALING PROBLEMS

The Boscastle event was selected as the inspiration to conduct further laboratory experiments and was simplified and scaled down for experimental purposes. For scaling problems, it is important to ensure that the flow conditions in a model are similar in terms of geometry, motion and dynamic similarity to the prototype (Chanson, 2004b). Dimensional analysis is an important tool used by engineers when planning experimental tests but also when interpreting experimental results. All physical hydrodynamic quantities are presented in their fundamental dimensions in Table 3-7 and this permits rescaling of the data for different case studies (Chadwick et al., 2004)

For open channel flow, when a model is created, in order to reproduce the physical properties of the prototype, it needs to be scaled. In order for the models to be geometrically similar, *geometric similarity* can be obtained by calculating (Chadwick *et al.*, 2004):

$$\frac{length_{prototype}}{length_{model}} = \lambda$$

Table 3-7- Scale ratios for Froude and Reynolds number similarities (Heller, 2012)

Scale ratios for Froude models

Parameter	Dimension	Froude	Reynolds
	Geometric similarity		
Length	[L]	λ	λ
Area	[L^2]	λ^2	λ^2
Volume	[L^3]	λ^3	λ^3
Rotation	[-]	1	1
	Kinematic similarity		
Time	[T]	$\lambda^{1/2}$	λ^2
Velocity	[LT^{-1}]	$\lambda^{1/2}$	λ^{-1}
Acceleration	[LT^{-2}]	1	λ^{-3}
Discharge	[L^3T^{-1}]	$\lambda^{5/2}$	λ
	Dynamic similarity		
Mass	[M]	λ^3	λ^3
Force	[MLT^{-2}]	λ^3	1
Pressure and stress	[$ML^{-1}T^{-2}$]	λ	λ^{-2}
Energy and work	[ML^2L^{-2}]	λ^4	λ
Power	[ML^2T^{-3}]	$\lambda^{7/2}$	λ^{-1}

In order to achieve complete similarity, there are two more conditions that need to be met: kinematic similarity and dynamic similarity (McKinley, 2013). Kinematic similarity requires the model velocity V_m to be proportional to the prototype velocity V_p by a constant factor and the dynamic similarity needs all forces to also be proportional by a constant factor (McKinley, 2013). The two standard dimensionless groups used to obtain these similarities are the dimensionless parameters: Reynold's number and Froude number. Froude similarity is a very widely used similarity in open channel flow problems, where the gravity forces are dominating the flow. It is based on the constant Froude number ratio between prototype and model. The Froude number, shown in Equation 3-1, is the square route of the ratio of inertial and gravity forces, u is the water velocity (m/s) and d is the hydraulic mean depth (m) (Chadwick et al., 2004).

$$Froude\ number\ F = \left(\frac{Inertial\ force}{Gravity\ force}\right)^{\frac{1}{2}} = \frac{u}{(gd)^{1/2}} \qquad \textit{Equation 3-1}$$

The dimensional similarity for the Boscastle case, was calculated based upon the following geometric similarity. A width of a $10\ m$ building was taken as the prototype length (see Figure 3-12) and was scaled to $0.2\ m$ in the laboratory, obtaining a scale of 1 in 50. Therefore,

$$\lambda = \frac{length_{prototype}}{length_{model}} = \frac{10}{0.2} = 50$$

Figure 3-12- Photograph showing the flooded Penally Hill and blockage of the bridge. The house highlighted in the yellow dashed square has been used to determine the prototype length used for the geometric similarity. The highlighted building has a width of 10 m.

Maintaining then the Froude similarity, $(Fr)_{model} = (Fr)_{prototype}$, the different quantities, such as flow rate and velocity, were calculated using dimensional analysis (Chanson, 2004b). Quantities such as flow rate and velocity were calculated and summarised in Table 3-8. From Figure 3-6, a maximum prototype velocity was taken as $u_{prototype} = 10\, m/s$.

Thus,

$$(Fr)_{model} = (Fr)_{prototype}$$

$\frac{u_m}{\sqrt{g_m d_m}} = \frac{u_p}{\sqrt{g_p d_p}}$ where $g_m = g_p$ therefore,

$$\frac{u_m}{u_p} = \sqrt{\frac{d_m}{d_p}} = \sqrt{\frac{1}{\lambda}} \Rightarrow u_m = \sqrt{\frac{1}{\lambda} {u_p}^2} = 1.41\, m/s$$

From Figure 3-5, the prototype flow was taken as $Q_{prototype} = 140\, m^3/s$. Using Table 3-7, the flow rate in the model is calculated:

$$\frac{Q_p}{Q_m} = \frac{\lambda^3}{\sqrt{\lambda}} \Rightarrow Q_m = \frac{Q_p \sqrt{\lambda}}{\lambda^3} = 0.079\, m^3/s = 79\, l/s$$

Table 3-8- Quantities (length, velocity, flow rate) calculated for the Boscastle model dimensional similarity

Quantity	Prototype	Value	Model	Value
Length (m)	Lp	10	Lm	0.2
Velocity (m/s)	Vp	10	Vm	1.41
Flow ($m3 \ \ /s$)	Qp	140	Qm	0.0079

The experiment was therefore designed in the configuration shown in Figure 3-13. It consisted of an elevated reservoir, followed by a $1/20$ ramp (slope of Penally Hill) followed by a flat area, the urban settlement where only the single building from Figure 3-12 was positioned in the middle of the setup. The setup and experimental analysis will be further described in the next chapter.

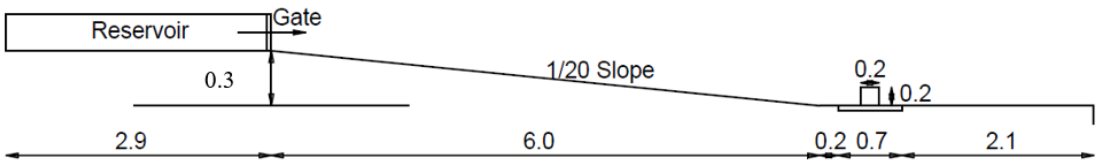

Figure 3-13- Schematic representation of experimental set up showing the reservoir and gate followed by a six meter 1/20 ramp and a flat area were a 0.2 x 0.2 m building is installed

The importance of physical modelling in relation to numerical modelling has been widely discussed, physical models provide insight into complex hydrodynamic regimes and non-linear phenomena with fewer simplifications and assumptions present (Chanson, 2004b; Chaudhry, 2008; Pinto, 2012). Nevertheless, the behaviour of the model and prototype is sometimes different, and this is attributed to scaling, laboratory or measurement effects. Laboratory effects can be due to the three-dimensionality of the experiment, the reflections or the turbulence intensity and finally measurement effects due to the equipment and their calibration (Pinto, 2012).

When using the Froude similarity, most of the possible scaling issues are associated with the gravitational force g which cannot be scaled using Froude scaling (Chaudhry, 2008; Heller, 2011). But as scaling issues will always be present, the question is whether they can be

neglected. Therefore, the following approaches were considered when the experiments were planned (Chanson, 2004b; Heller, 2011, 2012; Pinto, 2012):

- Not all parameters are affected in the same way therefore an *inspectional analysis* will be undertaken to describe some of the processes mathematically and compare with the experimental results.
- Dimensionless parameters were used to formulate criteria for the dynamic similarity allowing for an expression of the results through a function of dimensionless parameters. By using *dimensional analysis* therefore, scaling errors were moderated.
- The larger the geometric scaling factor λ, the larger the scaling effects. Here, a λ of 50 was used.

Scale effects may also have a "damping effect", therefore judgement was used comparing with field data from the Boscastle flood to decide upon the level of effect.

4 EFFECT OF LAND USE AND INTENSITY ON FLASH FLOOD CHARACTERISTICS: AN EXPERIMENTAL STUDY

4.1 INTRO

The main aim of this experimental work was to generate flash floods in a controlled laboratory environment for validation of numerical hydrodynamic models. As previously discussed, the dam break process consists of many different stages (i.e. water release from the reservoir, accelerated water flow on ramp and interaction of high Froude number flow with structures) each with different requirements and this gave the need for a new methodology which would incorporate the simulation of all the aforementioned stages. This chapter describes a series of experiments on high Froude number flows generated by a dam break on ramps of different resistance and on impact of these flows on buildings. This was achieved using a new experimental methodology which allows generating such flows in a controlled environment.

4.2 EXPERIMENTAL APPARATUS DESCRIPTION

4.2.1 Wave Flume

The experiments were conducted in a flume located in the Department of Mechanical Engineering in University College London (UCL). The horizontal flume is glass walled and is $20\ m$ long, $1.2\ m$ wide and was instrumented along its length. An elevated reservoir was built in the upstream part of the experimental apparatus separated by a gate and containing a controlled volume of water allowed to be released instantly upon the opening of the gate. The water was then discharged onto a $6\ m$ long ramp with $1/20$ gradient followed by a horizontal floodplain area, where buildings were installed, the urban settlement (Figure 4-1).

Figure 4-2 shows photos of the experimental setup looking up-slope from the urban settlement towards the gate (left) and down-slope from the gate to the urban settlement (right). The arrow in the photo indicates the direction of the flow. With a scale factor of λ=50, the reservoir was constructed with a length of $2.9\ m$, a width of $1.2\ m$ and a depth of 0.2 metres resulting in a maximum volume of water of $0.696\ m^3$ and the gate was designed such that a watertight seal was ensured on the elevated upstream reservoir. A $3\ cm$ difference in height between the reservoir and the ramp permitted the tight sealing of the reservoir and

allowed for a smooth removal of the gate minimising the total disturbance of the water. It will be later discussed in this chapter that the release was quick enough to be considered instantaneous and close to the theoretical approximations.

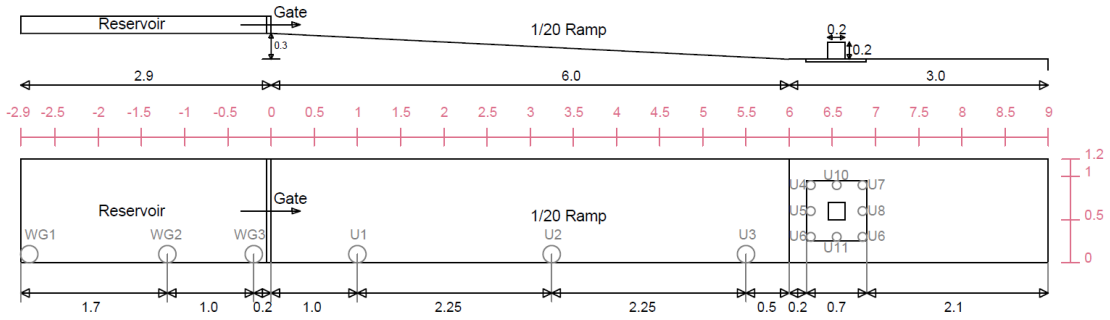

Figure 4-1- Side (top part of image) and plan (bottom part of image) view of experimental set up dimensions. The grey circles represent the sensor locations (wave gauges WG and ultrasonic sensors U). The coordinate system is represented in red.

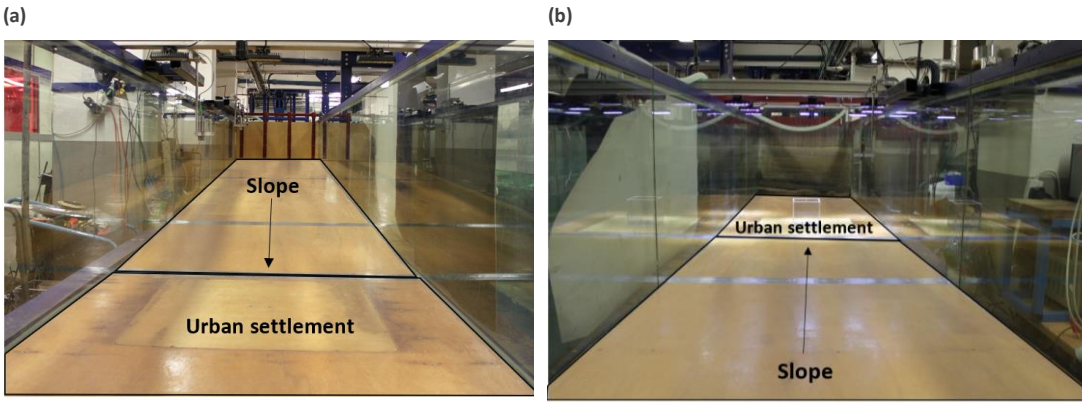

Figure 4-2- Photos of 6 meter-long 1/20 ramp and urban settlement looking (a) in the upstream direction from the urban settlement towards the gate and (b) in the downstream direction from the gate to the urban settlement. The arrow indicates the direction of the flow and that of the ramp's slope.

4.2.2 Roughness layer

Artificial grass was laid on the ramp for the roughness layer cases denoted by the letter "G". Different samples were investigated (Figure 4-3) but the Grass Direct Pemba artificial grass was selected. It has a $4\ mm$ thickness with a pile weight of $900\ gr/m^2$. Considering the scale factor $\lambda = 50$, this results in an actual geometrical thickness of $0.2\ m$ which is realistic for real grass.

Figure 4-3- Artificial grass samples for roughness layer and selected Pemba artificial grass with 4 mm thickness

4.2.3 Urban settlement

Once the gate was released, the water flowed down the ramp accelerating until it slowed down reaching the flat part and interacted with the urban settlement were the buildings are located. During each experiment, measurements were taken looking at different aspects of the flow and its interaction with buildings. The water level in the tank was monitored with three wave gauges (WG) and ultrasonic probes (U) were used to measure the water depth evolution along the ramp and around the buildings of the urban settlement. In the urban settlement, a two-camera system was installed obtaining a side and top view of the buildings. The experiment was designed to produce two dimensional results in the reservoir and on the ramp with the ultrasonic sensors mounted only on the one side of the flume. In the flat part of the experiment, the ultrasonic sensors were mounted around the buildings therefore providing three-dimensional capturing of the flow. See Figure 4-1 for an illustration of the sensor locations.

4.2.4 Gate

Over the years, different types of gates have been used in dam break experiments; the main two types being lift gates and swing gates (Goseberg et al., 2017). Stolle et al. researched the influence of swing gates on the dam break's hydrodynamic evolution. They concluded that as the opening of a swing gate is a process strongly influenced by hydrostatic pressure, a reduction in gate opening time was observed, no effect on the wave profile was noted (Stolle et al., 2018).

For the purpose of this experiment, a swing gate was designed (Figure 4-4), with a horizontal axis hinged on the top of the reservoir allowing it to rotate upwards using a weight system. This resulted in an accelerated flow at the bottom due to the pressure drop thus mimicking instantaneous release. A release mechanism was used to open the gate where weights connected to a lever arm were used to accelerate the opening (Figure 4-4).

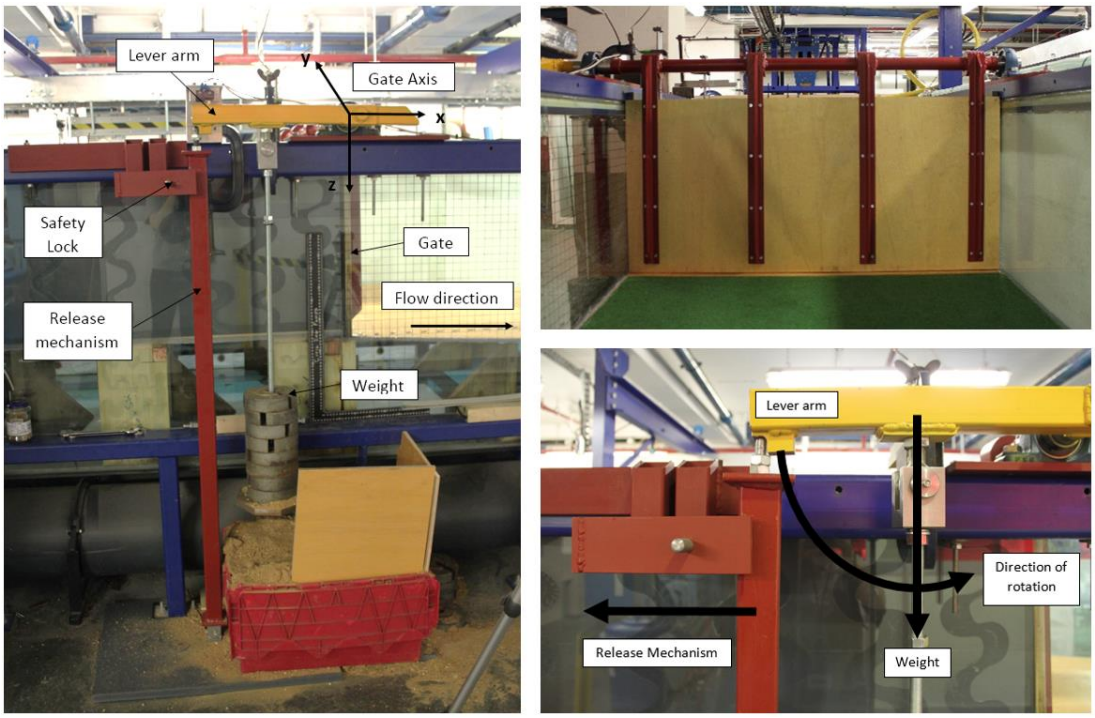

Figure 4-4- Side view from the RH side of flume glass wall showing the experimental gate design. The swing gate's horizontal axis was hinged on the top of the reservoir allowing it to rotate upwards using a weight system. A release mechanism was used to open the gate where weights connected to a lever arm were used to accelerate the opening. A safety lock was also installed for health and safety.

In order to assess whether the release of the gate could be considered instantaneous, two criteria were used for calculating the gate opening time t_{op1} and t_{op2}. Vischer and Hager's criterion specifies $t_{op1} \leq 1.25\sqrt{H_o/g}$ (Vischer and Hager, 1998), where H_o is the initial water depth in the reservoir. For $H_o = 0.2m$ and $H_o = 0.1m$ used in our experiments this gives $t_{op1\_0.2} = 0.178s$ and $t_{op1\_0.1} = 0.126s$ respectively. Secondly, Lauber and Hager's criterion was assessed $t_{op2} \leq \sqrt{2H_o/g}$ (Lauber and Hager, 1998) which gives $t_{op2\_0.2} = 0.202s$ and $t_{op2\_0.1} = 0.142s$.

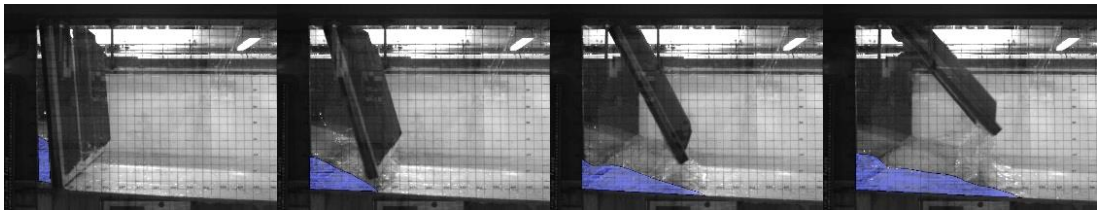

Figure 4-5- Gate opening for H=0.2 m. From left to right, t=0.08 s, t=0.172 s, t=0.22 s and t=0.28 s

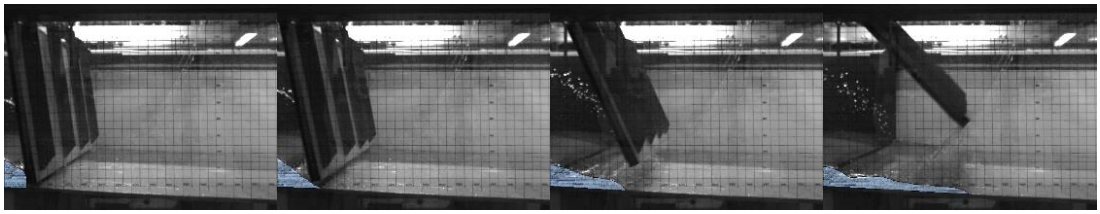

Figure 4-6- Gate opening for H=0.1 m. From left to right, t=0.1 s, t=0.124 s, t=0.2 s and t=0.28 s

The experimental gate opening times were calculated using high speed cameras (250 frames per second) and they were found to be $t_{op\_0.2} = 0.172s$ and $t_{op\_0.1} = 0.124s$ for the tested initial water depths $H_o = 0.2m$ and $H_o = 0.1m$ respectively thus satisfying both criteria. The gate opening time was defined as the time it takes from the start of the experiment to the gate opening without interfering with the flow. Figure 4-5 shows the gate opening for $H = 0.2\ m$ at $t = 0.08\ s$, $t = 0.172\ s$, $t = 0.22\ s$, $t = 0.28\ s$ and Figure 4-6 shows the gate opening for $H = 0.1\ m$ for $t = 0.1\ s$, $t = 0.124\ s$, $t = 0.2\ s$ and $t = 0.28\ s$. For a larger version of Figure 4-5 and Figure 4-6, see Appendix B.1.

4.3 MEASURING EQUIPMENT

In this section, the data acquisition process will first be described, the details of the free surface and flow visualisation measurements provided and finally the specifics of the instrumented buildings in the urban settlement shown.

4.3.1 Data acquisition

All instruments used were synchronised. The experiment and all measuring equipment were controlled by a 16-channel data acquisition board system connected to a PC. A trigger was installed on the gate that upon release the data collection on the data board was instantly triggered, thus allowing the synchronisation of all the instruments.

4.3.2 Free surface measurements

The water free surface was measured using wave probes in the reservoir and ultrasonic sensors along the ramp and around the urban settlement. Refer to Figure 4-1 for the location of the sensors and to Table 4-1 for their x-coordinates.

Table 4-1- Location and x-coordinates of all sensors (wave gauges and ultrasonic sensors) in meters where the gate is located at +0.00 m

Location	Sensor	x-coordinate [m]
Reservoir	WG1	-2.90
	WG2	-1.20
	WG3	-0.20
Gate	n/a	0.00
Ramp	U1	1.00
	U2	3.25
	U3	5.50
Urban Settlement	U4/U5/U6	6.20
	U10/U11	6.50
	U7/U8/U9	6.80

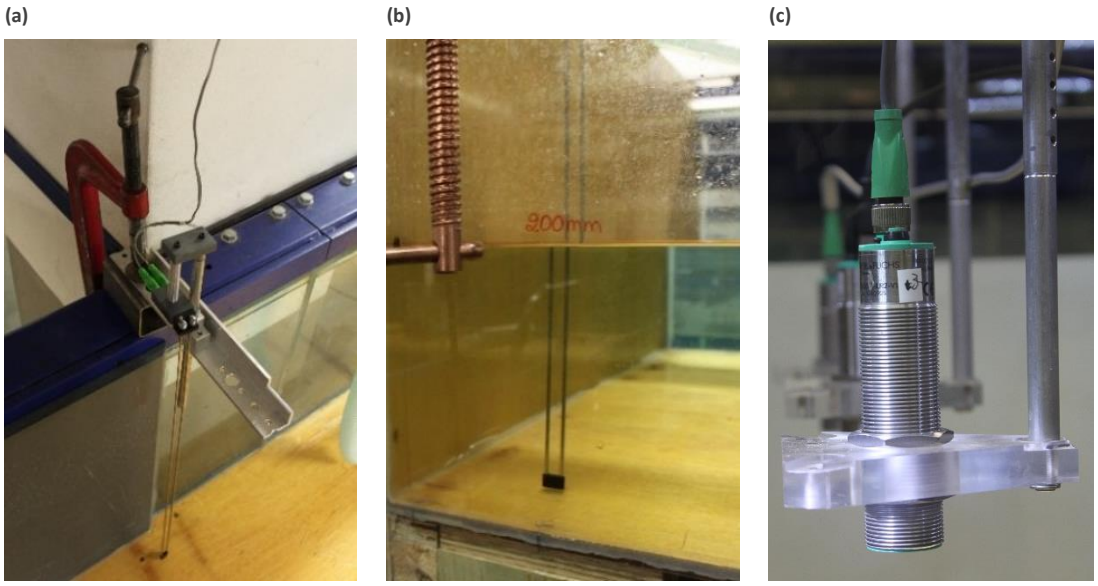

Figure 4-7- Free surface measurement equipment: (a) wave gauges in the reservoir, (b) wave gauges pair of 1.5 mm diameter stainless steel wires spaced 12.55 mm apart and (c) ultrasonic sensors suspended from the top of the flume in different locations (U1-U11)

4.3.2.1 Wave probes

Three resistance type wave gauges were installed along the reservoir's length to measure the change in water depth at locations WG1-WG3 (Figure 4-7 (a) and (b)). Each probe consisted of a pair of $1.5\ mm$ diameter stainless steel wires spaced $12.55\ mm$ apart. Wave gauges work by measuring the current that flows between the immersed steel wires and then converting it to an output voltage that is directly proportional to the water depth. The

length of the instrument cables was reduced to be as small as possible in order to reduce potential for noise from external sources. The wave gauges were connected to a Churchill Controls Wave Monitor Module, Ltd (2001) and then to the data logger.

4.3.2.2 Ultrasonic sensors

To measure water depths along the channel and around the urban settlement, three ultrasonic-sensors (Figure 4-7 (c)) were employed in 11 different locations (U1-U11). Ultrasonic sensors transmit a short ultrasonic wave to the bed of the experimental setup and measure the time it takes for the pulse to travel to the water surface and reflect back to the sensor. This distance is then subtracted from the height of the sensor above the bed, resulting in the final water depth (Gillespie, 2017). The sensors used in this experiment, were calibrated before the start of the experiments and had a sensing range from $50\ mm$ to $550\ mm$ and a transducer frequency of 1 kHz. To obtain measurements in the 11 selected locations, each set of experiments was repeated for times with the sensors in different locations for each repeat: (i) U1, U2 and U3, (ii) U4, U5 and U6, (iii) U7, U8 and U9 and finally (iv) U10 and U11 (Figure 4-14).

4.3.3 Flow visualisation

4.3.3.1 Lighting

In order to ensure sufficient lighting for the cameras in high shutter speeds, spotlights were installed around the urban settlement. Different lighting combinations were attempted in combination with a white background to ensure the optimal clarity in the photos and videos.

4.3.3.2 Digital still cameras

Two identical high-speed Mako G-030 PoE monochrome cameras were used, with a capture rate of 250 frames per second positioned outside the flume, parallel and perpendicular to the flow (mounted on a rail). For the synchronisation of the cameras with the rest of the instruments, a set of lights was used which was lit by the signal from the trigger starting data collection. A separate PC was used to control the cameras and 250fps was found to be enough to record the changes in water depth. Movavi Video Converter software was used to view the videos and convert them to the required format and the necessary frames for the analysis were extracted using Matlab and post-processing enhancements to the picture were undertaken afterwards.

4.3.3.3 Digital video camera

A Sanyo 1920x1080 Xacti MPEG-4 AVC/H.264 full HD digital video camera was used to record video footage of the cross-waves at the back of the buildings in the urban settlement. The camera allowed footage at a 1920 x 1080 resolution at 60 fps and was manually controlled and not connected to the rest of the measuring equipment.

4.3.4 Instrumented buildings

In the urban settlement, four Perspex (clear acrylic) boxes representing buildings were instrumented in three different ways: two of them contained load cells (Figure 4-8 (a)) one contained pressure sensors (Figure 4-8 (b)) and the final one a GoPro camera (Figure 4-8 (c)). Their positions was interchangeable in different combinations of a single building, two or four buildings.

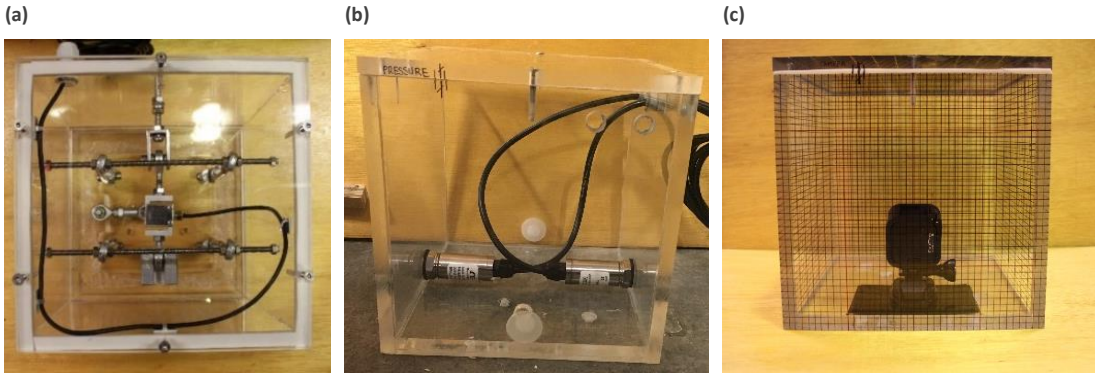

Figure 4-8- Four Perspex (clear acrylic) boxes representing buildings were instrumented in three different ways: two of them contained (a) load cells, (b) one contained pressure sensors, and (c) a GoPro camera

The load cell buildings which were the main buildings used in this thesis, were made of two parts: a base fixed to the bed of the flume and a moving box-top. These two parts were attached by a load cell which read axial force. Stainless steel links and rod ends were fixed from the box to the base to restrict movement and rotation in all directions except for axial displacement. To minimise accidental water ingress, once in place, the gaps between the moving joints were filled with silicone grease and the load cell was positioned above water level in the building to ensure it would not be damaged by accidental water entry. Two F232-Z4615 NOVATECH load cells were used to measure the load along the x-axis as a function of time.

4.4 INSTRUMENT CALIBRATIONS

4.4.1 Wave probes

The three wave gauge probes were statically pre-calibrated at the beginning of the tests in the two water depths used in the experiment $0.2\ m$ and $0.1\ m$. Figure 4-9 and Figure 4-10 show the calibration curves for initial water depths of $0.2\ m$ and $0.1\ m$ respectively.

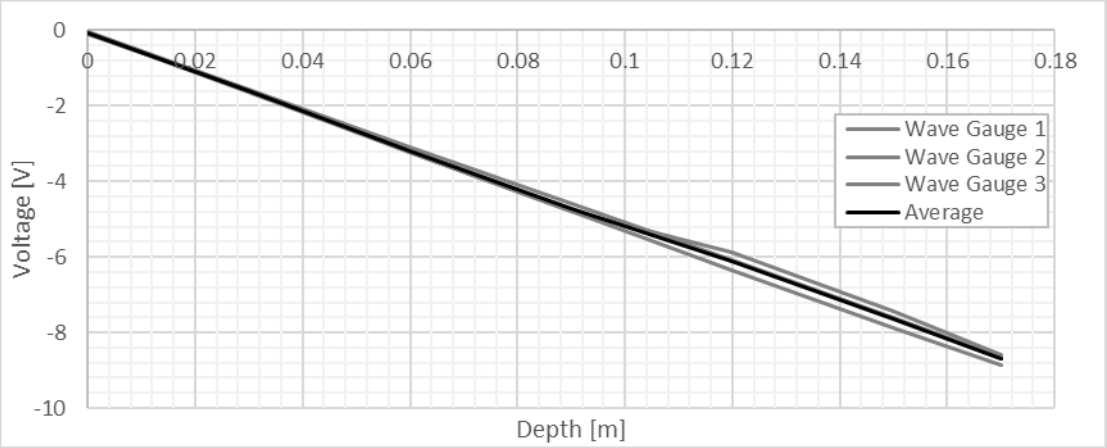

Figure 4-9- Wave gauge calibration curve for the three different wave gauges which were calibrated in-situ in the reservoir for an initial water depth of 0.2 m

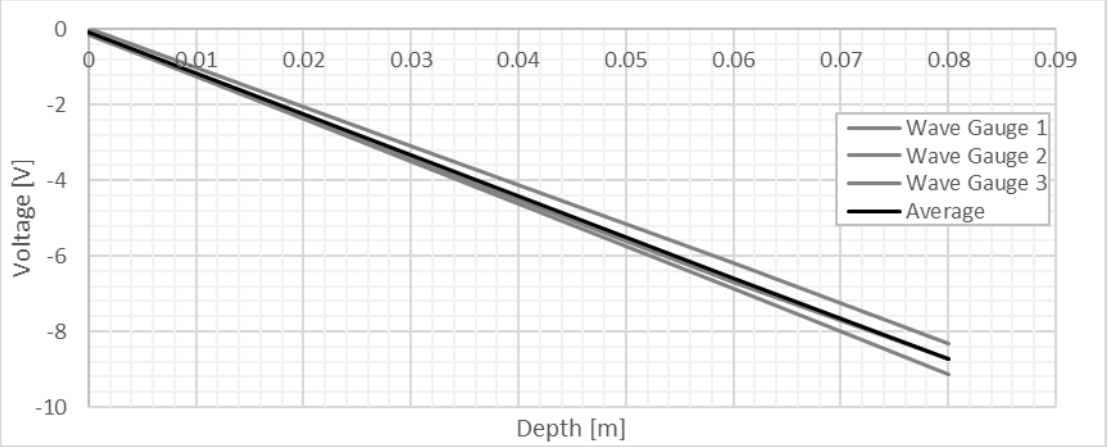

Figure 4-10- Wave gauge calibration curve for the three different wave gauges which were calibrated in-situ in the reservoir for an initial water depth of 0.1 m

4.4.2 Load cells

The two load cells were pre-calibrated by the manufacturers but were also calibrated in-situ at the urban settlement. For their in-situ calibration, a pulley system was created (Figure 4-11 (a) and (b)) and the load cells were calibrated both for tension and compression before and after every experiment to ensure the accuracy of the measurements. The calibration curves for the two load cell buildings are presented in Figure 4-12 and Figure 4-13.

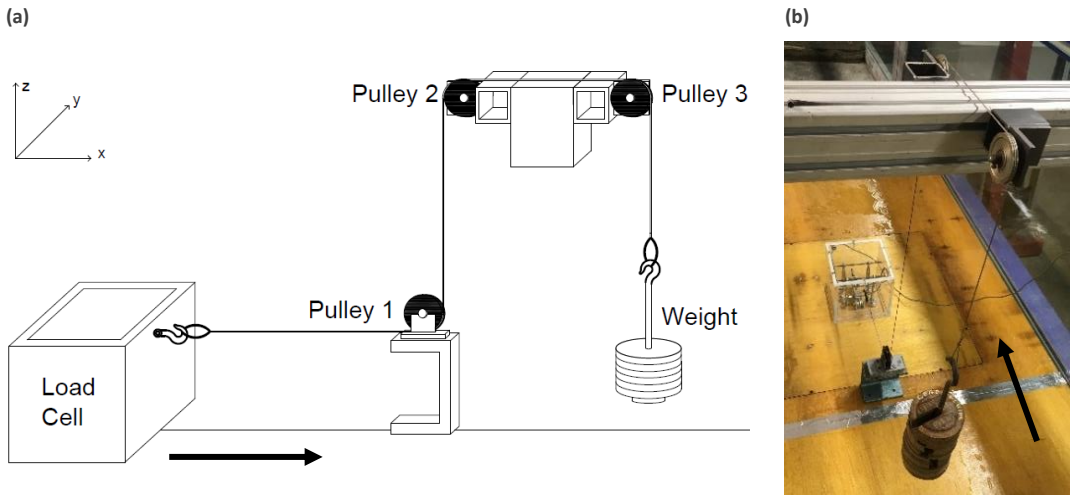

Figure 4-11- Load cell calibration in-situ: (a) schematic of load cell calibration in compression and (b) photo from the experiment where load cell is being calibrated in tension. The arrow indicates the direction of the flow.

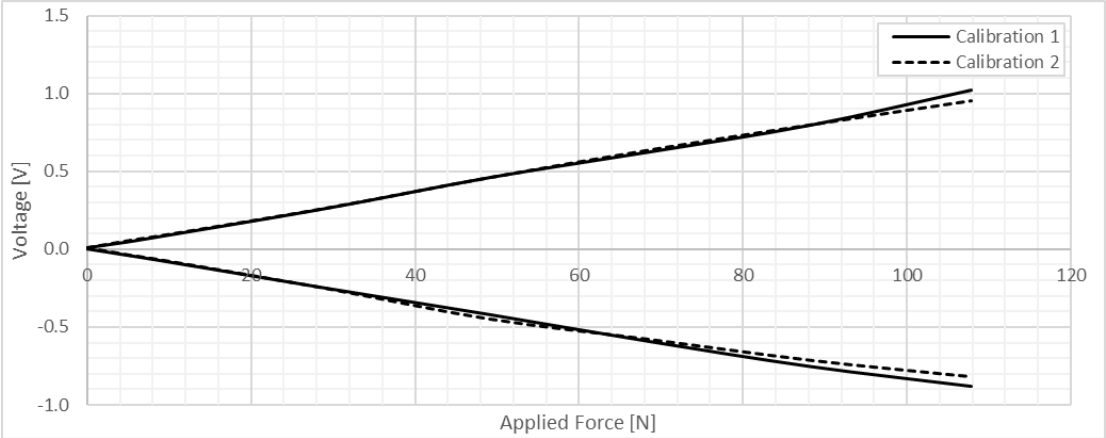

Figure 4-12- Load cell 1 calibration data from two different calibrations in-situ in the urban settlement

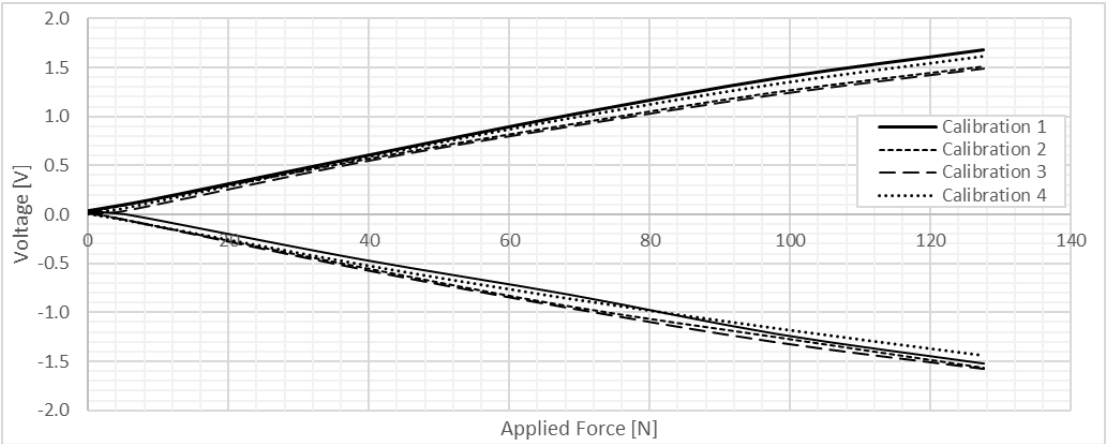

Figure 4-13- Load cell 2 calibration data from four different calibrations in-situ in the urban settlement

4.5 TEST CASES

As part of this research, 18 test cases were examined considering: different initial water levels in the reservoir, different roughness layers on the ramp (vegetated and un-vegetated ramp), different densities of the urban texture (none, one, two and four buildings) and different angles of the buildings (90°, 45° from the direction of the flow). For the scope of this research eight main cases will be presented (shown in Table 4-2) and four additional for comparative reasons when discussing blockage in the urban settlement (presented in Table 4-3).

Table 4-2- 8 main experimental test cases considered

Set	Initial depth [m]	Roughness layer	Building(s)	Angle [°]	Name
Set 01	0.2	No	None	90	B0_H200
	0.2	No	Single	90	B1_H200
Set 02	0.1	No	None	90	B0_H100
	0.1	No	Single	90	B1_H100
Set 03	0.2	Yes	None	90	B0_H200G
	0.2	Yes	Single	90	B1_H200G
Set 04	0.1	Yes	None	90	B0_H100G
	0.1	Yes	Single	90	B1_H100G

Table 4-3- Additional experimental test cases considering multiple buildings

Set	Initial depth [m]	Roughness layer	Building(s)	Angle [°]	Name
Set 01	0.2	No	Two	90	B2_H200
	0.2	No	Four	90	B4_H200
Set 02	0.1	No	Two	90	B2_H100
	0.1	No	Four	90	B4_H100

The setup for the single, two and four buildings and the position of the ultrasonic sensors is shown in plan view in Figure 4-14 below.

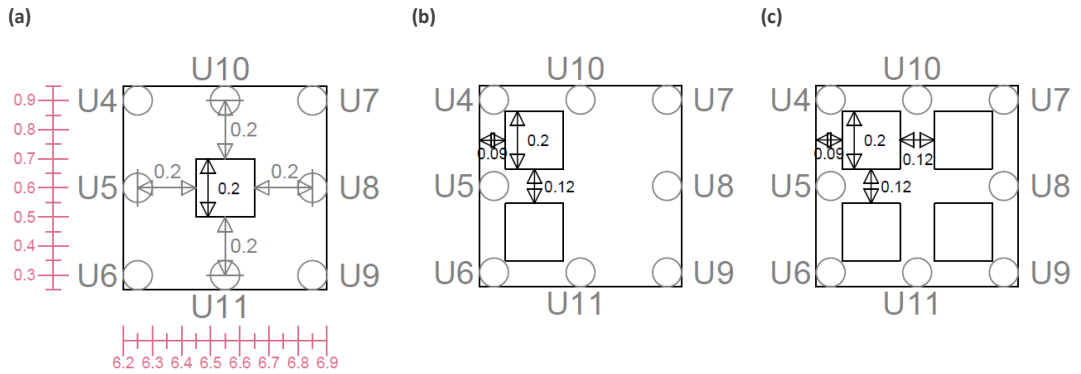

Figure 4-14- Plan view of building arrangement in urban settlement for (a) single building, (b) two buildings and (c) four buildings. The black squares represent the buildings, the grey circles the ultrasonic sensor locations U4-U12 and the coordinate system is shown in red.

To ensure the repeatability of the experiment, each test was repeated three times. Furthermore, data was collected multiple times at each measuring location establishing even further confidence in the repeatability. For example, the water depth evolution in the reservoir was measured with the wave gauges for all H200 and H100 experiments and similarly the water depth evolution along the ramp was also systematically measured at locations U1, U2 and U3 during many of the experiments. The confidence ranges from different repetitions of the wave gauge measurements will be shown and discussed in the results and analysis section.

Initially a series of tests was conducted without any buildings in the urban settlement in order to validate the proposed technique. Water depths were measured in the reservoir, along the ramp and in the urban settlement and videos were taken through the flume's glass side. Below the baseline test for the B0_H100 case will be presented followed by a case with a single building in the urban settlement B1_H100 for comparison.

4.5.1 Baseline test, B0_H100 case

The case B0_H100 has an initial water depth in the reservoir of $0.1\ m$ ($0.348\ m^3$ of water volume), no roughness layer and no building in the urban settlement. Figure 4-15 presents a schematic representation of the case and measurement points. In the urban settlement, U5, U8 and U10 were selected as the key measurement points due to their location in the urban settlement at equal distances at $x = 6.20\ m$, $6.50\ m$ and $6.80\ m$ respectively.

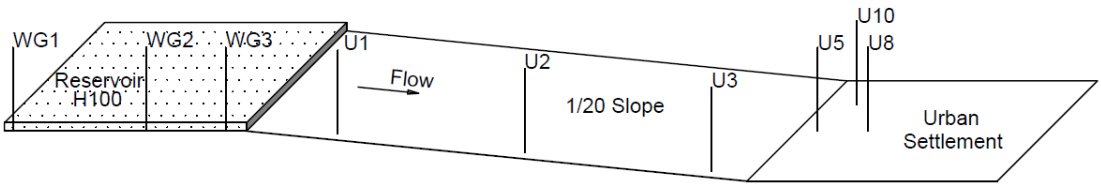

Figure 4-15- Schematic representation of B0_H100 case showing the location of some key instruments

Once the gate was released, a dam break wave starts propagating downstream along the ramp and a negative wave starts moving upstream within the reservoir. The first instruments to record a change were the wave gauges (WG1-WG3) in the reservoir which recorded the change in water depth during the emptying of the reservoir.

Figure 4-16 shows the water depth changes over time first for the three wave gauges WG1-WG3 and then for the three ultrasonic probes U1-U3 (at $x = 1.0\ m$, $3.25\ m$ and $5.50\ m$ respectively) along the ramp (bottom). WG3 being the closest to the gate ($-0.2\ m$) is the first instrument to record a sudden change in water depth which reduces from $0.1\ m$ to $0.06\ m$ in $1.2\ s$ and decreases to $0.055\ m$ where it reaches a plateau. The negative wave reaches WG2 after just under $1\ s$, which decreases to $0.055\ m$ less suddenly. WG1 has the most delayed response when the negative wave reaches it $2.5\ s$ later and also decreases to $0.055\ m$. When all wave gauges reach the same water depth, they start decreasing presenting an exponential decay.

Temporal variation of water depths at points is visible from the ultrasonic probes U1-U3 where the arrival of the dam break wave at different distances is recorded by the probes (Figure 4-18). The flow on the ramp is supercritical and characterised by two components, the propagation of the dam break wave and the existence of a uniform flow (flow properties at a particular point in space do not vary with time) between U2 and U3 from $t = 4 - 7\ s$. The increase in velocity is apparent from the arrival of the dam break wave to the ultrasonic sensors as it travels a distance of $2.25\ m$ from U1 ($x = 1.0\ m$) to U2 ($x = 3.25\ m$) in $1.6\ s$ ($1.4\ m/s$) and the same distance from U2 to U3 ($x = 5.5\ m$) in $1.35\ s$ ($1.6\ m/s$). After $t = 8\ s$, the data presents an exponential decay which is evident for all 3 sensors with a very small difference in water depth between them. It is important to note the first peak noticeable in U1 ($x = 1.0\ m$) at $t = 0.6\ s$ can be attributed to splashing from the gate opening. The opening is not completely instantaneous and the flow, due to the friction and

the small sealing step, takes some time to organise after the gate opening, thus creating the different shape in water depth evolution between U1 and U2, U3.

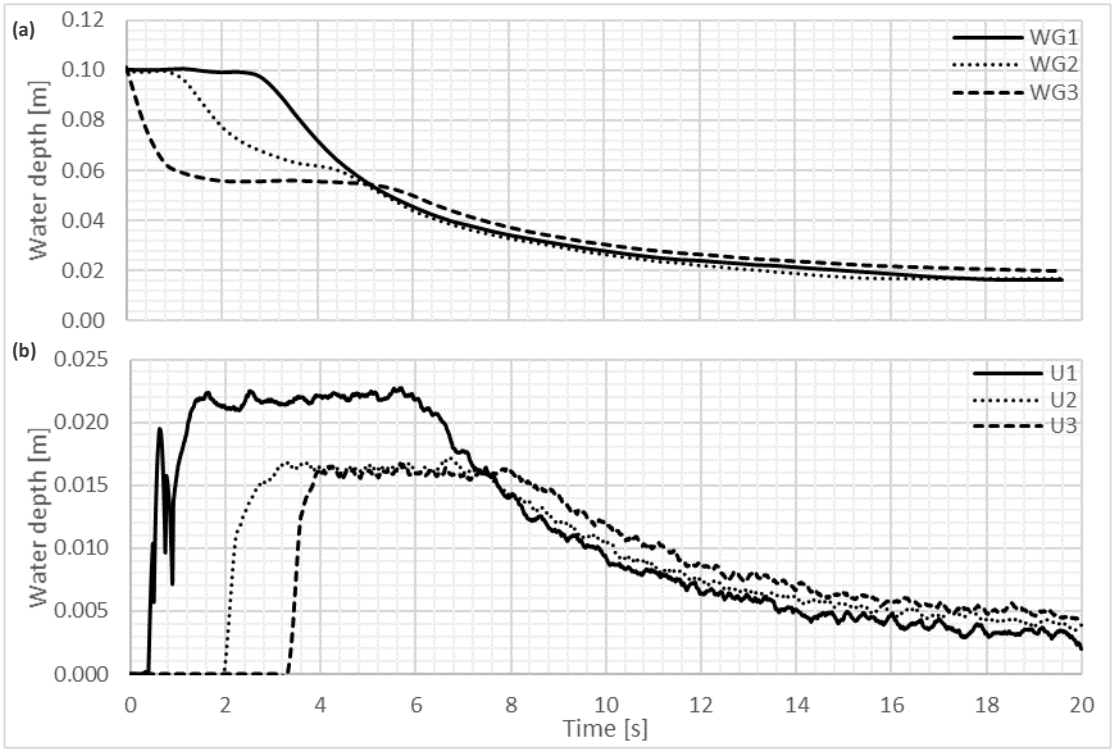

Figure 4-16- Water depth evolution (a) in the reservoir at locations WG1, WG2 and WG3 and (b) along the ramp at locations U1, U2 and U3 for H100

Figure 4-17 shows the evolution of the water depths in the urban settlement comparing three different locations U5, U8 and U10 (at $x = 6.20\ m$, $6.50\ m$ and $6.80\ m$ respectively). When the water reaches the flat part of the urban settlement it slows down, taking $0.2\ s$ to travel $0.3\ m$ from U5 to U10 ($1.5\ m/s$) and $0.3\ s$ to travel the same distance from U10 to U8 ($1\ m/s$) compared to a $1.6\ m/s$ velocity on the ramp (up to $x = 5.50\ m$). As the flow is quasi-steady in this case, the higher water depths in the horizontal section are therefore attributed to the loss of specific energy by the supercritical flow.

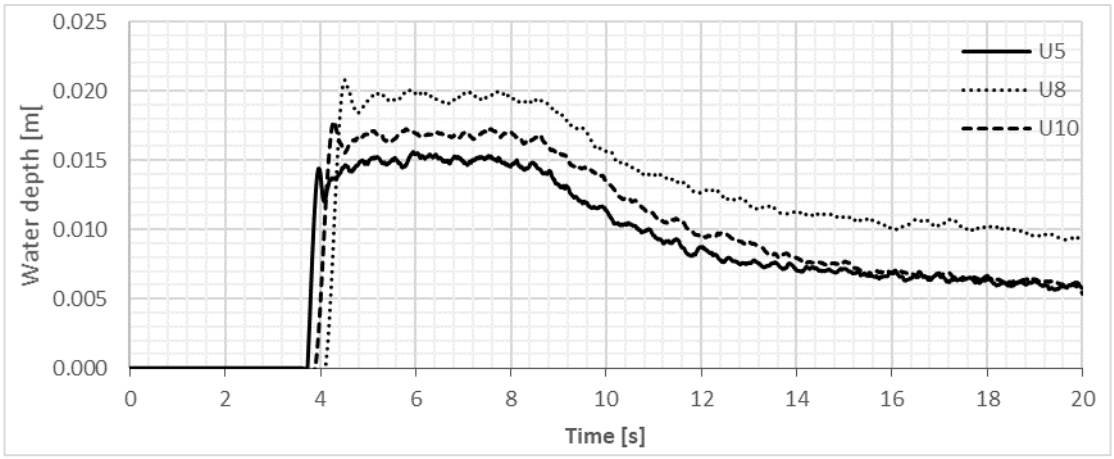

Figure 4-17- Water depth evolution in the urban settlement for H100 with no building

4.5.2 Base line test with a single building, B1_H100

The case B1_H100 has an initial water depth in the reservoir of $0.1\ m$, no roughness layer and a single building in the urban settlement. Figure 4-18 presents a schematic representation of the case, showing the location of the selected measurement points which are the same as for the previous case: U5 is the sensor located $0.2\ m$ in front of the building ($x = 6.20\ m$); U8 $0.2\ m$ behind the building ($x = 6.80\ m$) and U10 $0.2\ m$ to the side of the building ($x = 6.5\ m$).

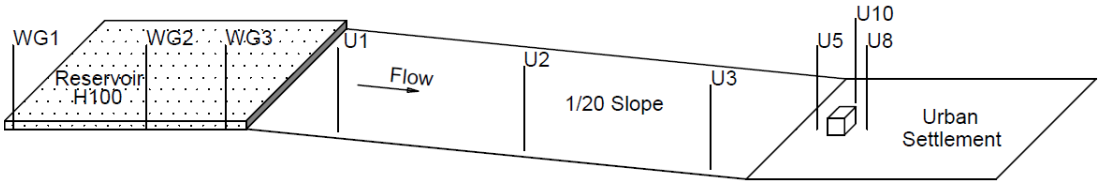

Figure 4-18- Schematic representation of B1_H100 case showing the location of some key measuring equipment

The evolution of water depth over time in the reservoir and the propagation down the ramp is identical to the previous case (B0_H100) as no change was made in the water depth nor the roughness on the ramp. Thus, the results will not be presented again here, but refer to Figure 4-16 for more information.

Figure 4-19 compares the water depth evolution for B0_H100 (no building) and B1_H100 (single building), thus comparing the changes in water depth in the urban settlement due to the blockage created by the single building. The highest water depth is in front of the building

as would be expected due to the blockage and the creation of the hydraulic jump. U8 ($x = 6.80\ m$ behind the building) is less affected by the blockage, resulting in similar water depths to those observed for the B0_H100 case. U10 ($x = 6.50\ m$ side of building) shows an increase that is attributed to the hydraulic jump created from the blockage thus increasing the water depth in the B1_H100 case. Looking at the photos in Figure 4-20, photos A_1,B_1 represent the first small peak shown on the graph at the front of the building (U5) ($t = 4.18\ s$) and the photos A_2,B_2 correspond to the maximum water depth where 2/5 of the building's height is submerged ($t = 5.16\ s$). At the same time due to the blockage it can be observed that there is not a lot of water on the back of the building (U8) while the reflected wave on the side (U10) can be seen clearly. Furthermore, in the side view photos of Figure 4-20 it is also interesting to observe the creation of a strong hydraulic jump after the first impact which leads to an increased water depth between 6 and $10\ s$ during which the highest applied load is also seen on the building. Figure 4-21, shows the comparison between B0_H100 (A_1-A_3) and B1_H100 (B_1-B_3) case for $t = 4\ s$, $t = 4.7\ s$ and $t = 12\ s$. Here, it is worth noticing that the first peak at $t = 4\ s$ at U5 (Fig 4.21a) corresponds to both cases and has an identical result. The second and major peak visible in the B1_H100 case ($t = 6\ s$) is caused by the reflection from the building itself and the creation of the hydraulic jump as discussed previously.

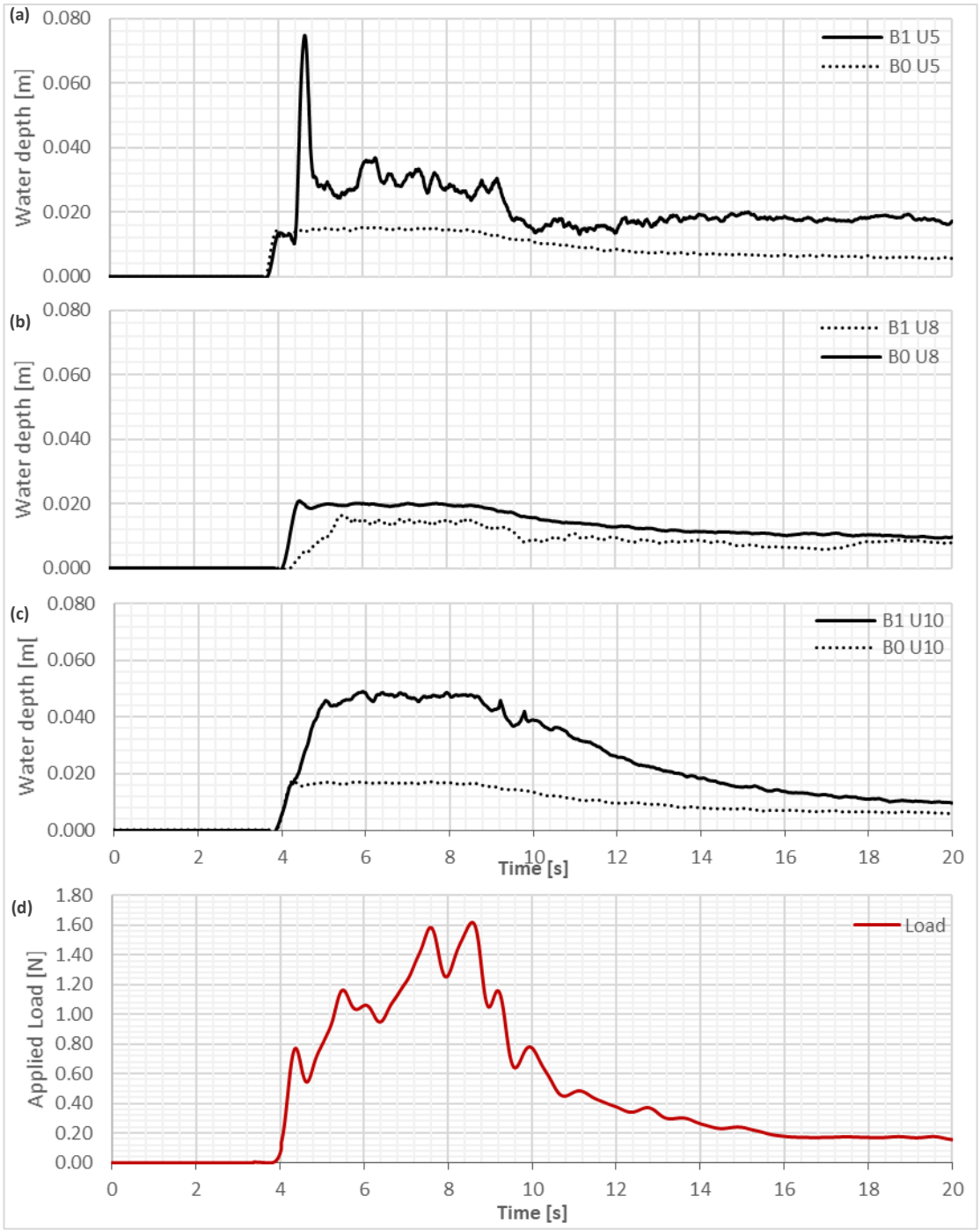

Figure 4-19- Water depth evolution around the building for B0_H100 and B1_H100 and load acting on the structure for B1_H100. The water depth evolution over time for B0_H100 and B1_H100 is shown at locations (a) U5, (b) U8, (c) U10. Fig. 4.21d shows the applied load [N] acting on the front side of the building

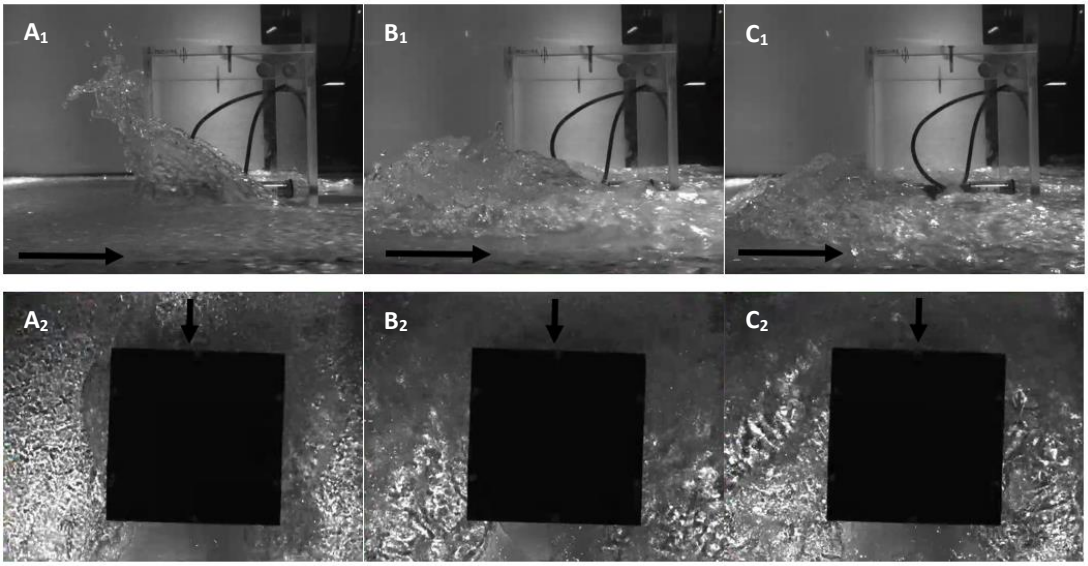

Figure 4-20- Photos of water impact on building for B1_H100 case at times t=4.18 s (A_1, A_2), t=5.16 s (B_1, B_2) and t=10 s (C_1, C_2) from side view (top photos) and top view (bottom photos)

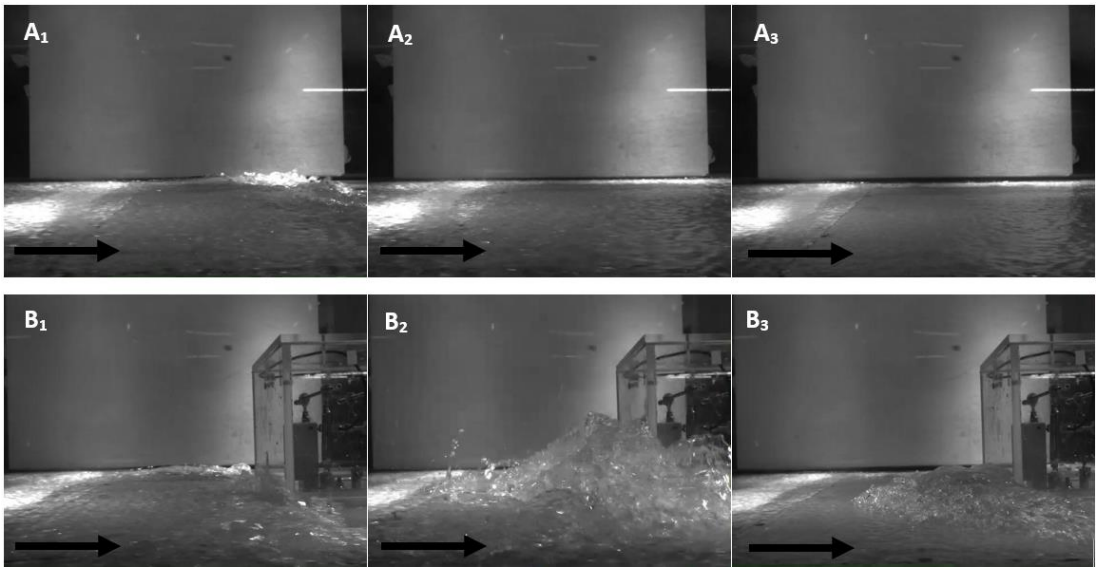

Figure 4-21- Comparison of B0_H100 (Greenshields) and B1_H100 (bottom photos) for t=4 s (A_1, B_1), t=4.7 s (A_2, B_2) and t=12 s (A_3, B_3)

4.6 Results and analysis

The next section is presented in three parts: the evolution of water depth within the reservoir, on the ramp and around the urban settlement. First, the repeatability of the reservoir measurements will be discussed and the emptying of the reservoir will be compared to the ideal dam break theory with the dam break wave propagating downstream and the negative wave moving upstream within the reservoir. Secondly, the flow on the ramp

and the characteristics of the supercritical flow will be described and discussed. The Froude number for different parts of the flow will be calculated and Manning's coefficient determined for each of smooth and roughness layers. Next, the impact on the downstream urban settlement will be described in three distinctive stages (more detail in section 4.6.3) and finally the applied load on the building will be investigated for different scenarios.

4.6.1 Evolution of water depth within the reservoir

The evolution of the water depth over time in the reservoir was only affected by the initial water depth in the reservoir, $0.1\ m$ for H100 and $0.2\ m$ for H200. Figure 4-22 shows the water depth results for H200 over time.

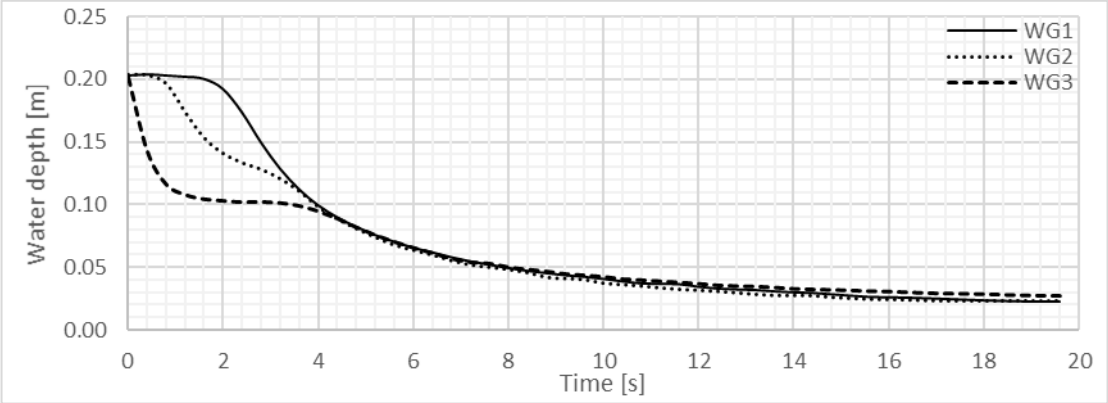

Figure 4-22- Timeseries of water depth evolution in reservoir for H200 at wave gauge locations WG1 (x=0 m), WG2 (x=1.7 m) and WG3 (x=2.7 m)

As previously discussed, repeatability of the experimental results was a basic requirement for this research. Figure 4-23 shows the water depth during the reservoir emptying for the two basic cases (H100 and H200) and the lines in red represent the confidence ranges for the wave gauges input from 20 different repetitions. It was found that the difference between the maximum and minimum measurements ranged between 2 and 10 mm depending on the individual case. The root mean square error (RMSE) was calculated from Equation 4-1 where μ is the average value for the reservoir water depths, n is the number of observations and x is the maximum or minimum value of all reservoir water depths (Meyer, 2012).

$$RMSE = \sqrt{\frac{1}{n}\sum_{i=1}^{n}(x_i - \mu)^2}$$

Equation 4-1

Table 4-4- RMSE root mean square error calculated for the upper and lower limits of the wave gauge measurements.

Location		RMSE	
		Upper	Lower
H200	WG1	0.00073	0.00079
	WG2	0.00085	0.00095
	WG3	0.00094	0.00084
H100	WG1	0.00053	0.00060
	WG2	0.00054	0.00055
	WG3	0.00052	0.00062

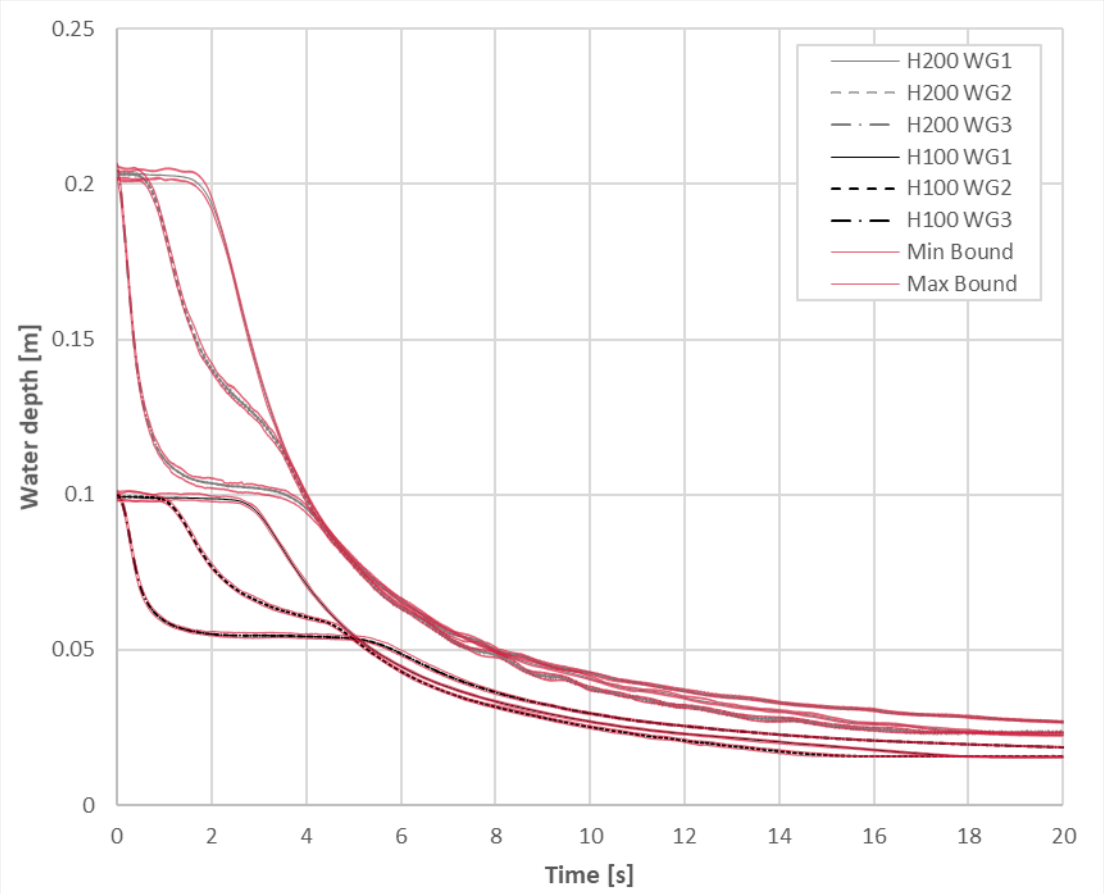

Figure 4-23- Timeseries of mean water depth for 20 repetitions at three wave gauges. Red lines demonstrate the confidence ranges which vary from 2 and 10 mm depending on the individual case. The maximum error is observed in WG1 that is affected by the propagation of the negative wave within the reservoir

Comparison of experimental results with dam break theory

In this section we compare results of our experiments with the theoretical analysis of the ideal dam break presented in Chapter 2.

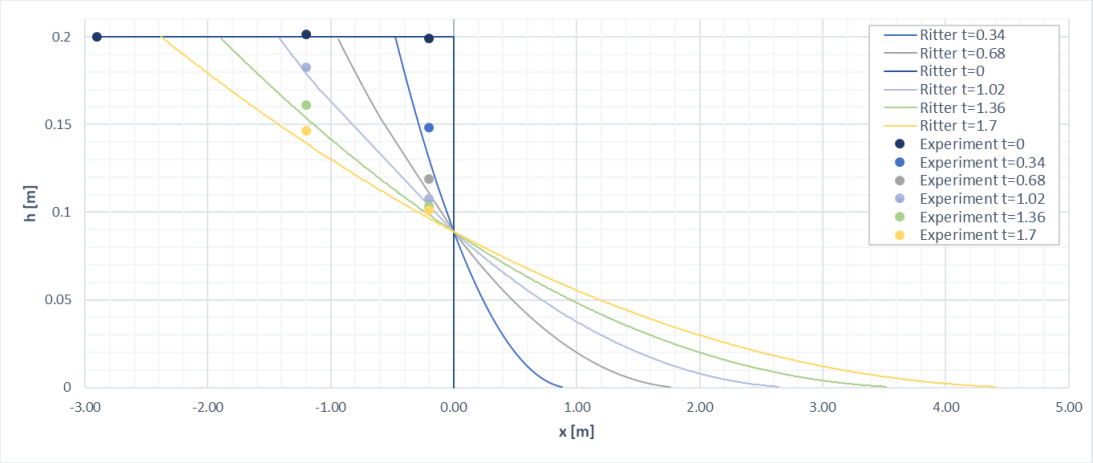

Figure 4-24- Comparison of experimental and Ritter's analytical water surface evolution for t=0 s, t=0.34 s, t=0.68 s, t=1.02 s, t=1.36 s and t=1.7 s for the H200 case. The experimental points were plotted from the experimental water depths at locations WG1 (x=0 m), WG2 (x=1.7 m) and WG3 (x=2.7 m)

Figure 4-23, shows the decrease in water depth in the reservoir over time at the three wave gauges for H100 and H200. The point where all three wave gauge measurements merge for each of the cases is considered to be the experimental critical depth.

$$h = \frac{1}{9g}\left[2(gh_o)^{1/2} - \frac{x}{t}\right]^2$$ *Equation 4-2*

Figure 4-24 shows the comparison of experimental and Ritter's analytical water surface evolution for $t = 0\ s$, $t = 0.34\ s$, $t = 0.68\ s$, $t = 1.02\ s$, $t = 1.36\ s$ and $t = 1.7\ s$. The x-axis represents the length in the x-direction where 0 is the origin (gate) and the y-axis represents the water depth. The experimental results were plotted at locations WG1 ($x = 0\ m$), WG2 ($x = 1.7\ m$) and WG3 ($x = 2.7\ m$) for the selected timesteps. The water depths calculated using Ritter's analytical equations were calculated at the same locations using Equation 4-2 where h_o is the initial water depth in the reservoir. When the critical depth is reached, the flow conditions at the origin (gate $x = 0$) are critical and Froude Number Fr=1. Using Ritter's equations (Equation 2-4 and Equation 2-5) the critical depth and critical

velocity were calculated and compared with the experimental results showing a reasonable agreement with the theory for the H200 cases (Table 4-5).

Table 4-5- Critical depth and critical velocities at the origin (gate)

		Theory	Measured	Relative Error
$H200, h_o = 0.2m$	$h_{(x=0)}$	$4/9\, h_o = 0.088\, m$	$0.084\, m$	4.5 %
	$V_{(x=0)}$	$2/3\sqrt{g h_o} = 0.934\, m/s$	$0.907\, m/s$	2.9 %
$H100, h_o = 0.1m$	$h_{(x=0)}$	$4/9\, h_o = 0.044\, m/s$	$0.054\, m$	22.7 %
	$V_{(x=0)}$	$2/3\sqrt{g h_o} = 0.660\, m$	$0.727\, m/s$	10.2 %

4.6.2 Evolution of water depth along the ramp

The evolution of the water depth over time in the reservoir was affected firstly by the initial water depth in the reservoir $0.1\, m$ for H100 and $0.2\, m$ for H200 and secondly by the roughness layer in the cases H100G and H200G. Figure 4-25 shows the water depth evolution along the ramp for H200 without a roughness layer.

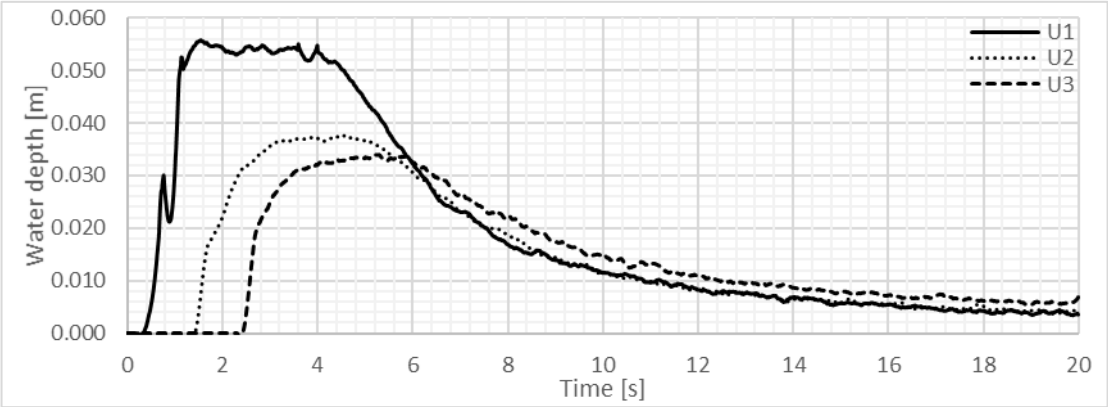

Figure 4-25- Timeseries of the water depth evolution along the ramp at U1 (x=1 m), U2 (x=3.25 m) and U3 (x=5.5 m) for H200 without a roughness layer

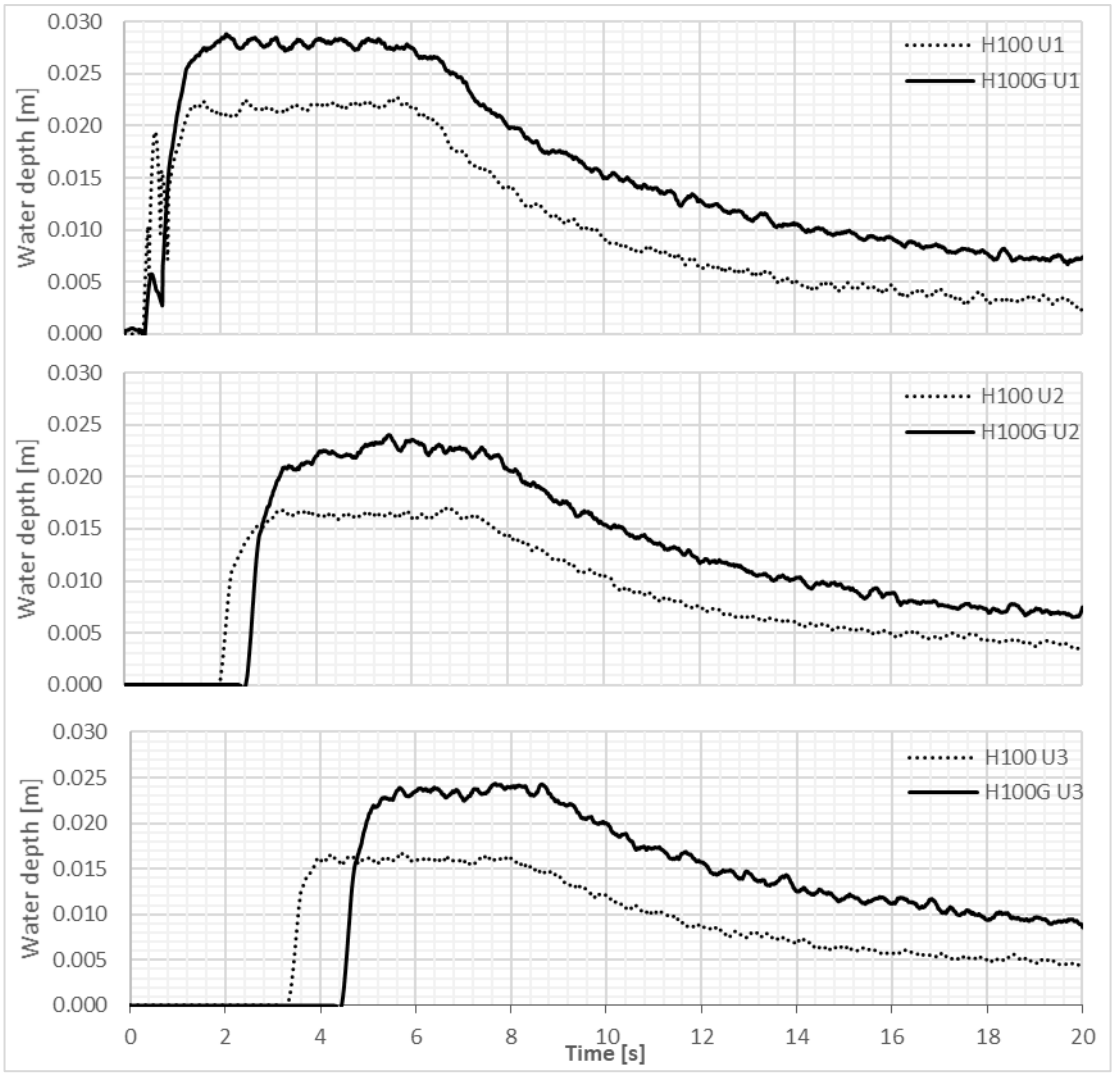

Figure 4-26- Timeseries of the water depth evolution along the ramp at (top) U1 (x=1 m), (middle) U2 (x=3.25 m) and (bottom) U3 (x=5.5 m) and comparison for H100 and H100G (with roughness layer)

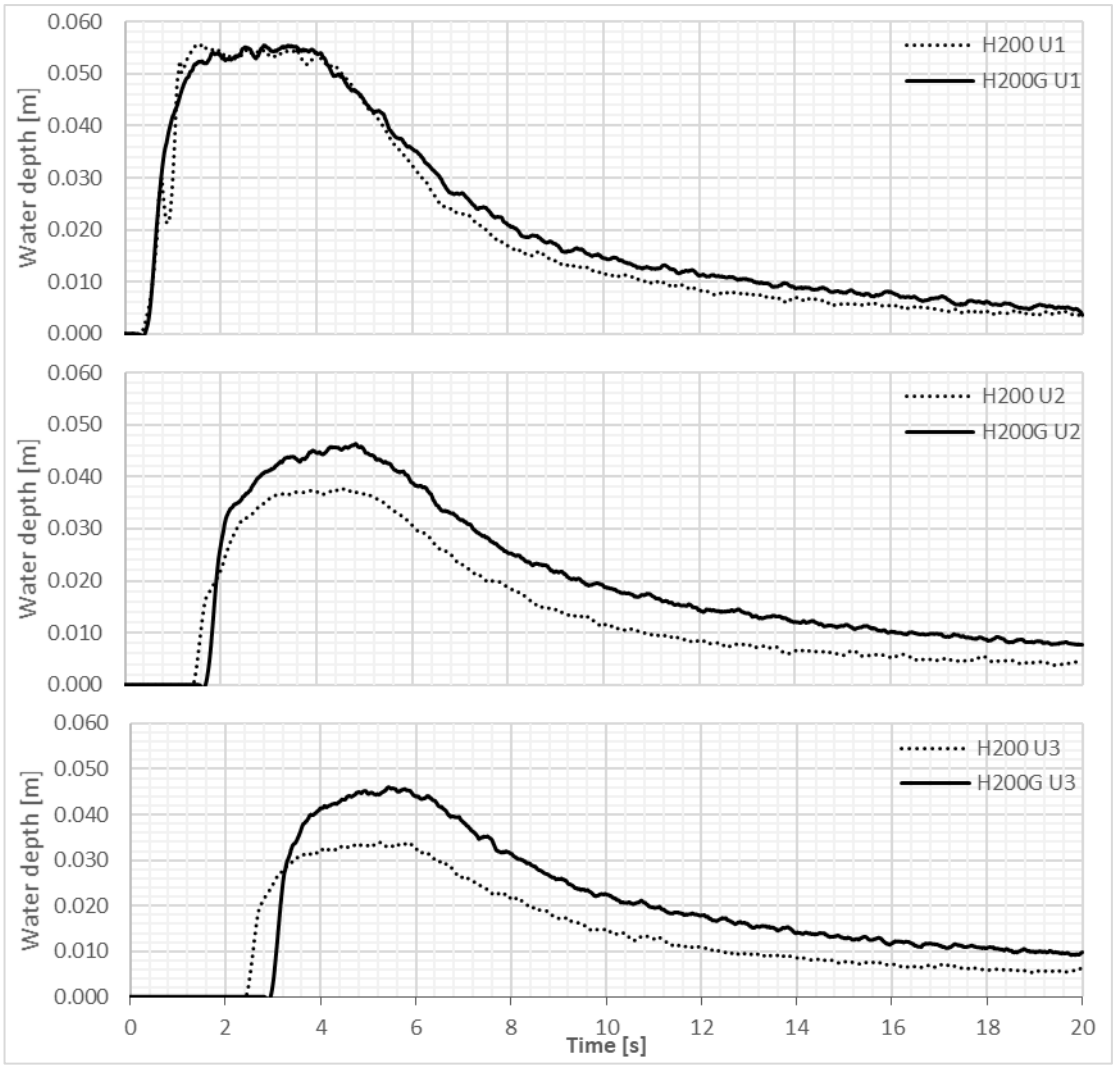

Figure 4-27- Timeseries of the water depth evolution along the ramp at (top) U1 (x=1 m), (middle) U2 (x=3.25 m) and (bottom) U3 (x=5.5 m) and comparison for H200 and H200G (with roughness layer)

Figure 4-26 and Figure 4-27 show the water depth evolution at each ultrasonic sensor with and without roughness for H100 and H200 respectively. What is evident from the comparisons between the cases with and without the roughness layer on the ramp is the lower velocity for the cases with higher roughness. In both Figure 4-26 and Figure 4-27, the water reaches the first sensor (U1 $x = 1.0\ m$) simultaneously regardless of the roughness layer. But as the water propagates down the ramp, the velocity decrease is more visible. When comparing the time it takes the dam break wave to reach U3 ($x = 5.50\ m$), it is 1.37 and 1.2 times slower with the roughness layer than without for H100 and H200, respectively, showing that the change in roughness has a more important effect with lower water depths and lower velocities.

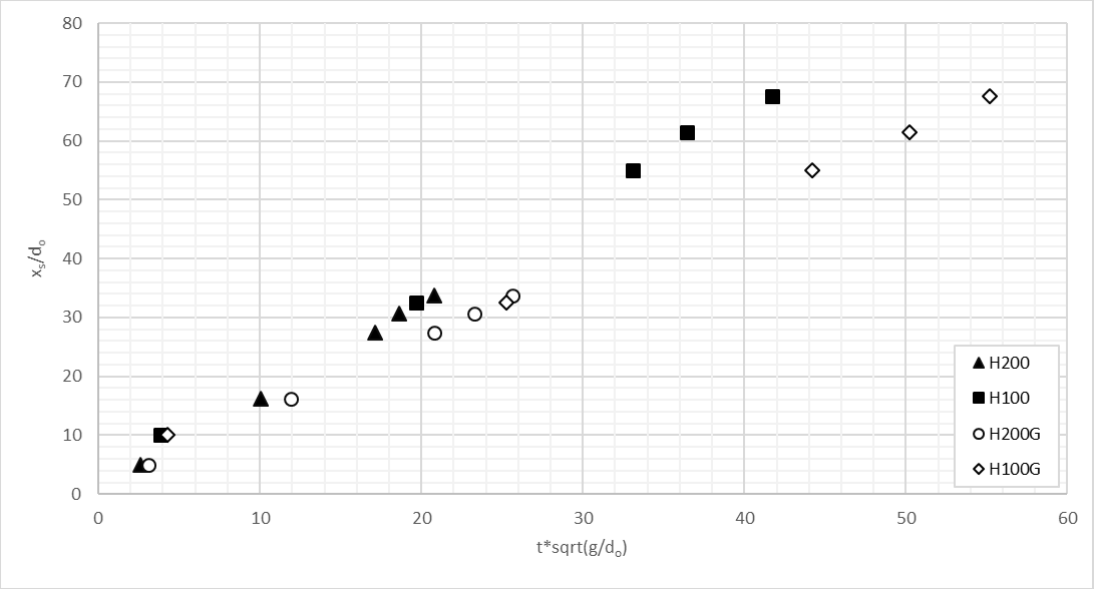

*Figure 4-28- Propagation of dam break wave front represented as instantaneous free- surface profiles for each of the four cases (H200, H100, H200G and H100G). The profiles show the instantaneous dimensionless flow depth x_s/d_o as a function of dimensionless time t*sqrt(g/d_o)*

From the initial validation cases without buildings (B0_H100, B0_H100G, B0_H200 and B0_H200G), the propagation of the dam break wave front from the gate to the urban settlement was analysed. Plotting the dimensionless locations of wave front x_s/d_o as a function of the dimensionless time (where x_s is the location of the wave front at a specific time t and d_o is the initial water depth in the reservoir), these results provide quantitative information on the propagation and show the differences between the four main test cases. The measurements were taken at locations U1, U2, U3, U5 and U8 (at $x = 1.0\,m$, $3.25\,m$, $5.50\,m$, $6.20\,m$ and $6.80\,m$ respectively) for each of the test cases and Figure 4-28 shows the dam break wave front propagation.

The results were then plotted in comparison to Ritter's solution suggesting good agreement between experimental and analytical results.

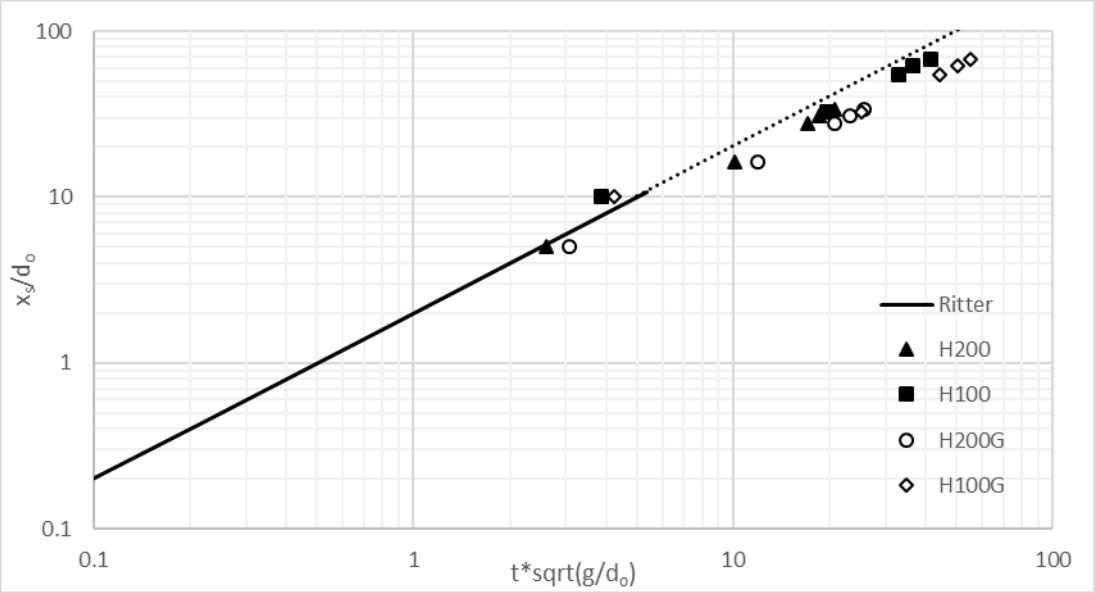

*Figure 4-29- Propagation of dam break wave front and comparison of experimental dataset with Ritter's solution. The propagation profiles show the instantaneous dimensionless flow depth x_s/d_o as a function of dimensionless time t*sqrt(g/d_o). The graph is in log scale showing Ritter's solution with the black line and the results for the four experimental cases (H200, H100, H200G and H100G) with the triangle, square, circle and rhombus respectively.*

Flow description, Froude number calculation

Further analysis was then undertaken to describe the flow on the ramp. The Froude number was initially calculated $Fr = u/(gD)^{1/2}$ (where D is the hydraulic mean depth m) for different parts of the flow and presented in a schematic representation in Figure 4-30 and Figure 4-31 showing a side view of the reservoir release for the four different cases H100 and H100G and H200 and H200G. The figures show that the flow is initially highly unsteady (time dependent) and highly non-uniform (different flow velocity per unit area), it is always subcritical in the reservoir (Fr<1) and supercritical with a high energy state on the ramp (Fr>1). The cases without the roughness layer on the ramp H200 and H100 have the highest Froude numbers as the velocities are higher.

H100, no roughness layer *H100G, roughness layer*

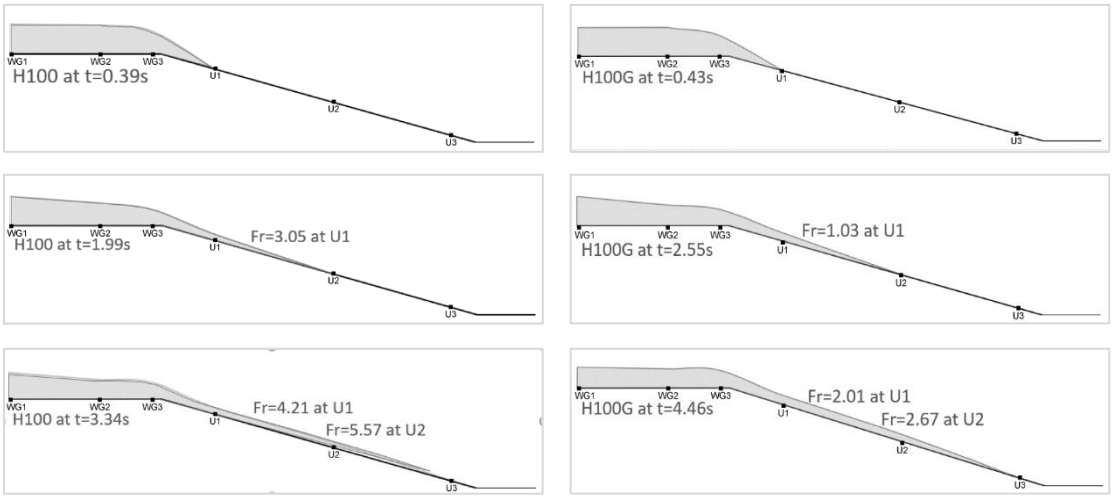

Figure 4-30- Schematic of dam break wave propagation for H100 without (left) and with grass (right) and related Froude numbers based on the wave front velocity

The schematic representation was created using the measured water depths at WG1-WG3 and U1-U3 for different timesteps. In both figures, each of the images (from top to bottom) represent the timestep that the flow reaches U1, U2 and U3 respectively. Each of the Froude numbers was determined using the flow rate approximated from the reservoir release and calculating the velocity at the different points $u(x,t)$.

H200, no roughness layer *H200G, roughness layer*

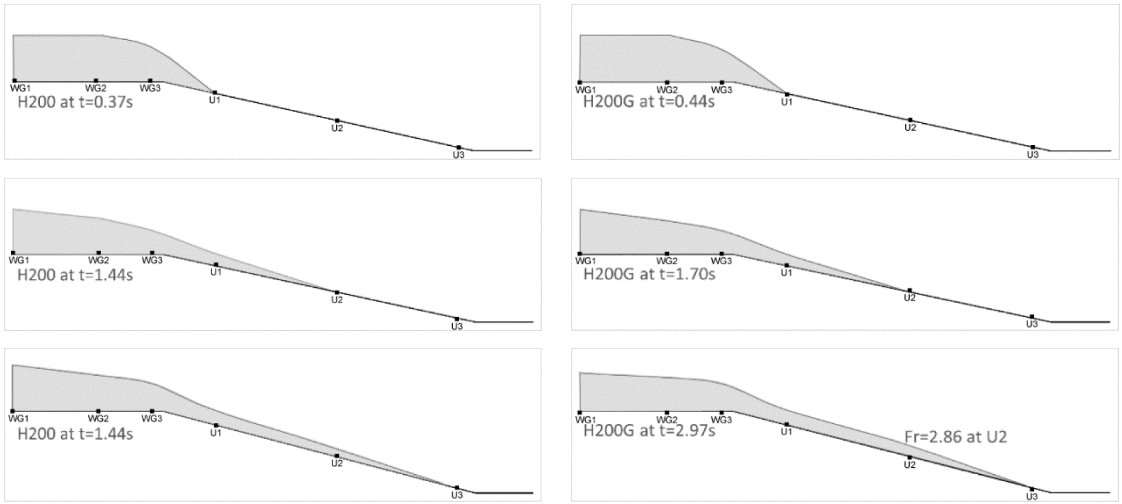

Figure 4-31- Schematic of dam break wave propagation for H200 without (left) and with grass (right) and related Froude numbers

Specific energy

The specific energy curves were plotted for the supercritical flow (Figure 4-32) for different times representing different flow rates.

$$y_c = \frac{Q^2}{gA^2}$$ *Equation 4-3*

$$E = y + \frac{Q^2}{2gA^2}$$ *Equation 4-4*

The critical depth y_c was calculated from Equation 4-3 and the Specific Energy from Equation 4-4 (Chaudhry, 2008). Where y is the flow depth in m, Q is the flow rate in m^3/s, A is the area of flow in m^2, y_c is the critical depth in m and E is the specific energy in m.

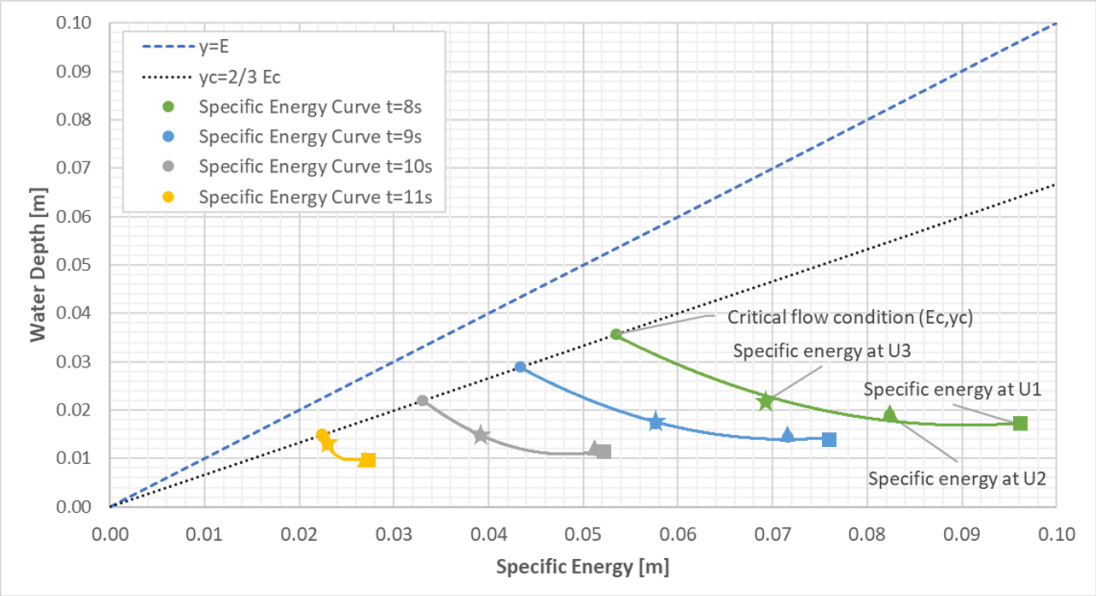

Figure 4-32- Specific energy curve for H200. The different colour curves on the graph correspond to the calculated results for four different timesteps green is for t=8 s, blue is for t=9 s, grey is for t=10 s and yellow is for t=11 s. The four points in each curve, correspond to four different locations measured during the experiment. The point on the black dashed line is the critical depth calculated for each of these time steps and moving away the next points correspond to U3 (star), U2 (triangle) and U1 (square) with the highest specific energy.

Figure 4-32 shows the specific energy curve for the H200 case. The different colour curves on the graph correspond to the calculated results for four different timesteps $t = 8\,s$, $t = 9\,s$, $t = 10\,s$ and $t = 11\,s$. The four points in each curve, correspond to four different locations measured during the experiment for these timesteps. The point on the black dashed line is the critical depth calculated for each of these time step and moving away the

next points correspond to U3, U2 and U1 respectively. Furthermore, the flow discharge decreases over time in the experiment, the different timesteps therefore correspond to different local values of Q, where $Q_{(t=11s)} < Q_{(t=10s)}$. All curves plotted in Figure 4-32 for H200 showed that all measured data are below the critical depth line (black dashed line y_c), meaning that the flow is supercritical at all times on the ramp.

Manning's n coefficient

Assuming uniform flow, the energy slope is considered equal to the bed slope (S_0=S_f) and thus Manning's equation (Equation 4-5) is used to connect the Manning's roughness coefficient with the channel characteristics. Manning's roughness coefficient was therefore calculated using Equation 4-6 for the two cases with and without roughness layer, where n is Manning's roughness coefficient, A is the cross-sectional area of the flow, P is the wetted perimeter and S_o is the slope. Thus re-arranging for n, Manning's roughness coefficient is expressed in Equation 4-5 (Chanson, 2004b).

$$Q = V \cdot A = \frac{1}{n} \cdot \frac{A^{5/3}}{P^{2/3}} \cdot S_o^{1/2} \qquad \textit{Equation 4-5}$$

$$n = \frac{1}{Q} \cdot \frac{A^{5/3}}{P^{2/3}} \cdot S_o^{1/2} \qquad \textit{Equation 4-6}$$

Manning's coefficient was calculated using water depth data at two different locations and for two different instantaneous flow rates and then an average was taken between the calculated values. The results are presented in Table 4-6 and compared with the ranges found in literature for laminated timber and low grass floodplains (Wilson and Horritt, 2002; Wilson, 2007). As can be seen from the table, the calculated values fit well within the ranges suggested in literature and result in an average value of 0.012 for the smooth to 0.020 for the roughened ramp.

Table 4-6- Summary of Manning's coefficient calculation for the different test cases (H100, H200, H100G, H200G)

Test Case		**Location**	**Instantaneous Flow Rate [L/s]**	**Depth [m]**	**Manning's**	**Average value**	**Literature Range**
No vegetation	H100	U1	10.7	0.009	0.010	0.012	0.010 - 0.014
		U2	10.7	0.010	0.012		
	H200	U1	12.3	0.011	0.013		
		U2	12.3	0.012	0.013		
Vegetation / Roughness	H100 G	U1	12.0	0.015	0.020	0.020	0.015 - 0.025
		U2	12.0	0.015	0.021		
	H200 G	U1	17.0	0.017	0.017		
		U2	17.0	0.019	0.021		

4.6.3 Urban settlement

As previously discussed, once the water reached the flat part of the urban settlement, it slowed down regardless of the level of blockage. The water depth results in this part of the experiment were affected by three factors: the initial water depth in the reservoir, $0.1\ m$ for H100 and $0.2\ m$ for H200; the roughness layer in the cases H100G and H200G, and finally the level of the blockage B0 for no building, B1 for a single building, B2 for two buildings and B4 for four buildings. In all the single building cases, the reflected wave created from the buildings' blockage resulted in the formation of a hydraulic jump, a stationary surge wave through which the depth of the flow increases and happens in a situation where the flow upstream is supercritical and downstream subcritical (Chaudhry, 2008).

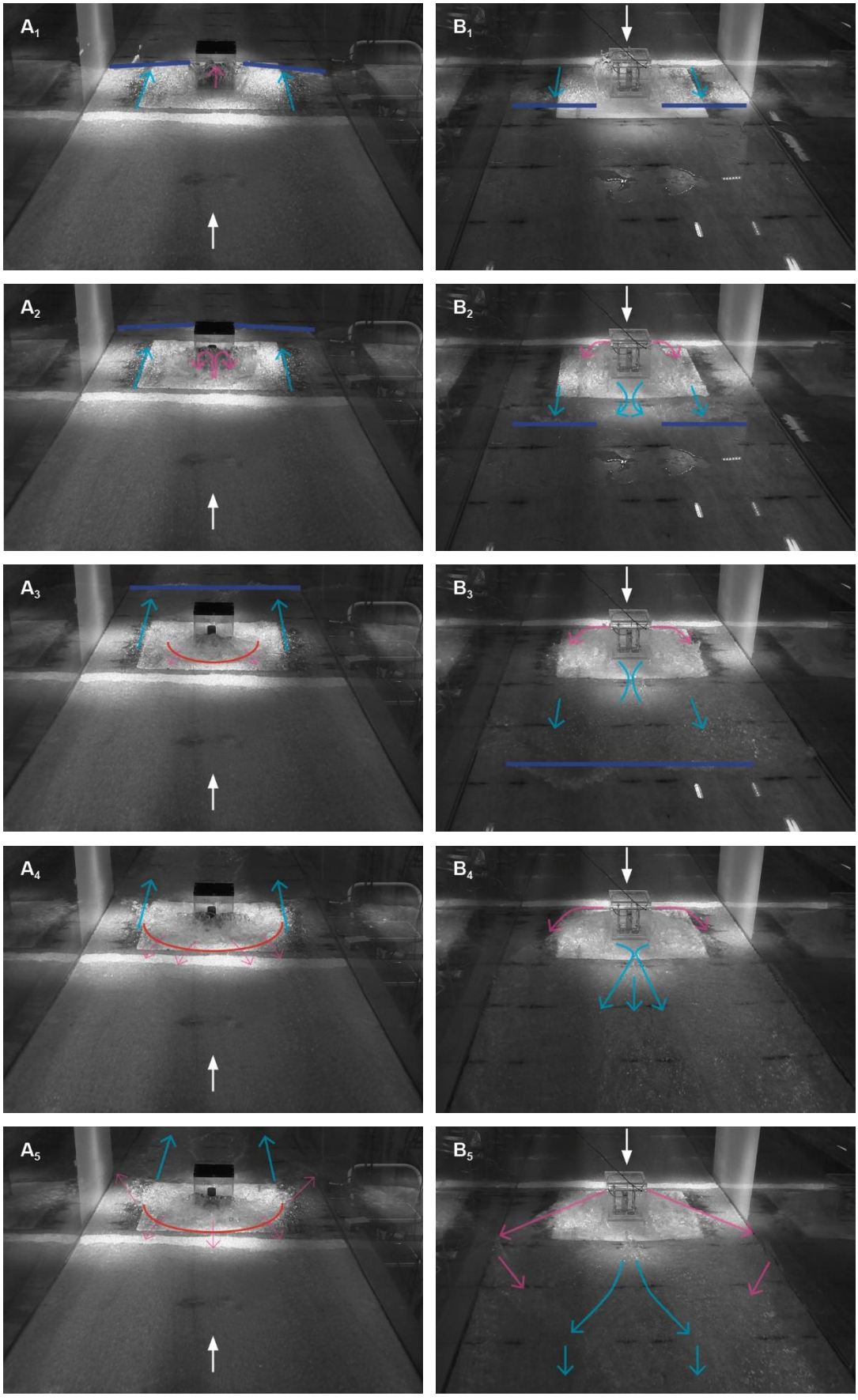
A1
B1
A2
B2
A3
B3
A4
B4
A5
B5

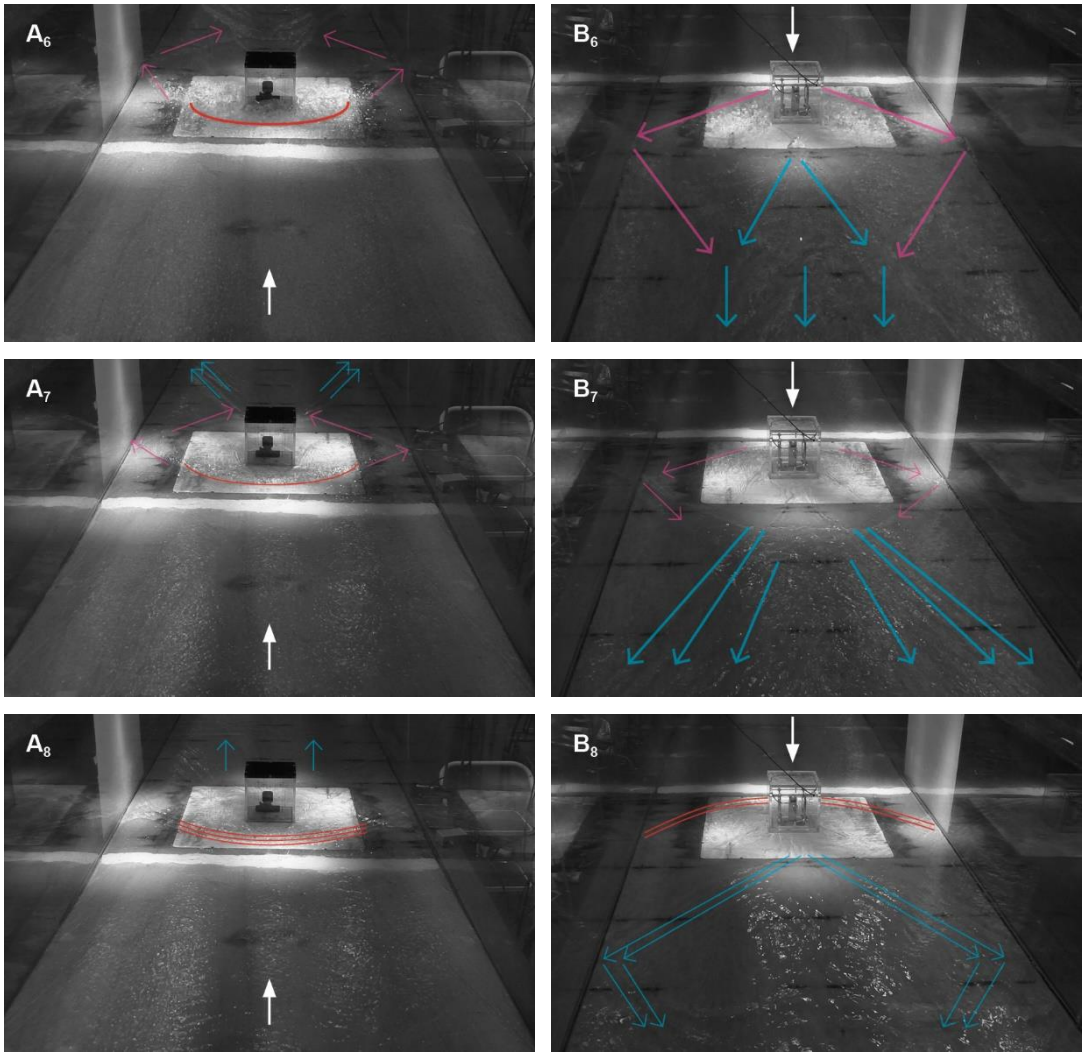

Figure 4-33- Flood wave propagation for the B1_H100 case looking down-slope from the ramp to the urban settlement (A_1-A_8) and up-slope from the urban settlement to the ramp (B_1-B_8). The white arrow in the photo indicates the direction of the flow, the blue solid lines the dam break wave front propagation, the cyan arrows the direction of the dam break flow, the red solid line the hydraulic jump front propagating upstream and the magenta arrows the direction of the flow due to the building obstruction. A_1-B_1 show the impact moment, A_2-B_2 the reflected wave, A_3-B_3 the creation of the hydraulic jump, A_4-B_4 the strengthened hydraulic jump, A_5-B_5 the more apparent flows reflected from the side walls, A_6-B_6 the amplified wake width, A_7-B_7 the creation of cross waves and A_8-B_8 the ripples and cross-waves

Figure 4-33 shows the flood wave propagation for the B1_H100 case looking down-slope from the ramp to the urban settlement (left A_1-A_8) and up-slope from the urban settlement to the ramp (right B_1-B_8). The white arrow in the photo indicates the direction of the flow, the blue solid lines the dam break wave front propagation, the cyan arrows the direction of the dam break flow, the red solid line the hydraulic jump front propagating upstream and the magenta arrows the direction of the flow due to the building obstruction. Figures A_1 and B_1 show the first moment of impact where the flow moves around the building at the sides; and in the centre, the building creating an obstruction, makes the water move upwards the front face of the building (pink arrow). Following this, the dam break front continues to

propagate downstream (blue solid line), the flow on the front face of the building is reflected (A_2) and the rest of the flow moves around the building (cyan arrows) creating a dry area directly behind the back face of the building (B_2). The flow becomes rapidly varying and hydraulic jump (red solid line) develops after that first impact and starts propagating opposite to the direction of the flow (A_3). Meanwhile the dry area behind the building becomes smaller (B_3). Next, we observe a stronger hydraulic jump with the flow depth increasing at the front of the building (A_4) and the building creating strong flows (magenta arrows) towards the flume sides (B_4). In this high Froude flow, the flow around the side of the building (magenta arrows) becomes more apparent (A_5, B_5), reflects from the side walls of the flume and merges with the wake (cyan arrows) created at the back side of the building (B_5). As the flow starts to become decaying quasi-steady flow (showing slow changes with time) the effect of the reflected waves at the back of the building gets amplified increasing the width of the wake (A_6, B_7). The flow rate decreases and the reflected wave from the front of the building is small (A_7) while the reflected waves from the side walls (pink arrows) interact with the wake creating cross-waves. A cross-wave is a wave caused by the interaction of the reflected flow from the sides of the flume and the waves created from the wake at the back of the building. The two flows, cross at slanting angles to each other and the resultant cross-wave is a stationary wave orientated approximately parallel to the flume walls. Finally, in low flow, ripples appear in the reflected wave (A_8) and the cross-wave formation at the back of the building becomes more apparent (B_8).

Figure 4-34 and Figure 4-35 compare the water depth at the locations U8 and U10 for the four experimental set ups: H100, H200, H100G and H200G. Notably, behind the building at U8 (Figure 4-34), for H200 the roughness ramp (H200G) results in a larger peak compared to the H100 case where the initial peak is reduced. Both roughness cases (H200G and H100G) result in a second peak after $10\ s$ resulting in a larger water depth for a longer period of time which can be attributed to the wake. On the side of the building U10 (Figure 4-35), in both test cases the peak is reduced in the roughness test cases (H200G and H100G) and after $10\ s$ all water depths are similar throughout the test cases. The three impact stages that will be discussed in the next paragraph on applied load are evident in the non-roughness cases behind the building (H200 and H100) and all four cases on the side of the building.

Figure 4-36 shows photos of the water impact on the single building for the B1_H200 case at times $t = 2.96\ s$, $t = 3.45\ s$ and $t = 10\ s$. The side photos (A_1-C_1) show the hydraulic jump and the large depths on the front and sides of the building.

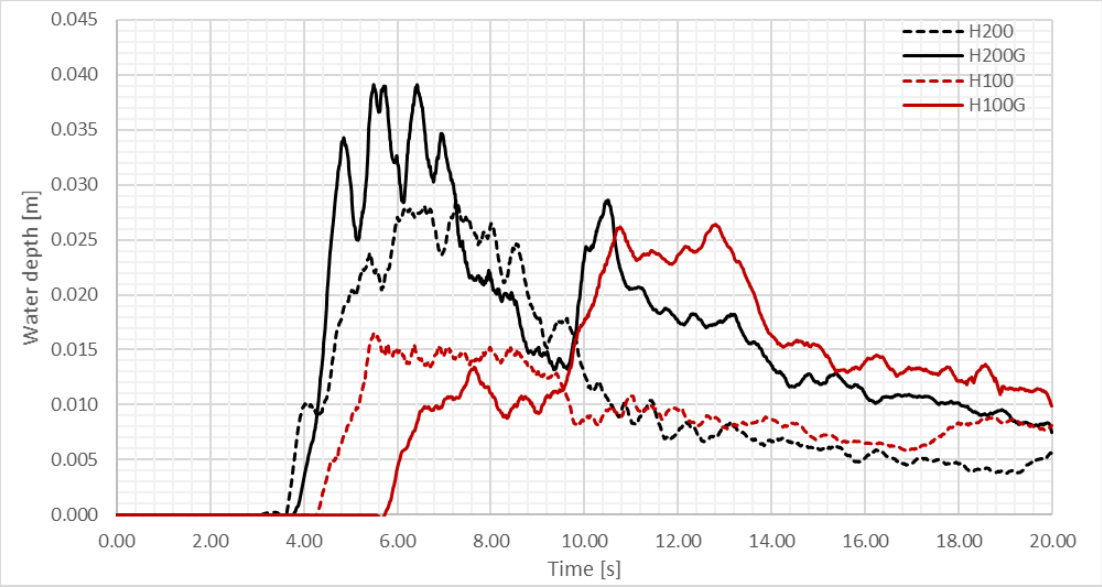

Figure 4-34- Timeseries of the water depth evolution at U8 (behind the building) for H200 (black line) and H100 (red line), with (solid line) and without (dashed line) the roughness layer

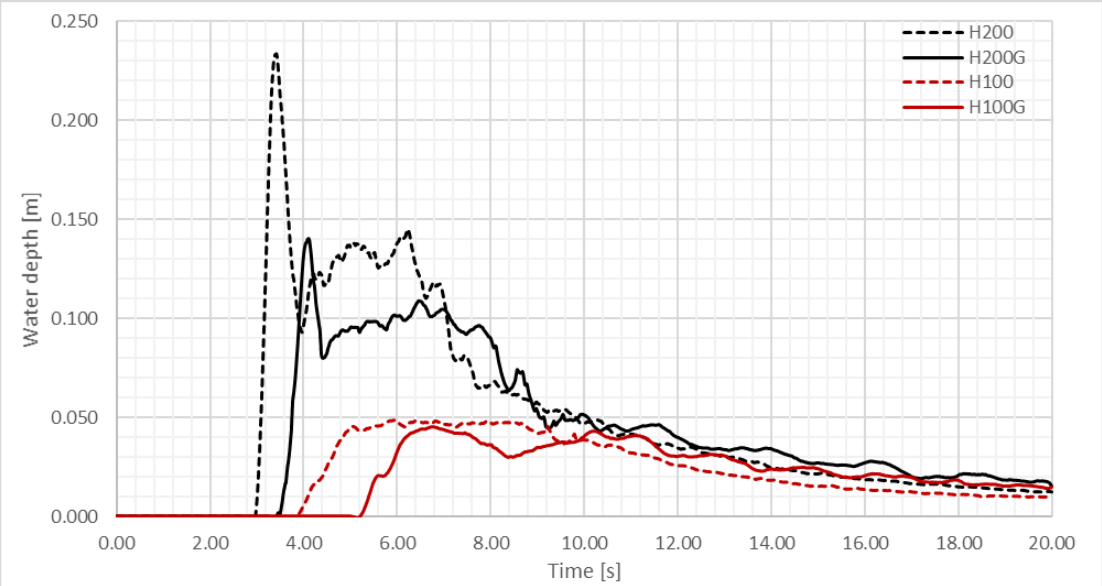

Figure 4-35- Timeseries of the water depth evolution at U10 (on the side of building) for H200 (black line) and H100 (red line), with (solid line) and without (dashed line) the roughness layer

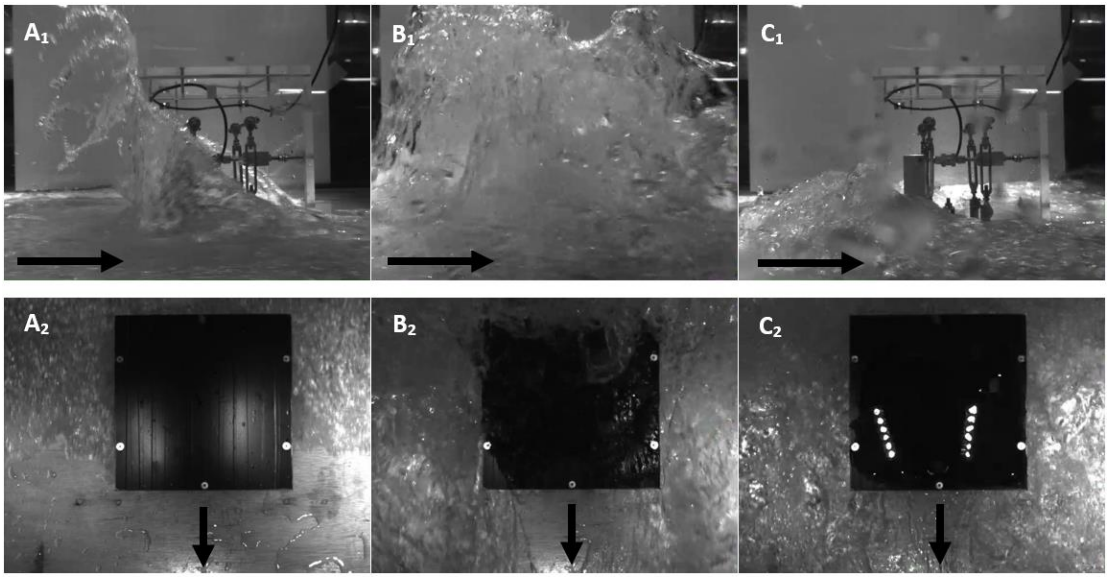

Figure 4-36- Photos of water impact on building for B1_H200 case at times t=2.96 s (A_1, A_2), t=3.45 s (B_1, B_2) and t=10 s (C_1, C_2) from side (top photos) and top view (bottom photos).

The impact on the downstream urban settlement can be explained by the behaviour of an object in supercritical flow and can be described in four distinctive stages: (i) impact, (ii) development of the hydraulic jump, (iii) steady high Fr flow (around an obstacle) and (iv) decaying quasi-steady flow with decreasing high Fr number. The (i) impact stage is defined from the moment the load increases from zero to the first peak, the (ii) development of the hydraulic jump is characterised by the stage of increased load as the jump is developing in front of the building, the (iii) steady high Fr flow is apparent whilst the flow is still fast but the hydraulic jump has dissolved and thus the load has started to decrease and finally the (iv) decaying quasi-steady flow stage shows a decreasing applied load with a gradual decline as the Fr number is decreasing as well.

Figure 4-37 and Figure 4-38 have been synchronised for the moment of impact and show the load over time for the H100 and H100G and for the H200 and H200G cases, respectively. The roughness layer decreases the peak load for H200 but creates a higher peak load in the H100 case which is attributed to the slower flow and increased water depth around the building. In Figure 4-36 and Figure 4-37, for H100 the impact state occurs during the first $0.6\ s$, then the hydraulic jump forms between $0.6\ s$ and $4\ s$, the steady high Fr number flow occurs between $4\ s$ and $7\ s$ and the decaying quasi-steady flow is seen after $7\ s$. For H200 the impact state occurs during the first $2\ s$, then the hydraulic jump forms between $2\ s$ and $3.5\ s$, the steady high Fr number flow occurs between $3.5\ s$ and $8\ s$ the decaying quasi-

steady flow after $8\ s$. Figure 4-39 and Figure 4-40 show photos for the H100 and H200 case respectively at times $0\ s$, $2\ s$, $4\ s$, $8\ s$, $10\ s$ and $12\ s$ corresponding to the synchronised graphs in Figure 4-37 and Figure 4-38.

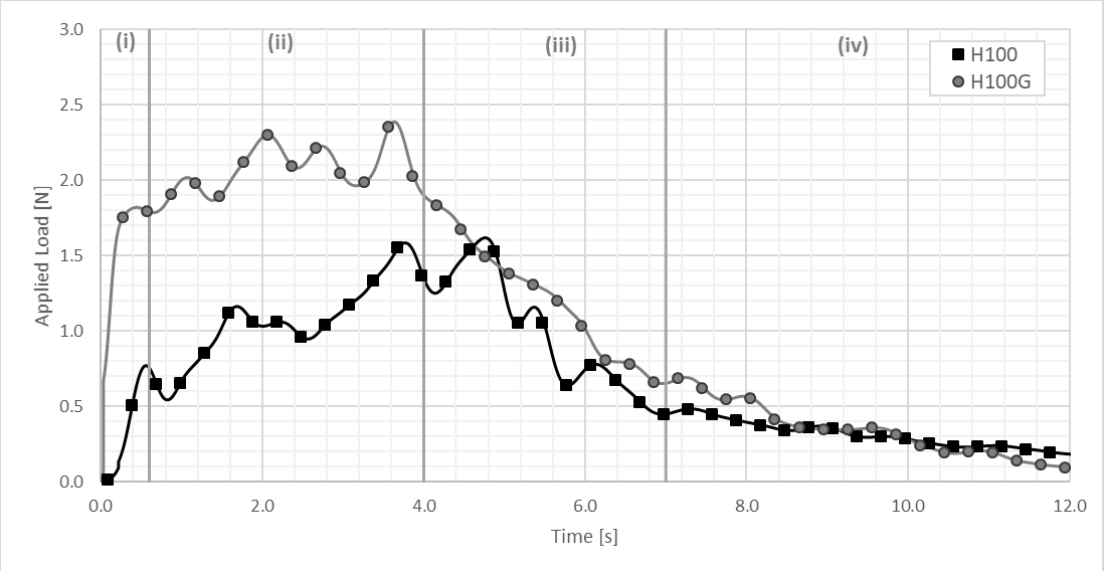

Figure 4-37- Applied load over time for H100 and H100G where the black line and grey lines represent the cases without (H100) and with (H100G) a roughness layer respectively. The vertical lines represent four stages (i) impact stage, (ii) development of the hydraulic, (iii) steady high Fr flow and (iv) decaying quasi-steady flow stage. All cases have been synchronised at the moment of impact for comparative reasons

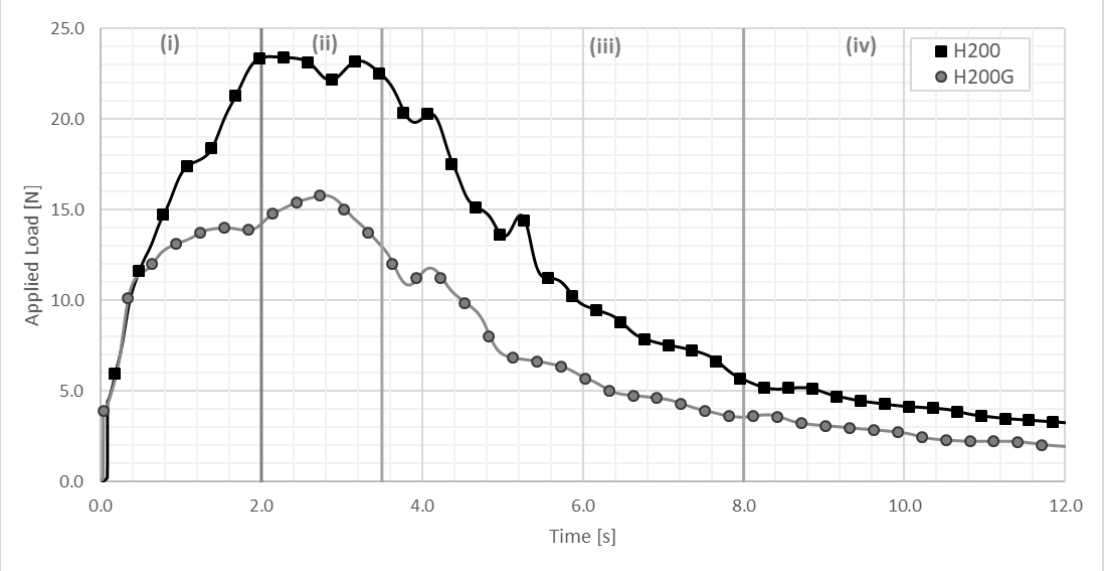

Figure 4-38- Applied load over time for H200 and H200G where the black line and grey lines represent the cases without (H200) and with (H200G) a roughness layer respectively. The vertical lines represent four stages (i) impact stage, (ii) development of the hydraulic, (iii) steady high Fr flow and (iv) decaying quasi-steady flow stage. All cases have been synchronised at the moment of impact for comparative reasons

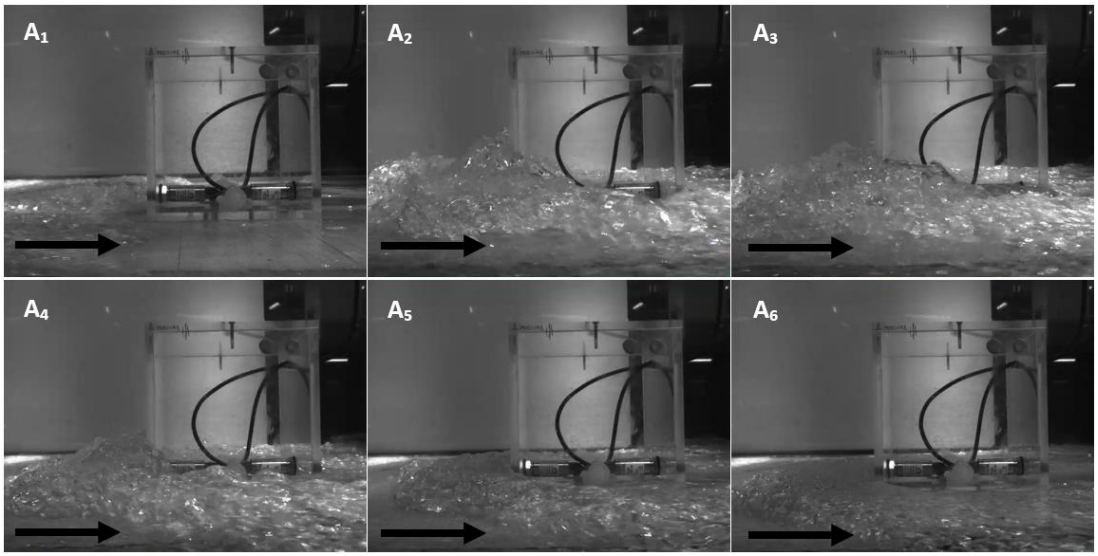

Figure 4-39- Photos of water impact on building for B1_H100 case at times t=0 s (A_1), t=2 s (A_2), t=4 s (A_3), t=8 s (A_4), t=10 s (A_5) and t=12 s (A_6).

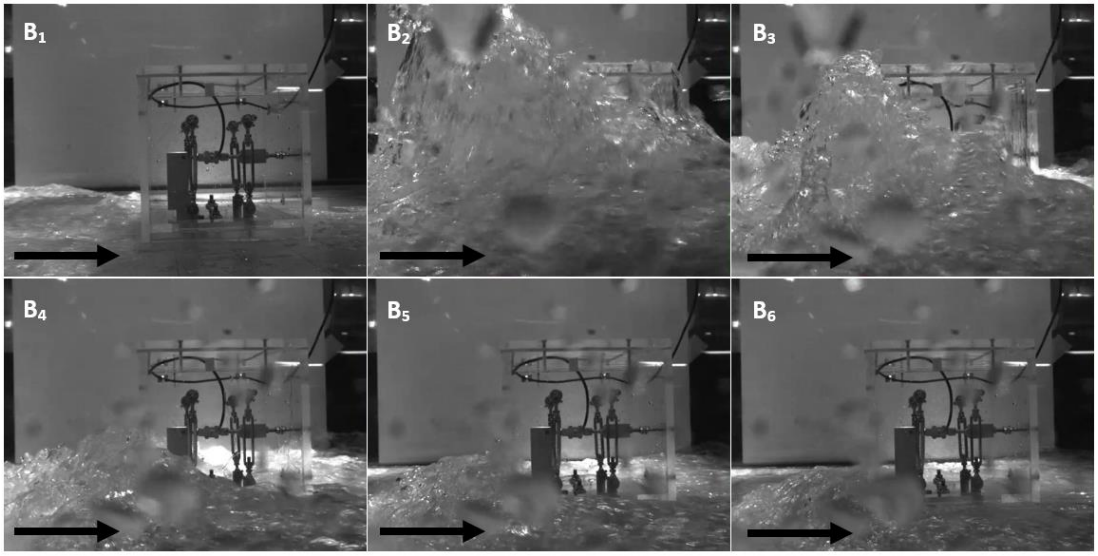

Figure 4-40- Photos of water impact on building for B1_H200 case at times t=0 s (B_1), t=2 s (B_2), t=4 s (B_3), t=8 s (B_4), t=10 s (B_5) and t=12 s (B_6)

In Figure 4-41 and Figure 4-42, the load on the building over time was plotted for the different cases presented in Table 4-7 for H200 and H100. For both H100 and H200 when considering the cases with the 4 buildings, the load on the building positioned at the back is almost zero. Furthermore, the blockage created when two buildings are present does not appear to have much effect on the load on the building.

Table 4-7- Description and characteristics of the six test cases examining applied load in the urban settlement. The arrow in the building layout represents the direction of the flow and the red square shows the examined building.

Test Case	Description	Building Layout
H200 B1	Initial water depth $h_o = 0.2$ One building No roughness layer on ramp	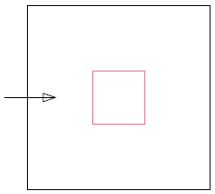
H200 B1T	Initial water depth $h_o = 0.2$ One building with small fence in front No roughness layer on ramp	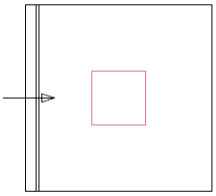
H200 B2	Initial water depth $h_o = 0.2$ Two buildings No roughness layer on ramp	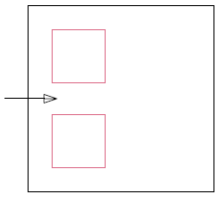
H200 B4 F	Initial water depth $h_o = 0.2$ Four buildings, front building No roughness layer on ramp	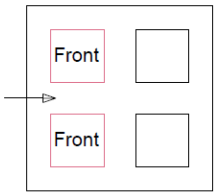
H200 B4 B	Initial water depth $h_o = 0.2$ Four buildings, back building No roughness layer on ramp	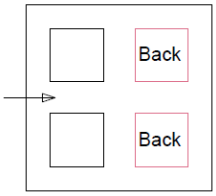
H200 G	Initial water depth $h_o = 0.2$ One building Roughness layer on ramp	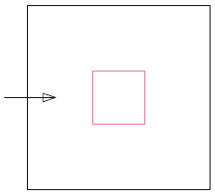

Specifically, in the H200 case (Figure 4-41), it is observed that the lowest load is found at the back building (B200 B4 B) and the roughness layer case (H200G) is the test case that results in the most considerable load decrease. Otherwise, when such a large amount of water is involved, the blockage created by the different number of buildings does not have a big effect on the loads applied (i.e. H200 B1T, H200 B2, H200 B4 F). Contrary to this, in the H100 case, (Figure 4-42) the load applied on the front building of the urban settlement with the four buildings (B100 B4 F), triples in magnitude as it leads more blockage and a deeper water depth around the buildings for longer periods of time. As previously mentioned, increasing the roughness in the H100 case, increases the applied load (H100G) mainly due to the hydrostatic load but the rest of the configurations do not have a strong effect compared to the initial results found by the simple case (B100_B1). Note the difference in magnitude between Figure 4-41 and Figure 4-42 as the effect seems much larger not taking into account the scale.

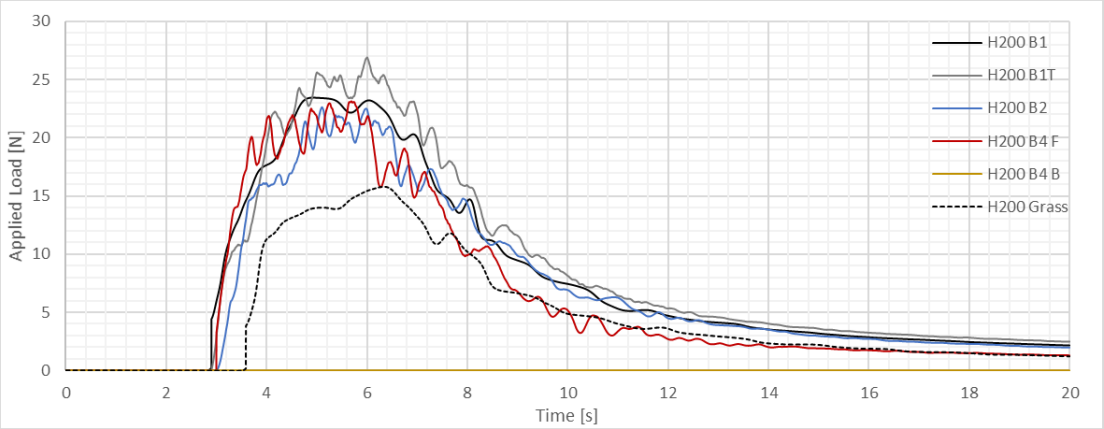

Figure 4-41- Applied load on front face of a single building for the initial depth H200. The different coloured lines represent different test cases. The black line represents the applied load for H200 B1, the dashed black line represents the H200 G case with the roughness layer, the grey line represents the B1T case where a small fence is installed 0.2 m from the building, the blue line shows the case with two buildings B2, the red and yellow lines represent the case with four buildings showing the applied load on the front and back side respectively.

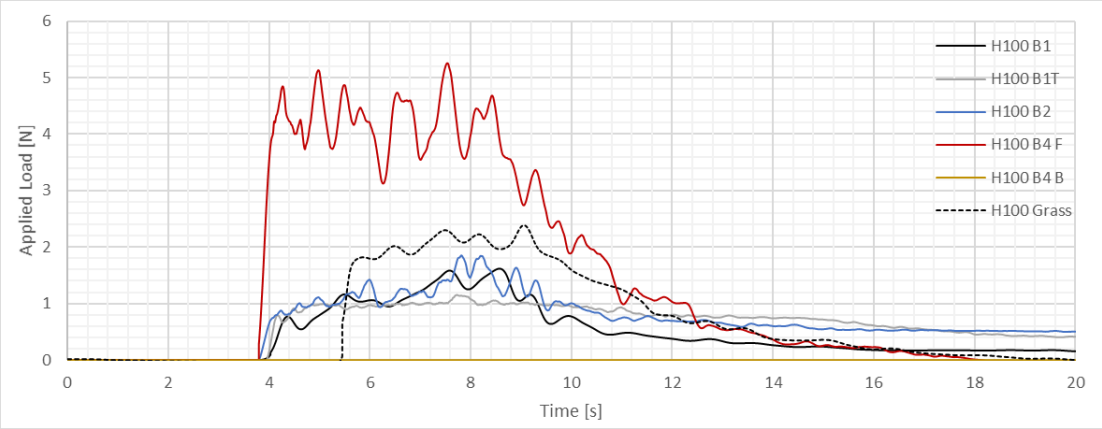

Figure 4-42- Applied load on front face of a single building for the initial depth H100. The different coloured lines represent different test cases. The black line represents the applied load for H100 B1, the dashed black line represents the H100 G case with the roughness layer, the grey line represents the B1T case where a small fence is installed 0.2 m from the building, the blue line shows the case with two buildings B2, the red and yellow lines represent the case with four buildings showing the applied load on the front and back side respectively.

4.7 SUMMARY AND CONCLUSION

To summarise this experimental work, flash floods were generated in a controlled laboratory environment for the validation of numerical hydrodynamic models. A new experimental methodology of generating high Froude number flows in a controlled environment was developed. This experimental study is important because even though high Froude flows can be easily produced in a laboratory setting (e.g. using a sluice gate), obtaining the impact stage found in the urban settlement would not be possible without a dam break experiment. Thus, this allowed for the effect of land use (vegetated, non-vegetated ramp) and the intensity of flash flood characteristics (different initial water depths) to be investigated in a controlled environment.

To summarise the findings of this experimental study. The water release in the reservoir is described accurately by the ideal dam break theory. After the gate is released, a dam break wave starts moving downstream on the ramp whilst a negative wave starts propagating upstream within the reservoir and the conditions at the gate are critical (Fr=1). Once the negative wave reaches the upstream reservoir wall, the water in the reservoir becomes horizontal, and the flow release from the reservoir starts decreasing exponentially. The flow on the ramp is always below the critical depth and is supercritical with high specific energy (Fr>1). Once the flow reaches the horizontal part of the experiment, the reflection and blockage from the building makes the flow subcritical thus creating a hydraulic jump in front

of the building. The different configurations affect the flow in a three-dimensional way creating different cross-waves and flow patterns depending on the blockage investigated. The blockage in the urban settlement will be further discussed in Chapter 5 through numerical modelling of this experiment.

As expected, the roughness ramp increased the friction, thus slowing down the flow and reducing its Froude number considerably. This translated to a decrease in applied load on the buildings in the higher water depth cases (H200, H200G).

In terms of applied load on the urban settlements, the level of blockage (one, two, four houses) had no effect on the higher water depth cases (H200) whilst in the lower water depths (H100) aggravated the applied load. This was attributed to the hydraulic jump created in the lower water depths resulting into the buildings being submerged for longer.

5 NUMERICAL MODELLING OF FLASH FLOODS

5.1 INTRODUCTION

The purpose of this chapter is to investigate flash floods numerically and, in particular, to develop a methodology and calibration parametrisation for the hydraulic modelling of these types of events. Using the experiment presented in Chapter 4 for validation, two-dimensional and three-dimensional OpenFOAM models were used to further investigate the interaction of the flood wave with the urban settlement of the experiment and provided insight on how to use it and parametrise it for this type of events.

First, a theoretical background is presented introducing fundamental concepts of fluid dynamics whilst developing a consistent terminology and notation. Next, two validation test cases have been used as the basis for the 2D and the 3D models respectively; the first based on a dam break flow experiment performed by Soares-Frazão (2007) as part of the IMPACT benchmarking programme (Soares-Frazão, 2007), and the second test is a dam break flow experiment investigating the impact on a tall structure from the University of Washington (Marrone et al., 2011).

A methodology is then presented describing in detail the selection of initial, boundary and control conditions for the simulation. The convergence analysis and the selection of the final parameters is defined in the model parametrisation section creating the optimal approach to model the flash flood experiments of the previous chapter.

This approach is then used to analyse in more depth the experiments and the methodology required for modelling flash floods. While some limitations were discovered and future work is suggested, the 2D and 3D models used in this study were able to provide a very accurate representation of the event and further insight into the modelling of flash floods and the proposed methodology required for their simulation.

5.2 THEORETICAL BACKGROUND

5.2.1 Fluid Flow

The flow in fluids is generally three-dimensional and unsteady, and when modelling water, the fluid itself is assumed incompressible. When modelling a river flow, the dimensions can

be confined to either one, two or three, assuming the flow is steady, incompressible and in shallow depths (Abbott and Basco, 1989).

To derive the conservation laws, consider a *control volume* within a *streamtube* (Figure 5-1). The closed boundary is called the *control surface* and everything outside the control surface can be defined as *surroundings*. The volume of the control volume is denoted V and S is the surface area. Inlet and outlet velocities are perpendicular to the control surface, measured relative to the control volume (Mohanty, 2006).

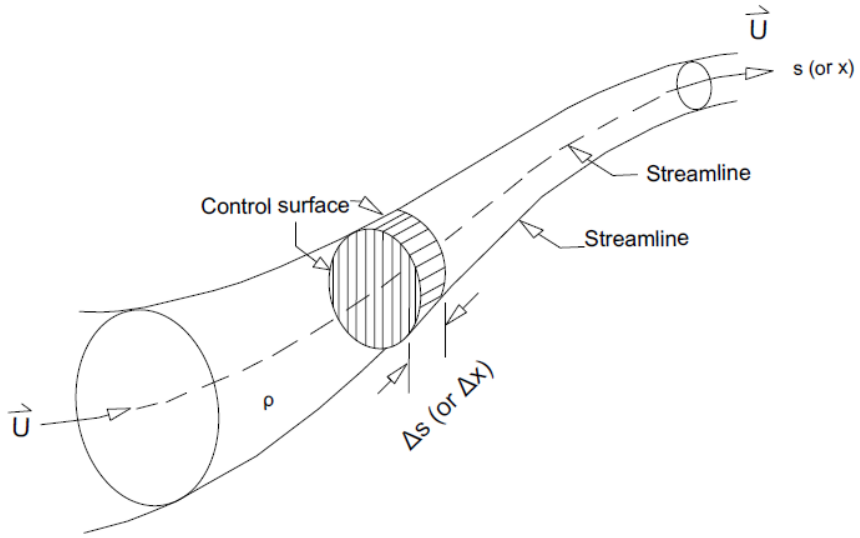

Figure 5-1- Control volume within a streamtube in the fluid stream used to derive the conservation laws (Abbott and Basco, 1989)

As matter can be neither created nor destroyed, the change in the mass within the control volume is equal to the mass entering the control volume minus the mass exiting the control volume (Abbott and Basco, 1989b). The general conservation of mass can be expressed as shown in Equation 5-1, where ρ is the mass density (dimensions M/L^3), $\vec{U}$ is the fluid velocity (L/S), $\vec{n}$ is a unit normal vector (no unit), dV the differential-sized control volume (dimensions L^3) and finally dS the differential-sized control surface area (dimensions L^2) (Abbott and Basco, 1989).

$$\int_v \frac{\partial \rho}{\partial t} dV + \int_s (\rho)\vec{U} \cdot \vec{n} dS = 0 \qquad \textit{Equation 5-1}$$

In fluid dynamics, Newton's Second Law states that the sum of all external forces acting on the control volume equals to the rate of change of momentum of mass within the control volume plus the rate of flux of momentum through the control surface (Abbott and Basco, 1989). The mathematical expression of this statement can be found in Equation 5-2 where $\vec{F}$ is the sum of all external forces and $(\rho\vec{U})$ is the *momentum flux density* (Abbott and Basco, 1989).

$$\int_v \frac{\partial(\rho\vec{U})}{\partial t} dV + \int_s (\rho\vec{U})\vec{U} \cdot \vec{n} dS = \vec{F} \qquad \textit{Equation 5-2}$$

5.2.2 Governing Equations

The governing equations in most fluid dynamic problems are the Shallow Water Equations (SWEs). They are derived from the Reynolds-averaged Navier–Stokes equations which in turn are derived from the equations for conservation of mass (continuity equation) and linear momentum (Chaudhry, 2008; Dawson and Mirabito, 2008).

The Navier Stokes Equations in 3D can be written analytically as:

Continuity Equation:

$$\frac{\partial u}{\partial x} + \frac{\partial v}{\partial y} + \frac{\partial w}{\partial z} = 0 \qquad \textit{Equation 5-3}$$

Momentum Equations:

$$\frac{\partial u}{\partial t} + u\frac{\partial u}{\partial x} + v\frac{\partial u}{\partial y} + w\frac{\partial u}{\partial z} = g_x - \frac{1}{\rho}\frac{\partial p}{\partial x} + \frac{\mu}{\rho}\nabla^2 u$$

$$\frac{\partial v}{\partial t} + u\frac{\partial v}{\partial x} + v\frac{\partial v}{\partial y} + w\frac{\partial v}{\partial z} = g_y - \frac{1}{\rho}\frac{\partial p}{\partial y} + \frac{\mu}{\rho}\nabla^2 v \qquad \textit{Equation 5-4}$$

$$\frac{\partial w}{\partial t} + u\frac{\partial w}{\partial x} + v\frac{\partial w}{\partial y} + w\frac{\partial w}{\partial z} = g_z - \frac{1}{\rho}\frac{\partial p}{\partial z} + \frac{\mu}{\rho}\nabla^2 w$$

Where: u, v and w are the velocity components in the x, y and z directions and $g = (g_x, g_y, g_z)^T$ is the gravitational force per unit mass, p is the pressure and ∇^2 is the Laplace operator, which can be written as follows (Chaudhry, 2008):

$$\nabla^2 = \frac{\partial^2}{\partial x} + \frac{\partial^2}{\partial y} + \frac{\partial^2}{\partial z} \qquad \textit{Equation 5-5}$$

By assuming the horizontal dimension is much larger than the vertical, and integrating the Navier Stokes Equations over depth, the following differential equations can be derived, the depth-averaged SWEs are:

$$\frac{\partial h}{\partial t}+\frac{\partial (uh)}{\partial x}+\frac{\partial (vh)}{\partial y}=0$$

$$\frac{\partial (uh)}{\partial t}+\frac{\partial \left(u^2h+\frac{1}{2}gh^2\right)}{\partial x}+\frac{\partial (uvh)}{\partial y}=gh\left(S_{0x}-S_{fx}\right) \qquad \textit{Equation 5-6}$$

$$\frac{\partial (vh)}{\partial t}+\frac{\partial (uvh)}{\partial x}+\frac{\partial \left(v^2h+\frac{1}{2}gh^2\right)}{\partial y}=gh\left(S_{0y}-S_{fy}\right)$$

The dependent variables of the equation are ***u***, ***v*** and ***h*** which represent the horizontal velocity, the vertical velocity and the water depth respectively (Zoppou and Roberts, 2000; Moler, 2011). The SWEs are usually expressed in a more concise manner, introducing the vectors ***u***, ***f*** and ***g*** *(Moler, 2011).*

$$\boldsymbol{u}=\begin{bmatrix} h \\ uh \\ vh \end{bmatrix}, \qquad \boldsymbol{f}=\begin{bmatrix} uh \\ u^2h+\frac{1}{2}gh^2 \\ uvh \end{bmatrix} \quad \text{and} \quad \boldsymbol{g}=\begin{bmatrix} vh \\ uvh \\ v^2h+\frac{1}{2}gh^2 \end{bmatrix} \qquad \textit{Equation 5-7}$$

The source term used is given in terms of the bed slopes and bed frictions which can then be expressed from Manning roughness law as (Zoppou and Roberts, 2000):

$$\boldsymbol{S}=\begin{bmatrix} 0 \\ gh\left(S_{0x}-S_{fx}\right) \\ gh\left(S_{0y}-S_{fy}\right) \end{bmatrix} \quad \text{where:} \quad S_{fx}=\frac{u\eta^2\sqrt{u^2+v^2}}{h^{4/3}} \quad \text{and} \quad S_{fy}=\frac{u\eta^2\sqrt{u^2+v^2}}{h^{4/3}}$$

where S_{fx} and S_{fy} represent the friction slope in the two Cartesian directions x and y.

Thus, the 2D shallow water equations can be written as a hyperbolic conservation law (Liang et al., 2007):

$$\frac{\partial \boldsymbol{u}}{\partial t}+\frac{\partial \boldsymbol{f}}{\partial x}+\frac{\partial \boldsymbol{g}}{\partial y}=\boldsymbol{S} \qquad \textit{Equation 5-8}$$

5.2.3 OpenFOAM software

OpenFOAM is an acronym for Open Field Operation and Manipulation. It is a C++ toolbox used for the solving of computational fluid dynamic problems (Damián, 2012) developed in the 1980s and finally released as an open-source software in 2004 (Damián, 2012). The multiphase solver *interFoam* (part of OpenFOAM's CFD solver library) which models the

interface between the water and the air was used here to provide further understanding into the physical processes of flash floods.

InterFoam, solves the Navier-Stokes equations and uses the VoF method (Volume of Fluid) to record the position of the water/air interface. Navier-Stokes equations are solved at each cell for every time step are (Schulze and Thorenz, 2014):

$$\nabla \cdot U = 0$$

$$\frac{\partial \rho U}{\partial t} + \nabla \cdot (\rho U U) = -\nabla p_{-\rho g h} + [\nabla \cdot (\mu \nabla U) + \nabla \mathrm{U} \cdot \nabla \mu] + \rho \cdot g + \int_s \sigma \kappa \delta (x - x_s) n dS(x_s) \qquad \textit{Equation 5-9}$$

$$\frac{\partial \alpha}{\partial t} + \nabla \cdot (U\alpha) + \nabla \cdot \big(U_r \alpha (1 - \alpha)\big) = 0$$

Where: ρ is density, U is the velocity, p_{-rgh} is the modified pressure (equal to the total pressure minus the hydrostatic pressure $p_{-rgh} = p - \rho g \cdot x$), μ is the dynamic viscosity, x is a special position vector, g is the gravitational acceleration, σ is the surface tension coefficient, κ is the surface curvature, δ is the Dirac delta function (a mathematical construct), $(x - x_s)$ is the vertical distance to the surface, n is the normal vector on the interface, S is the interface, α is the water volume fraction and U_r is the compressive velocity (Schulze and Thorenz, 2014).

OpenFOAM provides some ready-to-use tutorial cases for different types of simulations, which is used as a basis for all dam break simulations. The dam break tutorial case contains three folders in each directory (0, constant, system), each including text files containing the relevant information for the initial conditions, boundary conditions, constant parameters and control conditions. These files are used through UNIX style commands to run the simulation. The different folders (0, constant, system) and the contained files are shown schematically in Figure 5-2 and the main files are described in Table 5-1.

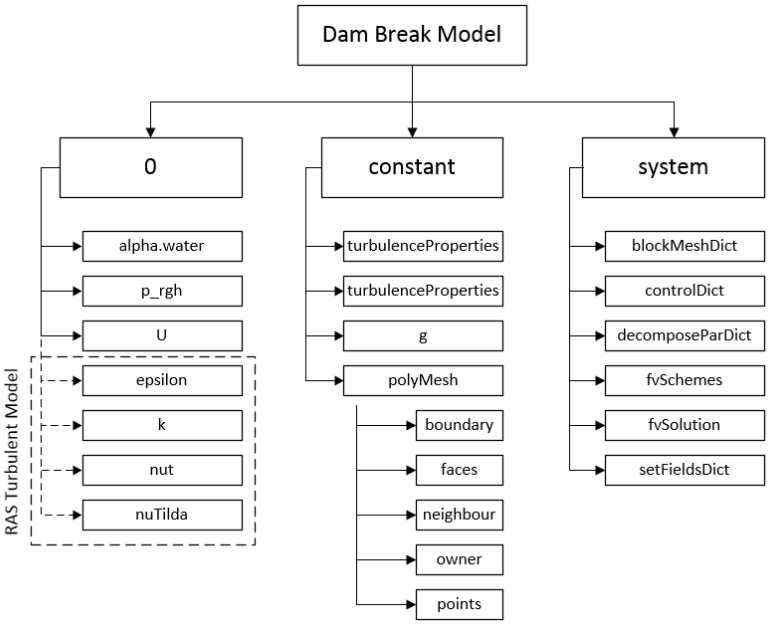

Figure 5-2- Schematic representation of OpenFOAM directory, folders (0, constant, system) and different files for laminar dam break simulation. Additional files in the RANS turbulent model represented with the dash line square

Table 5-1- Description of OpenFOAM main files (e.g. alpha.water, p_rgh, U etc.) from the OpenFOAM User Guide (Greenshields, 2015)

File Name	Description
alpha.water	Specifies the initial values of phase water and the associated boundary conditions.
p_rgh	Specifies the initial conditions of the fluid in terms of dynamic pressure and the associated boundary conditions.
U	Specifies the initial conditions of the fluid in terms of the velocity vector and the associated boundary conditions.
turbulenceProperties	Specifies the turbulence model.
transportProperties	Specifies the transport model.
g	Specifies gravitational acceleration.
polyMesh	A mesh is known in OpenFOAM as a polyMesh. The polyMesh description specifies the mesh faces, boundaries, assigned owner and neighbour cells, and points.
blockMeshDict	Specifies the basic blockMesh settings when the mesh is created using blockMesh.
controlDict	Specifies runtime control of the simulation. This dictionary can be changed while the simulation is running.
decomposeParDict	Specifies options to decompose a simulation into multiple mesh partitions for running in parallel.
fvSchemes	Specifies the interpolation and derivative approximation algorithms for each equation and field. This dictionary controls all the techniques needed to create a numerical approximation of a continuous mathematical function.
fvSolution	Specifies the solution algorithms for all the fields and equations contained within a simulation.
setFieldsDict	Specifies the initial condition for the volume fraction of the two fluids dividing the domain into two parts and giving different alpha values for each region.

In order to solve the Navier-Stokes equations OpenFOAM requires the initial conditions for each of the dependent variables found in the "0" folder to be specified, including: the water volume fraction α, the pressure, the velocity, and the turbulent variables for the turbulence models which will be described in detail later. As the focus here is the modelling of a dam break experiment, the system is initially at rest (Figure 5-3) and thus the initial values for pressure and velocity are set to zero. The water volume fraction α is a variable defined with values between 0 and 1 (air and water respectively), and therefore the water volume fraction in the reservoir is set to 1 (water) and the rest of the numerical domain to 0 (air).

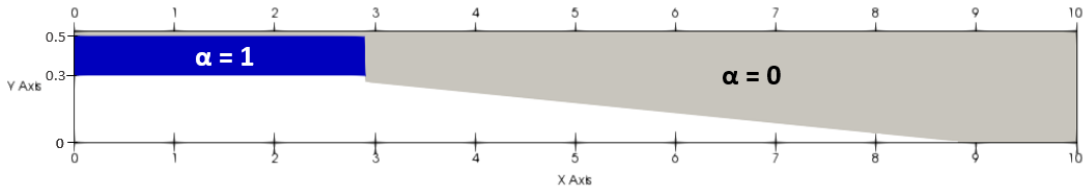

Figure 5-3- Side view of OpenFOAM dam break numerical simulation. Screenshot at t=0 s showing initial conditions. The water volume fraction α initial conditions are represented in where water in the reservoir is represented in blue (α=1) and air on the rest of the domain in grey (α=0).

5.2.4 Modelling of turbulence in OpenFOAM

Turbulent flow was defined by Lesieur (1994) as flow *characterised by unpredictable behaviour*. Pope (2000) further described turbulent flow motions as unsteady, chaotic and random with a range of scales apparent (from small bubbles to large eddies). The main difference with laminar flow is that particles in laminar flows move along smooth layers instead of irregular paths and are governed by Newton's law of viscosity (Chanson, 2004b).

Researchers generally agree that the requirements for turbulent flow include three-dimensionality, unsteady flow, strong vorticity and unpredictability (Ferziger, 1999). Even though 2D turbulent flows exist (e.g. large-scale geophysical flows), the turbulent flows considered in hydraulic engineering are always fully three-dimensional and unsteady. Furthermore, turbulent flows fluctuate in time and length scales. Their development is unpredictable and they typically contain different areas of high and low vorticity (Ferziger, 1999). However, turbulence is not only described by randomness, coherent structures do exist in turbulent flows. The difficulty in their accurate description appears, as within the same flow those structures are in general similar but not identical and their appearance is not regular (Ferziger, 1999). When flow is considered to be fully turbulent, it reaches an equilibrium state where the rate at which turbulence is produced and transformed is in

equilibrium (Ferziger, 1999). The most common way of predicting turbulent flows is through numerical simulations solving the Reynolds averaged Navier-Stokes equations (Equation 5-6) during which the flow variables (such as velocity u) are decomposed into the mean flow and its turbulent fluctuations $u(x,t) = \bar{u}(x,t) + u'(x,t)$. This is called Reynold's decomposition (Pope, 1985; Ferziger, 1999; Sánchez-Cordero et al., 2017).

The Reynolds-averaged simulation (RAS) model was selected here to represent the turbulence in the simulation which solves the Navier Stokes Equations incorporating the Reynold's decomposition of the velocity. The RANS model, is a computationally efficient turbulence model and is one of the most popular turbulence models due to its simplicity and enhanced performance for flows with separation zones (Lopes et al., 2012; Sánchez-Cordero et al., 2017). Even though it is robust, it has been shown that it performs well in small scale dam break applications but would not be applicable for larger scale simulations (Biscarini et al., 2009).

In the aforementioned modelling, the standard k-ε RANS model was selected. It is a two equation model that uses a transport equation and solves for the kinetic energy k (Equation 5-10) and turbulent dissipation ε (Equation 5-11) (Furbo, 2010; Sánchez-Cordero et al., 2017) which is the rate at which the energy created from turbulence is dissipated (Greenshields, 2015). The transport equations are Equation 5-10 and Equation 5-11 show that the rate of change of k or ε respectively, is equal to the transport of k or ε by diffusion plus the transport of k or ε by convection minus the rate of destruction of k or ε (Launder and Spalding, 1974):

$$\frac{Dk}{Dt} = \frac{1}{\rho}\frac{\partial}{\partial x_k}\left[\frac{\mu_t}{\sigma_k}\frac{\partial k}{\partial x_k}\right] + \frac{\mu_t}{\rho}\left(\frac{\partial U_i}{\partial x_k} + \frac{\partial U_k}{\partial x_i}\right)\frac{\partial U_i}{\partial x_k} - \varepsilon \qquad \textit{Equation 5-10}$$

$$\frac{D\varepsilon}{Dt} = \frac{1}{\rho}\frac{\partial}{\partial x_k}\left[\frac{\mu_t}{\sigma_\varepsilon}\frac{\partial \varepsilon}{\partial x_k}\right] + \frac{C_1\mu_t}{\rho}\frac{\varepsilon}{k}\left(\frac{\partial U_i}{\partial x_k} + \frac{\partial U_k}{\partial x_i}\right)\frac{\partial U_i}{\partial x_k} - C_2\frac{\varepsilon^2}{k} \qquad \textit{Equation 5-11}$$

Where: C_μ, C_1, C_2, σ_k, and σ_ε are empirical constants. $C_1 = 1.44$, $C_2 = 1.92$, $\sigma_k = 1.0$, and $\sigma_\varepsilon = 1.3$. The term μ_t in Equation 5-10 and Equation 5-11 represents the eddy viscosity and is calculated as shown in Equation 5-12 where C_μ is an empirical constant equal to 0.09 (Launder and Spalding, 1974).

$$\mu_t = \rho C_\mu \frac{k^2}{\varepsilon} \qquad \textit{Equation 5-12}$$

The eddy viscosity is a modelling term first introduced by Boussinesq (1877) and describes a scalar quantity which represents the energy extracted from the mean flow and transferred to the turbulent eddies (Olivari and Benocci, 2014). It is a property of the flow rather than a property of the fluid and is a way of relating the Reynolds stresses (the component of total stress accounting for turbulence) to the flow velocity gradients (Jenkins, 2013). The term μ_t, describes the properties of the flow rather than physical fluid properties and thus represents the macroscopic behavior of the turbulent flow (Olivari and Benocci, 2014). Cushman-Roisin (1974) in his book on Environmental Fluid Dynamics, presents Figure 5-4 which represents the process of turbulent energy cascade. This process describes the interaction between the eddies transferring energy from the larger to the smaller ones. The graph in Figure 5-4 shows three main things. First, that if the intensity of the turbulence is steady, then the rate at which the energy is passed on to the larger eddies (d_{max}) is equal to the rate that the energy is dissipated at the smaller eddies (d_{min}). Secondly, it shows that the eddies of the larger diameter have the highest velocities and thus the highest kinetic energy (Cushman-Roisin, 1974). Lastly, it shows that the energy supplied by external forces to the larger d_{max} eddies is transferred to the smaller eddies till it reaches the smallest d_{min} eddies where it is dissipated by the viscous forces (Cushman-Roisin, 1974).

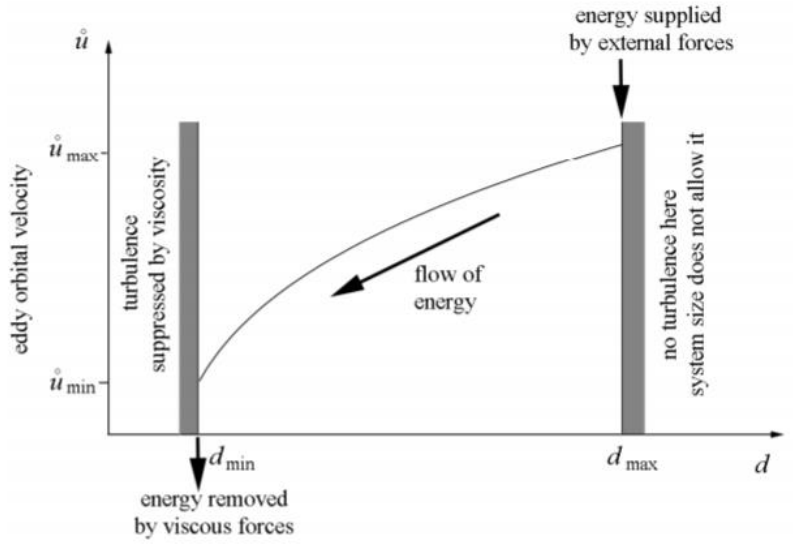

Figure 5-4- Graph representing the turbulent energy cascade process. Eddy orbital velocity is plotted against eddy diameter and shows that the energy supplied by external forces to the large eddies is transferred to the smaller eddies until it is dissipated by the viscous forces It is plotted in an (x,y) coordinate system where the x-axis represents the eddy diameter d and the y-axis the eddy orbital velocity u (Cushman-Roisin, 1974)

The scientific literature was found to contain very limited guidance on the choice and calculation of k and epsilon. Therefore, the RANS model was tested with different combinations of k and ε (and as a result μ_t) to find the best match to the experimental results. This will be further discussed in section 5.4.1. Through the search of the experimental eddy viscosity, the final selected values were $k = 0.2$ and $\varepsilon = 0.2$, resulting in an eddy viscosity of $\mu_t = 18\ m/s^2$, higher than OpenFOAM's default settings ($k = 0.1$, $\varepsilon = 0.1$, $\mu_t = 9$). A higher eddy viscosity μ_t means more energy is transferred to the eddies.

5.2.5 Validation of 2D and 3D OpenFOAM model

In order to validate the standard OpenFOAM numerical models (before changing any parametrisation of the simulations), both the 2D and 3D models were validated using known benchmark cases.

5.2.5.1 Validation of 2D OpenFOAM model

The dam break flow experiment performed by Soares-Frazão (2007) as part of the IMPACT project was selected as a relevant benchmark 2D case against which to validate the OpenFOAM software (Soares-Frazão, 2007). The experiment was performed in a horizontal rectangular flume with glass walks, a width of $0.5\ m$ and a length of $5.6\ m$ where a triangular sill of $0.065\ m$ height was positioned at distance $x = 1.61\ m$ from the reservoir. The water level in the reservoir upstream was $0.111\ m$, the bed was dry until the sill and downstream of the sill the water was at rest with a depth of $0.02\ m$. The experimental set up is shown in Figure 5-5 and the gauge positions are presented in Figure 5-6 (Soares-Frazão, 2007).

The OpenFOAM model was run for $40\ s$ using a uniform $0.001\ m$ mesh on a horizontal smooth bed. The comparison of the water depth evolution between experimental and numerical results was plotted for gauge 3 (Figure 5-7) which provided very good agreement to the experimental results. The computational time required for the simulation was 6 hours and was run in parallel on 16 distributed processors.

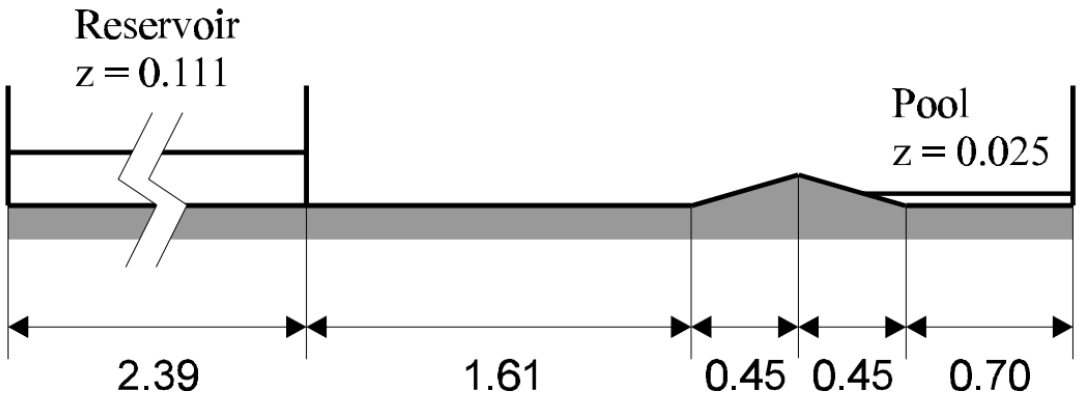

Figure 5-5- Side view of Soares-Frazão (2007) dam break experimental setup. It is a benchmark part of the IMPACT project and represents a dam break experiment over a triangular sill. A reservoir is located on the upstream end with a water depth z=0.111 and a gate separates it from the rest of the channel. The channel after the gate is horizontal and dry and a triangular 0.065 m high bump is located downstream. The downstream boundary is closed with a wall and between the triangular sill and the downstream wall a pool of z=0.025 is contained. In the drawing all units are in metres. (Soares-Frazão, 2007).

Gauge Number	Distance x (m)
Gauge 1	5.575
Gauge 2	4.925
Gauge 3	3.935

Figure 5-6- Gauge locations G1-G3 of Soares-Frazão's (2007) experimental set up (Soares-Frazão, 2007)

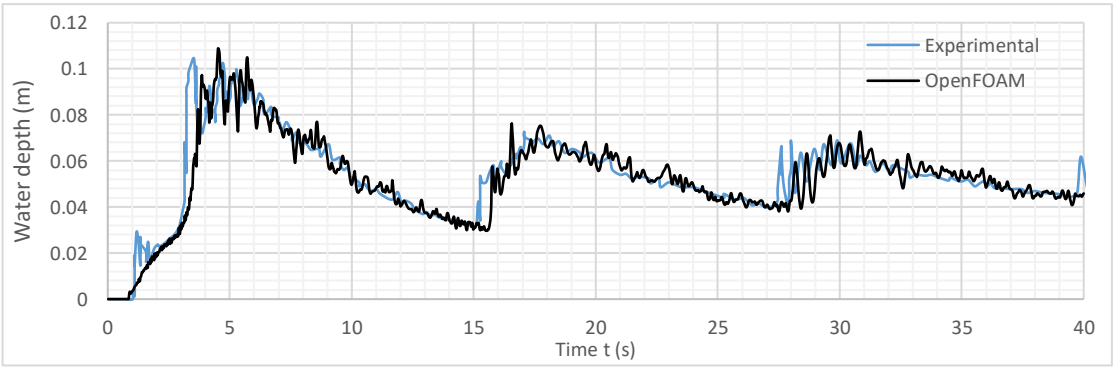

Figure 5-7- Validation of OpenFOAM with water depth propagation over time at Gauge 3. Blue line presents Soares-Frazão's (2007) experimental results and the black line the numerical OpenFOAM results

Thus, the standard 2D OpenFOAM dam break model was considered to be validated for this simple case considering the good agreement between the experimental and numerical results. When OpenFOAM will be used to model the experiment presented in Chapter 4,

further parametrisation will be investigated and a convergence analysis will be undertaken to match the more complicated dynamics of a dam break on a sloping channel.

5.2.5.2 Validation of 3D OpenFOAM model

Next, a 3D case was implemented to validate the ability of OpenFOAM to represent complex 3D flow occurring during a dam break. Marrone et al (2011) presented a dam break flow case against a tall structure using a δ-SPH smoothed particle model with diffusive terms which runs on the assumption that any fluid can be considered slightly compressible. They were particularly interested in the load acting on the vertical structure and compared their simulation results with measurements from an experiment conducted at the University of Washington (Marrone et al., 2011). The experimental set up is shown in Figure 5-8. The flume was horizontal, $1.6\ m$ in length and $0.6\ m$ in width and the reservoir was $0.3\ m$ in length, $0.6\ m$ in width and $0.3\ m$ depth. The downstream boundary was closed and vertical structure with dimensions 0.12 x 0.12 x $0.75\ m$ was located $0.5\ m$ from the reservoir.

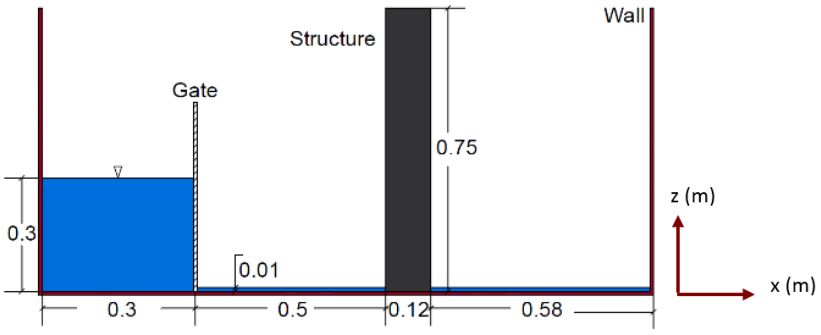

Figure 5-8- Experimental set up of Marrone et al. (2011) 3D case. The setup represents a dam break experiment in a closed box with a structure located at x=0.5 m from the gate.

Three different mesh sizes were used in OpenFOAM when modelling the dam break: a coarse mesh $0.03\ m$, a fine mesh $0.0125\ m$ and a finer mesh $0.005\ m$. The results are plotted in Figure 5-10 and compared against both the δ-SPH model results and the experimental data. Figure 5-9 shows the numerical simulation with the finer mesh ($0.005\ m$) for $t = 0.65\ s$ when the water has hit the structure and reached the right wall. The simulations were run in parallel on 16 distributed processors and the computational time required for the

simulations was 7 $minutes$ for the coarse mesh (148886 points), 2.1 $hours$ for the fine mesh (1124154 points) and 3.2 $hours$ for the finest mesh (2660620 points).

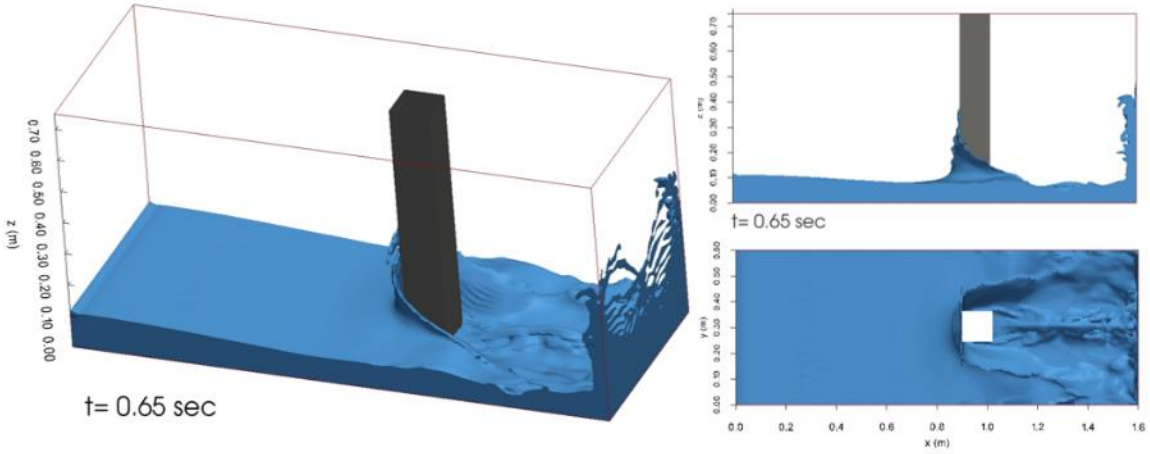

Figure 5-9- OpenFOAM numerical simulation (finer mesh 0.005 m) at t=0.65 s in a side view (top right), top view (bottom view) and axonometric view (left)

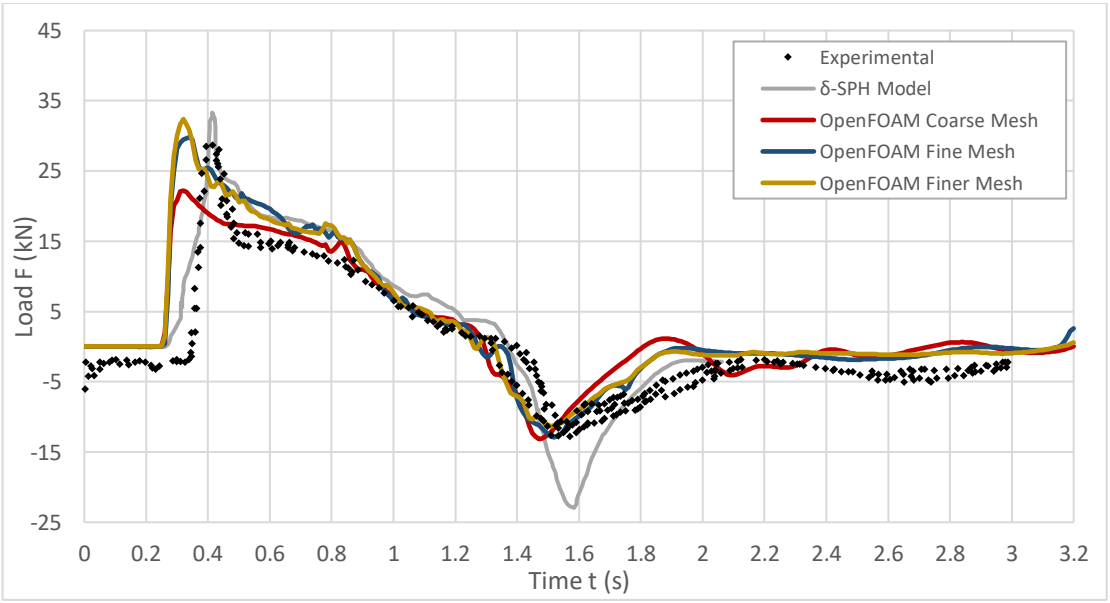

Figure 5-10- Validation of OpenFOAM model. Time history of load on upstream side of the building for 3D OpenFOAM simulation

The gate is released at $t = 0\ s$ and what is first observed from the results is that there is a delay in the first peak of the experimental and δ-SPH model results compared to the OpenFOAM results. This delay is attributed to the gate opening in the physical experiments

which is not as instantons as in the numerical simulation and the δ-SPH model results have been offset by the authors to match the experimental results. Even though the opening of the gate is an action that is considered instant, it does have an effect on short timescales ($0.1\ s$). But in this case, the magnitude of the first impact is the most important aspect for the design and it can be seen that both the fine and finer mesh produce close approximations. The negative peak at $t = 1.5\ s$ is due to the reflected wave of the wall applying a negative load on the structure and it is very accurately predicted by all three mesh sizes.

Therefore, the standard 3D OpenFOAM dam break model was also validated showing reasonable agreement between the experimental and numerical results. It was shown that the mesh refinement showed considerable improvement in the representation of the peak water depth. In the next sections that OpenFOAM will be used to model the experiment from Chapter 4, this will be therefore further investigated through convergence analysis. Furthermore, in future numerical simulations, all results will be offset to take into account the delay from the gate opening.

5.3 METHODOLOGY OF NUMERICAL SIMULATIONS

In this section, the methodology followed for modelling flash floods in OpenFOAM using the experiment presented in Chapter 4 will be discussed. Figure 5-11. presents schematically the methods used for the numerical simulations.

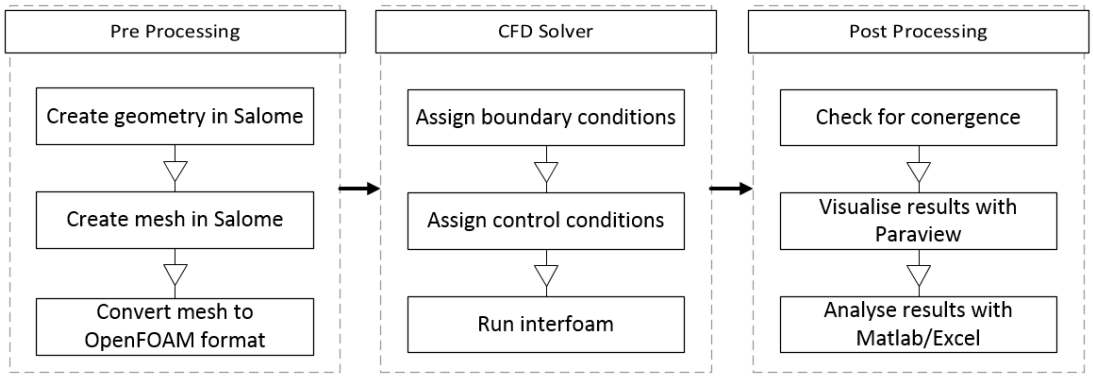

Figure 5-11- Methodology flow chart of numerical simulations divided in three stages: pre-processing, CFD solver and post-processing

The modelling is divided into three different stages: pre-processing, the CFD solver and post-processing. First, the geometrical model and uniform rectangular mesh were generated using Salome, an open-source software used to create geometrical models for numerical simulations. Next, the mesh generated in Salome was converted into an OpenFOAM format using the build-in 'ideasUnvToFoam' module. In the next stage (Computational Fluid Dynamic CFD Solver) the initial conditions, boundary conditions and control conditions were specified for the numerical simulation. In the post processing stage, the model outputs (water depth evolution) were checked for convergence and visualised using Paraview. The analysis and comparison between the different cases were achieved using Matlab and Microsoft Excel.

5.3.1 Specifying boundary conditions

Assigning boundary conditions is an important part of the CFD modelling process. The boundary condition at the inlet of the numerical simulation, the bottom part of the reservoir, the ramp, the urban settlement and the houses in the urban settlements were defined as 'walls'. The outlet and top of the numerical domain were set as open boundaries represented in OpenFOAM as 'patch' boundaries. The selected boundary conditions for the different test cases and models are showed in Table 5-2 and explanations of all defined boundary conditions can be found in Appendix C.1. It is important to note that the flow velocity is set to zero at the wall (no slip condition), and that this can result in underestimation of the flow velocity near the walls. As the experimental measuring locations were not near the walls but throughout the width of the setup, this will not affect the comparison of experimental and numerical results. Thus, making this an acceptable error for the scope of this work.

Table 5-2- Selected boundary conditions at inlet, outlet, top, bottom, sides in OpenFOAM's dam break simulation

Variable	Inlet	Outlet	Top	Bottom	Sides
alpha	type **zero Gradient**	type **inletOutlet** inletValue uniform 0 value uniform 0	type **inletOutlet** inletValue uniform 0 value uniform 0	type **zeroGradient**	type **empty**
U	type **noSlip**	type **pressureInlet OutletVelocity** value uniform(0 0 0)	type **pressureInlet OutletVelocity** value uniform(0 0 0)	type **noSlip**	type **empty**
p_rgh	type **fixedFlux Pressure** value uniform 0	type **totalPressure** p0 uniform 0	type **totalPressure** p0 uniform 0	type **fixedFlux Pressure** value uniform 0	type **empty**
k	type **kqRWall Function** value uniform 0.2	type **inletOutlet** inletValue uniform 0.2 value uniform 0.2	type **inletOutlet** inletValue uniform 0.2 value uniform 0.2	type **kqRWall Function** value uniform 0.2	type **empty**
epsilon	type **epsilonWall Function** value uniform 0.2	type **inletOutlet** inletValue uniform 0.2 value uniform 0.2	type **inletOutlet** inletValue uniform 0.2 value uniform 0.2	type **epsilonWall Function** value uniform 0.2	type **empty**
nut	type **nutkWall Function** value uniform 0	**type** **calculated** value uniform 0	**type** **calculated** value uniform 0	type **nutkWall Function** value uniform 0 **H100G/H200G** type **nutkRough Wall Function;** Ks uniform 0.00086 Cs uniform 0.5 value $internal Field	type **empty**
nuTilda	type **zeroGradient**	type **inletOutlet** inletValue uniform 0 value uniform 0	type **inletOutlet** inletValue uniform 0 value uniform 0	type **zeroGradient**	type **empty**

5.3.2 Application of surface roughness in OpenFOAM

As described in Chapter 4, Manning's n coefficient is calculated using the Equation 5-13 where n is Manning's roughness coefficient, A is the cross-sectional area of the flow, Q is the flow rate, P is the wetted perimeter and S_o is the slope:

$$n = \frac{1}{Q} \cdot \frac{A^{5/3}}{P^{2/3}} \cdot S_o^{1/2} \qquad \textit{Equation 5-13}$$

In OpenFOAM, as there is no direct way to apply Manning's coefficient on the surfaces, the surface roughness is applied using a boundary condition called nutkRoughWallFunction. This is directly implemented on the boundary "slope" thus directly applying a surface roughness condition on the ramp of the numerical domain. The condition is based on the turbulent kinetic energy and directly applies a turbulent kinematic viscosity condition in this case on the surface of the ramp. This is achieved by controlling the ε parameter to resolve the roughness effects (Greenshields, 2015). To define the boundary condition, two parameters need to be established, the roughness height k_s and a roughness constant c_s. The roughness height k_s represents the equivalent sand-grain roughness and for smooth walls its value is set to 0. The roughness constant c_s can range from $0.5 - 1.0$ and in all cases it is set as default to 0.5 (Greenshields, 2015).

Overall research relating the roughness height k_s with Manning's coefficient n is very limited. That being said, Jayaratne (2010) presented an equation (Equation 5-14) connecting Manning's coefficient n with the surface roughness k_s measured in millimetres (Jayaratne, 2010).

$$n \approx 0.012(k_s)^{\frac{1}{6}} \qquad \textit{Equation 5-14}$$

In Chapter 4, Manning's coefficient was calculated to be 0.020 and using Equation 5-14 this was translated to a k_s value. When this was applied to the 2D simulations, the numerical results did not seem to provide good agreement with the experimental results. Thus, different values of k_s were tested in the numerical simulations showing that a value of $k_s = 0.0086\,m$ was found to provide the best representation of surface roughness for both H100G and H200G cases presented in Chapter 4. Thus, considering the experimental Manning's coefficient $n = 0.020$ and the modelled surface roughness $k_s = 0.0086$ Equation 5-14 was changed to a new equation (Equation 5-15) changing the constant in Jayaratne's (2010) equation from 0.012 to 0.020.

$$n \approx 0.020(k_s)^{\frac{1}{6}} \qquad \textit{Equation 5-15}$$

The newly developed equation seemed to provide a much better agreement relating the roughness height k_s with Manning's coefficient n for the examined case, but further investigation of this equation is suggested by modelling different dam break experiments with known Manning's coefficients and examining in more depth the connection to the roughness height k_s.

5.3.3 Coupling of 2D and 3D OpenFOAM models

2D dam break modelling in OpenFOAM is limiting due to the fact that it only allows a simulation of such events modelling the longitudinal variation of water depth evolution. Therefore, when obstructions (e.g. buildings) are modelled, this results in a blockage in the x-direction and thus overestimates water depths, loads and velocities (see setup in Figure 5-3). Thus, this raised the need for the creation of a coupled 2D-3D model as it provides a unique possibility to efficiently and robustly model flood simulations whilst taking into account the three-dimensionality of the event.

After selecting a mesh size, two models are created to be ran separately. One 2D model of the reservoir and ramp (up to $x = 6\ m$) and one 3D model of the urban settlement (from $x = 6\ m$). First, the initial conditions are set for the 2D numerical model and the simulation is ran with an open boundary condition at the downstream boundary. Then, when post-processing the results, the velocity timeseries at the downstream boundary ($x = 6\ m$) is exported and saved in a .csv file. Following this, the new conditions are assigned to the 3D simulation which uses the velocity .csv file as input at the upstream boundary ($x = 6\ m$). The velocity initial condition file (Appendix C.2) translates the velocity timeseries from 2D to 3D along the flume's width and interpolates any additional values needed. Finally, when the simulation begins, the other initial conditions at the inlet are calculated from the velocity and the simulation continues. The described methodology is presented schematically in Figure 5-12 and the code used in the velocity U and water volume phase alpha files is presented in Appendix C.2

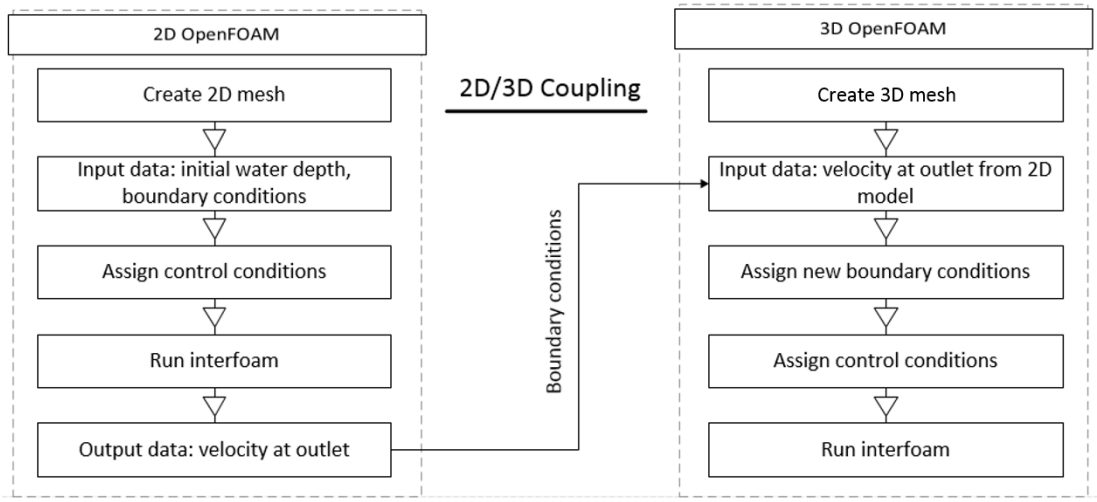

Figure 5-12- Methodology flow chart representing the 2D/3D coupling at the bottom of the ramp at x=6

5.4 MODEL SELECTION AND PARAMETRISATION

Both laminar and turbulent OpenFOAM models were used to compute the dam break surge of the B0_H100 and B0_H200 cases. For both cases, the numerically simulated water depth evolutions were compared with the experimental results only at U2 and U3, as U1 is very strongly affected experimentally by the gate opening. First a turbulence model was selected and after a sensitivity analysis for different mesh sizes, mesh R25 was selected, representative of a uniformly rectangular $0.00025\ m$ mesh, and was tested for different Courant numbers. Courant number is a dimensionless number defined as $Co = U \cdot \Delta t/\Delta x$, where U is the average velocity, Δt is the timestep and Δx is the mesh in the flow direction. In OpenFOAM simulations are controlled by maintaining the Courant condition using an adaptive time step to satisfy the maxCo requirement, which ensures the stability of the simulation. As for part of the experiment, the flow on the ramp is more streamlined, a laminar model was also tested for two different Courant numbers to investigate whether it could provide an accurate representation of the flow. The model parametrisation for both the RANS turbulence model and the Laminar will be presented, and finally a combination of the turbulent and laminar model is discussed.

5.4.1 Model parametrisation of RANS turbulence model

First a RANS turbulence model was examined. The sensitivity of the model to the mesh size was assessed by creating four different meshes: $R100 = 0.01$, $R50 = 0.005m$, $R25 = 0.0025m$ and $R12.5 = 0.00125m$. These meshes were tested and R25 was selected to be

the best mesh for the representation of this experiment taking into account accuracy, computation time and convergence with the finer meshes. Following that, a Courant number sensitivity was performed investigating six different maximum Courant number *maxCo* criteria ranging from $Co = 0.1$ to $Co = 1.0$. All test cases with their relevant timestep and computation time are presented in Table 5-3. The simulated water depth evolution was compared with the experimental results for all of these cases (Figure 5-13) and case $R25\_C0.2$ was selected as the most converged solution as it seemed to capture best the peak water depth. This is in agreement with Berberovic et al. (2009) who states that for open channel supercritical flow simulations, the Courant number criteria should be always set to less than 0.2. For reference the computation time for $R12.5\_C0.2$ was 163:41:6 which is very impractical. Simulations were ran on the University of Bath's High Performance Computer (HPC) using 16-cores in parallel.

Table 5-3- OpenFOAM test cases assessing Courant number sensitivity to water depth results. Simulations ran on the University of Bath's High Performance Computer HPC in 16-cores in parallel

Test Case	Mesh Size [mm]	Time Step [s]	Courant Number	Computation Time
R25_C1.0	0.0025	0.00064	1.0	03:37:58
R25_C0.6	0.0025	0.00038	0.6	15:42:09
R25_C0.4	0.0025	0.00025	0.4	20:52:11
R25_C0.3	0.0025	0.00019	0.3	n/a
R25_C0.2	0.0025	0.00013	0.2	31:43:08
R25_C0.1	0.0025	0.00006	0.1	48:35:43

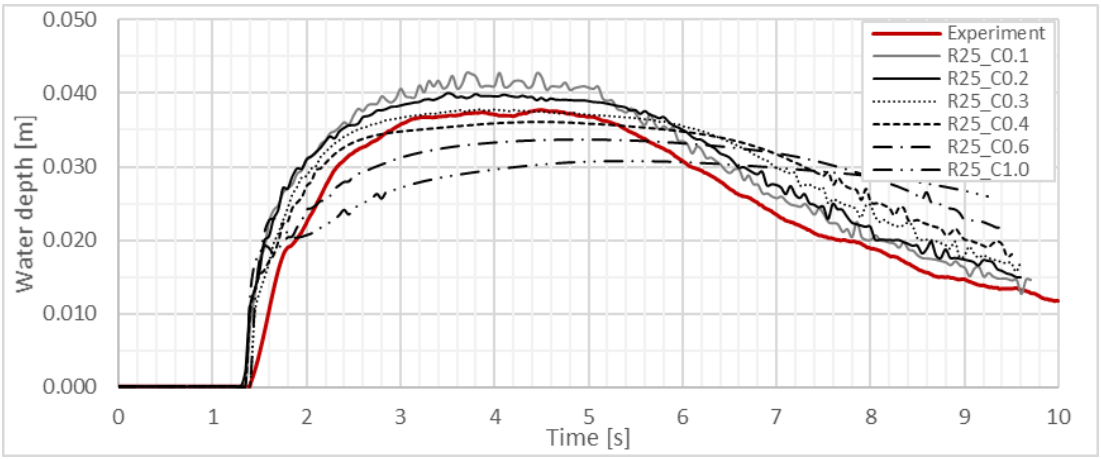

Figure 5-13- Water depth evolution at U2 for the H200 case comparing the experimental results (red line) with the different Courant number simulations presented in Table 5.3 (C0.1, C0.2, C0.3, C0.4, C0.6 and C1.0)

After having selected $R25\_C0.2$ as the desired mesh and Courant number, different turbulence parameters were tested (Table 5-4). Ten different test cases were assessed by changing the parameters k and ε and calculating μ_t for all cases using Equation 5-12. The turbulence parameters were evaluated are presented in Table 5-4.

Table 5-4- OpenFOAM test cases with R25 mesh and C0.2 Courant number. Table summarises different turbulence parameter combinations of k and ε and the resulting calculated μ_t from Equation 5-12

Test	k	ε	μ_t
1	0.1	0.1	9
2	0.01	0.01	9
3	0.001	0.001	9
4	0.0001	0.0001	9
5	0.2	0.2	18
6	0.316	0.5	18
7	0.255	0.255	23
8	0.3	0.3	27
9	0.5	0.5	45
10	1.0	1.0	90

Figure 5-14 shows the comparison of experimental results with different test cases to assess the sensitivity of turbulence parameters at location U2 for the H200 case. It is important to note that the simulation parameters were also validated in location U3 and the results showed both temporal and spatial agreement but for the scope of this chapter only the results at U2 will be presented. Three different cases with a resulting $\mu_t = 9$ show very little difference in the results and following this, the μ_t value was increased in order to obtain a better match with the experimental results. It was found that $\mu_t = 18$ provided the closest agreement for the representation of the water depth peak in the experimental results with $k = 0.2$ and $\varepsilon = 0.2$.

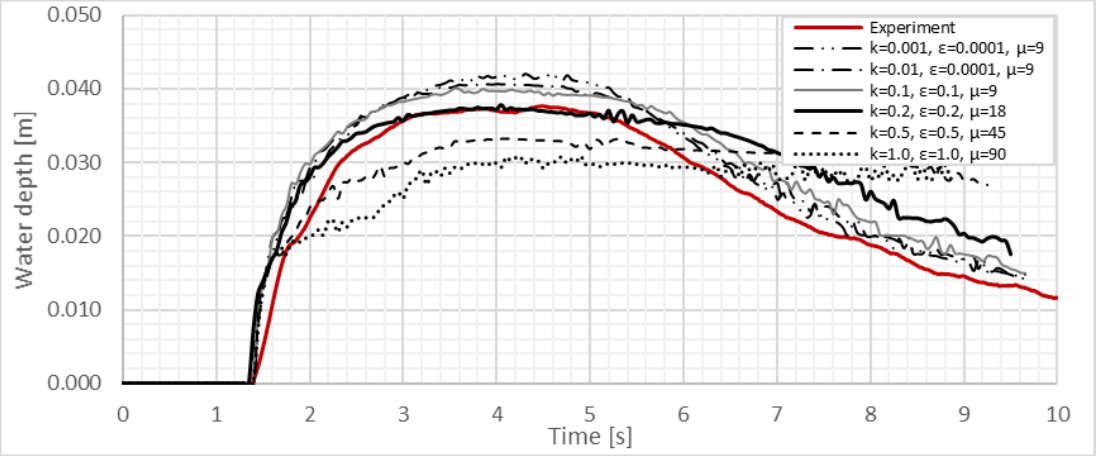

Figure 5-14- Water depth evolution at U2 for the H200 case comparing the experimental results (red line) with the R25_C0.2 (mesh 0.0025 m and Courant number 0.2) for different turbulence parameter summarised in Table 5.4

The above analysis suggests that especially for modelling the rising limb of the water depth and obtaining an accurate representation of the maximum depth, the parametrisation of such events is complex due to the range of specifications and variable factors. As there appears to be little guidance in the literature what value of eddy viscosity to select for these events, further research is suggested in this direction to obtain more specific guidance.

5.4.2 Model parametrisation of laminar model

As at the later stages of the flow the flow can be described as a decaying quasi-steady flow, a Courant number sensitivity was also performed investigating two different *maxCo* criteria $Co = 0.2$ and 0.3 for a laminar model. The two cases and their parametrisation are presented in Table 5-5 and the water depth evolution comparison is shown in Figure 5-15. It can be seen from the figure that changing the Courant number condition in the laminar model has very little effect on the water depth evolution. Therefore, it showed that the solution has converged and does not depend upon the Courant condition.

Table 5-5- Test cases assessing Courant numbers for laminar test cases. Simulations ran on the University of Bath's High Performance Computer HPC in 16-cores in parallel

Test Case	Mesh Size [mm]	Time Step [s]	Courant Number	Computation Time
R25_C0.3_L	0.0025	0.00019	0.3	13:51:15
R25_C0.2_L	0.0025	0.00013	0.2	20:29:54

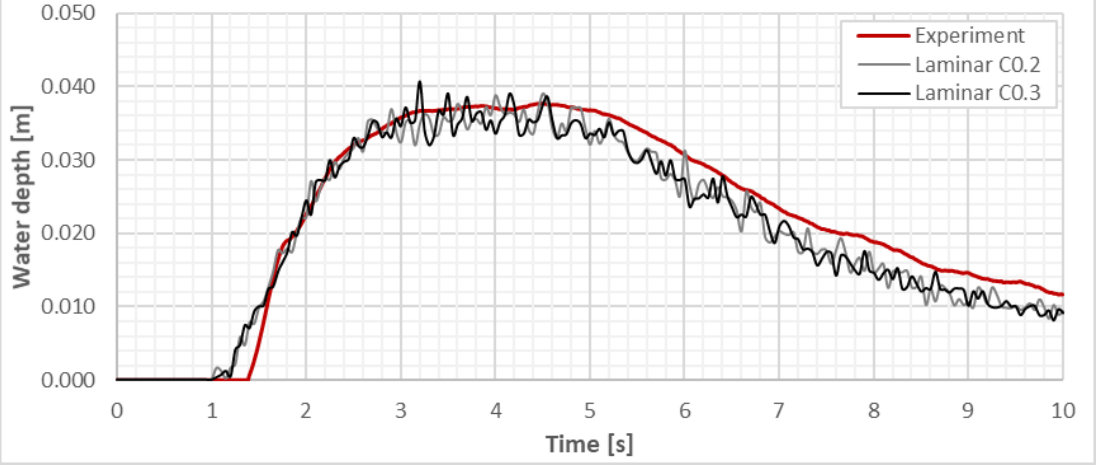

Figure 5-15- Water depth evolution at U2 (x=3.25 m) for the H200 case comparing the experimental results (red line) with two laminar test cases of different Courant numbers

In general, the laminar models provided reasonable agreement of the modelling of the 2D flow on the ramp. In both models (Fig 5.15) the gradient of the rising limb was not accurately represented and provided a more gradual increase to the maximum water depth, thus raising the need for a combination of the two models.

5.4.3 Combination of laminar and turbulence model

The two previous sections raised the need for a combined laminar and turbulence model depending on the flow characteristics of the dam break flow. This section will therefore present a combined turbulent and laminar model showing that the combined model provides a better fit to the experimental results than either of the individual models.

From the results in Figure 5-14 and Figure 5-15, it is seen that the each of the models (laminar and turbulent) provide better approximations either at the rising limb or the falling limb. The best representation of the first $3.5\ s$ and specifically the shape of the rising limb is provided by the turbulent $R25\_C0.2$ model where $k = 0.2$, $\varepsilon = 0.2$. From 3.5 to $10\ s$ the best

representation is found by the laminar $R25\_C0.2$ model as the turbulence model overpredicts the magnitude of the water depth evolution. Figure 5-16, shows the comparison of experimental results with the output from the turbulent and laminar models at location U2 for the H200 case. As previously described in Chapter 4, the flow on the ramp is characterised by two components: the propagation of the dam break wave and the formation of a uniform steady flow which becomes supercritical as it accelerates down the ramp towards the buildings. In the first few seconds from the gate release the flow is unstable and more turbulent but as it stabilises it becomes supercritical, but not turbulent, until it reaches the moment of interaction with the urban settlement. The effect of the gate opening is more pronounced in the first seconds until stabilisation is reached and thus the turbulence model represents the water depth evolution more precisely. For the first timesteps ($t > 3.5\,s$) of the flow on the sloping channel, however, the laminar model provides a better representation of the flow than the turbulence model.

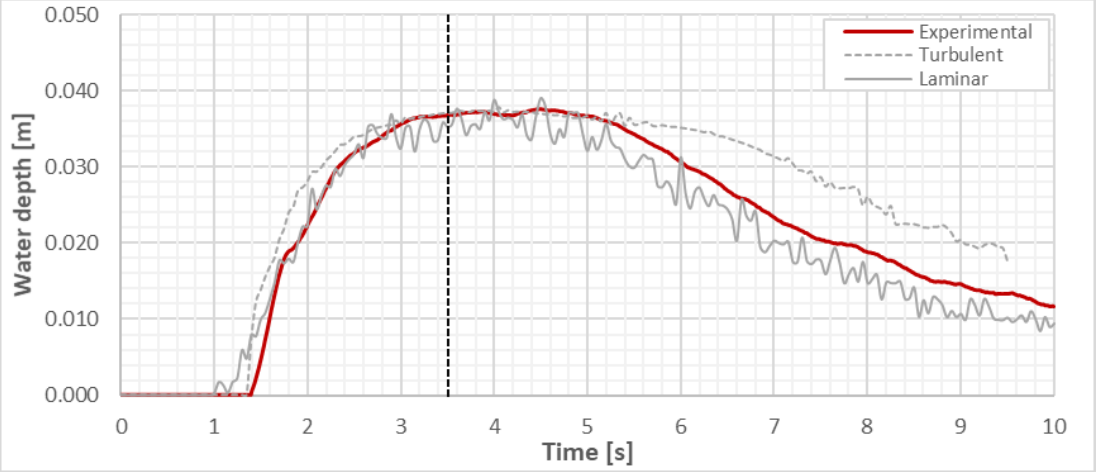

Figure 5-16- Comparison of experimental results with turbulent and laminar models at location U2 for the H200 case. The dashed black vertical line represents the point where the turbulence model represents best the rising limb and the laminar the falling limb.

A combination simulation was therefore run using output conditions of all variables (water depth, pressure and velocity) from the turbulence model at $3.5\,s$ as input conditions at the starting point of the laminar model. Even though the turbulent model represents well the shape of the water depth evolution up to $5\,s$, $t = 3.5\,s$ was selected to combine the two models in order to give the model some time to readjust before modelling the falling limb. As both simulations were ran using the same mesh size, the calculated values of alpha, U and pressure at all points at $t = 3.5\,s$ were used as initial conditions in the laminar model which

was run from 3.5 to $10\ s$. The result of the combination results is shown in Figure 5-17 and was selected as the model parametrisation for all H200 and H200G cases.

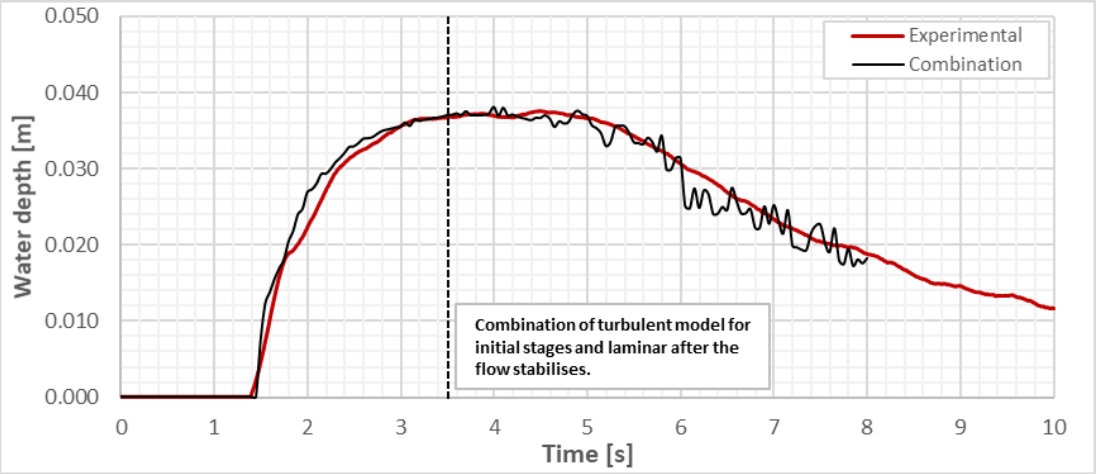

Figure 5-17- Comparison of experimental results with combination case at location U2 for the H200 case. Turbulence model used for the initial stages up to t=3.5 s and a laminar model up to t=10 s.

This combined output proves the complexity of these flows and the importance of correct parametrisation and analysis.

5.5 RESULTS AND ANALYSIS

5.5.1 Baseline test, B0_H100 case

The same baseline test case B0_H100 previously presented in Chapter 4, is now used for a comparison with the 2D OpenFOAM numerical simulations. As previously described, the case has an initial water depth in the reservoir of $0.1\ m$, no roughness layer and no building in the urban settlement are present in this experiment.

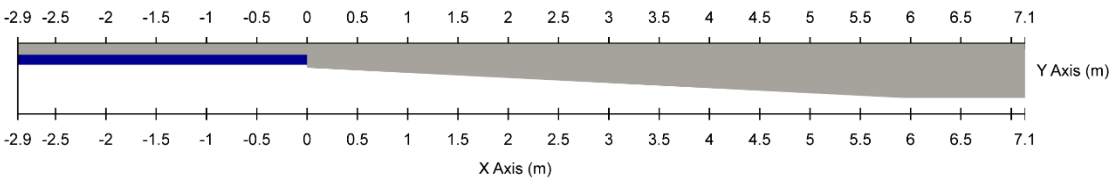

Figure 5-18- Side view of the 2D OpenFOAM setup where the blue colour represents the water in the reservoir and the gey the air

Figure 5-18 shows the OpenFOAM numerical set up for B0_H100 when the water in the reservoir is still at rest. In the figure, a side view of the experiment is shown where blue represents the water in the reservoir and grey the air. The numerical simulation presented here was parametrised as discussed in section 5.33 with a turbulent RANS model for the first $6.5\ s$ of the simulation, followed by a laminar model. Modelling the H100 and H100G cases, the combination time was chosen later than the $3.5\ s$ for H200 as the water is slower in the H100 and takes longer to reach the water depth peak. For both simulations the control conditions were the same: mesh of $R = 0.0025m$, Courant number of $Co = 0.2$, and timestep of $\Delta t = 0.00013s$. In the turbulence model the selected turbulence parameters were $k = 0.2$, $\varepsilon = 0.2$, $\mu_t = 18$.

Figure 5-19 shows the comparison of water depth between experimental and numerical results as a function of time for the three ultrasonic probes U1-U3 along the ramp. A good agreement is generally achieved between both experimental and numerical results for the three different locations (U1-U3). Moreover, from Figure 5-19 it can also be notice that the numerical predictions at location U1 do not simulate the first experimental peak at $0.6\ s$. As previously discussed, in Chapter 4, this failure is attributed to splashing from the gate opening and is an acceptable error for the numerical model.

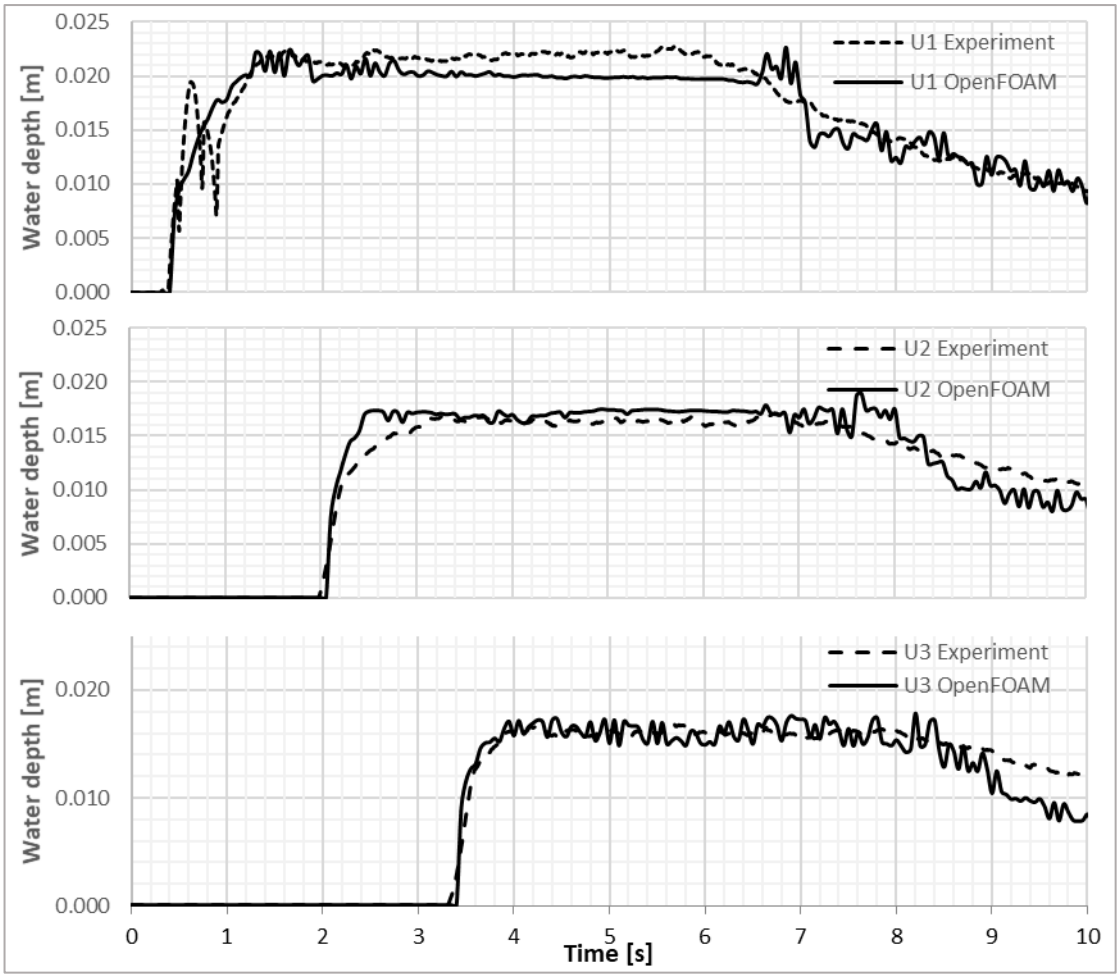

Figure 5-19- Timeseries of the water depth evolution along the ramp at (top) U1 (x=1 m), (middle) U2 (x=3.25 m) and (bottom) U3 (x=5.5 m) for H100. Comparison of experimental (dashed line) and 2D numerically simulated water depth (solid line)

5.5.2 2D Simulations

Figure 5-20 to Figure 5-22 show the comparison between experimental and simulated water depth results over time for the three ultrasonic probes U1-U3 along the ramp for H200, H100G and H200G, respectively. As before, it can be seen that a very good agreement is achieved between the model simulations and the experimental data at locations U2 and U3 and disparities are found at location U1, especially in Figure 5-20 and Figure 5-21, due to the opening of the gate and the time it takes to stabilise the flow.

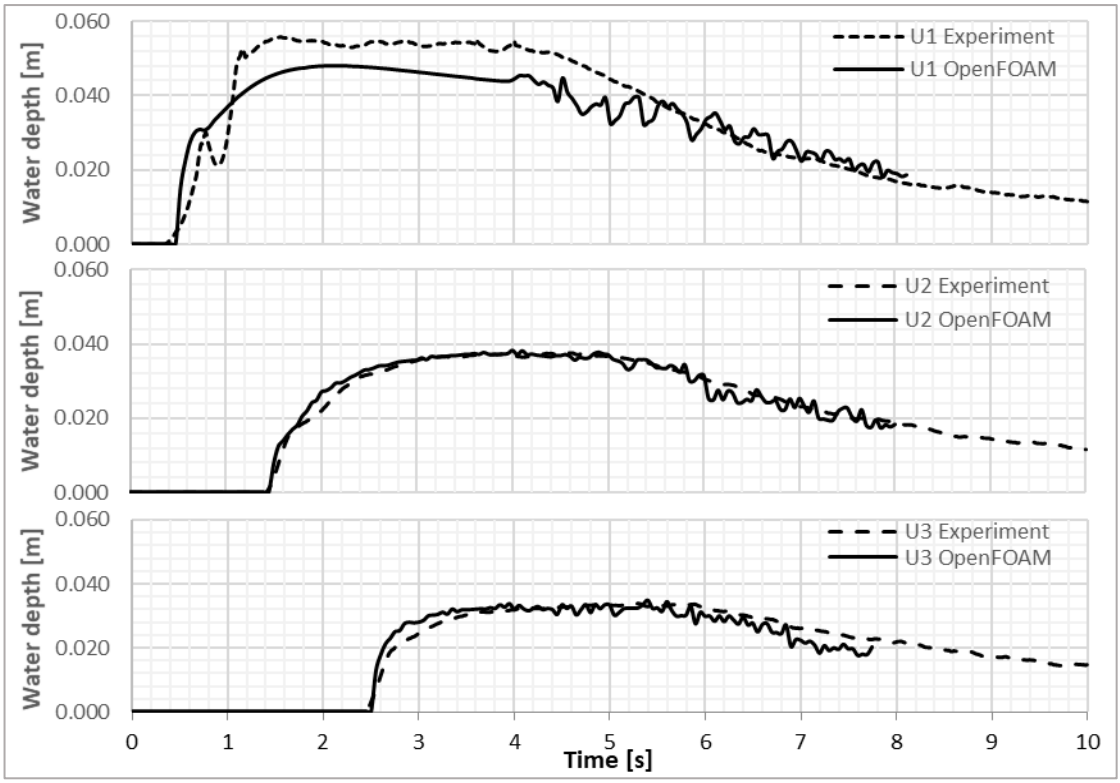

Figure 5-20- Timeseries of the water depth evolution along the ramp at (top) U1 (x=1 m), (middle) U2 (x=3.25 m) and (bottom) U3 (x=5.5 m) for H200. Comparison of experimental (dashed line) and 2D numerically simulated water depth (solid line)

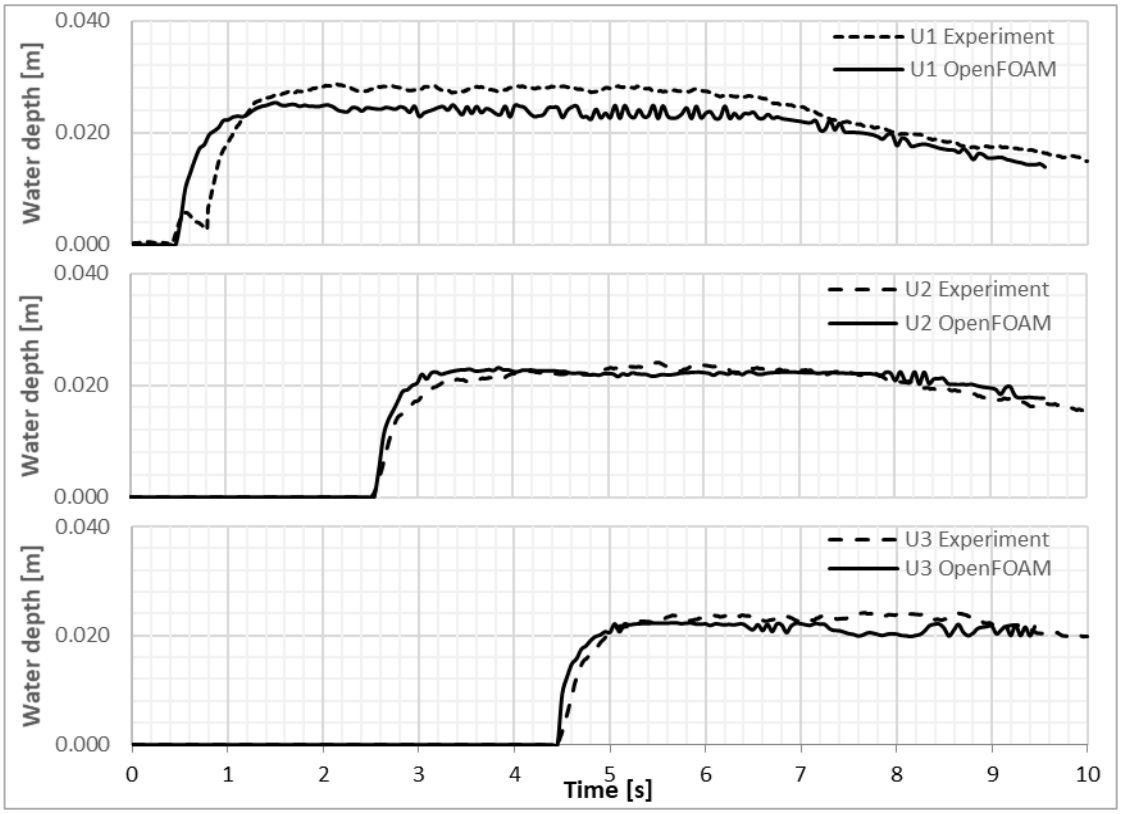

Figure 5-21- Timeseries of the water depth evolution along the ramp at (top) U1 (x=1 m), (middle) U2 (x=3.25 m) and (bottom) U3 (x=5.5 m) for H100G. Comparison of experimental (dashed line) and 2D numerically simulated water depth (solid line)

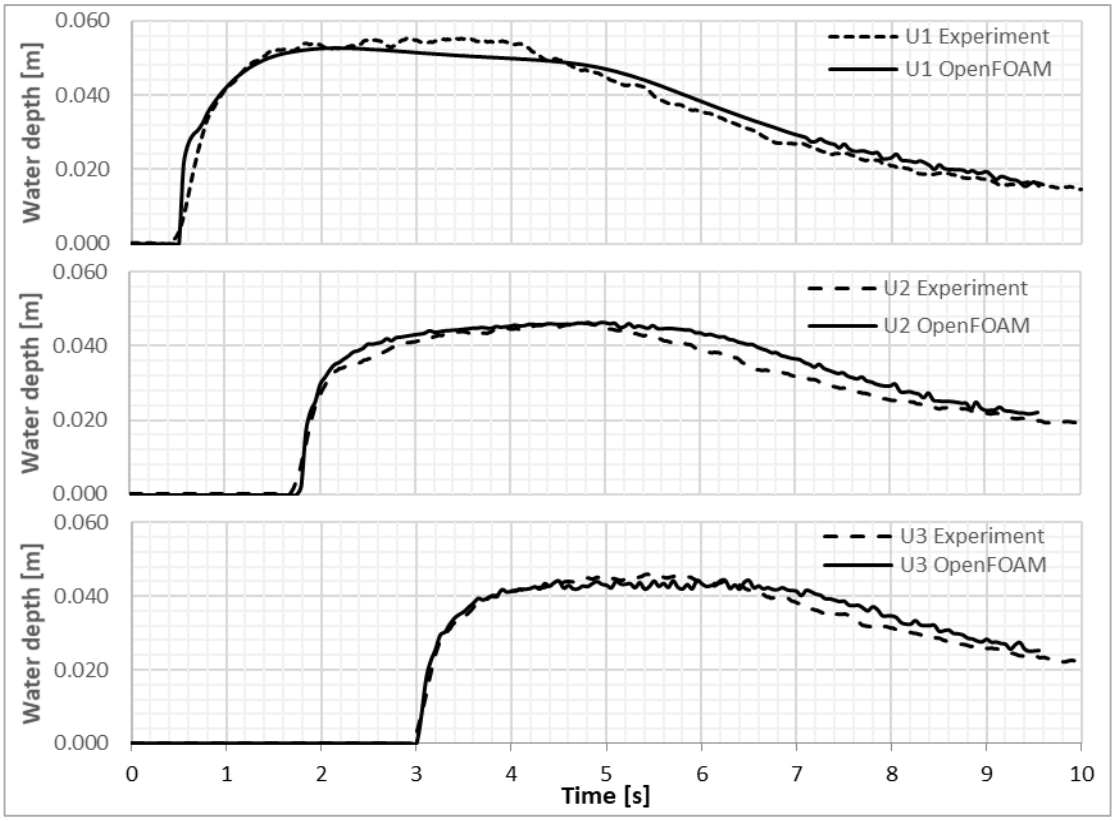

Figure 5-22- Timeseries of the water depth evolution along the ramp at (top) U1 (x=1 m), (middle) U2 (x=3.25 m) and (bottom) U3 (x=5.5 m) for H200G. Comparison of experimental (dashed line) and 2D numerically simulated water depth (solid line)

For simplicity, the most important 2D results are summarised in Table 5-6 where maximum water depths along the ramp in three different locations and maximum velocity and flow rate at the bottom of the ramp are compared for the four different test cases H100, H200, H100G and H200G.

Table 5-6- Summary of important 2D OpenFOAM results: Maximum water depths, velocities and flow rates were compared for the different H100, H200, H100G and H200G cases

		OpenFOAM 2D Test Cases			
Variables		**H100**	**H200**	**H100G**	**H200G**
Max Water Depth [m]	**U1**	0.023	0.048	0.025	0.053
	U2	0.019	0.038	0.023	0.046
	U3	0.018	0.035	0.022	0.044
Max Velocity [m/s]		2.564	2.890	1.211	1.755
Max Flow Rate [m^3/s]		0.053	0.110	0.032	0.090

In the 2D numerical simulations, using the combination of turbulent and laminar flow the model outputs were found to be provide a very good fit to the experimental results in all four cases. In terms of the numerical simulation, the application of a 2D OpenFOAM model has highlighted the sensitivity of the flow to the model's parametrisation, the two-dimensionality of the flow in this part of the experiment but has also shown that OpenFOAM is capable of simulating very accurately the supercritical flow on the ramp.

5.5.3 3D Simulations

While the dam break itself and the accelerated supercritical flow on the ramp described in the previous section were 2D in nature, and could be accurately approximated in a two-dimensional plane, as previously discussed in Chapter 4, modelling of the interactions between the urban settlement and the dam break wave requires three dimensions.

Even though the methodology of the coupled 2D-3D model (presented in section 5.33) was attempted in this case, due to the limited length of both the experiment and numerical domain ($10\ m$ in the x-direction), it was found that the computation time and cost was the same as for running a fully 3D case. Therefore, the 3D case results presented here are from a fully 3D model with a single building considering the whole experiment (Figure 5-23) with the previously determined optimal parameters for this case $R = 0.005m$ mesh-size, Courant number of $Co = 0.2$ and timestep of $dt = 0.00013s$.

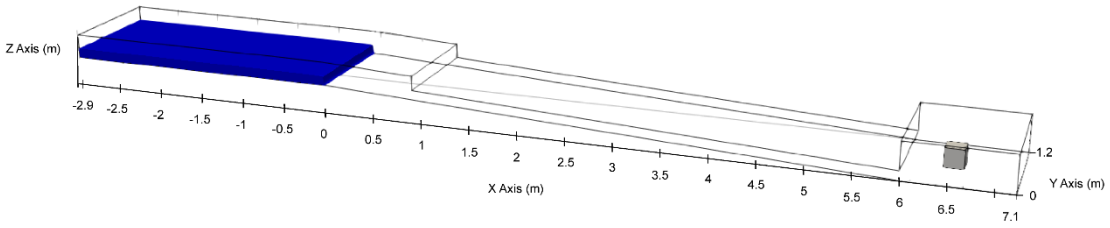

Figure 5-23- OpenFOAM 3D Numerical Setup. The blue rectangle represents the water in the reservoir and the grey cube the single building in the urban settlement

Figure 5-24 to Figure 5-27 show the evolution of the water depths in the urban settlement, comparing three different locations U5, U8 and U10 located at $x = 6.20\ m$, $x = 6.50\ m$ and $x = 6.80\ m$, respectively. Starting with Figure 5-25, all three locations (U5, U8 and U10) show a generally reasonable agreement between observed and simulated water depths; both in terms of magnitude and shape, except for the large peak in the experimental results at U5 which is not represented in the numerical simulation. The added roughness grass layer (H100G) on the ramp changes the results considerably. Comparing the experimental with the

numerical water depths in the same locations (Figure 5-26), U8 and U10 are accurately represented up to 7.5 s after which OpenFOAM overestimates the depths. At location U5 water depth is underestimated by OpenFOAM and once more the first peak is not apparent in the numerical simulation. This is probably due to the splash travelling through the sensor's footprint and thus the horizontal motion might stay apparent for longer in the measurements. It has been shown that when the flow field was highly turbulent and extensive splashing was occurring in the first impact, the ultrasonic sensor measurements were affected recording a higher experimental peak (Weber, 2003; Strunz et al., 2004). In effect, all the large peaks measured in the experimental results (Figure 5-24 to Figure 5-27) are indicative of areas where the flow was suddenly transitioned to highly turbulent (Figure 5-24 shows the hydraulic jump in front of the building (U5) and the turbulent areas/wake on the sides (U10) and at the back of the building (U8)) and thus are not explicitly included in the numerical simulations. Nevertheless, more research is suggested to further investigate these discrepancies.

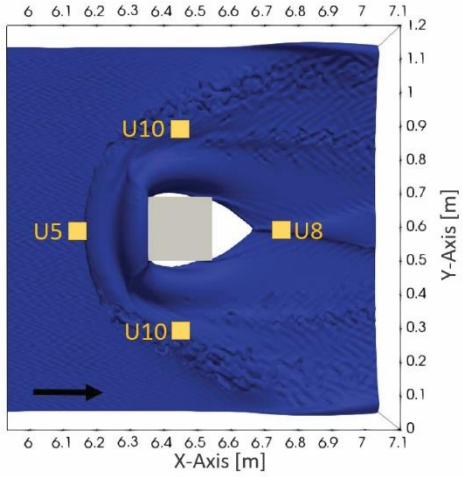

Figure 5-24- Numerical snapshot of water interaction with building in the H100 3D OpenFOAM simulation showing the U5, U8 and U10 locations. The black arrow represents the direction of the flow, the grey square shows the position of the building and the yellow squares show the ultrasonic sensor positions. A hydraulic jump is created in front of the building , propagating opposite to the direction of the flow towards U5.

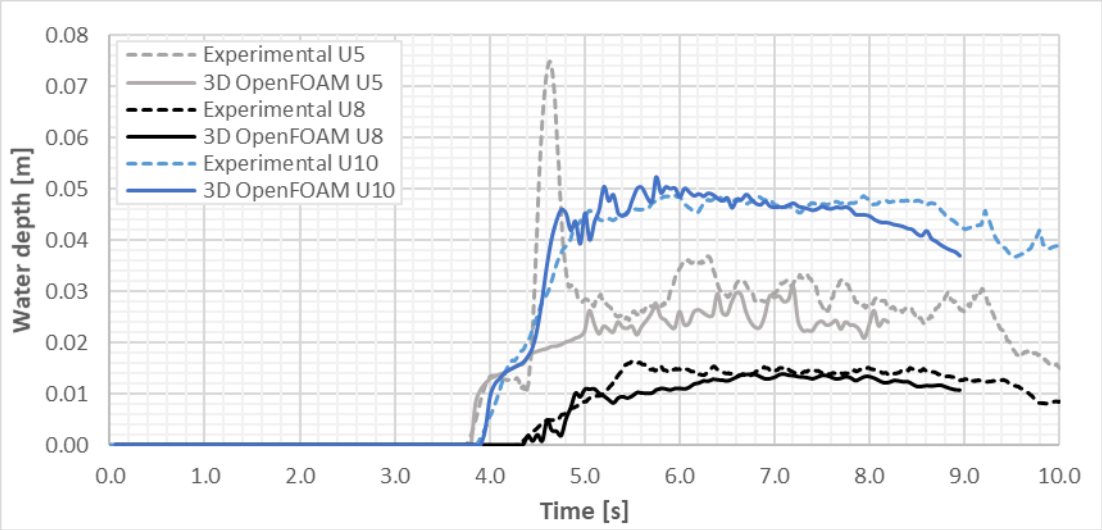

Figure 5-25- Timeseries of the water depth evolution along the ramp at U5 (x=6.2 m), U8 (x=6.5 m) and U10 (x=6.8 m) for H100. Comparison of observed (dashed line) and simulated (solid line) water depths at U5 (grey), U8 (black) and U10 (blue). The dashed grey peak water depth at U5 is a splash.

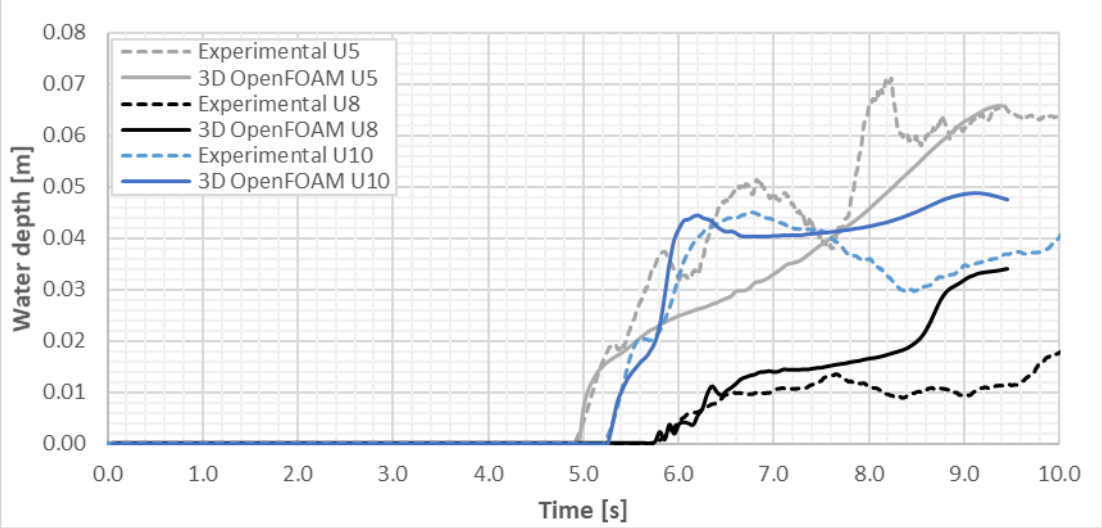

Figure 5-26- Timeseries of the water depth evolution along the ramp at U5 (x=6.2 m), U8 (x=6.5 m) and U10 (x=6.8 m) for H100G. Comparison of observed (dashed line) and simulated (solid line) water depths at U5 (grey), U8 (black) and U10 (blue).

The water depths for the H200 case at locations U5, U8 and U10 are shown in Figure 5-27. For this case there are no U5 experimental measurements (due to hardware failure during the experiments) so no comparison can be made at this location. At location U8 the observed water depths are accurately represented by the numerical simulations, if slightly overestimated by OpenFOAM. At location U10 the numerical simulations fail to represent the observed peak at $t = 3.5\ s$ thus leading to a numerical underestimation. In reality, this water depth was again extremely turbulent and thus for the aforementioned reasons likely

overestimated by the ultrasonic sensors. The corresponding results when adding the grass layer (H200G) are shown in Figure 5-28. Here the peak in water depth observed at U10 is not represented in the model outputs from OpenFOAM. The results at U8 show a generally reasonable agreement between observations and model simulations, even though the model slightly overestimated. Finally, the observed water depth at U5 is underestimated by 50% for the majority of the simulation. Possible reasons for this include: (i) mesh size of OpenFOAM simulation, (ii) measuring of highest point of the turbulent area in experimental results, (iii) different turbulence parameters to capture the eddies more accurately or (iv) different numerical scheme required to model the more complex dynamic features of the flow (hydraulic jumps, cross waves). Another conclusion that may be drawn is that in general OpenFOAM showed closer agreement in the simple cases without a roughness layer (H100 and H200, Figure 5-25 and Figure 5-27) in contrast to the roughness layer cases (H100G and H200G, Figure 5-26 and Figure 5-28).

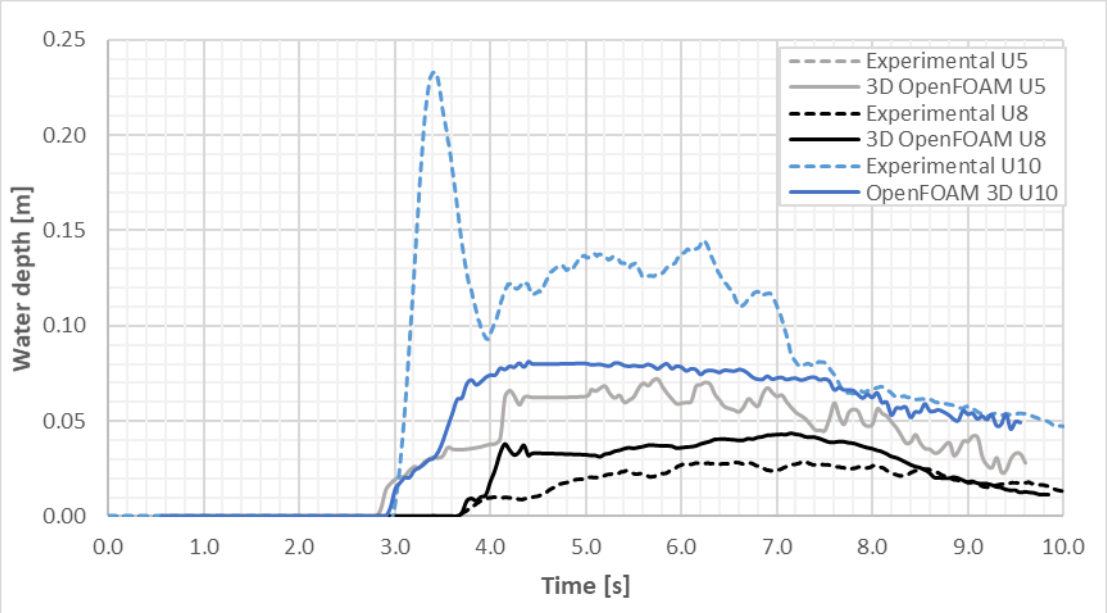

Figure 5-27- Timeseries of the water depth evolution along the ramp at U5 (x=6.2 m), U8 (x=6.5 m) and U10 (x=6.8 m) for H200. Comparison of observed (dashed line) and simulated (solid line) water depths at U5 (grey), U8 (black) and U10 (blue).

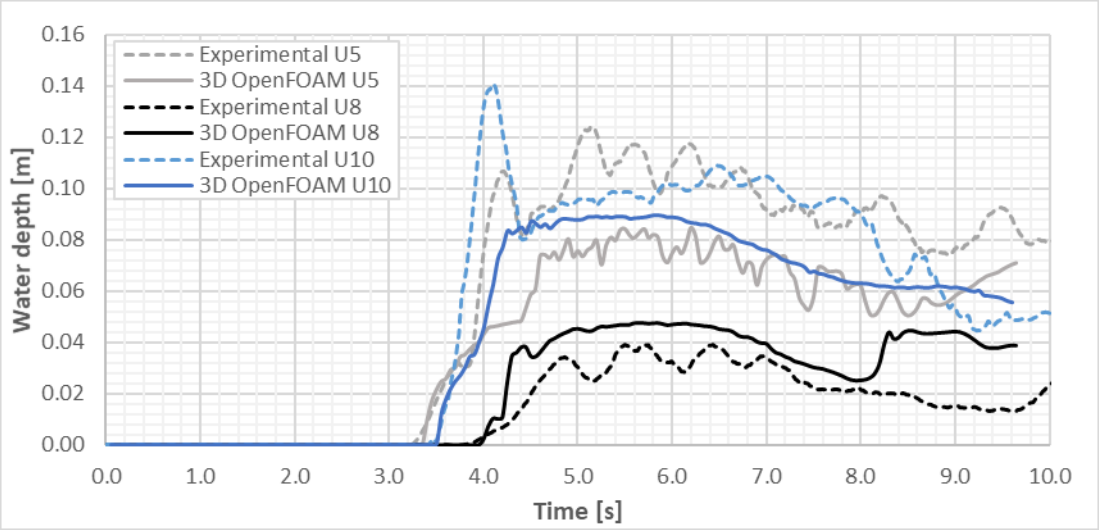

Figure 5-28- Timeseries of the water depth evolution along the ramp at U5 (x=6.2 m), U8 (x=6.5 m) and U10 (x=6.8 m) for H200G. Comparison of observed (dashed line) and simulated (solid line) water depths at U5 (grey), U8 (black) and U10 (blue).

To assess the ability of the model to simulate applied load force on the urban settlement, the modelled load was compared to the forces observed during the experiment from the load cell. The comparison of experimental and numerical results for the applied load with and without the roughness layer for H100, H100G and H200, H200G are found in Figure 5-29 and Figure 5-30, respectively. In general, the modelled flow around the urban settlement provided an overall a reasonable representation but further investigation is required for the correct parametrisation of the modelling of the more complex hydraulic features. At this point it is worth noting the difference in magnitude between Figure 5-29 and Figure 5-30.

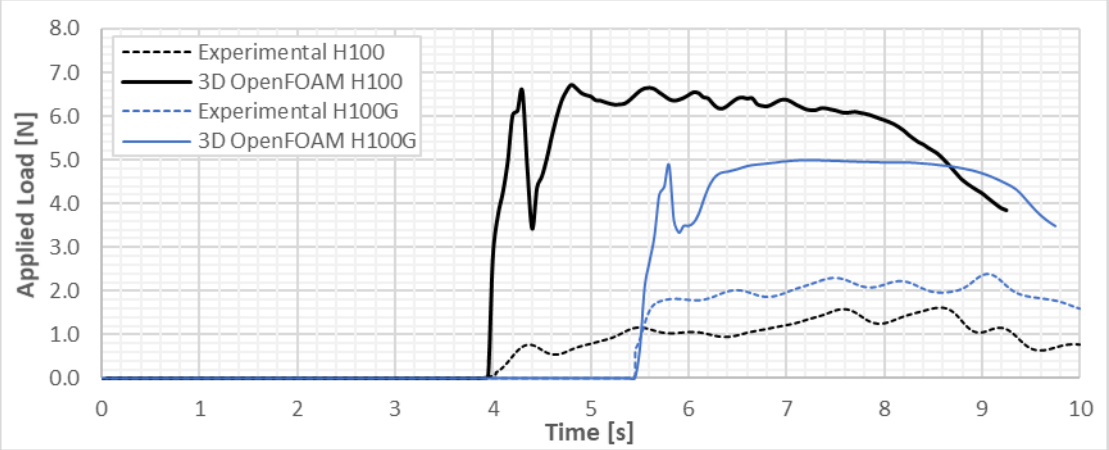

Figure 5-29- Timeseries of applied load on the front face of the single building for H100, H100G. Comparison of experimental (dashed line) and numerical results (solid line), with (blue line) and without (black line) the roughness layer

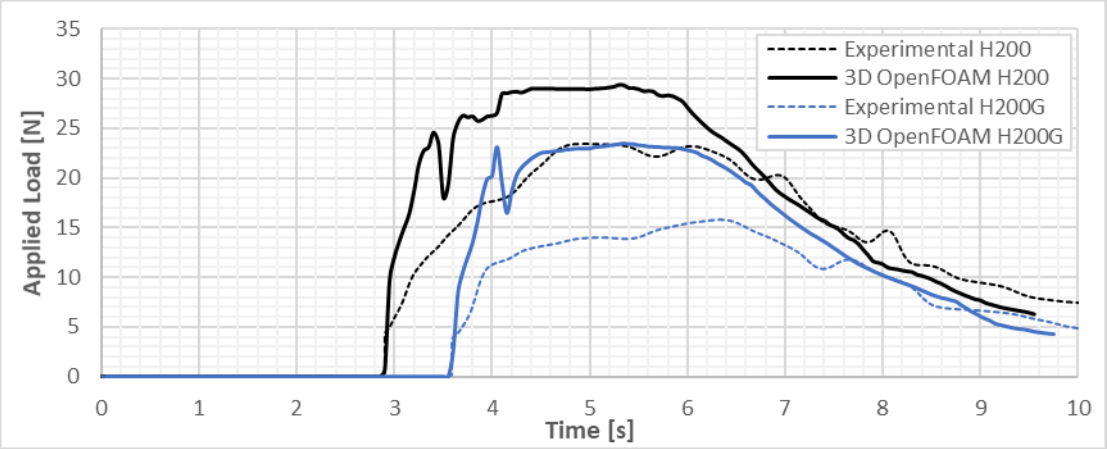

Figure 5-30- Timeseries of applied load on the front face of the single building for H200, H200G. Comparison of experimental (dashed line) and numerical results (solid line), with (blue line) and without (black line) the roughness layer

The impact of the flood wave on the downstream urban settlement can be described in four distinctive stages (as described in Chapter 4): (i) Impact, (ii) Development of the hydraulic jump, (iii) Steady high Fr flow (around an obstacle) and (iv) Decaying quasi-steady flow with decreasing high Fr number. In general, the modelled loads on the buildings exhibit an overestimation when compared to the corresponding observed loads. These discrepancies between the experimental and modelled results can be ascribed mainly due to the calculation procedure in OpenFOAM for applied load which is not how it was measured in the experiment. In the experiment, the load was measured using a load cell located at about $1/2$ from the bottom of the building. In contrast, OpenFOAM calculates automatically the total pressure using the acting velocity field and the water depth across the entire surface area of the building. Therefore, the outputs from OpenFOAM represent an average applied load according to equation Equation 5-16, where p is the pressure (Pa), $\vec{n}$ is the normal direction and ds is the control surface area (m^2). Consequently, it is an expected result to provide a higher value than the experimental measurement.

$$\int_s p \cdot \vec{n} \cdot ds \qquad \textit{Equation 5-16}$$

To further review this, Equation 5-16 shows that the load is the integral of the total pressure on the building surface. Reversing this approach and deriving the pressure from the experimentally measured applied force, we can calculate the average acting pressure and compare it with the modelled pressure results. In reality, this approach is a simplification as friction forces and shear stresses are not accounted for but provides a comparative test to

compare the magnitude of the two values. Figure 5-31 shows the correlation of the experimental (derived) pressure and the OpenFOAM pressure for case B1_H100. This comparison demonstrates that the experimental and numerical pressures are of the same magnitude, therefore proving that the modelled numerically calculated load in OpenFOAM is indeed an average applied load and thus suggests that both the experimental and numerical results in Figure 5-29 and Figure 5-30 to be correct.

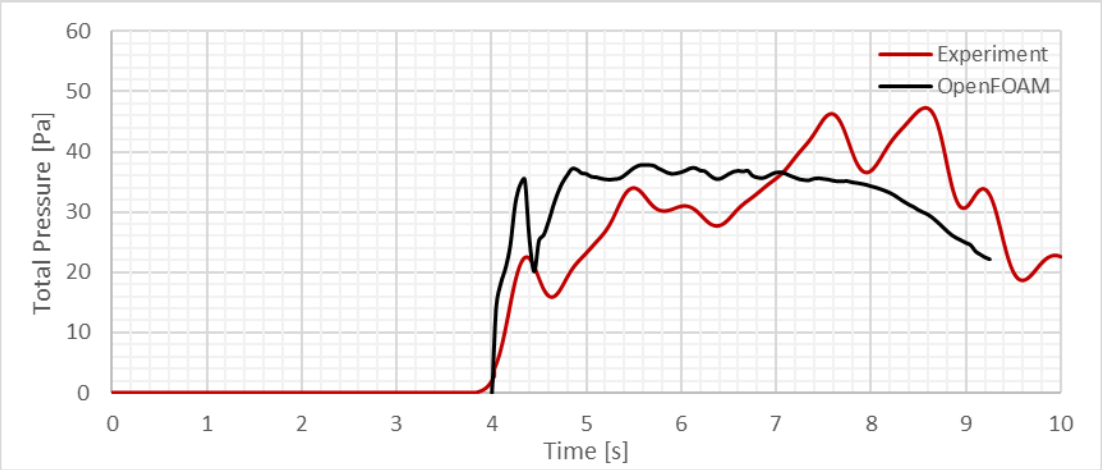

Figure 5-31- Comparison of experimentally calculated total pressure and numerically derived total pressure on single building in B1_H100 case

All 3D results are summarised in

Table 5-7, showing the comparison between experimental and numerical results (water depth and applied loads) for the four main experiments: H100, H200, H100G and H200G. The differences between the experimental and numerical results have been explained throughout this section and thus providing confidence in the accuracy of the 3D model.

Table 5-7- Summary of 3D OpenFOAM results for cases with single building

		OpenFOAM 3D Test Cases with single building							
Variables		**H100** Experimental	**H100** OpenFOAM	**H200** Experimental	**H200** OpenFOAM	**H100G** Experimental	**H100G** OpenFOAM	**H200G** Experimental	**H200G** OpenFOAM
Max Water Depth [m]	**U5**	0.075	0.031	n/a	0.072	0.071	0.066	0.124	0.085
	U8	0.016	0.014	0.029	0.043	0.026	0.034	0.039	0.048
	U10	0.049	0.052	0.233	0.081	0.045	0.049	0.140	0.089
Max Applied Load [N]		1.62	6.72	23.45	29.41	2.39	4.99	15.80	23.50

Finally, the previously presented experimental photos of B1_H100 and B1_H200 shown in Chapter 4 are compared here in Figure 5-32 and Figure 5-33 with the relevant modelled snapshots in the 3D OpenFOAM simulations.

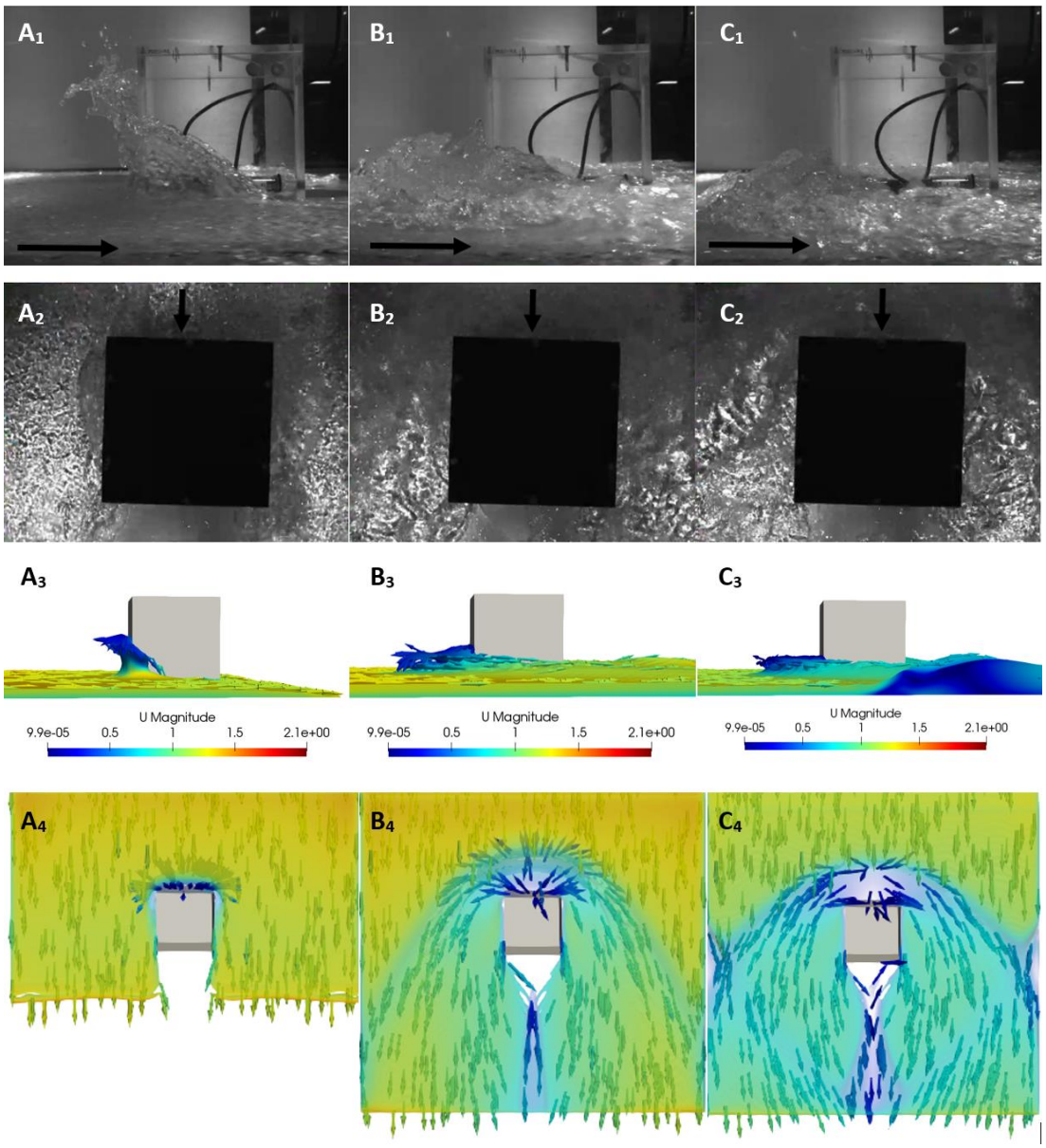

Figure 5-32- Comparison of photos and numerical snapshots of water impact on building for B1_H100 case at times t=4.18 s (A_1, A_2, A_3, A_4), t=5.16 s (B_1, B_2, B_3, B_4) and t=10 s (C_1, C_2, C_3, C_4) from side (first and third row) and top view (second and fourth row). Arrows show the velocity direction and the different colours represent the range of the velocity magnitude from blue to red representing a range of 0.00021 *to* $2.1\ m/s$.

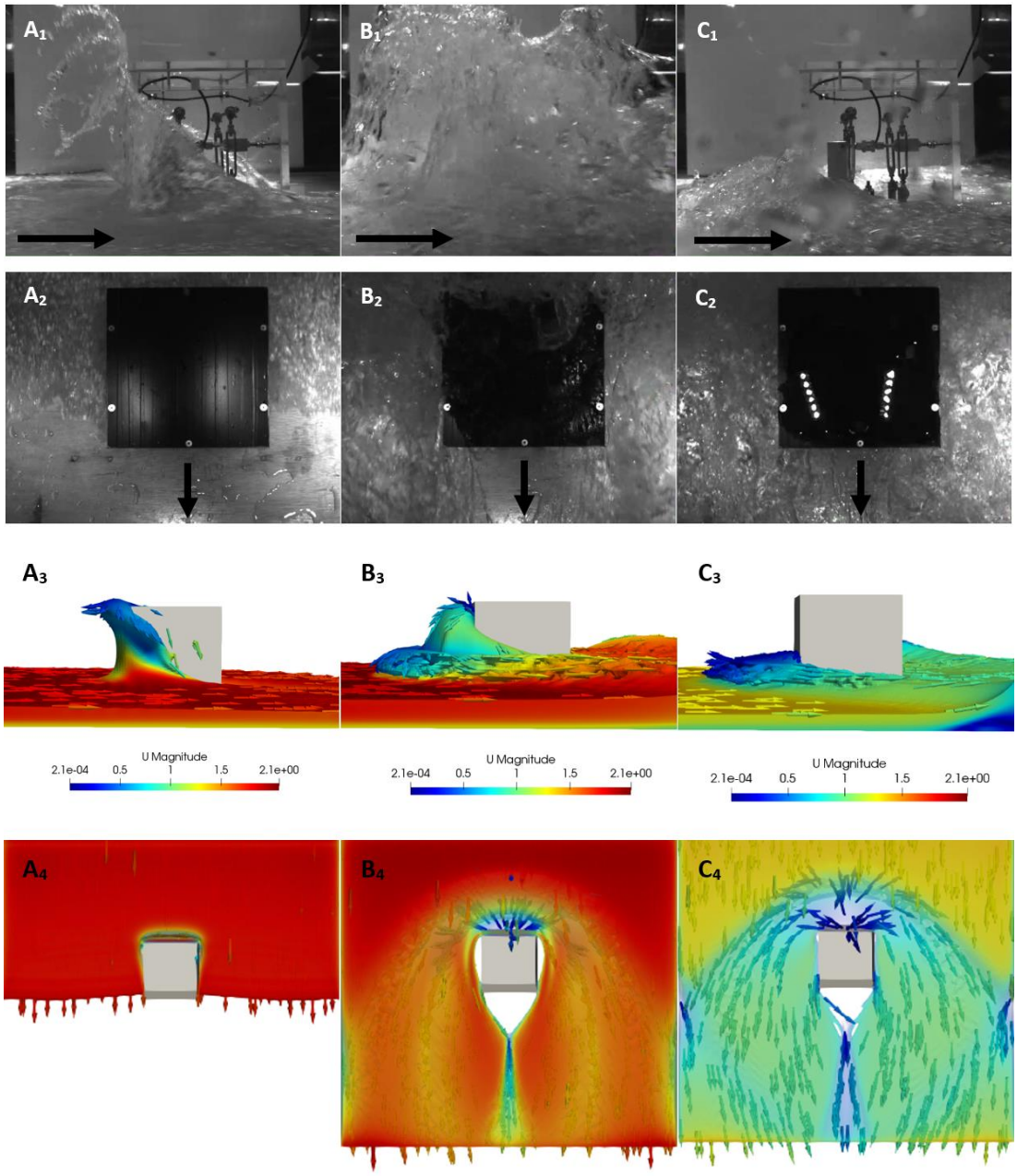

Figure 5-33- Comparison of photos and numerical snapshots of water impact on building for B1_H100 case at times t=2.96 s (A_1, A_2, A_3, A_4), t=3.45 s (B_1, B_2, B_3, B_4) and t=10 s (C_1, C_2, C_3, C_4) from side (first and third row) and top view (second and fourth row). Arrows show the velocity direction and the different colours represent the range of the velocity magnitude from blue to red representing a range of 0.00021 *to* $2.1\ m/s$.

Figure 5-32 represents the results from B1_H100 showing the creation of a weak hydraulic jump and the expected increase in water depth in front and on the sides of the building (Figure 5-25). Figure 5-33 shows the photos and model snapshots from B1_H200. Here the creation of a strong hydraulic jump after the first impact can be clearly identified and very strongly represented with velocity direction pointing upstream. The hydraulic jump

combined with the strong submersion on the front and sides of the building was also seen in U5 and U10 in Figure 5-27.

5.6 SUMMARY AND CONCLUSION

The aim of this chapter was to simulate flash floods numerically in OpenFOAM to select the optimal parametrisation for the modelling of these events. The OpenFOAM models have shown that the model is capable of representing complex 2D and 3D flows, and also that the interactions between flood waves and urban settlement structures can be adequately simulated with correct parametrisation.

It was demonstrated that the 2D numerical models can be used to accurately reproduce the high Froude flow on the ramp but that a 3D simulation is required for representing the three-dimensionality of the flow in the urban settlement. In the 2D simulations, the model outputs were found to be very strongly affected by the choice of the model, turbulence model and control parameters. Hence, the selection of these parameters is crucial to ensure an accurate representation, thus why a parametric analysis is suggested to be conducted by practicing engineers and consultants working on similar problems.

It was found, that the initial stages of a flash flood can be modelled in a sufficiently short timescale using very detailed 2D models. Although 3D models are more computationally expensive, the modelling of the three-dimensional flow around the urban settlement demonstrated their necessity for the correct simulation of the interactions between flood wave and built structures.

For modelling the three-dimensional aspects of the flow, a coupled 2D/3D model was developed but as explained in section 5.5.3 its results were not presented in this Chapter. As the simulation domain was small in length, in this case a fully 3D model was better suited as it provided a chance for a deeper understanding of the three-dimensional model and did not add substantial extra simulation time. However, the development in the OpenFOAM code provides a forward step in 2D/3D coupling in OpenFOAM and offers an opportunity for future researchers to advance in the simulation of larger flash flood events using OpenFOAM.

The flow around the urban settlement was modelled precisely but the calculation of applied load showed considerable discrepancies when compared to the experimental results. By integrating the force on the building's surface, it was found that the estimated pressures on the building were of the same magnitude as the pressures observed during the experiment thus offering confidence in the simulation of the applied loads. Further work on refining load

calculations is suggested in order to accurately model the high applied load peak which can provide a future reference for structural innovations for resilient designs and constructions in flash food prone areas.

Finally, the use of a roughness layer was shown to decrease the water depths and applied loads in all cases but the direct connection suggested by Jayaratne (2010) between Manning's coefficient and the roughness height k_s, was not found suitable. The numerical investigation conducted in the frame of this research in order to match the experimental results lead to the development of a new equation for the connection of Manning's coefficient and the roughness height k_s. The new equation is $n \approx 0.020(k_s)^{\frac{1}{6}}$ changing the constant in Jayaratne's (2010) equation from 0.012 to 0.020. As such, further investigation on this equation is suggested considering different Manning's coefficients to explore in more depth their connection to the roughness height k_s.

The next chapter will investigate further the abovementioned outcomes in the numerical modelling of flash floods and will apply the parametrised OpenFOAM model to the benchmark dam break case found in the report produced by Defra and Environment Agency (2010).

6 BENCHMARKING OF FLASH FLOOD MODELS

The aim of this chapter is to investigate the ability of industry models to replicate flash flood events and compare OpenFOAM with them using the Defra and Environment Agency (2010) benchmark case. The Defra and Environment Agency (2010) report will first be presented and the benchmark case explained. Next, the results from the existing industry models will be presented and compared with OpenFOAM's performance. Finally, a roughness layer is applied to the benchmark case to investigate how the applied loads are affected and eventually provide further recommendations into the modelling of flash floods.

6.1 THE ISOLATED BUILDING TEST CASE

Defra and Environment Agency (2010) created a report on the benchmarking of 2D hydraulic modelling packages as part of the flood and coastal erosion risk management research and development programme. The benchmarking cases were provided to all 2D flood inundation software developers in the UK and the aim of the report was to provide evidence and establish the capability of 2D hydraulic modelling packages to accurately model the physical processes involved in flood risk modelling. Many of the tested models are currently used for the basis of flood risk management decisions and thus the correct modelling of these events is essential for the decision-making process. Secondly, the report was designed to provide a comparative dataset for future evaluations of numerical models (Defra and Environment Agency, 2010).

A total of 8 cases were presented in the report and among these, the test case relevant to flash floods — and by extension relevant to this research — is a dam break case, Test 6A, simulating shocks and wake zones resulting from a dam failure (Defra and Environment Agency, 2010). This benchmark case, was based on a laboratory experiment from the IMPACT project analysing the flow from a dam break interacting with an isolated obstacle conducted in the Université Catholique de Louvain (UCL) in Belgium (Soares-Frazão and Zech, 2002a; Soares-Frazão et al., 2003a). The experimental set up is shown in Figure 6-1 to Figure 6-3. It consists of a trapezoidal channel (Figure 6-3), a dam with an $1\ m$ long opening and an isolated building is located downstream. The building is positioned at a 64° angle, has a $0.8\ m$ length, a $0.4\ m$ width and is $0.2\ m$ in height.

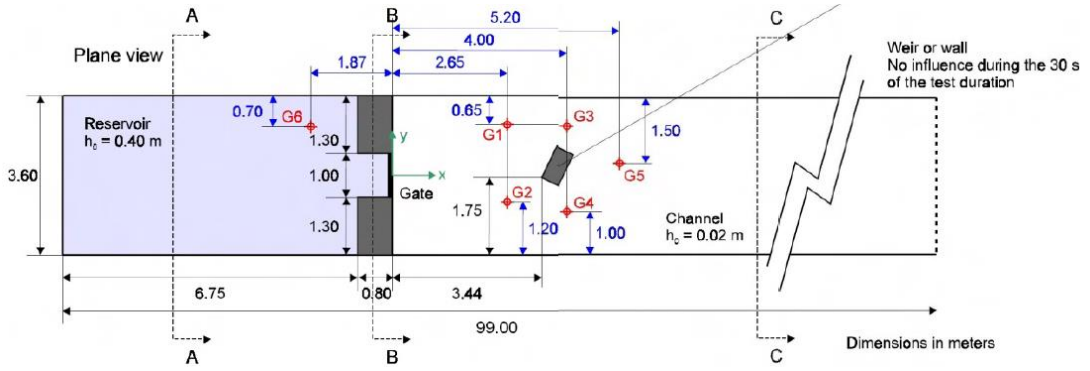

Figure 6-1- Plan view of experimental setup of IMPACT benchmark case. The experiments were conducted in UCL Belgium in a trapezoidal channel (Defra and Environment Agency, 2010)

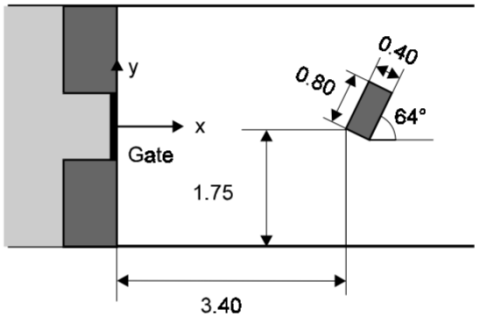

Figure 6-2- Detail of experimental setup of IMPACT benchmark case showing the dam with the 1 m long opening and the isolated obstacle located downstream at an angle of 64°. The building has a length of 0.8 m, a width of 0.4 m width and is 0.2 m in height (Soares-Frazão et al., 2003a)

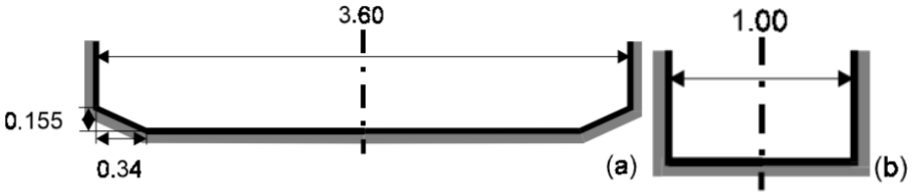

Figure 6-3- Cross section of experimental setup (a) in the upstream reservoir and downstream channel and (b) between the two columns at the dam location (Soares-Frazão et al., 2003a)

After the dam break is released, the dam break wave travels rapidly downstream where it reaches the isolated building in less than $2\ s$ and submerges it. Following that, the flow undergoes a separation where side shock waves created from the reflection waves and hydraulic jump formations interact with the building. Meanwhile, downstream, a wake zone appears on the back side of the building (Soares-Frazão et al., 2003a). The experiment reported water depths and velocities measured at 6 different locations G1 to G6 (Figure 6-1).

In the Defra report, seven different 2D models were used to model the benchmarking test: InfoWorks2D, ISIS2D (Flood Modeller 2D), MIKE FLOOD, SOBEK, TUFLOW, ANUGA and TUFLOW FV which all solve the SWEs. The benchmarking case was modelled with 2D

horizontal models and thus the simulations were able to represent the isolated obstruction. The models showed a variety of accuracies at the different gauge locations G1-G6 (Defra and Environment Agency, 2010). The water depth results presented in the report are reconstructed in Figure 6-4 for clarity for all seven different models and these results are compared with the experimental dataset to benchmark the seven different 2D models. Broadly, all tested models were able to represent levels observed at G6 which is located in the reservoir, and close agreement between experimental and numerical results was also found in G3. The worst represented gauge appeared to be G2 where the reflection wave from the interaction with the building was not accounted for by many of the models (Soares-Frazão et al., 2003a; Defra and Environment Agency, 2010). In general, none of the models consistently demonstrated an accurate representation of the experiment at all gauge locations and some of the most simplified models' predictions were inaccurate (Defra and Environment Agency, 2010). This means that either the Defra and Environment Agency (2010) benchmarking scheme is not appropriate and needs to be reviewed or that the 2D models did not prove to be suitable for modelling extreme events. In the next section, a 3D OpenFOAM model is applied to the same benchmark case in order to investigate this further.

Figure 6-4- Comparison of the water depth evolution timeseries for the EA Benchmarking of 2D hydraulic models. The experimental results (grey line) are compared with the seven different 2D SWEs models (InfoWorks in red, MIKE FLOOD in yellow, TUFLOW in purple, TUFLOW FV in cyan, ISIS2D in blue, SOBEK in orange and ANUGA in green) in gauge locations (a) G1, (b) G2, (c) G3, (d) G4, (e) G5 and (f) G6 (Defra and Environment Agency, 2010)

6.2 OPENFOAM BENCHMARKING

6.2.1 Introduction

The 3D parametrised RANS turbulent OpenFOAM model used in Chapter 5 was also applied to the benchmarking case following the specifications provided by Defra and Environment Agency (2010). The initial conditions were set to an upstream water level in the reservoir of $h_0 = 0.4m$, a downstream water level after the dam and around the building of $h_0 = 0.02m$ and a uniform Manning's Coefficient on the bed of $n = 0.01$. Although the wake zone was very intense downstream of the building no eddy viscosity was specified for the models. The simulation results had to be provided in a $R = 0.10m$ mesh and for $t = 2\ min$. The 3D RANS OpenFOAM model was applied to investigate the need for detailed models in the representation of the different parameters of such and even though in the benchmarking case both water depths and velocities were recorded, for the scope research only water depths at the six locations (G1-G6) will be discussed.

Five models were investigated each with different specifications and parameters (mesh size, roughness coefficients and eddy viscosity):

1. **R0.10_μ9**: Standard 3D OpenFOAM model with $R = 0.10\ m$ uniform rectangular mesh
2. **R0.05_μ9**: Standard 3D model with $R = 0.05\ m$ uniform rectangular mesh
3. **R0.05_μ9_N**: Standard 3D model with $R = 0.05\ m$ uniform rectangular mesh and Manning's $n = 0.01$
4. **R0.05_μ18**: 3D model with $R = 0.05\ m$ uniform rectangular mesh and eddy viscosity $\mu = 18$
5. **R0.05_μ9_G**: 3D model with $R = 0.05\ m$ uniform rectangular mesh and roughness layer ($ks = 0.00086$)

The first 3D model, R0.10_μ9, had the required $0.1\ m$ mesh and used the standard parametrisation provided in the dam break tutorials in OpenFOAM resulting in an eddy viscosity of μ=9. The computational time required was 03:58:38 on the 16-core High performance Computer (HPC). Following that, the grid was refined from 0.10 to $0.05\ m$ and the same parametrisation was used for the R0.05_μ9 model. Next, in the R0.05_μ9_N model, a Manning's roughness coefficient was applied to investigate its effect on the water depth evolution. As previously discussed in Chapter 5, the required Manning's coefficient 0.01 was applied using the equation $n \approx 0.020(k_s)^{1/6}$, thus resulting in a k_s value of 0.016. Then, the eddy viscosity was increased to μ18 (R0.05_μ18) and finally a roughness grass layer was

modelled (R0.05_μ9_G) to assess its effect on the applied loads on the building. All R0.05 cases increased considerably the computational time by quintupling it to 21 - 24 hours. In all cases the upstream water level was set to $0.40\ m$ and the downstream level was $0.02\ m$. The model was run for $t = 30\ s$ to compare it appropriately with the full length of the experimental results.

As mentioned in Chapter 5, OpenFOAM uses a finite volume method but in this case the discretisation schemes and their order are important because not all flow features can be simulated by all schemes (Soares-Frazão et al., 2003a). OpenFOAM's discretisation scheme for the first time derivative $\partial/\partial t$ used is the Euler scheme which is a first order, bounded and implicit scheme, the gradient terms of the equations are discretised using a second order Gaussian integration interpolation scheme and the divergence terms using a Gaussian linear interpolation scheme. The Gaussian discretisation schemes use a standard finite volume discretisation during which the values for each mesh cell are interpolated from the centre of the cell to the centre of the side faces (Greenshields, 2015).

6.2.2 Results and discussion

The OpenFOAM modelled water surface elevations compared to the benchmarking water surface elevations at the six wave gauge locations are presented below. For clarity, only results from two sets of tests are presented for comparison (R0.10_μ9 and R0.05_μ9) and related directly with the experimental results due to the otherwise extremely high number of results. Figure 6-5 shows a plan section of the experimental set up including the wave gauge locations G1-G6, and the exact location of the six gauges are compiled in Table 6-1.

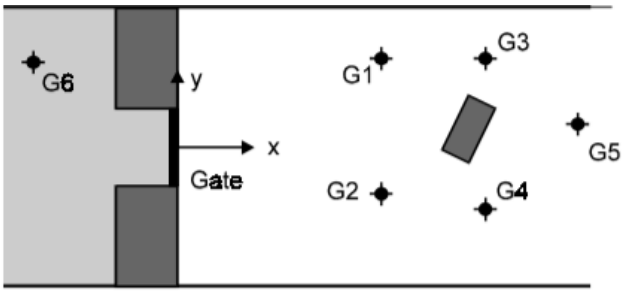

Figure 6-5- Plan of experimental set up showing the position of the wave gauges (Soares-Frazão et al., 2003a)

Table 6-1- Location (x, y) of all gauges G1-G6

Gauge Name	x [m]	y [m]
G1	10.20	2.95
G2	10.20	1.20
G3	11.55	2.95
G4	11.55	1.00
G5	12.75	2.10
G6	5.68	2.90

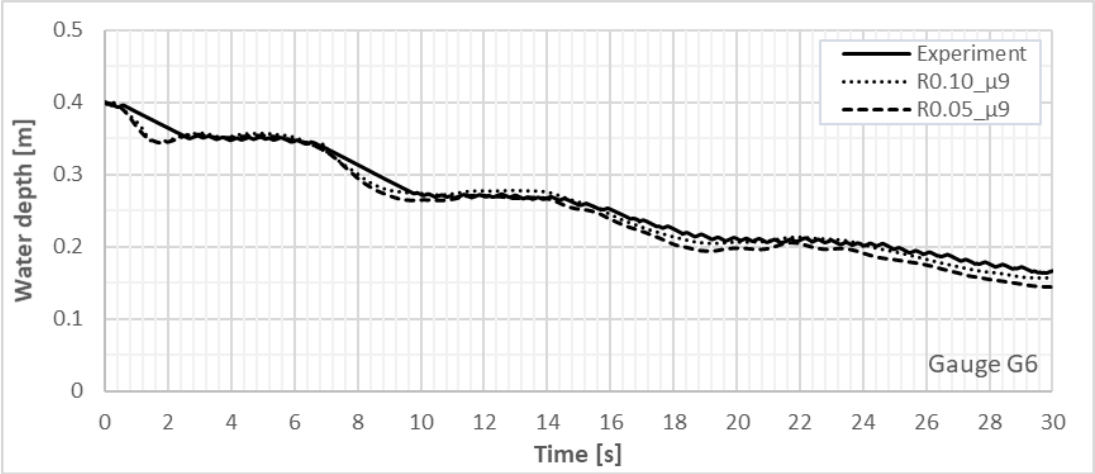

Figure 6-6- Experimental versus numerical water depth results at gauge G6

Figure 6-6 shows the comparison of the experimental results with the OpenFOAM results using two different mesh sizes at gauge G6 which as is positioned in the reservoir and gives a representation of the flow release from the reservoir over time. OpenFOAM provides an exceptionally good representation of the reservoir emptying with both mesh sizes. The behaviour of the flow through the gate, as pointed out by Defra (Defra and Environment Agency, 2010), is periodic with a period ~$9\ s$, and this behaviour is well represented in OpenFOAM with the same period.

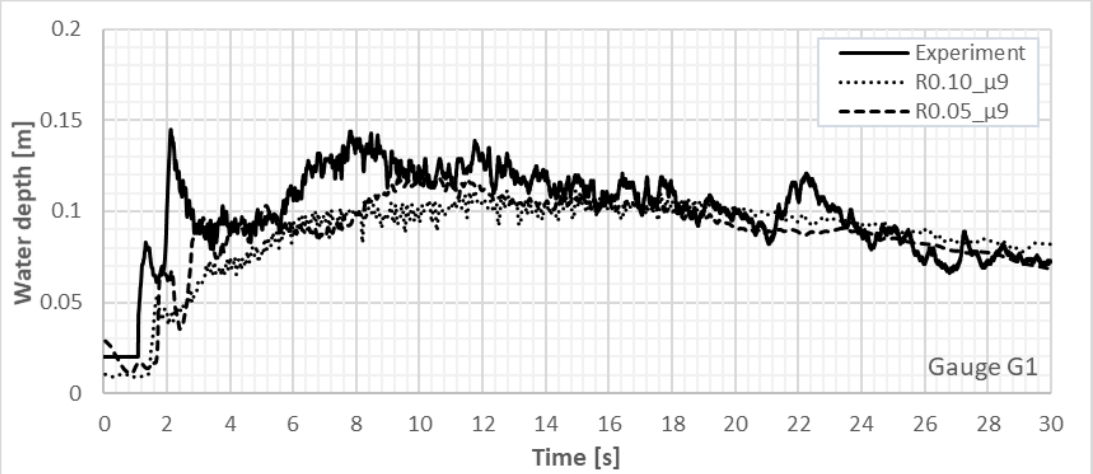

Figure 6-7- Experimental versus numerical water depth results at gauge G1

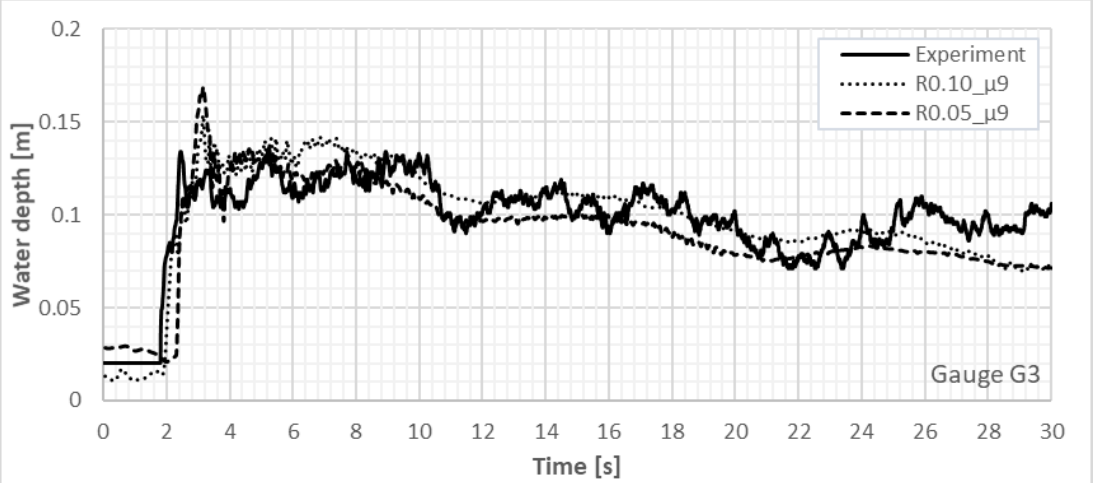

Figure 6-8- Experimental versus numerical water depth results at gauge G3

The water depths at Gauges 1 and Gauge 3 are very accurately represented from the OpenFOAM model and this can be seen in the comparison between experimental and numerical results shown in Figure 6-7 and Figure 6-8 respectively.

Gauge 1 is located upstream of the building, on the lengthwise side of it, and the increase in water depth represents the main reflective wave from the building. OpenFOAM shows reasonable agreement with the experimental results but overestimates the initial shark peak. This is attributed mainly to the mesh size being too coarse (R0.1 ad R0.05). Consequently, as the mesh is larger than the downstream water depth ($0.02\ m$), OpenFOAM provides a poor prediction of the initial water depths by both models. Figure 6-9 shows a plan and a side view representation of downstream depths for R0.05 at $t = 0\ s$.

Gauge 3 is located on the side of the building where the flow is quasi-steady for the majority of the experiment. After the initial impact, the measurement represents the increase in water depth due to the hydraulic jump created on the side of the building. OpenFOAM provides very reasonable agreement and validates the benchmarking case (Figure 6-8). The sharp initial peak is underestimated but the finer mesh model R0.05 models accurately that there are two peaks, one smaller at $t = 1.38\ s$ and one bigger at $t = 2.21\ s$, a feature not modelled by the majority of the 2D models.

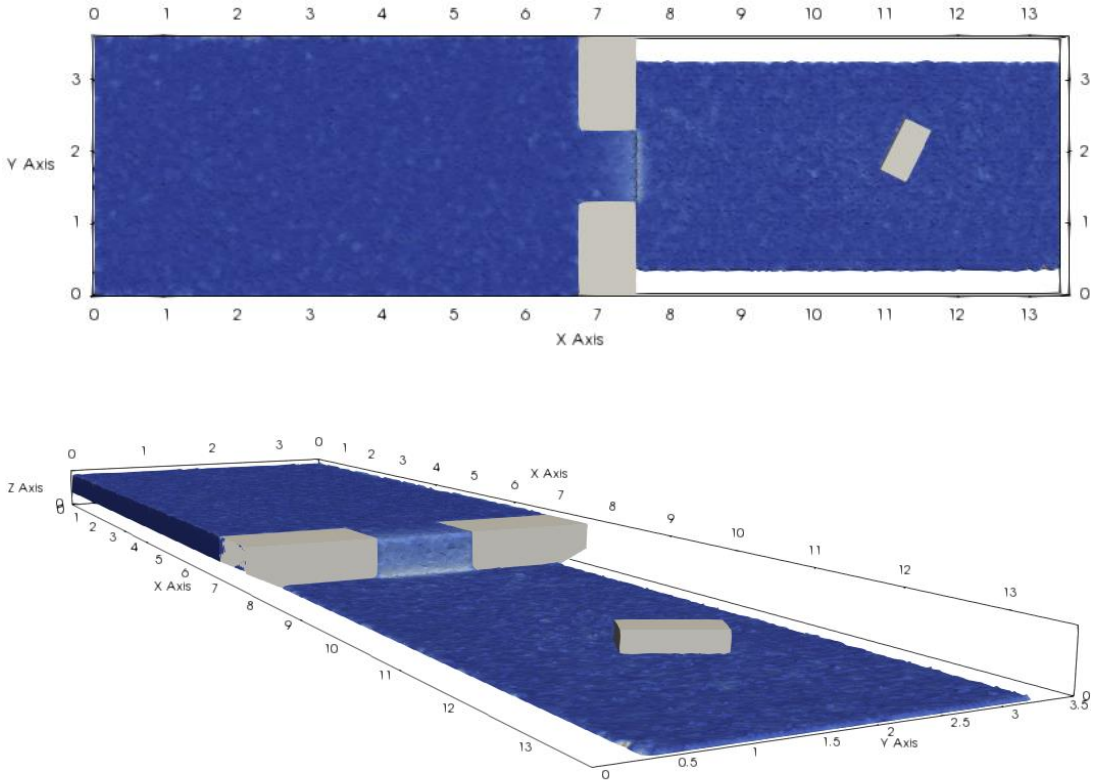

Figure 6-9- OpenFOAM 3D simulations at t=0 s from top to bottom: plan view of R0.05_μ9 and side view of R0.05_μ9

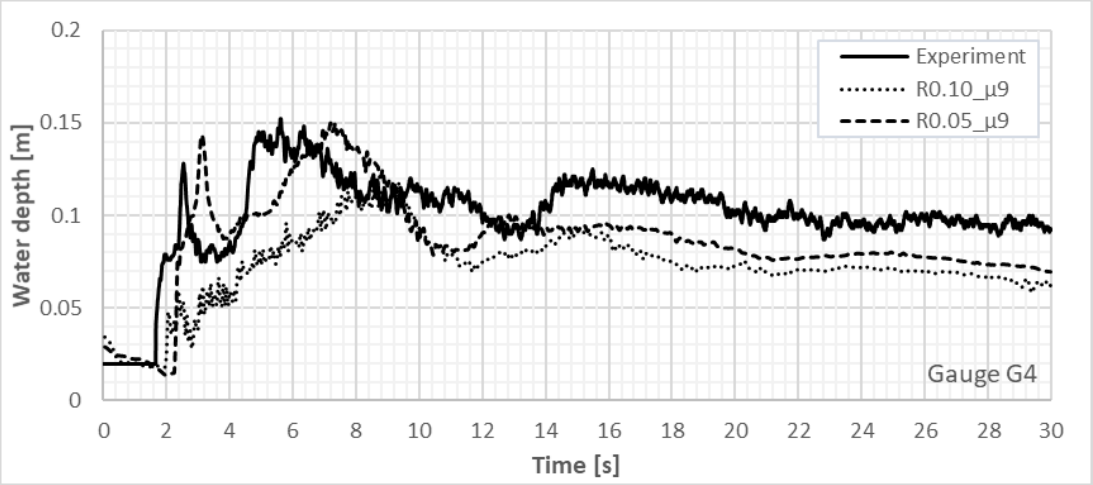

Figure 6-10- Experimental versus numerical water depth results at gauge G4

Gauge 4 is also positioned on the side of the building and in this case the first peak is attributed to the first splashing from the reflection wave on and the second one due to the formation of a hydraulic jump. Figure 6-10 shows the comparison between experimental and numerical results at G4. Here the mesh refinement provides a much more realistic representation of the event. The sharp initial peak is accurately modelled straight away by the R0.05 model but non-existent in the R0.10 model. Furthermore, the sudden drop in depth at $t = 4\ s$ after the initial peak is also predicted very accurately contrary to the 2D models which do not predict this flow pattern.

Gauges 2 and 5 (Figure 6-11 and Figure 6-12) are the most poorly represented by OpenFOAM which is also the case in the 2D cases. The increase at $t = 14\ s$ in Gauge 2 is attributed to the hydraulic jump caused by wave reflection. This is completely missed by R0.10 but modelled slightly by R0.05. During the IMPACT project research, it was pointed out that only first-order accurate schemes with finer meshes modelled this hydraulic jump (Soares-Frazão et al., 2003a). OpenFOAM predicts the initial supercritical flow accurately, and thus the hydraulic feature at $t = 20\ s$ is modelled with the R0.05 model. This suggests that it is possible to improve further the modelling of the hydraulic jump with the use of a finer mesh.

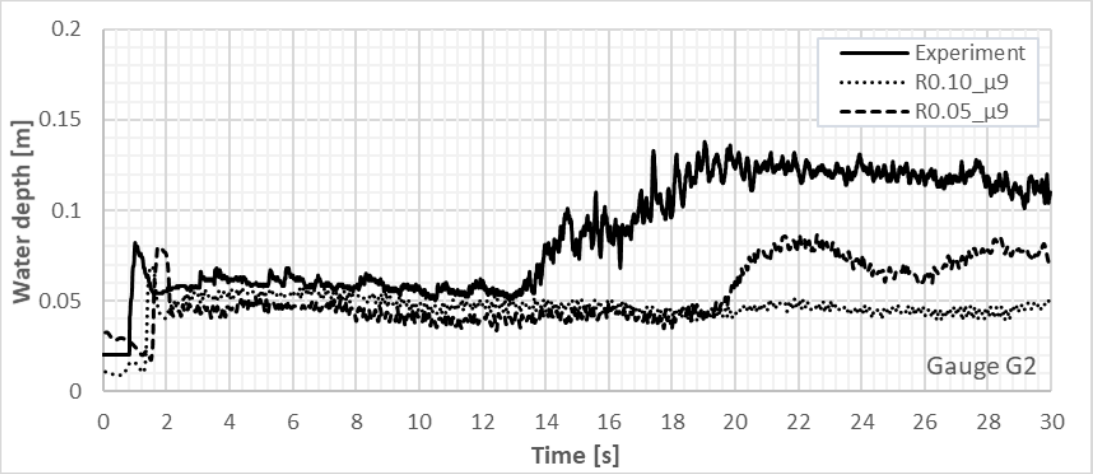

Figure 6-11- Experimental versus numerical water depth results at gauge G2

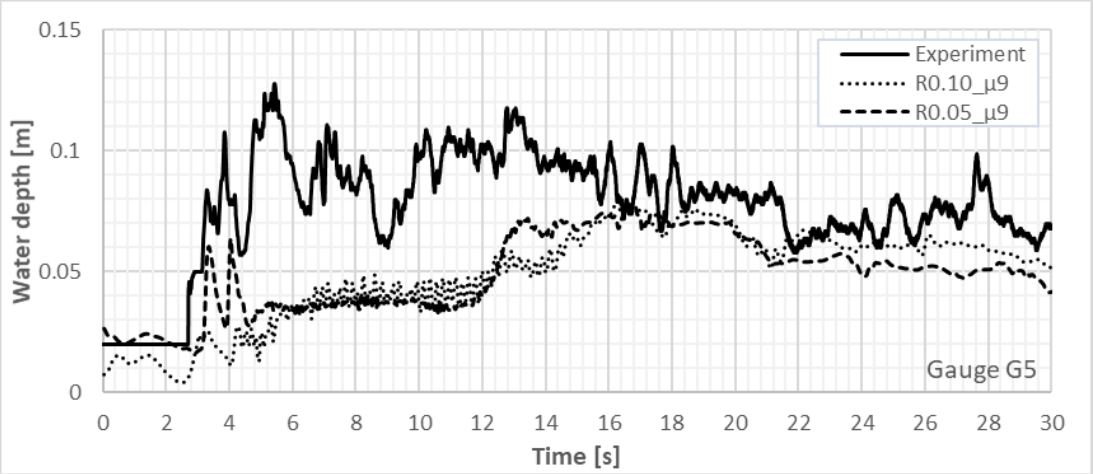

Figure 6-12- Experimental versus numerical water depth results at gauge G5

Gauge 5 is located in the wake zone downstream of the building. The experiment measured many oscillations and irregularities in the water flow which was shown only to be modelled accurately by second-order models (Soares-Frazão et al., 2003a). Once more, the R0.05 models some of the oscillations but further research into the parametrisation especially in terms of eddy viscosity is required to model this accurately.

The eddy viscosity was then increased from μ9 to μ18 and the two cases were compared with the experimental dataset. Figure 6-13 shows this comparison at Gauges 1 and 3. The graphs show this increase in eddy viscosity does not affect the results considerably. It is known that eddy viscosity depends upon the flow and not the fluid and increases for the more turbulent flows. Thus, to accurately model the flow, especially downstream of the building where the wake zone is very strong and the eddies dominant, higher values of eddy

viscosity need to be tested. Therefore, further research is suggested to find the appropriate eddy viscosity coefficient to this experimental setup.

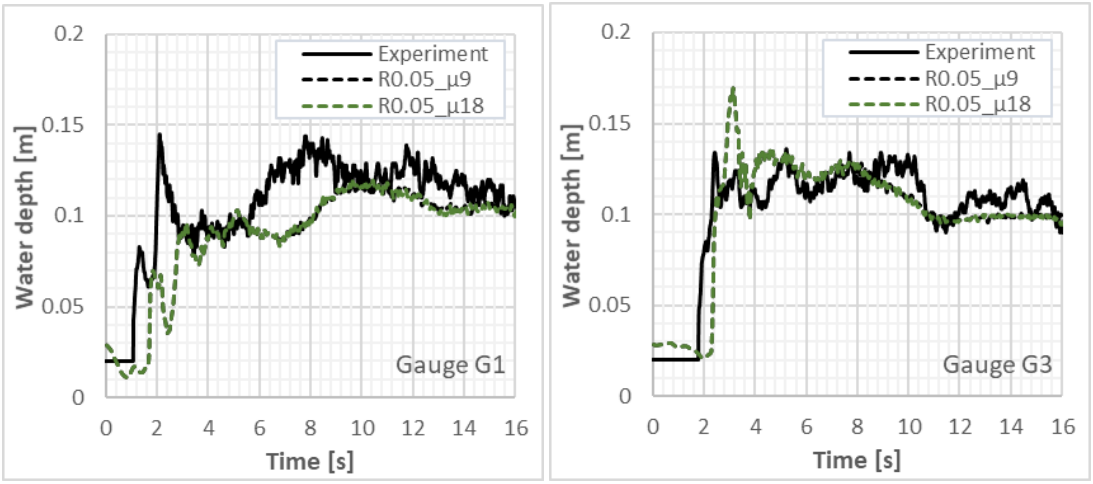

Figure 6-13- Experimental versus numerical water depth results at gauges G1 and G3 for different eddy viscosities (µ9 and µ18)

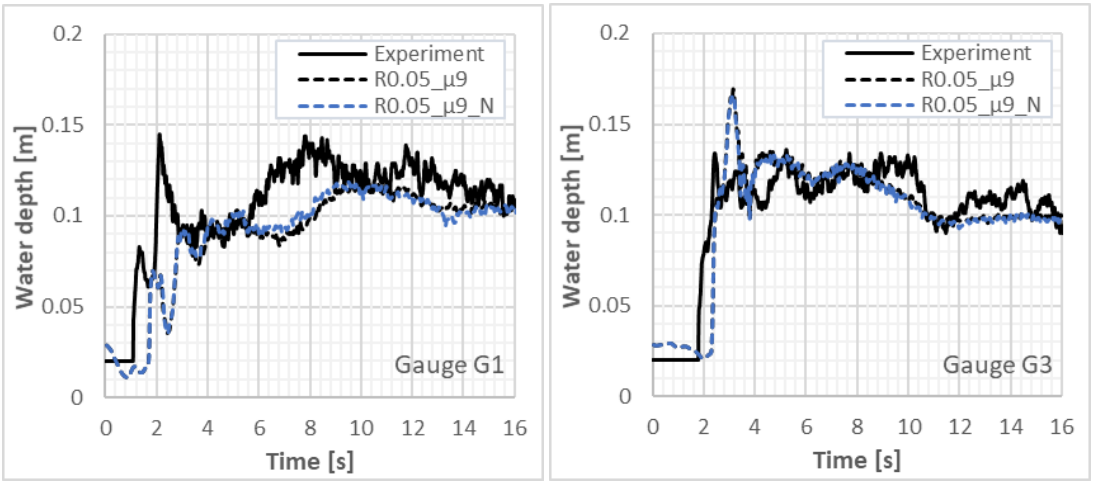

Figure 6-14- Experimental versus numerical water depth results at gauges G1 and G3 with and without a Manning's coefficient (µ9 and µ9_N) The experimental results are shown with a black solid line, the numerical results from the R0.05_µ9 model are shown with a dotted black line and the results with the applied Manning's coefficient (R0.05_µ9_N) are shown with a blue dotted line.

A Manning's coefficient was applied to the model in terms of a k_s value to meet the requirements provided by the benchmark case. The experimental versus numerical water depth results at gauges G1 and G3 with and without the applied Manning's coefficient (µ9 and µ9_N) is shown in Figure 6-14.. No difference is observed between the two modelled cases and this is attributed to the OpenFOAM standard parametrisation which represents a

very smooth and frictionless surface. A Manning's coefficient of 0.01 also represents very smooth surface and thus does not alter the results considerably.

In general even with coarse meshes, the peak values are accurately predicted by OpenFOAM which is considered one of the most important considerations in food modelling (Defra and Environment Agency, 2010). Some of the general reasons, pointed out by the project researchers, for the modelling discrepancies in their models were space and time resolution, mesh refinement and alignment, treatment of source terms, order of accuracy of numerical model, building representation (solid or high friction area) (Soares-Frazão et al., 2003a; Defra and Environment Agency, 2010).

6.3 LOAD REDUCTION USING ROUGHNESS LAYER

In order to further investigate the effect of roughness layers discussed in Chapter 4 and Chapter 5, the same roughness layer was applied to the benchmark case to further examine and understand how the applied loads are affected. The results for the applied force on the structure are presented in Figure 6-15.

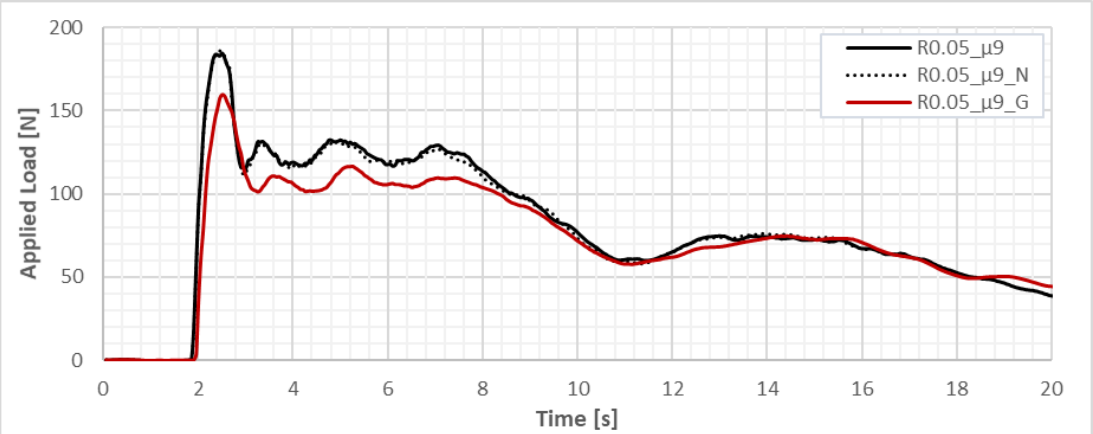

Figure 6-15- Comparison of applied force with (R0.05_µ9_G) and without (R0.05_µ9) roughness layer and Manning's coefficient (R0.05_µ9_N). The numerical results from the R0.05_µ9 model are shown with a solid black line, results from the R0.05_µ9_N model with the applied Manning's coefficient are shown with a dotted black line and the roughness data R0.05_µ9_G, obtained from further simulations, are plotted with a solid red line.

The maximum applied load simulated with the roughness layer is smaller than without the roughness layer. Figure 6-15 shows the comparison between the horizontal components of the dam break wave load with and without the roughness layer, respectively and suggests that the roughness layer R0.05_µ9_G reduces the magnitude of the applied load. A velocity

reduction can be observed from the applied force data. The first impact with the building occurs at $1.75\ s$ and at $1.9\ s$ without and with the roughness layer respectively which corresponds to an 8% reduction in velocity from $6.28\ m/s$ to $5.78\ m/s$. What is interesting to observe is that the maximum applied force occurs simultaneously in both cases at $t = 2.5\ s$. The sharp initial peak is decreased from $184.9\ N$ to $160\ N$ equivalent to 13.5% and the total average load from $t = 0$ to $t = 11\ s$ by 12%. After $t = 11\ s$, the applied load between experimental and numerical results is very similar and the reduction is only in the order of 2%. In general, the reduction in applied load is much smaller than the reduction measured in the experiments in Chapter 4 which was of the order of 32.6%. This is attributed to the magnitude difference in the volume of water in this benchmarking case. The reservoir water depth is double the one in the experiment in Chapter 4 and the isolated obstacle is closer to the reservoir. Therefore, the difference in magnitude between the applied loads in Chapter 4 and the benchmark case and the smaller effect of the tested roughness layer are expected.

The four stages described in Chapter 4 referring to the load acting on a building are (i) Impact, (ii) Development of the hydraulic jump, (iii) Steady high Fr flow (around an obstacle) and (iv) Decaying quasi-steady flow with decreasing high Fr number. Here not all stages are clearly visible. The first stage of impact is clearly apparent from $t = 0$ to $t = 3\ s$ with a sudden increase of the applied load reaching its maximum value at the first peak. Following that the development of the hydraulic jumps are also apparent from $t = 3\ s$ to $t = 7\ s$ where a periodical behaviour is observed with a period of ~1.8 and the building is submerged. Finally, after $t = 11\ s$, it reaches the decaying quasi-steady flow stage with the decreasing high Froude number and the same periodic behaviour of the flow seen at Gauge 6 is visible with the same period ~$9\ s$. This difference in distinctive stages is associated with the more complicated patterns of the flow in this benchmark case. The building is positioned at an angle to the flow, therefore resulting in a more complicated interaction between hydraulic jumps, reflective and cross waves.

6.4 DISCUSSION

The analysis undertaken has shown that the Defra and Environment Agency (2010) benchmarking scheme is appropriate for the modelling of extreme events but needs to be reviewed in terms of the mesh requirement. The $R = 0.10m$ mesh is a very coarse mesh requirement (especially when the downstream water depth is $h_0 = 0.02m$). That being said

it is difficult to distinguish which models do not perform well because of their governing equations, numerical schemes and specifications and which would perform better with a more refined mesh.

In terms of the RANS turbulent 3D OpenFOAM model, it was found that it is capable of modelling dam break events and capturing the detail of the flow. The model is capable of reproducing the different flow characteristics, hydraulic jumps and wake zones and match substantially the arrival time of reflected waves. Yet, the parametrisation of such events is complex due to the range of specifications and variable factors, that include mesh accuracy, refinement and alignment, the choice of the order of accuracy of the numerical model and the selection of the eddy viscosity and roughness coefficients. It has been shown that mesh refinement (from the $0.1\,m$ specified to $0.05\,m$) considerably improved the model calibration and thus all three-dimensional characteristics were able to be clearly reproduced. Simulation run time (03:58 for the R0.1 in a Quad Core PC) for coarse meshes is practical for consultants, engineers and designers and the additional detail provided in a 3D model leads to a deeper understanding of the fluid dynamics of the events, confirming that the use of 3D models can have positive effects on flood risk management decision making.

Several modelling issues can be established using 3D modelling approaches which would not have been easy to identify using the majority of the 2D models used in industry and other theoretical approaches which cannot accurately account for the complexity of the flow. Even if the models are run with finer meshes, thus increasing their computation time considerably, the preparation time for the models is not significant and the 3D visualisation of the dataset could make up for the time it would take an engineering team to fully assess 2D results.

7 SYNTHESIS

The aim of this chapter is to present a summary of the thesis and its different chapters and then to provide conclusions to the objectives originally set in the Introduction chapter. Finally, proposals for future work and recommendations are suggested.

7.1 SUMMARY OF THESIS

The overall aim of the thesis was to provide further insight into flash floods and their numerical simulation. Flash flood modelling is a complex process and numerical simulation of the phenomena requires a deep understanding of the event and complex, three-dimensional modelling if the processes involved are to be replicated in high level of detail.

The introduction provided context for the relevance of the research as an increase in the frequency and magnitude of flooding is expected. Flash floods were defined, and the hydraulic modelling of floods and more specifically flash floods was discussed. Through this, the research problem was introduced and the importance of the research highlighted. The research questions and objectives that were presented in the introduction were:

- **Question 1:** Is a dam break a good representation of a flash flood? Does it guarantee the main characteristic features of flash floods?
    - **Objective 1:** Experimental and analytical description of the different phases of a dam break to assess the flash flood analysis.
- **Question 2:** Which parameters most affect the flash flood propagation?
    - **Objective 2:** Develop a new high-quality flash flood data set in a large-scale test facility for the development and calibration of numerical models for extreme events.
- **Question 3:** How does the roughness affect velocities and impact forces associated with flash floods on the built environment?
    - **Objective 3:** Experimental and numerical examination of velocities and impact forces associated with flash floods on the build environment.
- **Question 4:** Can the initial stages of a flash flood be modelled using a 2D model?

- **Question 5:** Is a 3D model required for the prediction of flow, velocities and applied load in the urban settlement?
    - **Objective 4:** Evaluate the performance of 2D and 3D hydrodynamic models considering the movement of the flood wave during flash flood propagation.
- **Question 6:** Can mitigation strategies be developed from the analysis of flow interaction with urban settlements?
    - **Objective 5:** Develop mitigation strategies to re-assess building guidelines in flash flood prone areas.
- **Question 7:** Is OpenFOAM an appropriate open source CFD model for simulating the critical transition from subcritical flow to supercritical flow needed when modelling flash floods?
    - **Objective 6:** Validate OpenFOAM model with experimental data.
- **Question 8:** Is Defra's benchmarking scheme appropriate? Does it need to be reviewed for extreme events?
    - **Objective 7:** Compare OpenFOAM with existing industry models for the modelling of dam breaks.

Towards these aims, Chapter 2 was a literature survey which first discussed the available research on the topic of hydrodynamic modelling including: the numerical schemes involved, Riemann problems, meshing approaches, fitting of the complex boundaries and the tracking of the wet/dry interface. The widely investigated dam break problem was then examined, mathematical, experimental and numerical approaches were presented and the most recent advances in the field discussed. Finally, research on wave structure interaction and its relation to flash foods was explored. Finding the gap in the different aspects of these fields and placing where this research fits, Chapter 3 followed by providing a conceptual overview of flash floods including important terminologies. Differences between riverine floods and flash floods were presented and parameters that affect flash floods reviewed.

Examples of flash floods in the UK include the Boscastle flash flood in 2004, the 2005 event in Helmsley and the 1952 flash flood in Lynmouth. The inspiration for the experimental and numerical modelling undertaken was the August 2004 Boscastle flash flood and a detailed description of the catchment and its characteristics was included in Chapter 3. An idealistic laboratory model of the event was designed using dimensional similarity for scaling the

prototype to the model scale and final dimensions and flow rates, velocities and impact loads were calculated.

Flash floods were generated in a controlled laboratory environment in the Department of Mechanical Engineering in University College London (UCL) for validation of numerical hydrodynamic models. The series of dam break experiments on ramps of different resistance were described in Chapter 4 and the generated high Froude number flows were analysed theoretically and experimentally. The impact of these flows on buildings was also investigated and the whole experiment provided further insight into the analysis of the effect that land use and intensity have on flash flood propagation.

Following the experimental aspect of the research, Chapter 5 described the simulation of flash floods numerically using the open-source software OpenFOAM and specifically its interfoam solver. The aim was to validate the model for extreme flood events and select the optimal parametrisation. First, both 2D and 3D models were validated against known experimental cases and then the models were applied to the experiment presented in Chapter 4. The OpenFOAM models showed that although OpenFOAM is capable of representing complex 2D and 3D flows, the three-dimensionality of flow around the urban settlement and the interactions between flood wave and built structures (e.g modelling of cross waves, hydraulic jumps and modelling of the wake) make 3D models necessary.

Finally, Chapter 6 benchmarked the above OpenFOAM model and compared it with existing industry models for the modelling of dam breaks using a (Defra and Environment Agency, 2010) benchmark case. The same roughness layer used in the experiments presented in Chapter 4 was applied to the benchmarking case and its effect on the applied loads on the building was assessed.

7.2 THESIS CONCLUSIONS

In the following section, each of the research questions will be answered and how each of the objectives was reached will be explained.

The first question **(R1)** inquired whether a dam break is a good representation of a flash flood and whether it guarantees the main characteristic features of flash floods. The first part of this question had already been answered in literature and specifically by (Archer and Fowler, 2015) who defined flash floods in terms of their characteristic features the rapid onset and the rate of rise in water depth, characteristics identical to dam breaks. Following this, in Chapter 4, the different stages of the dam break were clearly defined, described qualitatively

and compared with the known theory. The experimental set up was designed to clearly separate the three stages of the dam break: the emptying of the reservoir, the water flowing down a ramp and finally the interaction of the high Froude number flow with structures. All stages have been researched, analysed and modelled individually in literature but this research found that looking at all three stages of the dam break in combination is closer to the physical processes of flash floods.

The second research question (**R2**) considered which parameters affect most the flash flood propagation. This was answered firstly by researching a catchment's susceptibility to flash floods and translating the variables involved to variables that could be tested in the experimental set up. During the experiments, different reservoir water depths were considered, different roughness layers (vegetated ramp) on the ramp, and different densities of the urban settlement. The experiments thus provided a new high-quality flash flood data set for different parameters. It was found that increasing the friction of the ramp slowed down the flow, thereby reducing its Froude number. In the cases with higher water depth in the reservoir (H200), the reduction of the Froude number resulted in a decrease in applied load on the buildings. The lower reservoir water depth (H100) resulted in overall lower water depths, velocities and loads but when the roughness layer was applied (H100G) even though it decreased the water depths and velocities it did not lower the applied load on the building. Finally, in terms of applied load on the urban settlements, the level of the urban settlement density (one, two, four houses) had no effect on the higher water depth cases whilst in the lower water depths resulted in an increased applied load on the buildings.

Next, a specific question (**R3**) challenged how roughness affects velocities and the impact forces of flash floods on the built environment. This was answered through a combination of experimental and numerical results which suggested a decrease in water depth and velocities and a decrease in impact forces for the higher water depths. In Chapter 6, the same roughness layer was applied to the (Defra and Environment Agency, 2010) benchmark case which consisted of a numerical domain of similar length but with a higher initial water depth ($h_0 = 0.4m$). Interestingly, the outcome was the same as with the experimental test case of Chapter 4. Even a small roughness layer representative of low grass can result in a decrease in applied load of up to 30%.

The performance of 2D and 3D hydrodynamic models was evaluated through two research questions **(R4 & R5)**. Firstly, the potential to model the initial stages of a flash flood using a 2D model was investigated using a 2D OpenFOAM model validated against the experimental

results. It was found that the results showed reasonable agreement with the experimental results and were modelled at a sufficiently short timescale using 2D models with very fine mesh size. The question of whether a 3D model is required for the prediction of flow, velocities and applied load in the urban settlement, was confirmed in Chapter 5 through the 3D simulations of the experimental setup. This was further shown in the benchmarking case in Chapter 6 where the 3D OpenFOAM model, simulated the majority of the hydraulic features even when a very coarse mesh was used.

Through both the experimental and benchmark case, OpenFOAM was validated through peak water depth calibration with two different sets of large-scale experimental data **(R7)** and showed to be an appropriate open source CFD model for simulating the critical transition from subcritical flow to supercritical flow a characteristic feature in flash floods modelling.

Whether the Defra's benchmarking scheme is suitable **(R8)** was discussed at the end of Chapter 6, which argued that the selected dam break benchmarking case is an appropriate example of flash floods but needs to be reviewed in terms of the mesh requirement. The requirements provided for the benchmarking of the different models are considered to be inadequate especially in terms of the mesh refinement. Using a 3D OpenFOAM model and only a 0.1 m mesh in the depth-direction (z-direction) this research showed that in order to obtain a clear understanding of these events and attain a pragmatic assessment of the performance of different models, especially in 2D, a finer mesh requirement needs to be demanded. This will provide a deeper understanding of the model performance but also of the disadvantages of each of the modelling techniques.

Finally, the concluding remarks and the proposal of possible mitigation strategies **(R6)** will be concluded in the last section of this chapter: (i.e. 7.4 Flash Flood Modelling for Flood Risk Analysis).

7.3 FUTURE WORK AND RECOMMENDATIONS

The future work and recommendations are presented in the following section in three categories: experimental, numerical and field recommendations.

Experimental recommendations

The practicality of the experimental setup was demonstrated both during the laboratory testing, the numerical simulations but also by comparing the model to theoretical processes and obtaining an accurate representation. Future experimental studies of dam break interaction with urban settlements could be considered for a similar experimental setup but

with changing characteristics. In a future design, changing ramps could be incorporated, a wider range of initial water depths could be tested and finally different types of roughness layers could be considered.

One other avenue for further development of the experimental modelling of flash floods and development of mitigations strategies would be to investigate the installation of different types of fences in front of the urban settlements. A well-designed fence could effectively act as a breakwater and reduce the force of the flood's first impact. Therefore, fences of different heights, widths, lengths and distances from the urban settlement should be researched to propose an ideal design for flash flood prone areas.

Numerical recommendations

New research topics in the numerical modelling of flash floods have emerged from the outcomes of this thesis. The described 3D OpenFOAM model should be further developed before applying the 2D/3D coupling of these models. The test cases should be examined using a more refined mesh to determine a range of suitable turbulence parameters and eddy viscosities for the modelling of flash floods in order to provide guidance for the parametrization of different models

Furthermore, different order of numerical schemes (already incorporated in the OpenFOAM source code) and their effect on the modelling of the transition from supercritical to subcritical flow should also be investigated. Long-term, new methods should be developed for obtaining the appropriate modelling values and numerical schemes for a variety of different flash flood events based on some basic characteristics.

Finally, another direction in which further research could advance is the validation of the newly created and used equation relating Manning's coefficient n with the surface roughness k_s. This could be achieved numerically by modelling different dam break experiments with known Manning's coefficients n and examining the connection to the roughness height k_s in more depth.

Field work recommendations

As data from real flash floods representing complete real-world flash flood events does not exist, it is suggested to pursue the capture of a small-scale real event. A potentially exciting

avenue to pursue would incorporate the long-term and secure installation of sensors, cameras and measuring equipment in a flash flood prone catchment in order to record the event. This would provide a non-idealised dataset for the validation of numerical model leading to more accurate predictions of flash flood events.

7.4 FLASH FLOOD MODELLING FOR FLOOD RISK ANALYSIS

An increase in the frequency and magnitude of flooding is one of the severe expected consequences of climate change. Flash floods are challenging in nature and as they are expected to be exacerbated by climate change, therefore understanding flash flood dynamics and the effect different drivers have on the flood wave propagation is essential. It is therefore crucial to know how to accurately predict flood propagation and inundation extents in order to contribute to the development of better adaptation and preparedness strategies in flash flood prone areas.

As discussed in earlier chapters and as testimonies from the Boscastle case have shown, flash floods can be unpredictable, but a factor that worsens them is land use due to human activities, projects and river interventions which strengthens the deterioration of the eco-geological systems (Arlikatti et al., 2018).

In terms of mitigation strategies, research has shown that in flood prone areas, the lack of preparation planning for recovery and mitigation strategies results inevitably in higher susceptibility and a deficient approach (Arlikatti et al., 2018). Mitigation strategies that can be considered in flash flood management can be separated into two categories: (i) structural mitigations and (ii) non-structural mitigations. These include but are not limited to: erosion control mats, sustainable drainage systems SuDS, permeable paving, river dredging and realignment, overflow culverts, defence walls, rebuilding of bridges and flood protection structures, books, leaflets and documentaries.

The findings of this research provide an opportunity for further mitigation initiatives in addition to the mitigations already in place, mainly applicable to the UK:

- Flash flood prone catchment areas should be identified especially in catchments with historical flash floods (e.g. Boscastle). The local administration should invest in numerical modelling of the area in case of a flash flood to obtain more detailed information on inundation extents, water depths and applied loads on the buildings.

- Policies and building guidelines in flash flood prone areas should then be re-assessed. Legal frameworks should therefore be put in place for future construction in these areas and a list of structural mitigations should be considered for the reinforcement of existing structures in the urban settlements.
    - Blockage level: Depending on how many buildings there are in an urban settlement and how much blockage these would create in case of a flash flood, the residents should invest together on the reinforcement for example of the front houses from the end of the ramp.
    - Fence: Further work has already been recommended in this area (Section 7.3) for the investigation of different types of fences (heights, widths and distance from the building) in order to effectively provide a breakwater for the first impact wave, ensuring that such a fence would not create additional water submersion for the buildings.
    - Wall reinforcement: Reinforcement of an existing wall should be considered for the buildings that would be strongly impacted by the flood waves.
- Low-vegetated slopes and higher roughness roads (e.g. dirt or gravel roads) should be incorporated in catchment management plans as it has been shown that they can lead to a considerable reduction in the applied loads on the buildings.
- Outreach programs with educational material (e.g. videos) are necessary to emphasise the dangers and raise awareness for flash floods in flash flood prone areas. Residents need to be aware of potential solutions that can even be applied on a resident level and visual aids are a strong persuasion tool.

The direction of research should therefore be to find the most suitable ways to manage flash flood prone catchments in order for extreme events not to overwhelm and overthrow existing mitigation strategies. In that regard, this thesis provided a forward step towards a clearer understanding of flash floods by highlighting the importance of well-defined modelling. As it was proposed, further research should be conducted to hone the currently available tools and to create additional ones that will allow to predict accurately flash floods. In 1988 Purseglove wrote: *"A river is a symbol of changeless change. Rivers have always been boundaries, as well as route-ways"* (Purseglove, 1988). Today more than ever these routes need to be paved appropriately in order to prevent the catastrophic and life-threatening consequences of sudden flash floods.

REFERENCES

Abbott, M.B. and Basco, D.R., 1989. *Computational fluid dynamics: an introduction for engineers.* Longman Scientific & Technical.

Adrien, N.G., 2004. *Computational Hydraulics and Hydrology: An Illustrated Dictionary.* 1st ed.: CRC Press.

Ahmadian, R., Falconer, R.A. and Wicks, J., 2018. Benchmarking of flood inundation extent using various dynamically linked one- and two-dimensional approaches. *Journal of Flood Risk Management,* 11, pp. 314-328.

Ahrens, C.D., 2006. *Meteorology Today: An Introduction to Weather, Climate and the Environment.* 8th ed.: Thomson Learning.

Alestalo, M. and Savijärvi, H., 1985. Mesoscale circulations in a hydrostatic model: coastal convergence and orographic lifting. *Tellus A: Dynamic Meteorology and Oceanography,* 37(2), pp. 156-162.

Ambrose, P., 2011. *Flooding in Bournemouth: 18th August 2011.*

Archer, D.R. and Fowler, H.J., 2015. Characterising flash flood response to intense rainfall and impacts using historical information and gauged data in Britain. *Journal of Flood Risk Management*, pp. S121-S133.

Arlikatti, S., Maghelal, P., Agnimitra, N. and Chatterjee, V., 2018. Should I stay or should I go? Mitigation strategies for flash flooding in India. *International Journal of Disaster Risk Reduction,* 27, pp. 48-56.

Arntsen, A., Collados, X.R. and Tørum, A., 2011. Impact forces on a vertical pile from plunging breaking waves. *Coastal Structures*, pp. 533-544.

Audusse, E., Bouchut, F., Bristeau, M.-O., Klein, R. and Perthame, B.t., 2004. A Fast and Stable Well-Balanced Scheme with Hydrostatic Reconstruction for Shallow Water Flows. *SIAM Journal on Scientific Computing,* 25(6), pp. 2050-2065.

Aureli, F., Dazzi, S., Maranzoni, A., Mignosa, P. and Vacondio, R., 2015. Experimental and numerical evaluation of the force due to the impact of a dam-break wave on a structure. *Advances in Water Resources,* 76, pp. 29-42.

Bai, W. and Eatock Taylor, R., 2007. Numerical simulation of fully nonlinear regular and focused wave diffraction around a vertical cylinder using domain decomposition. *Applied Ocean Research,* 29(1), pp. 55-71.

Balsara, D.S., 2013. The Hydrodynamical Riemann Problem. *Numerical PDE Techniques for Scientists and Engineers* [Online]. University of Notre Dame. Available from: *https://www3.nd.edu/~dbalsara/Numerical-PDE-Course/*.

Bates, P.D., Stewart, M.D., Siggers, G.B., Smith, C.N., Hervouet, J.M. and Sellin, R.H.J., 1998. Internal and external validation of a two-dimensional finite element code for river flood

simulations. *Proceedings of the Institution of Civil Engineers-Water Maritime and Energy,* 130(3), pp. 127-141.

Bellos, C.V., 2004. Experimental Measurements of Flood Wave Created by a Dam Break. *European Water,* 7(8), pp. 3-15.

Bellos, C.V. and Hrissanthou, V., 2011. Numerical Simulation of a Dam-Break Flood Wave. *European Water,* 33, pp. 45-53.

Bellos, C.V., Soulis, J.V. and Sakkas, J.G., 1991. Computation of two-dimensional dam-break-induced flows. *Advances in Water Resources,* 14(1), pp. 31-41.

Berberovic, E., van Hinsberg, N.P., Jakirlic, S., Roisman, I.V. and Tropea, C., 2009. Drop impact onto a liquid layer of finite thickness: dynamics of the cavity evolution. *Phys Rev E Stat Nonlin Soft Matter Phys,* 79(3 Pt 2), pp. 1-15.

Biscarini, C., Di Francesco, S. and Manciola, P., 2010. CFD modelling approach for dam break flow studies. *Hydrology and Earth System Sciences,* 14(4), pp. 705-718.

Biscarini, C., Francesco, S.D. and Manciola, P., 2009. CFD modelling approach for Dam break flow studies *Hydrol. Earth. Syst. Sci. Discuss.*, pp. 6759–6793.

Blazek, J., 2005. *Computational fluid dynamics : principles and applications.* 2nd ed. ed. Amsterdam ;: Elsevier.

Boccotti, P., 2015. Calculation of Wave Forces on Three-Dimensional Space Frames. *Wave Mechanics and Wave Loads on Marine Structures*.

Boris, J.P. and Book, D.L., 1971. Flux-Corrected Transport. *Journal of Computational Physics,* 135, pp. 172–186.

Braud, I., Roux, H., Anquetin, S., Maubourguet, M.-M., Manus, C., Viallet, P. and Dartus, D., 2010. The use of distributed hydrological models for the Gard 2002 flash flood event: Analysis of associated hydrological processes. *Journal of Hydrology,* 394(1–2), pp. 162-181.

British Geological Survey, 2006. *Guide to Permeability Indices.* Keyworth, Nottingham.

British Geological Survey, 2016. *Geology of Britain Viewer* [Online]. Available from: http://mapapps.bgs.ac.uk/geologyofbritain/home.html [Accessed 15 March].

Bukreev, V. and Zykov, V., 2008. Bore impact on a vertical plate. *Journal of Applied Mechanics and Technical Physics,* 49, pp. 926-933.

Bukreev, V.I., 2009. Force action of discontinuous waves on a vertical wall. *Journal of Applied Mechanics and Technical Physics,* 50(2), pp. 278-283.

Burt, S., 2005. Cloudburst upon Hendraburnick Down: The Boscastle storm of 16 August 2004. *Waether,* 60(8).

Canelas, R., Murillo, J. and Ferreira, R.M.L., 2013. Two-dimensional depth-averaged modelling of dam-break flows over mobile beds. *Journal of Hydraulic Research,* 51(4), pp. 392-407.

Carrillo, S.A., 2013. *Cartesian Grid Generation.*

Castro-Orgaz, O. and Chanson, H., 2017. Ritter's dry-bed dam-break flows: positive and negative wave dynamics. *Environmental Fluid Mechanics,* 17(4), pp. 665-694.

Causon, D.M., Ingram, D.M., Mingham, C.G., Yang, G. and Pearson, R.V., 2000. Calculation of shallow water flows using a Cartesian cut cell approach. *Advances in Water Resources,* 23(5), pp. 545-562.

Chadwick, A., Morfett, J. and Borthwick, M., 2004. *Hydraulics in civil and environmental engineering.* 4th ed. Oxon: Spon Press.

Chanson, H., 2003. Two-phase flow charasteristics of an unsteady dam break wave flow. *IAHR Congress*, Thessaloniki.

Chanson, H., 2004a. Experimental study of flash flood surges down a rough sloping channel. *Water Resources Research,* 40.

Chanson, H., 2004b. *Hydraulics of Open Channel Flow.* Second ed.

Chanson, H., 2004c. Turbulent shear flows. In: H. Chanson, ed. *Environmental Hydraulics of Open Channel Flows.* Oxford: Butterworth-Heinemann, pp. 49-64.

Chanson, H., 2009. Application of the method of characteristics to the dam break wave problem. *Journal of Hydraulic Research,* 47(1), pp. 41-49.

Chaudhry, M.H., 2008. *Open-Channel Flow.* New York: Springer.

Chella, M.A., Tørum, A. and Myrhaug, D., 2012. An Overview of Wave Impact Forces on Offshore Wind Turbine Substructures. *Energy Procedia,* 20, pp. 217-226.

Chen, H.Y., Xu, W.L., Deng, J., Xue, Y. and Li, J., 2014a. Experimental investigation of pressure load exerted on a downstream dam by dam-break flow. *Journal of Hydraulic Engineering,* 140, pp. 199-207.

Chen, L.F., Zang, J., Hillis, A.J., Morgan, G.C.J. and Plummer, A.R., 2014b. Numerical investigation of wave–structure interaction using OpenFOAM. *Ocean Engineering,* 88, pp. 91-109.

Christensen, E., Bredmose, H. and Hansen, E., 2005. Extreme wave forces and wave run-up on offshore wind- turbine foundations. *Proceedings of Copenhagen Offshore Wind Conference*.

Climate Data, 2018. *Climate: Aberystwyth* [Online]. Available from: *https://en.climate-data.org/location/6805/* [Accessed 28 June].

Collier, C.G., 2007. Flash flood forecasting: What are the limits of predictability? *Quarterly Journal of the Royal Meteorological Society,* 133(622), pp. 3-23.

Collier, C.G. and Fox, N.I., 2003. Assessing the flooding susceptibility of river catchments to extreme rainfall in the United Kingdom AU - Collier, C.G. *International Journal of River Basin Management,* 1(3), pp. 225-235.

Colombo, A.G., Hervás, J. and Arellano, A.L.V., 2002. *NEDIES Project: Guidelines on Flash Flood Prevention and Mitigation.* Available from: https://esdac.jrc.ec.europa.eu/Esdb_Archive/eusoils_docs/other/EUR20386EN.pdf.

COMET UCAR, 2010. *Flash Flood Early Warning System Reference Guide.* University Corporation for Atmospheric Research.

Corps of Engineers, 1960. *Flood Resulting from suddenly breached dams.* Mississippi.

Corte, C. and Grilli, S.T., 2006. Numerical Modeling of Extreme Wave Slamming On Cylindrical Offshore Support Structures*The Sixteenth International Offshore and Polar Engineering Conference*, 2006/1/1/ San Francisco, California, USA. ISOPE: International Society of Offshore and Polar Engineers, p. 8. https://doi.org/

Costabile, P. and Macchione, F., 2015. Enhancing river model set-up for 2-D dynamic flood modelling. *Environmental Modelling & Software,* 67, pp. 89-107.

Coulthard, T., Frostick, L., Hardcastle, H., Jones, K., Rogers, D., Scott, M. and Bankoff, G., 2007. *The June 2007 floods in Hull*

Craft, T.J., 2010. ***Body-Fitted Grids*** [Online]. Available from: http://cfd.mace.manchester.ac.uk/twiki/pub/Main/TimCraftNotes_All_Access/ms4-bodyfg.pdf [Accessed 19 September].

Craya, A., 1946. Calcul graphique regime variable dans le canaux, la Houille Blanche. *New Ser.,* 1, pp. 19-38.

Cushman-Roisin, B., 1974. *Environmental Fluid Mechanics.* 1st ed.: John Wiley & Sons.

Damián, S.M., 2012. Description and utilization of interFoam multiphase solver. Available from: http://infofich.unl.edu.ar/upload/3be0e16065026527477b4b948c4caa7523c8ea52.pdf [Accessed 19 September].

Dawson, C. and Mirabito, C.M., 2008. *The Shallow Water Equations.* University of Texas at Austin. Available from: http://users.oden.utexas.edu/~arbogast/cam397/dawson_v2.pdf.

Defra and Environment Agency, 2004. *Extreme rainfall event recognition phase 2 work package 5: Establishing a user requirement for a decision-support tool. .* Department of the Environment, Food and Rural Affairs, London, UK.

Defra and Environment Agency, 2010. *Benchmarking of 2D Hydraulic Modelling Packages.* Bristol.

Deng, X., Liu, H. and Lu, S., 2018. Analytical Study of Dam-Break Wave Tip Region. *Journal of Hydraulic Engineering,* 144(5).

DHI, 2011. *MIKE 21 FLOW MODEL FM.*

Dillingham, J., 1981. Motion Studies of a Vessel with Water on Deck. *Marine Technology,* 18(1), pp. 38-50.

Dressler, R.F., 1952. Hydraulic resistance effect upon the dam-break functions. *Journal of Research of the National Bureau of Standards,* 49(3).

Dressler, R.F., 1954. Comparison of Theories and Experiments for the Hydraulic Dam-break Wave. *Association of Scientific Hydrology,* 38.

EEA, 2015. European Past Floods. European Environment Agency. Available from: *https://www.eea.europa.eu/data-and-maps/data/european-past-floods*.

Eguiazaroff, J.B., 1935. Regulation of the water level in the reaches of canalized rivers. *XVI International Congess of Navigation, Brussels*.

EMDAT, 2017. *Number of disasters* [Online]. Université catholique de Louvain, Brussels, Belgium [Accessed 23 January 2019].

Environment Agency, 2016. *Catchment Data Explorer* [Online]. Available from: *http://environment.data.gov.uk/catchment-planning/WaterBody/GB108049007170* [Accessed 8 February].

ESSL, 2018. *Deadly flash floods in 2018* [Online]. Available from: *https://www.essl.org/cms/deadly-flash-floods-in-2018/* [Accessed 14 December].

Euler, L., 1770. *Vollstandige Anleitung zur Algebra* Academy of Sciences, St Peterburg

Falconer, R.A., 2012. Modelling extreme flood events and associated proxesses in rivers, estuaries and coastal environments*10th International Conference on Hydroscience and Engineering (ICHE 2012)*, 4-8 November Orlando, USA.

Fent, I., Zech, Y. and Soares-Frazão, S., 2019. Dam-break flow experiments over mobile bed: velocity profile. *Journal of Hydraulic Research,* 57(1), pp. 131-138.

Ferreira, R.M.L., Alves, E.C.T.L., Leal, J.G.A.B. and Cardos, A.H., 2006. River Flow 2006, Two Volume Set. *International Conference on Fluvial Hydraulics*, Lisbon, Portugal. CRC Press.

Ferziger, J.H., 1999. Introduction to the physics and simulation of turbulence. Von Karman Institute for Fluid Dynamics, Rhode Saint Genese, Belgium, pp. 1-41.

Fewtrell, T.J., Bates, P.D., Wit, A.d., Asselman, N. and Sayers, P., 2009. Comparison of varying complexity numerical models for the prediction of flood inundation in Greenwich, UK. *Flood Risk Management: Research and Practice*, pp. 95-104.

Flow Science, 2016. *Grid Systems* [Online]. Available from: https://www.flow3d.com/home/resources/cfd-101/general-cfd/grid-systems [Accessed 20 September].

Fraccarollo, L., Rosatti, G. and Begnudelli, L., 2010. Experimental study of dam-break problem over a bed step. *IAHR Congress*, Edimbourgh.

Fraccarollo, L. and Toro, E.F., 1995. Experimental and numerical assessment of the shallow water model for two-dimensional dam-break type problems. *Journal of Hydraulic Research,* 33(6).

Furbo, E., 2010. *Evaluation of RANS turbulence models for flow problems with significant impact of boundary layers* (Master), Uppsala Universitet.

Gillespie, K., 2017. *Using an Ultrasonic Level Sensor* [Online]. Available from: https://www.maxbotix.com/articles/water-depth-sensing.htm [Accessed 25 April].

Goda, Y., Haranaka, S. and Kitahata, M., 1966. Study of Impulsive Breaking Wave Forces on Piles. *Report of Port and Harbor Research Institute,* 5(6).

Godunov, S.K., 1959. A difference method for numerical calculation of discontinuous solutions of the equations of hydrodynamics. *Mat. Sb.,* 47(89)(3), pp. 271–306.

Golding, B., Clark, P. and May, B., 2005. The Boscastle flood: Meteorological analysis of the conditions leading to flooding on 16 August 2004. *Weather,* 60(8).

Goseberg, N., Stolle, J., Derschum, C. and Nistor, I., 2017. Swing gate generated dam-break waves.*37th IAHR world congress*Kuala Lumpur, Malaysia. IAHR.

Greenshields, C.J., 2015. *OpenFOAM:The Open Source CFD Toolbox, User Guide.*

Halcrow Group Ltd, 2017. *Boscastle Flood Defences.*

Hamza, S.B., Habli, S., Saïd, N.M., Bournot, H. and Palec, G.L., 2015. Numerical Simulation of Wave-Structure Interaction around an Obstacle. *Design and Modeling of Mechanical Systems - II. Lecture Notes in Mechanical Engineering*.

He, Z., Wu, T., Weng, H., Hu, P. and Wu, G., 2017. Numerical simulation of dam-break flow and bed change considering the vegetation effects. *International Journal of Sediment Research,* 32(1), pp. 105-120.

Heller, V., 2011. Scale effects in physical hydraulic engineering models. *Journal of Hydraulic Research,* 49(3), pp. 293-306.

Heller, V., 2012. *Model - Prototype Similarity*. [Accessed.

Hogg, A. and Pritchard, D., 2004. The effects of hydraulic resistance on dam-break and other shallow inertial flows. *Journal of Fluid Mechanics,* 501, pp. 179-212.

Horritt, M.S. and Bates, P.D., 2001. Predicting floodplain inundation: raster-based modelling versus the finite-element approach. *Hydrological Processes,* 15(5), pp. 825-842.

Horritt, M.S. and Bates, P.D., 2002. Evaluation of 1D and 2D numerical models for predicting river flood inundation. *Journal of Hydrology,* 268(1-4), pp. 87-99.

Hou, J., Liang, Q., Simons, F. and Hinkelmann, R., 2013. A stable 2D unstructured shallow flow model for simulations of wetting and drying over rough terrains. *Computers & Fluids,* 82, pp. 132-147.

Hou, J., Liang, Q., Zhang, H. and Hinkelmann, R., 2014. Multislope MUSCL method applied to solve shallow water equations. *Computers & Mathematics with Applications,* 68(12, Part A), pp. 2012-2027.

HR Wallingford, 2005a. The Boscastle flood of 16 August 2004: Characteristics, causes and consequences*40th Defra Flood and Coastal Management Conference*, 5-7 July York, UK.

HR Wallingford, 2005b. *Flooding in Boscastle and North Cornwall, August 2004.*

Hu, H., Zhang, J. and Li, T., 2018. Dam-Break Flows: Comparison between Flow-3D, MIKE 3 FM, and Analytical Solutions with Experimental Data. *Applied Sciences,* 8(2456).

Huang, W., Cao, Z.-X., Qi, W.-J., Pender, G. and Zhao, K., 2015. Full 2D hydrodynamic modelling of rainfall-induced flash floods. *Journal of Mountain Science,* 12(5), pp. 1203-1218.

Huang, Y., Zhang, N. and Pei, Y., 2014. Well-Balanced Finite Volume Scheme for Shallow Water Flooding and Drying Over Arbitrary Topography. *Engineering Applications of Computational Fluid Mechanics,* 7(1), pp. 40-54.

Hunt, B., 1982. Asymptotic solution for dam-break problem. *Journal of the Hydraulics Division,* 108(1), pp. 115-126.

Hunt, B., 1984. Perturbation solution for dam-break floods. *Journal of Hydraulic Engineering,* 110(8), pp. 1058–1071.

Hunter, N.M., Bates, P.D., Neelz, S., Pender, G., Villanueva, I., Wright, N.G., Liang, D., Falconer, R.A., Lin, B., Waller, S., Crossley, A.J. and Mason, D.C., 2008. Benchmarking 2D hydraulic models for urban flooding. *Proceedings of the Institution of Civil Engineers - Water Management,* 161(1), pp. 13-30.

Huppert, H.E., 2006. Gravity currents: a personal perspective. *Journal of Fluid Mechanics,* 554, pp. 299-322.

Iglesias, V.C.M., Pinzon, A.B. and Montes, D.V., 2006. A new approach to solbing boundary conditions in shallow water equations using a Riemann sikver. *International Conference on Fluvial Hydraulics*, Lisbon, Portugal.

Into Cornwall, 2015. *Boscastle* [Online]. Available from: *http://www.intocornwall.com/engine/azabout.asp?guide=Boscastle* [Accessed 15 March].

IPCC, 2007. *Climate Change 2007: Synthesis Report.* Geneva, Switzerland: IPCC.

IPCC, 2014. *Climate Change 2014: Synthesis Report.* Geneva, Switzerland: IPCC.

IPCC, 2017. Scoping of the IPCC sixth assessment report (AR6). *Forty-sixth session of the IPCC*, 6-10 September Montreal, Canada.

Jamieson, S.R., Lhomme, J., Wright, G. and Gouldby, B., 2012. A highly efficient 2D flood model with sub-element topography. *Proceedings of the ICE - Water Management,* 165(10), pp. 581-595.

Jayaratne, R., 2010. Hydraulic roughness – links between Manning's coefficient, Nikuradse's equivalent sand roughness and bed grain size. *5th Annual Conference Proceedings of Advances in Computing and Technology*, The School of Computing and Technology, University of East London. pp. 27-32.

Jenkins, C., 2013. *Eddy viscosity* [Online]. University of Colorado. Available from: *http://instaar.colorado.edu/~jenkinsc/AdOc2013/lectures/eddyvisc_2013.pdf* [Accessed 2 February].

Jianchu, X., Eriksson, M., Ferdinand, J. and Merz, J., 2006. *Managing Flash Floods and Sustainable Development in the Himalayas.* Kathmandu, Nepal.

Johnson, M.W., 2013. A novel Cartesian CFD cut cell approach. *Computers & Fluids,* 79, pp. 105-119.

Kirshbaum, J.D., Adler, B., Kalthoff, N., Barthlott, C. and Serafin, S., 2018. Moist Orographic Convection: Physical Mechanisms and Links to Surface-Exchange Processes. *Atmosphere,* 9(3).

Kjeldsen, T.R., Macdonald, N., Lang, M., Mediero, L., Albuquerque, T., Bogdanowicz, E., Brázdil, R., Castellarin, A., David, V., Fleig, A., Gül, G.O., Kriauciuniene, J., Kohnová, S., Merz, B., Nicholson, O., Roald, L.A., Salinas, J.L., Sarauskiene, D., Šraj, M., Strupczewski, W., Szolgay, J., Toumazis, A., Vanneuville, W., Veijalainen, N. and Wilson, D., 2014. Documentary evidence of past floods in Europe and their utility in flood frequency estimation. *Journal of Hydrology,* 517, pp. 963-973.

Kleefsman, K.M.T., Fekken, G., Veldman, A.E.P., Iwanowski, B. and Buchner, B., 2005. A volume-of-fluid based simulation method for wave impact problems. *Journal of Computational Physics,* 206(1), pp. 363-393.

Kobiyama, M. and Goerl, R.F., 2007. Quantitative method to distinguish flood and flash flood as disasters. *SUISUI Hydrological Research Letters,* 1, pp. 11-14.

Kong, C., 2011. *Comparison of Approximate Riemann Solvers.* (Master of Science in Mathematical and Numerical Modelling of the Atmosphere and Oceans), University of Reading.

Korobkin, A. and Oguz, Y., 2008. The initial stage of dam-break flow. *Journal of Engineering Mathematics,* 63, pp. 293–308.

Larocque, L.A., Imran, J. and Chaudhry, M.H., 2013. 3D numerical simulation of partial breach dam-break flow using the LES and k–e turbulence models,. *Journal of Hydraulic Research,* 51(12), pp. 145-157.

Lauber, G. and Hager, W.H., 1998. Experiments to dambreak wave: Horizontal channel. *Journal of Hydraulic Research,* 36(3), pp. 291-307.

Launder, B.E. and Spalding, D.B., 1974. The numerical computation of turbulent flows. *Computer Methods in Applied Mechanics and Engineering,* 3(2), pp. 269-389.

Lee, T.-h., Zhou, Z. and Cao, Y., 2001. Numerical Simulations of Hydraulic Jumps in Water Sloshing and Water Impacting. *Journal of Fluids Engineering,* 124(1), pp. 215-226.

Lesieur, M., 1994. *La turbulence.* 1st ed. France: Presses Universitaires de Grenoble.

Levin, L., 1952. Evolution of wave created by breach of large dams*Yogoslav, Nat. Committee on Large Dams II meeting*. pp. 104-118.

Lhomme, J., Gutierrez-Andres, J., Weisgerber, A., Davison, M., Mulet-Marti, J., Cooper, A. and Gouldby, B., 2010. Testing a new two-dimensional flood modelling system: analytical tests and application to a flood event. *Journal of Flood Risk Management,* 3(1), pp. 33-51.

Liang, Q. and Borthwick, A.G.L., 2009. Adaptive quadtree simulation of shallow flows with wet–dry fronts over complex topography. *Computers & Fluids,* 38(2), pp. 221-234.

Liang, Q., Borthwick, A.G.L. and Stelling, G., 2004. Simulation of dam- and dyke-break hydrodynamics on dynamically adaptive quadtree grids. *International Journal for Numerical Methods in Fluids,* 46(2), pp. 127-162.

Liang, Q., Zang, J., Borthwick, A.G.L. and Taylor, P.H., 2007. Shallow flow simulation on dynamically adaptive cut cell quadtree grids. *International Journal for Numerical Methods in Fluids,* 53(12), pp. 1777-1799.

Lin, M.-Y. and Huang, L.-H., 2012. Numerical simulation of wave–structure interaction using a Lagrangian vortex method. *Ocean Engineering,* 44, pp. 11-22.

Lincoln, W.S., Zogg, J. and Brewster, J., 2016. Addition of a Vulnerability Component to the Flash Flood Potential Index. Available from: *https://www.weather.gov/media/lmrfc/tech/2016_Vulnerability_Component_FFPI.pdf* [Accessed 15 April 2017].

Liu, H. and Liu, H., 2017. Experimental Study on Dam-Break Hydrodynamic Characteristics Under Different Conditions. *Journal of Disaster Research,* 12(1), pp. 198-207.

Liu, H., Liu, H., Guo, L. and Lu, S., 2017. Experimental study on the dam-break hydrographs at the gate location. *Journal of Ocean University of China,* 16(4), pp. 697–702.

Liu, X., 2014. Open-Channel Hydraulics: From Then to Now and Beyond. *Handbook of Environmental Engineering.* Springer, pp. 127-158.

Lobovský, L., Botia-Vera, E., Castellana, F., Mas-Soler, J. and Souto-Iglesias, A., 2014. Experimental investigation of dynamic pressure loads during dam break. *Journal of Fluids and Structures,* 48, pp. 407-434.

Lopes, P., Leandro, J., Carvalho, R.F.d. and Martins, R., 2012. Hydraulic behaviour of a gully under surcharge conditions. *9th InternationalConference on Urban Drainage Modelling*, Belgrade.

Marques, J.M.F., 2014. Introduction to the Finite Volumes Method. Application to the Shallow Water Equations.

Marrone, S., Antuono, M., Colagrossi, A., Colicchio, G., Le Touzé, D. and Graziani, G., 2011. δ-SPH model for simulating violent impact flows. *Computer Methods in Applied Mechanics and Engineering,* 200(13-16), pp. 1526-1542.

Marsh, T.J. and Hannaford, J., 2007. *The summer 2007 floods in England and Wales – a hydrological appraisal* [Online]. ed. Available from: [Accessed 20 September].

Marsooli, R. and Wu, W., 2014. 3-D finite-volume model of dam-break flow over uneven beds based on VOF method. *Advances in Water Resources,* 70, pp. 104-117.

Marsooli, R. and Wu, W., 2015. Three-Dimensional Numerical Modeling of Dam-Break Flows with Sediment Transport over Movable Beds. *Journal of Hydraulic Engineering,* 141(1).

Martin, J.C. and Moyce, W.J., 1952. An Experimental Study of the Collapse of Liquid Columns on a Rigid Horizontal Plane. *Philosophical Transactions of the Royal Society of London Series a-Mathematical and Physical Sciences,* 244(882), pp. 312-324.

McKinley, G., 2013. *Similarity* [Online]. Available from: *https://ocw.mit.edu/courses/mechanical-engineering/2-25-advanced-fluid-mechanics-fall-2013/dimensional-analysis/MIT2_25F13_Similarity.pdf* [Accessed 20 September].

McMullin, N., 2015. *Numerical and experimental modelling of dam break interaction with a sediment bed.* (PhD thesis), University of Nottingham.

Meesuk, V., Vojinovic, Z., Mynett, A.E. and Abdullah, A.F., 2015. Urban flood modelling combining top-view LiDAR data with ground-view SfM observations. *Advances in Water Resources,* 75, pp. 105-117.

Merz, R. and Bloschl, G., 2003. A process typology of regional floods. *Water Resources Research,* 39(12), pp. 5.1-5.20.

Met Office, 2010a. *UK Climate* [Online]. Available from: *https://www.metoffice.gov.uk/public/weather/climate/#?tab=climateMaps* [Accessed 27 August].

Met Office, 2010b. *UK climate averages: Bude* [Online]. Available from: *https://www.metoffice.gov.uk/research/climate/maps-and-data/uk-climate-averages/gchc0ssk0* [Accessed 15 February].

Met Office, 2011a. *Birmingham climate* [Online]. Available from: *https://www.metoffice.gov.uk/public/weather/climate/gcqdt4b2x* [Accessed 14 January].

Met Office, 2011b. *Keswick climate* [Online]. Available from: *https://www.metoffice.gov.uk/public/weather/climate/gcty8njjs* [Accessed 14 January].

Met Office, 2013. *Exceptionally wet weather - November 2012* [Online]. Available from: *https://www.metoffice.gov.uk/climate/uk/interesting/november-2012* [Accessed 28 June].

Meyer, T., 2012. Root Mean Square Error Compared to, and Contrasted with, Standard Deviation. *Surveying and Land Information Science,* 72.

Miao, Q., Yang, D., Yang, H. and Li, Z., Establishing a rainfall threshold for flash flood warnings in China's mountainous areas based on a distributed hydrological model. *Journal of Hydrology*.

Mohanty, A.K., 2006. *Fluid Mechanics.* 2nd ed. New Delhi: Prentice-Hall of India Private Limited.

Moler, C., 2011. Shallow Water Equations. *Experiments with MATLAB.*

Morison, J.R., Johnson, J.W. and Schaaf, S.A., 1950. The Force Exerted by Surface Waves on Piles. *Journal of Petroleum Technology,* 2(05), pp. 149-154.

Muchan, K.M., Nikos; Barker, Lucy; Turner, Stephen; Lewis, Melinda; Clemas, Sandie, 2018. *Hydrological summary for the United Kingdom: May 2018.*: U. Wallingford, (CEH Project no. C04954).

Murray, S.J., Smith, A.D. and Phillips, J.C., 2012. A Modified Flood Severity Assessment for Enhanced Decision Support: Application to the Boscastle Flash Flood of 2004. *Weather and Forecasting,* 27(5), pp. 1290-1297.

NEXTfoam, 2014. *Boundary Conditions - OpenFOAM-2.3.0.*

Nicholas Pearson Associates, 2012. *Boscastle Flood Alleviation Scheme* [Online]. Available from: *http://www.npaconsult.co.uk/projects.asp?gid=99&pid=16&pkeyword=&prelated=&pproject* [Accessed 5 April].

Nielsen, C., 2011. *Introduction and Overview of TUFLOW FV and its application* [Workshop Presentations]. Available from: *http://www.edenvaleyoung.com/en/bits/dloads/TUFLOW2011/TWS2011_W1_P1_TUFLOW_FV.pdf*

Ning, D.Z., Zang, J., Liu, S.X., Eatock Taylor, R., Teng, B. and Taylor, P.H., 2009. Free-surface evolution and wave kinematics for nonlinear uni-directional focused wave groups. *Ocean Engineering,* 36(15), pp. 1226-1243.

North Cornwall District Council, 2004. *North Cornwall District Council* [Online]. Available from: *www.ncdc.gov.uk* [Accessed 2 April].

Novatech, 2015. Certificate of product test / calibration.

O'Brien, J., Julien, P. and Fullerton, W., 1993. Two-Dimensional Water Flood and Mudflow Simulation. *Journal of Hydraulic Engineering,* 119(2).

Oertel, M. and J.Bung, D.B., 2012. Initial stage of two-dimensional dam-break waves: Laboratory versus VOF. *Journal of Hydraulic Research,* (50), pp. 89-97.

Ogden, F.L., Sharif, H.O., Senarath, S.U.S., Smith, J.A., Baeck, M.L. and Richardson, J.R., 2000. Hydrologic analysis of the Fort Collins, Colorado, flash flood of 1997. *Journal of Hydrology,* 228(1–2), pp. 82-100.

Olivari, D. and Benocci, C., 2014. Introduction to the modelling of turbulence. Von Karman Institute for Fluid Dynamics, Rhode Saint Genese, Belgium.

Open TELEMAC, 2016. *TELEMAC-2D - Two-dimensional hydrodynamic* [Online]. Available from: *http://www.opentelemac.org/index.php/presentation?id=17* [Accessed 10 August].

Ordnance Survey, 2017. *Boscastle Centre* [Online]. GB: Ordnance Survey. Available from: *http://edina.ac.uk/digimap* [Accessed 2 February].

Oxford University Press, 2010. *Oxford Dictionary of English,.* 3rd ed.: Oxford University Press.

Oxford University Press, 2018. *Oxford Index.*

Ozmen-Cagatay, H., Kocaman, S. and Guzel, H., 2014. Investigation of dam-break flood waves in a dry channel with a hump. *Journal of Hydro-environment Research,* 8(3), pp. 304-315.

Peng, S.H., 2012. 1D and 2D Numerical Modeling for Solving Dam-Break Flow Problems Using Finite Volume Method. *Journal of Applied Mathematics,* 2012, pp. 1-14.

Peng, S.H. and Chen, S.C., 2006. Comparison of numerical and experimental study of dam-break induced mudflow. *Sediment Dynamics and the Hydromorphology of Fluvial Systems,* 306, pp. 548-555.

Pilotti, M., Tomirotti, M., Valerio, G. and Bacchi, B., 2010. A simplified prediction model for the outflow hydrograph due to partial dam break. *Journal of Hydraulic Engineering,* 136(10).

Pinto, F.T., 2012. Scaling Issues in Hydraulic Modelling. *World Register of Marine Species*.

Pohle, F.V., 1950. *The Lagragian equations of hydrodynamics: solutions which are analytic functions of time.* PhD Thesis.

Pope, S., 1985. Pdf methods for turbulent reactive flows. *Prog. Energy Combust. Sci.,* 11, pp. 119–192.

Pope, S.B., 2000. *Turbulent Flows.* 1st ed. Cornell University.

Purseglove, J., 1988. *Taming the flood.* 3rd ed.: William Collins.

Qian, H., Cao, Z., Liu, H. and Pender, G., 2018. New experimental dataset for partial dam-break floods over mobile beds. *Journal of Hydraulic Research,* 56(1), pp. 124-135.

Raad, P.E. and Bidoae, R., 2005. The three-dimensional Eulerian–Lagrangian marker and micro cell method for the simulation of free surface flows. *Journal of Computational Physics,* 203(2), pp. 668-699.

Rashid, A.F., Kaur, B. and O.P.Aggarwal, 2012. Leh cloudburst and its medico-legal implications. *JK- Practitioner,* 17(1-3).

Re, R., 1946. A study of sudden water releases from a body of water to a canal by the graphical method: La Houille Blanche. 1(3), pp. 181-187.

Reed, S., Schaake, J. and Zhang, Z., 2007. A distributed hydrologic model and threshold frequency-based method for flash flood forecasting at ungauged locations. *Journal of Hydrology,* 337(3–4), pp. 402-420.

Ritter, A., 1892. Die Fortpflanzung der Wasserwellen. . *Vereine Deutcher Ingenieure Zeitswchrift,* 36, pp. 947-954.

Roca, M. and Davison, M., 2010. Two dimensional model analysis of flash-flood processes: application to the Boscastle event. *Journal of Flood Risk Management,* 3(1), pp. 63-71.

Ros, X., 2011 Master thesis, , 2011. *Impact forces on a vertical pile from plunging breaking waves.* (Masters in the department of Civil and Transport Engineering), Norwegian University of Science and Technology, Trondheim.

Rowiński, P. and Radecki-Pawlik, A., 2015. *Rivers – Physical, Fluvial and Environmental Processes.* 1st ed. Switzerland: Springer.

Sánchez-Cordero, E., Gómez, M. and Bladé, E., 2017. Three-dimensional numerical analysis of a dam-break using OpenFOAM *Proceedings of the Institute for System Programming of the RAS,* 29(6), pp. 311-320.

Sawaragi, T. and Nochino, M., 1984. Impact forces of nearly breaking waves on a vertical circular cylinde. *Coastal Engineering in Japan,* 27, p. 249 263. .

Schoklitsch, A., 1917. Über dambruchwellen. *Königliche Akademie der Wissenschaften, Vienna*. pp. 1489–1514.

Schulze, L. and Thorenz, C., 2014. The Multiphase Capabilities of the CFD Toolbox OpenFOAM for Hydraulic Engineering Applications In: B.f. Wasserbau, ed. *ICHE*Hamburg.

Sene, K., 2013. *Flash Floods: Forecasting and Warning.* 1st ed.: Springer.

Shigematsu, T., Liu, P.L.F. and Oda, K.J., Numerical modeling of the initial stages of dam-break waves. *Journal of Hydraulic Research,* 42, pp. 183-195.

Shrestha, A.B., Shah, S.H. and Karim, R., 2008. *Resource Manual on Flash Flood Risk Management.* Kathmandu.

Smith, G., 2003. Determining the hydrologic response of FFMP basins to heavy rain by analyzing their physiographic characteristics. Available from: http://www.cbrfc.noaa.gov/papers/ffp_wpap.pdf [Accessed 10 April 2017].

Soares-Frazão, S., 2007. Experiments of dam-break wave over a triangular bottom sill. *Journal of Hydraulic Research,* 45(sup1), pp. 19-26.

Soares-Frazão, S., Noël, B., Spinewine, B. and Zech, Y., 2003a. *The isolated building test case : results from the IMPACT benchmark.* Louvain-la-Neuve, Belgium.

Soares-Frazão, S., Noël, B., Spinewine, B. and Zech, Y., 2003b. The isolated building test case: results from the IMPACT benchmark. *IMPACT Investigation of Extreme Flood Processes and Uncertainty.* Louvain-la-Neuve, Belgium.

Soares-Frazão, S. and Zech, Y., 2002a. *Dam-break flow experiment: The isolated building test case* [Online]. Available from: http://www.impact-project.net/wp3_technical.htm [Accessed 15 May].

Soares-Frazão, S. and Zech, Y., 2002b. Dam Break in Channels with 90° Bend. *Journal of Hydraulic Engineering*, pp. 956-968.

Soares-Frazão, S. and Zech, Y., 2007. Experimental study of dam-break flow against an isolated obstacle. *Journal of Hydraulic Research,* 45(SPEC. ISS., 2007), pp. 27-36.

Soares-Frazão, S. and Zech, Y., 2008. Dam-break flow through an idealised city. *Journal of Hydraulic Research,* 46(5), pp. 648-658.

Solantie, R., 1975. The influence of the Baltic Sea and the Gulf of Bothnia on the weather and climate of northern Europe, especially Finland, in autumn and in winter. *Finnish Meteorological Institute Contributions,* 70, p. 28.

Stansby, P.K., Chegini, A. and Barnes, T.C.D., 1998. The initial stages of dam-break flow. *Journal of Fluid Mechanics,* 374, pp. 407-424.

Stoker, J.J., 1957. Water Waves. The mathematical theory with applications. *Wiley-Interscience Publication*, New York. John Wiley & Sons.

Stolle, J., Ghodoosipour, B., Derschum, C., Nistor, I., Petriu, E. and Goseberg, N., 2018. Swing gate generated dam-break waves. *Journal of Hydraulic Research*, pp. 1-13.

Strunz, T., Wiest, A., Fleury, A. and Fröhlich, T., 2004. Influence of turbulence on ultrasonic flow measurements*5th IGHEM conference 2004*Lucerne.

Su, S.T. and Barnes, H., 1970. Geometric and frictional effects on sudden releases. *Journal of the hydraulics Division,* 96(11), pp. 2185-2200.

Testa, G., Zuccalà, D., Alcrudo, F., Mulet, J. and Soares-Frazão, S., 2007. Flash flood flow experiment in a simplified urban district. *Journal of Hydraulic Research,* 45(Extra issue), pp. 37-44.

Timbe, L., 2007. *River flooding analysis using quasi-2D hydraulic modeling and geospatial data.* (Doctorate of Engineering), Katholieke Universiteit Leuven.

Toombes, L. and Chanson, H., 2011. Numerical Limitations of Hydraulic Models. *34th IAHR World Congress - Balance and Uncertainty*, Brisbane, Australia. pp. 2322-2329.

Trinh, C.N., Ha, D.P. and Nguyen, M., 2018. Application of swash on modeling dam-break flow over a triangular bottom sill.

Trivellato, F., 2004. Experimental and numerical investigation of bore impact on a wall. *Trans Built Environ,* 71(3-12).

UNISDR, Wallemacq, P., Guha-Sapir, D. and McClean, D., 2015. *The Human Cost of Weather Related Disasters - 1995 - 2015.*

Vanderkimpen, P., Melger, E. and Peeters, P., 2009. Flood modeling for risk evaluation – a MIKE FLOOD vs. SOBEK 1D2D benchmark study. *Flood Risk Management: Research and Practice*.

Vasquez, J. and Roncal, J.J., 2009. Testing river 2D and flow 3D for sudden dam break flow simulations.

Vischer, D. and Hager, W.H., 1998. *Dam hydraulics.* Wiley.

Wang, B., Chen, Y., Wu, C., Peng, Y., Ma, X. and Song, J., 2017. Analytical solution of dam-break flood wave propagation in a dry sloped channel with an irregular-shaped cross-section. *Journal of Hydro-environment Research,* 14, pp. 93-104.

Wang, J.P. and Liang, Q., 2011. Testing a new adaptive grid-based shallow flow model for different types of flood simulations. *Journal of Flood Risk Management,* 4(2), pp. 96-103.
Wang, L.H. and Pan, C.H., 2014. An analysis of dam-break flow on slope. *Journal of Hydrodynamics,* 26(6), pp. 902-911.

Warren, R.A., Kirshbaum, D.J., Plant, R.S. and Lean, H.W., 2014. A 'Boscastle-type' quasi-stationary convective system over the UK Southwest Peninsula. *Quarterly Journal of the Royal Meteorological Society,* 140, pp. 240-257.

Webb, S., 2013. Heavy rain and flooding in and around Aberystwyth on 8–9 June 2012. *Waether,* 68(6), pp. 162-165.

Weber, F.J., 2003. *Ultrasonic Beam Propagation in Turbulent Flow* (Partial Fulfillment of the Requirements for the Degree of Doctor of Philosophy).

Wemmenhove, R., Gladso, R., Iwanowski, B. and Lefranc, M., 2010. Comparison of CFD calculations and experiment for the dambreak experiment with one flexible wall. *20th ISOPE, June*.

Werner, M. and Cranston, M., 2009. Understanding the Value of Radar Rainfall Nowcasts in Flood Forecasting and Warning in Flashy Catchments. *Meteorological Applications,* 16(1), pp. 41-55.

Whitham, G.B., 1955. The effects of hydraulic resistance in the dambreak problem. *Proc. R. Soc. Lond.,* 227, pp. 399–407.

Wienke, J. and Oumeraci, H., 2005. Breaking wave impact force on a vertical and inclined slender pile—theoretical and large-scale model investigations. *Coastal Engineering,* 52(5), pp. 435-462.

Wilson, C.A.M.E., 2007. Flow resistance models for flexible submerged vegetation. *Journal of Hydrology,* 342, pp. 213–222.

Wilson, C.A.M.E. and Horritt, M.S., 2002. Measuring the flow resistance of submerged grass. *Hydrological Processes,* 16, pp. 2589 –2598.

World Meteorological Organisation, 2007. *Guidance on Flash Flood Management - Recent Experience from Central and Eastern Europe.* Geneva, Switzerland.

World Meteorological Organisation, 2012. *Management of Flash Floods.*

World Meteorological Organisation, 2017. *Flash Flood Guidance Systems.* Geneva, Switzerland.

World Weather & Climate, 2016. *CLimate in Boscastle* [Online]. Available from: *https://weather-and-climate.com/average-monthly-precipitation-Rainfall-inches,boscastle-cornwall-gb,United-Kingdom* [Accessed August].

Xia, J., Falconer, R.A. and Lin, B., 2011a. Incipient velocity for partially submerged vehicles in floodwaters AU - Shu, Caiwen. *Journal of Hydraulic Research,* 49(6), pp. 709-717.

Xia, J., Falconer, R.A., Lin, B. and Tan, G., 2011b. Modelling flash flood risk in urban areas. *Proceedings of the Institution of Civil Engineers - Water Management,* 164(6), pp. 267-282.

Xia, J., Falconer, R.A., Xiao, X. and Wang, Y., 2014. Criterion of vehicle stability in floodwaters based on theoretical and experimental studies. *Natural Hazards* 70.

Xia, J., Teo, F., Falconer, R.A., Chen, Q. and Deng, S., 2016. Hydrodynamic experiments on the impacts of vehicle blockages at bridges. *Journal of Flood Risk Management,* (11), pp. S395–S402

Yang, C., Lin, B., Jiang, C. and Liu, Y., 2010. Predicting near-field dam-break flow and impact force using a 3D model. *Journal of Hydraulic Research,* 48(6), pp. 784-792.

Yu, C. and Duan, J., 2014. Two-Dimensional Finite Volume Model for Sediment Transport in Unsteady Flow. In: A.S.o.C.E. (ASCE), ed. *World Environmental and Water Resources Congress 2014: Water Without Borders - Proceedings of the 2014 World Environmental and Water Resources Congress*Portland, United States. pp. 1432-1441.

Zang, J., Taylor, P.H., Morgan, G., Tello, M., Grice, J. and Orszaghova, J., 2010. Experimental study of non-linear wave impact on offshore wind turbine flundations *Coastlab10 – 3rd International Conference on the Application of Physical Modelling to Port and Coastal Protection*Barcelona, Spain.

Zech, Y., Soares-Frazão, S. and Van Emelen, S., 2015. Modelling of fast hydraulic transients: issues, challenges, perspectives. *La Houille Blanche,* (5), pp. 5-15.

Zhainakov, A.Z. and Kurbanaliev, A.Y., 2013. Verification of the open package OpenFOAM on dam break problems. *Thermophysics and Aeromechanics,* 20(4), pp. 451-461.

Zhao, D., H.Shen, G.Tabios, Lai, J. and Tan, W., 1994. Finite-Volume Two-Dimensional Unsteady-Flow Model for River Basins *Journal of Hydraulic Engineering,* 120(7), pp. 863-883.

Zhou, J.G., Causon, D.M., Mingham, C.G. and Ingram, D.M., 2001. The Surface Gradient Method for the Treatment of Source Terms in the Shallow-Water Equations. *Journal of Computational Physics,* 168(1), pp. 1-25.

Zhou, Z.Q., Kat, J.O.D. and Buchner, B., 1999. A nonlinear 3D approach to simulate green water dynamics on deck*Seventh International Conference on Numerical Ship Hydrodynamics*. pp. 1-4.

Zogg, J. and Deitsch, K., 2013. The Flash Flood Potential Index at WFO Des Moines. *Technical Report,* [Online]. Available from: *http://www.crh.noaa.gov/Image/dmx/hydro/FFPI/FFPI_WriteUp.pdf* [Accessed 11 April 2019].

Zolghadr, M., Hashemi, M.R. and Zomorodian, S.M.A., 2010. Assesment of MIKE21 model in dam and dike-break simulation. *Transactions of Civil Engineering,* 35(C2), pp. 247-262.

Zoppou, C. and Roberts, S., 2000. Numerical solution of the two-dimensional unsteady dam break. *Applied Mathematical Modelling,* 24(7), pp. 457-475.

APPENDICES

APPENDIX A: SUPPLEMENTAL INFORMATION

A.1 Features of riverine floods and flash floods

Table A- 1- Original work by Jianchu et al. (2006) presenting the features of riverine floods and flash floods

Table 1: Features of riverine floods and flash floods		
	Riverine floods	**Flash floods**
Features	• slow water level rise beyond natural channels • reaches peak flow within hours to days • slow recession (within several hours to days) • mostly coinciding with high baseflow levels • medium to long lag times	• rapid water level rise above natural channels • reaches peak flow within minutes up to a few hours • rapid recession (within minutes to a few hours) • often dissipating quickly • not necessarily related to baseflow levels • short lag times
Causes	• prolonged seasonal precipi-tation of low to high intensity • seasonal snow and glacial melt	• very high intensity rainstorms/ cloudbursts • rapid snow/glacial melt • dam (both artificial and natural) breaks
Associated problems	• inundation	• often carry high sediment and debris loads • very high hydraulic force and herewith erosive power
Frequency	• annually during rainy season	• occasional, any time during the year
Affected areas	• river plains and valleys • local to regional extent • large areas can be affected	• river plains and valleys • alluvial fans • mostly local extent • generally small to medium areas are affected
Issues	• with appropriate technology and measures in place forecasting is easily possible	• very difficult to forecast
Potential mitigation measures	• real-time flood forecasting • community preparedness and awareness • appropriate emergency measures	• early warning systems • community preparedness and awareness • appropriate emergency measures

A.2 Flood defence mitigation for Boscastle

Figure A- 1- Flood defence mitigation for Boscastle presented by Nicholas Pearson Associates (2012)

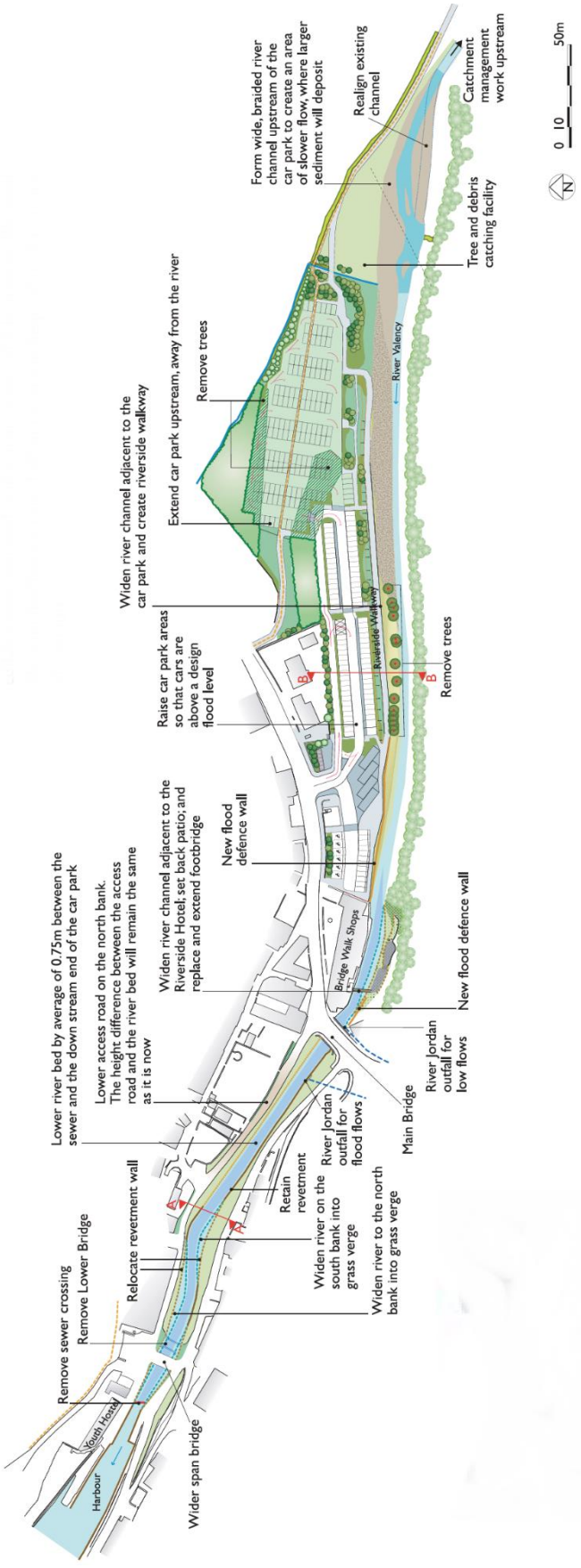

APPENDIX B: EXPERIMENTAL SETUP

B.1 Gate opening

Figure A- 2- Gate opening for H=0.2 m. From left to right, t=0.08 s, t=0.172 s, t=0.22 s and t=0.28 s

(a) $t = 0.08\ s$

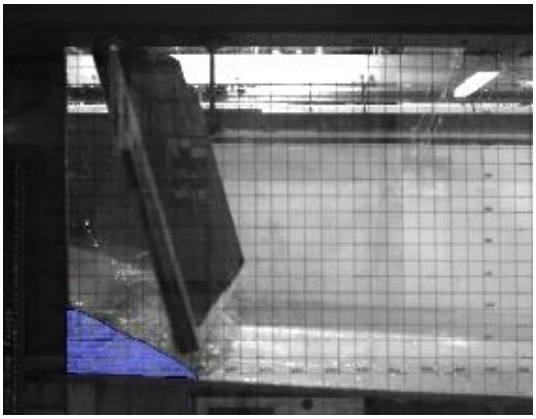

(b) $t = 0.172\ s$

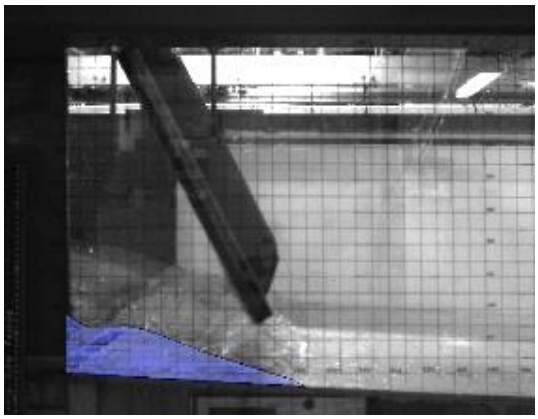

(c) $t = 0.22\ s$

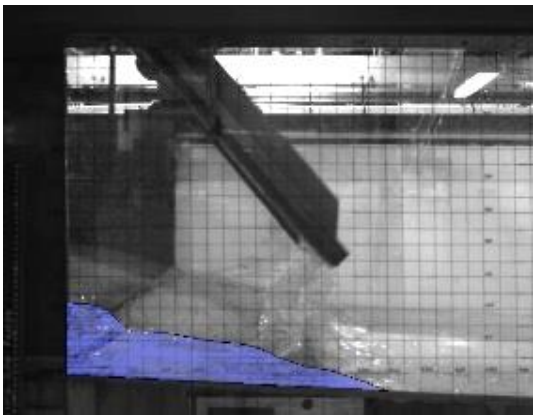

(d) $t = 0.28\ s$

Figure A- 3- Gate opening for H=0.1 m. From left to right, (a) t=0.1 s, (b) t=0.124 s, (c) t=0.2 s and (d) t=0.28 s

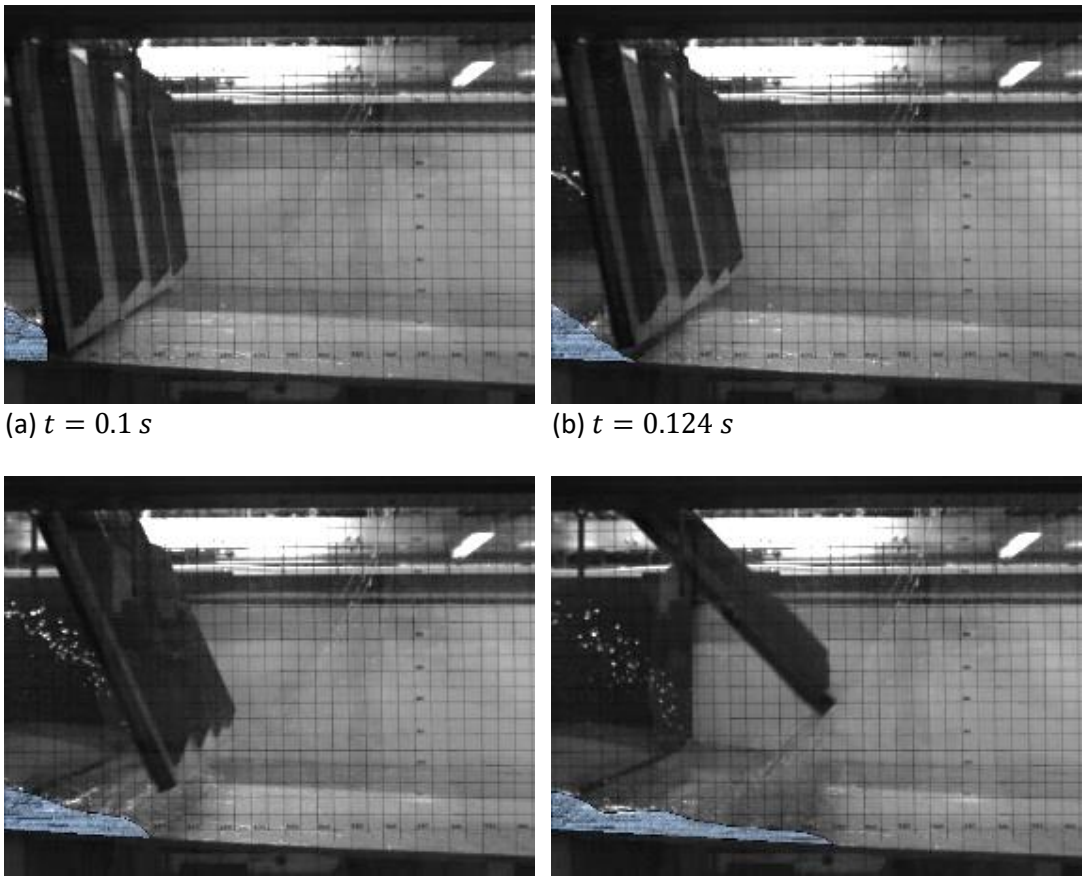

(a) $t = 0.1\ s$ (b) $t = 0.124\ s$

(c) $t = 0.2\ s$ (d) $t = 0.28\ s$

APPENDIX C: OPENFOAM

C.1 Boundary conditions

Table A- 2- Definitions of OpenFOAM boundary conditions (NEXTfoam, 2014; Greenshields, 2015)

Boundary Condition	Definition
`zeroGradient`	This boundary condition applies a zero-gradient condition from the patch internal field onto the patch faces.
`inletOutlet`	This boundary condition provides a generic outflow condition, with specified inflow for the case of return flow.
`noSlip`	This boundary condition fixes the velocity to zero at walls.
`pressureInletOutletVelocity`	This velocity inlet/outlet boundary condition is applied to pressure boundaries where the pressure is specified. A zero-gradient condition is applied for outflow (as defined by the flux); for inflow, the velocity is obtained from the patch-face normal component of the internal-cell value.
`fixedFluxPressure`	This boundary condition adjusts the pressure gradient such that the flux on the boundary is that specified by the velocity boundary condition.
`totalPressure`	This boundary condition provides a total pressure condition. Four variants are possible: incompressible subsonic (default), compressible subsonic, compressible transonic and compressible supersonic.
`kqRWallFunction`	This boundary condition is applied to turbulence k, q, and R when using wall functions, and simply enforces a zero-gradient condition (Neumann boundary).
`epsilonWallFunction`	This boundary condition provides a turbulence dissipation wall function condition for high Reynolds number, turbulent flow cases. The condition can be applied to wall boundaries, whereby it calculates ε (turbulence dissipation field) and G (turbulence generation field) and inserts near wall epsilon values directly into the epsilon equation to act as a constraint.
`nutkWallFunction`	This boundary condition provides a turbulent kinematic viscosity condition when using wall functions, based on turbulence kinetic energy.
`nutkRoughWallFunction`	This boundary condition provides a turbulent kinematic viscosity condition when using wall functions for rough walls, based on turbulence.
`calculated`	This boundary condition is not designed to be evaluated; it is assumed that the value is assigned via field assignment, and not via a call.

C.2 2D-3D Coupling code

```
/*--------------------------------*- C++ -*----------------------------------*\
| =========                 |                                                 |
| \\      /  F ield         | OpenFOAM: The Open Source CFD Toolbox           |
|  \\    /   O peration     | Version:  5                                     |
|   \\  /    A nd           | Web:      www.OpenFOAM.org                      |
|    \\/     M anipulation  |                                                 |
\*---------------------------------------------------------------------------*/
FoamFile
{
    version     2.0;
    format      ascii;
    class       volVectorField;
    location    "0";
    object      U;
}
// * * * * * * * * * * * * * * * * * * * * * * * * * * * * * * * * * * * * * //

dimensions      [0 1 -1 0 0 0 0];

internalField   uniform (0 0 0);

boundaryField
{
    inlet
    {
        type            codedFixedValue;
        value           uniform (0 0 0);
        name            hydrographUFixedValue;
        codeInclude     #{
                              #include <vector>
                              #include <utility>
                            #};

         localCode        #{
         const std::vector< std::pair<double, double> > myhydrograph =
                              {
                               #include "../../velocityNew2.csv"
                              };
                            #};

        code             #{
         size_t i = 0;
         double time_hours = this->db().time().value() / 3600.0;
         while (myhydrograph.at(i).first < time_hours)
                 {
                 i = i + 1;
                 }
         double dt = myhydrograph.at(i).first - myhydrograph.at(i-1).first;
         double dh = myhydrograph.at(i).second - myhydrograph.at(i-1).second;
         double h =myhydrograph.at(i-1).second +dh *(time_hours - myhydrograph.at(i-1).first) /dt;
         double target_u = h;

         operator==( Vector<double>(target_u, 0.0, 0.0) );
                           #};
    }
```

```
    outlet
    {
        type            pressureInletOutletVelocity;
        value           uniform (0 0 0);
    }
    bottom
    {
        type            noSlip;
    }
    atmosphere
    {
        type            pressureInletOutletVelocity;
        value           uniform (0 0 0);
    }
    sides
    {
        type            noSlip;
    }
}


// ************************************************************************* //
```

```
/*--------------------------------*- C++ -*----------------------------------*\
| =========                 |                                                 |
| \\      /  F ield         | OpenFOAM: The Open Source CFD Toolbox           |
|  \\    /   O peration     | Version:  5                                     |
|   \\  /    A nd           | Web:      www.OpenFOAM.org                      |
|    \\/     M anipulation  |                                                 |
\*---------------------------------------------------------------------------*/
FoamFile
{
    version     2.0;
    format      ascii;
    class       volScalarField;
    object      alpha.water;
}
// * * * * * * * * * * * * * * * * * * * * * * * * * * * * * * * * * * * * * //

dimensions      [0 0 0 0 0 0 0];

internalField   uniform 0;

boundaryField
{
    inlet
    {
        type            inletOutlet;
        inletValue      uniform 1;
        value           uniform 1;
    }


    outlet
    {
        type            inletOutlet;
        inletValue      uniform 0;
        value           uniform 0;
    }


    bottom
    {
        type            zeroGradient;
    }

    atmosphere
    {
        type            inletOutlet;
        inletValue      uniform 0;
        value           uniform 0;
    }

    sides
    {
        type            zeroGradient;
    }

}

// ************************************************************************* //
```